

# DOTTORATO DI RICERCA IN MECCANICA E SCIENZE AVANZATE DELL'INGEGNERIA

Ciclo 37

Settore Concorsuale: 09/C2 - FISICA TECNICA E INGEGNERIA NUCLEARE

**Settore Scientifico Disciplinare:** ING-IND/10 - FISICA TECNICA INDUSTRIALE

## CONTROL-ORIENTED MODEL OF REFRIGERATION UNITS FOR RESIDENTIAL AND INDUSTRIAL APPLICATIONS

Presentata da: Michael Giovannini

**Coordinatore Dottorato** 

Lorenzo Donati

**Supervisore** 

Marco Lorenzini

**Co-supervisore** 

Matteo Zanzi

Sandro Manservisi

Esame finale anno 2025

#### **ABSTRACT**

The Vapour Compression System (VCS) is the leading technology in the refrigeration sector, and it is also employed for Heat Pump (HP). The dynamical modelling could play a paramount role in the optimisation of such systems, from the design phase to the development of real-time control applications as Digital Twins. In this context, this work describes in detail the realisation of a dynamical model of a VCS in Simulink<sup>®</sup>. The model is validated employing experimental data obtained with a test machine, composed of a reciprocating compressor, two brazed-plate Heat Exchangers (HEXs) in counterflow arrangement, the electronic expansion valve and some auxiliaries. The HP behaviour is investigated during different transients of compressor speed and valve opening. The test ring is analysed, and the reliability of the available measurements for the investigation of transients is assessed. The model of each component is developed and validated experimentally; a numerical verification is proposed where suitable data are not available. The model of the compressor, the expansion valve, the piping and the vessels are faced with a lumped parameter approach. Much effort is devoted to the HEXs model using a finite volume approach. The work proposes some measures useful to enhance its accuracy and stability and reduce its computational load. The full machine model can predict the process variables with reasonable accuracy. The refrigerant mass flow rate is calculated within 5% of the experimental data. The average pressure deviation in the two HEX settles around 20-40 kPa, corresponding to less than 1 °C in the estimation of the saturation temperature. All the temperatures of the working fluids are estimated with an absolute deviation of less than 1 °C.

## CONTENTS

Cc	nten	ts	ii
Lis	st of S	Symbol	s vi
Su	bscri	pts v	viii
Ał	brev	iations	ix
Gl	ossar	У	x
		-	xi
		Tables	XX
Int	trodu	ction	xxi
1	Vap	our Co	mpression Systems modelling 1
	-		r Compression Systems 1
		-	ture overview 4
			se of numerical models 6
2	_		ling of dynamical systems 8
	2.1		mical systems 8
		-	System response and stability 9
	2.2	Static	systems 10
		2.2.1	When can a physical system be treated as non-
			dynamical? 10
	2.3	Stiffne	ess 11
3	Exp	erimen	tal facility and data processing 13
	3.1	Test a	pparatus 13
		-	Compressor 14
			Brazed plate heat exchanger 16
		-	Expansion valve 16
			Refrigerant accumulators 17
			Pipes 17
	3.2		rement instrumentation 17
		-	Mass flow rate 18
			Temperature 19
			Pressure 19
		-	Electric power consumption 19
	3.3		processing 20
		3.3.1	Data acquisition 20
		3.3.2	Measurements employed and calculated quanti-
		2.2.2	ties 20
			Data analysis 21 Dynamic behaviour of the temperature sensor 25
			D ( 11)
	2.4		Data smoothing 27 erformed 29
	J•4	rest p	C1101111C4 29

4	Phy	sical properties of the working fluids 33
	4.1	7 1 1
		4.1.1 Simulink <sup>®</sup> Lookup Tables 34
		4.1.2 Required tables 34
		4.1.3 Operating limits 36
		4.1.4 Evaluation of the partial derivatives 39
		4.1.5 Saturation curve 40
5	The	governing equation 41
	5.1	Balance equations 41
		5.1.1 Mass balance equation 41
		5.1.2 Energy balance equation 41
	5.2	Heat transfer 42
6	Con	pressor 43
		Compressor modelling 43
	6.2	Physically-based model 45
		6.2.1 Efficiencies evaluation 46
	6.3	Polynomial approach 48
	-	Validation of the compressor models 49
	·	6.4.1 Mass flow rate 50
		6.4.2 Power consumption 51
		6.4.3 Refrigerant outlet temperature 52
		6.4.4 Dynamic outlet refrigerant conditions 53
		6.4.5 Concluding remarks on the dynamic correction
		of the temperature 60
7	Pipi	ng 62
	7.1	Pressure losses due to friction 63
		7.1.1 Distributed pressure losses 63
	7.2	Friction factor 64
		7.2.1 Friction factor in two-phase flow 65
		7.2.2 Localised pressure losses 68
		7.2.3 The order of magnitude of the pressure losses 69
	7.3	Model realization 69
8	Exp	ansion valve 72
	8.1	Expansion valve operation 72
		8.1.1 Thermostatic valve 72
		8.1.2 Electrically actuated valve 73
	8.2	Numerical modelling 74
		8.2.1 The manufacturer correlation 74
		8.2.2 The valve block 75
	8.3	Validation and tuning 76
9	_	d storage vessels 78
-	9.1	Numerical model 78
	•	9.1.1 Solution algorithm 78
		9.1.2 Function block structure 79
	0.2	Numerical tests for the accumulator 81

		9.2.1	Results and discussion 82
		9.2.2	Numerical considerations 85
10	Heat	exchai	ngers numerical modelling 95
	10.1	Finite	volume approach 96
			Basic assumptions 96
			Block interface 97
			Development of the model equations 98
	10.2	_	on schemes 100
		10.2.1	First scheme 101
		10.2.2	Second scheme with mass flow rate filtering 103
			Third scheme with secondary fluid states 104
	10.3	-	values analysis 105
	-	_	ransfer rate 107
	'		Correlations for the heat transfer coefficients 108
	10.5	•	nentation 109
	,		Boundary values 109
		-	Initial conditions 110
			Zones extension 111
		0 0	Heat Transfer Coefficient calculation tricks 111
			Outlet conditions 113
		10.5.6	Integration time step 114
	10.6	-	ation 114
11	Full	machir	ne simulation 116
	11.1	Nume	rical setup 116
			Basic configuration 119
	11.2		of the number of elements 119
	11.3	Tuning	g to enhance accuracy 129
		_	Tuning according to data from Test 2 with R450A 129
			Tuning verification under Test 1 with R450A con-
		_	ditions 133
	11.4	Full m	odel analysis 138
		11.4.1	Validation of Full Model in Test 2 with R450A 138
		11.4.2	Validation of the Full Model in Test 1 with R450A 146
		11.4.3	Evaluation of the pressure losses in the HEXs 149
	11.5	Comp	ressor and expansion valve 153
		11.5.1	Simplified Model Test 1 with R450A 153
		11.5.2	Simplified Model Test 2 with R450A 154
		11.5.3	Full Model Test 1 with R450A 157
		11.5.4	Full Model Test 2 with R450A 159
	11.6	Summ	ary of the results 161
12	Cond	clusion	s 164
4	Func	dament	als of heat transfer 167
	A.1	Conve	ctive heat transfer at constant wall temperature 167
		A.1.1	Exponential temperature profile 167
		A 1 2	Linear temperature profile 168

		A.1.3	Comparison of the accuracy of two methods 168
В	Hea	t Trans	fer Correlations 170
	B.1	Heat 7	Transfer Correlations for BPHEX 170
		B.1.1	Brazed Plate Heat Exchanger (BPHEX) geometri-
			cal parameters 170
		B.1.2	Single phase flow 170
		B.1.3	Refrigerant two phase flow: boiling 171
		B.1.4	Condensation 172

# LIST OF SYMBOLS

Symbol	Description	Unit
A	area	$m^2$
$A_{c}$	cross sectional area	$m^2$
ρ	density	${\rm kg}{\rm m}^{-3}$
D	diameter	m
λ	eigenvalue	-
$\eta_{em}$	electromechanical efficiency	-
w	frequency	Hz
f	friction factor	-
g	gravity acceleration	$\mathrm{m}\mathrm{s}^{-2}$
g Q	heat transfer rate	W
α	HTC	${\rm W}{\rm m}^{-2}{\rm K}^{-1}$
U	internal energy	J
$\eta_{is}$	isoentropic efficiency	-
L	lenght	m
m	mass	kg
ṁ	mass flow rate	$ m kgs^{-1}$
G	mass flux	$kg s^{-1} m^{-2}$
$\mathfrak{u}_{\mathfrak{m}}$	mean velocity	$\mathrm{m}\mathrm{s}^{-1}$
$V_n$	nominal displacement	$cm^3$
$n_p$	number of polar pairs	-
Ω	number of revolutions	Hz
p	pressure	Pa
pr	pressure ratio	-
Re	Reynolds number	-
$\epsilon$	roughness	μm
S	slip ratio	
h	specific ehthalpy	$J kg^{-1}$
ġ	specific heat transfer rate	${ m Wm^{-2}}$
u	specific internal energy	$\rm Jkg^{-1}$
S	thickness	mm
τ	time constant	S
$\Delta t$	time step	S
$k_v$	valve flow coefficient	${\rm m}^3{\rm h}^{-1}$
χ	vapour quality	-
μ	viscosity	Pas
γ	void fraction	-
V	volume	$m^3$

$\eta_{vol}$ volumetric efficiency $\dot{V}$ volumetric flow rate $\dot{B}$ width	$m^{3} s^{-1}$

## SUBSCRIPTS

Symbol	Description
a	air, all
ch	channel
cnd	condenser
cor	corrected
D	discharge
e	electric, equilibrium
evp	evaporator
f	fluid
i	input, inlet section
is	isoentropic
1	liquid
m	mean
0	output, outlet section, outer side
r	refrigerant
sat	saturation
S	secondary fluid
stat	static
S	suction
$\mathbf{V}$	vapour
W	wall

## **ABBREVIATIONS**

Symbol	Description
BPHEX	Brazed Plate Heat Exchanger
COP	Coefficient of Performance
CPU	Central Processing Unit
DAE	Differential Algebraic system of Equation
EXV	Expansion Valve
FDD	Fault Detection and Diagnosis
fs	Full Scale
FV	Finite Volume
GWP	Global Warming Potential
HEX	Heat Exchanger
HP	Heat Pump
HVACR	Heating, Ventilation, Air Conditioning and Refrigeration
IO	Input-Output
ISO	Input-State-Output
LNG	Liquified Natural Gas
LR	Liquid Receiver
MB	Moving Boundary
NTU	Number of Transfer Units
ODE	Ordinary Differential Equation
PDC	Positive Displacement Compressor
PDE	Partial Differential Equation
PWM	Pulse-Width Modulation
RTD	Resistence Temperature Detector
rv	Reading value
SA	Suction Accumulator
SC	Subcooled liquid
SH	Superheated vapour
SP	single phase
TP	two phase
UoM	Unit of Measurement
VCS	Vapour Compression System

## GLOSSARY

Notation	Description
condenser model	
dynamical system	
evaporator model	
Full Model	
Lookup Table	
Matlab®	
Modelica <sup>®</sup>	
run time	Calculation time
Simplified Model	
Simulink <sup>®</sup>	
static system	section 2.2
Test 1 with R450A	section 3.4
Test 2 with R450A	section 3.4
time scale	
Tune o	table 20
Tune 1	table 20
Tune 2	table 20

## LIST OF FIGURES

Figure 1	Basic scheme of a subcritical VCS with the corresponding thermodynamic processes represented	
	on the p-h diagram.	
Figure 2	Layout of the experimental facility at the Milan	
	Polytechnic. 14	
Figure 3	Operating envelope of compressor Frascold D3.13.13	Y
Figure 4	Accuracy evaluation of the refrigerant mass flow	
	rate measurements and smoothing solutions	
	comparison. 22	
Figure 5	Accuracy evaluation of the water mass flow rate	
	measurements in the hot secondary circuit and	
	smoothing solutions comparison. 22	
Figure 6	Accuracy evaluation of the refrigerant tempera-	
	ture measurements at the condenser inlet. 23	
Figure 7	Accuracy evaluation of the refrigerant tempera-	
	ture measurements at the condenser inlet. 23	
Figure 8	Accuracy evaluation of the refrigerant pressure	
C	measurements at the compressor inlet and smooth-	
	ing solutions comparison. 24	
Figure 9	Accuracy evaluation of the refrigerant pressure	
0	measurements at the condenser inlet and smooth-	
	ing solutions comparison. 24	
Figure 10	Accuracy evaluation of the comparison of com-	
O	pressor electric power measurements and smooth-	
	ing solutions. 25	
Figure 11	Temperature transducer RTD Pt100 by Carel	
O	Carel, 2023. 26	
Figure 12	Simulink <sup>®</sup> scheme of the temperature transducer	
O	model. 27	
Figure 13	Verification of the effect of the transducer dy-	
0 9	namics on the refrigerant outlet temperature	
	evaluated by the compressor physical model.	
	The experimental data (Exp data) are compared	
	with the values calculated using the physical	
	model of the compressor (Physical) and with	
	the same values filtered by the sensor model	
	$(T_{\text{out}} \text{ sensor}).$ 28	
Figure 14	Controlled input during the Test 1 with R450A.	30
		,

Figure 15	Controlled input during the Test 2 with R450A. 30
Figure 16	Experimental behaviour of secondary fluids dur-
O	ing Test 1 with R450A. From the top: inlet and
	outlet temperature of the secondary fluids in
	the condenser and in the evaporator, and their
	mass flow rate. 31
Figure 17	Experimental behaviour of secondary fluids dur-
0 7	ing Test 2 with R450A. From the top: inlet and
	outlet temperature of the secondary fluids in
	the condenser and in the evaporator, and their
	mass flow rate. 32
Figure 18	P-h diagram for R <sub>4</sub> 50A. 36
Figure 19	T-s diagram for R <sub>4</sub> 50A. 37
Figure 20	P-u diagram for R450A. 37
Figure 21	Saturation curve relative to R <sub>4</sub> 50A refrigerant. 40
Figure 22	Physically-based model of the compressor real-
O	ized in the Simulink <sup>®</sup> environment. 47
Figure 23	Simulink <sup>®</sup> scheme of the compressor model ac-
0 9	cording the polynomial approach. Each block
	evaluates one polynomial corresponding to one
	process variable: the mass flow rate $\dot{\mathfrak{m}}_{r}$ , the
	outlet temperature T <sub>r,out</sub> and the electric power
	consumption $P_e$ . 49
Figure 24	The Simulink® code of the mass flow rate poly-
	nomial of the compressor model; each 2D Lookup
	Table evaluates the coefficients $a_i$ by linear in-
	terpolating the tabulated data. 50
Figure 25	Compressor mass flow rate validation during
	Test 1 with R450A. 51
Figure 26	Compressor mass flow rate validation during
	Test 2 with R450A. 52
Figure 27	Validation of the electric power consumption of
	the compressor during Test 1 with R450A. 53
Figure 28	Validation of the electric power consumption of
	the compressor during Test 2 with R <sub>4</sub> 50A. 54
Figure 29	Refrigerant outlet temperature validation dur-
	ing Test 1 with R450A. 55
Figure 30	Refrigerant outlet temperature validation dur-
	ing Test 2 with R450A. 56
Figure 31	Block for evaluating the dynamic behaviour of
	the refrigerant outlet temperature, with only the
	thermal capacity effect named version o

Figure 32	Block for evaluating the dynamic behaviour of	
	the refrigerant outlet temperature, which is as-	
	sumed equal to the temperature of the shell,	
	second approach, named version 1. 57	
Figure 33	Enhanced version of the block for evaluating	
0 33	the dynamic behaviour of the refrigerant outlet	
	temperature, with a linear interpolation tuning	
	on the heat transfer coefficient on the refrigerant	
	side, named version 2. 58	
Figure 34	Function block for evaluating the dynamic be-	
0 91	haviour of the refrigerant outlet temperature,	
	which is decoupled from that of the wall, ver-	
	sion 4. 59	
Figure 35	Validation of the dynamic prediction of the com-	
	pressor refrigerant outlet temperature during	
	Test 1 with R450A. The different versions of the	
	dynamic correction of the outlet temperature	
	are compared, see table 17. 60	
Figure 36	Validation of the dynamic prediction of the com-	
rigare jo	pressor refrigerant outlet temperature during	
	Test 2 with R450A. The different versions of the	
	dynamic correction of the outlet temperature	
	are compared, see table 17. 61	
Figure 37	Comparison between the homogeneous models	
116416 37	for the pressure drop evaluation in a circular	
	tube with R450A. 70	
Figure 38	Model of the pipe realized in Simulink <sup>®</sup> 70	
Figure 39	Simulink <sup>®</sup> scheme of the expansion valve. 76	
Figure 40	Simulink <sup>®</sup> scheme of the numerical test rig em-	
1180110 40	ployed for the validation of the EXV model. 76	
Figure 41	Tuning of the EXV flow coefficient with experi-	
	mental data under Test 2 with R450A, see sec-	
	tion 3.4. 77	
Figure 42	Validation of the valve tuning against two valve	
0 4-	opening transients, from Test 1 with R450A, see	
	section 3.4.	
Figure 43	Model of the accumulator realized in Simulink <sup>®</sup> .	81
Figure 44	Numerical test set-up with two accumulation	
0 IT	devices and one pipe, in Simulink <sup>®</sup> . 82	
Figure 45	Numerical test rig with two accumulations de-	
0 10	vice and two pipes models, in Simulink <sup>®</sup> . 83	

Figure 46 First numerical test with two accumulators (V=0.5 m<sup>3</sup> for both) and a pipe. Starting from the top, mass flow rate through the pipe, pressure in the two vessels and deviation between them normalised by the pressure in the upstream vessel. First numerical test with two accumulators (V=0.5 m<sup>3</sup> Figure 47 for both) and a pipe. Starting from the top: temperatures, vapour quality and mean density in the two vessel. Figure 48 Second numerical test with two accumulators  $(V_1=2.8 \text{ dm}^3 \text{ V}_2=0.5 \text{ m}^3)$  and a pipe. Starting from the top, mass flow rate through the pipe, pressure in the two vessels and deviation between them normalised by the pressure in the upstream vessel. Second numerical test with two accumulators Figure 49  $(V_1=2.8 \text{ dm}^3, V_2=0.5 \text{ m}^3)$  and a pipe. Starting from the top: temperatures, vapour quality and mean density in the two vessels. Figure 50 Third numerical test with two accumulators (both V=2.8 dm<sup>3</sup>) and two pipes. Starting from the top, mass flow rate through the two pipes, pressure, the vapour quality and temperature in each vessel. Figure 51 Numerical test of the accumulators (V=0.5 m<sup>3</sup> for both) and pipe. Starting from the bottom, mass flow rate through the pipe, pressure in the two vessels and deviation between them normalised by the pressure in the upstream vessel. In this case, the time constant of the pipe is imposed 10 times those of the upstream vessel, with a time step of 0.1 s. Numerical test of the accumulators ( $V_1$ =2.8 dm<sup>3</sup> Figure 52  $V_2$ =0.5 m<sup>3</sup>) and pipe. Starting from the top, mass flow rate through the pipe, pressure in the two vessel and deviation between them normalised by the pressure in the upstream vessel. In this case the  $\tau_p$  of the pipe is imposed to 25 times the  $\tau_1$  of the upstream vessel and the solver time step in the same way.

Figure 53	Numerical test of the accumulators ( $V_1$ =2.8 dm <sup>3</sup> $V_2$ =0.5 m <sup>3</sup> ) and pipe. Starting from the top, mass flow rate through the pipe, pressure in the
	two vessels and deviation between them nor-
	malised by the pressure in the upstream vessel.
	In this case, the $\tau_p$ of the pipe is imposed to
	50 times the $\tau_1$ of the upstream vessel and the
	solver time step in the same way. 93
Figure 54	Scheme of the Simulink® code of the condenser. 115
Figure 55	Scheme of the Simulink® code of the full VCS
	model composed by compressor, expansion valve,
T	condenser and evaporator. 117
Figure 56	Scheme of the Simulink® code of the full VCS
	model composed by compressor, expansion valve,
	condenser, evaporator, LR and SA with the cor-
T.	responding pipes. 118
Figure 57	Condenser pressure: Simplified Model, Test 2
T. 0	with R450A, HEX model with 20 elements. 120
Figure 58	Condenser pressure: Simplified Model, Test 2
	with R450A, HEX model with 30 elements. 121
Figure 59	Condenser pressure: Simplified Model, Test 2
T	with R450A, HEX model with 40 elements. 121
Figure 60	Condenser saturation temperature: Simplified
	Model, Test 2 with R450A, HEX model with 30
	elements. 122
Figure 61	Condenser water outlet temperature: Simplified
	Model, Test 2 with R450A, HEX model with 30
T	elements. 122
Figure 62	Condenser water outlet temperature: Simplified
	Model, Test 2 with R450A, HEX model with 40
T	elements. 123
Figure 63	Condenser refrigerant outlet temperature: Sim-
	plified Model, Test 2 with R450A, HEX model
	with 30 elements. 123
Figure 64	Condenser refrigerant outlet temperature: Sim-
	plified Model, Test 2 with R450A, HEX model
T	with 40 elements. 124
Figure 65	Evaporator pressure: Simplified Model, Test 2
T! ((	with R450A, HEX model with 20 elements. 124
Figure 66	Evaporator pressure: Simplified Model, Test 2
П'	with R450A, HEX model with 40 elements. 125
Figure 67	Evaporator saturation temperature: Simplified
	Model, Test 2 with R450A, HEX model with 20
	elements. 126

Figure 68	Evaporator water glycol ethylene mixture out-
	let temperature: Simplified Model, Test 2 with
T	R450A, HEX model with 20 elements. 126
Figure 69	Evaporator water glycol ethylene mixture out-
	let temperature: Simplified Model, Test 2 with
	R <sub>450</sub> A, HEX model with 40 elements. 127
Figure 70	Evaporator refrigerant outlet temperature: Sim-
	plified Model, Test 2 with R450A, HEX model
	with 20 elements. 127
Figure 71	Evaporator refrigerant outlet temperature: Sim-
	plified Model, Test 2 with R450A, HEX model
	with 40 elements. 128
Figure 72	Condenser pressure: Simplified Model, Test 2
	with R450A, condenser model with 30 elements
	and Tune o. 130
Figure 73	Condenser refrigerant outlet temperature: Sim-
	plified Model, Test 2 with R450A, condenser
	model with 30 elements and Tune 0. 131
Figure 74	Condenser pressure: Simplified Model, Test 2
0 71	with R450A, condenser model with 30 elements
	and Tune 1. 132
Figure 75	Condenser refrigerant outlet temperature: Sim-
75	plified Model, Test 2 with R450A, condenser
	model with 30 elements and Tune 1. 132
Figure 76	Condenser pressure: Simplified Model, Test 2
1180110 70	with R450A, condenser model with 30 elements
	and Tune 2. 133
Figure 77	Condenser refrigerant outlet temperature: Sim-
118010 //	plified Model, Test 2 with R450A, condenser
	model with 30 elements and Tune 2. 134
Figure 78	Condenser pressure: Simplified Model, Test 1
rigure 70	with R450A, condenser model with 30 elements
Eiguro 70	3.
Figure 79	Condenser saturation temperature: Simplified
	Model, Test 1 with R450A, condenser model
Eigene 0a	with 30 elements and Tune 1. 135
Figure 80	Condenser refrigerant outlet temperature: Sim-
	plified Model, Test 1 with R450A, condenser
T. 0	model with 30 elements and Tune 1. 135
Figure 81	Condenser pressure: Simplified Model, Test 1
	with R450A, condenser model with 30 elements
	and Tune 2. 136
Figure 82	Condenser saturation temperature: Simplified
	Model, Test 1 with R450A, condenser model
	with 30 elements and Tune 2. 137

Figure 83	Condenser refrigerant outlet temperature: Sim-
	plified Model, Test 1 with R450A, condenser
Eiguro 84	model with 30 elements and Tune 2. 137 Condensor water outlet temperature: Simplified
Figure 84	Condenser water outlet temperature: Simplified Model, Test 1 with R450A, condenser model
	•••
Eigung 0=	with 30 elements and Tune 1. 138  Evaporator pressure: Simplified Model, Test 1
Figure 85	with R450A, evaporator model with 20 elements
E' 07	and Tune 1. 139
Figure 86	Evaporator saturation temperature: Simplified
	Model, Test 1 with R450A, evaporator model
E: 0	with 20 elements and Tune 1. 139
Figure 87	Evaporator refrigerant outlet temperature: Sim-
	plified Model, Test 1 with R450A, evaporator
T: 00	model with 20 elements and Tune 1. 140
Figure 88	Evaporator secondary fluid outlet temperature:
	Simplified Model, Test 1 with R450A, evaporator
<b>T.</b>	model with 20 elements and Tune 1. 140
Figure 89	Condenser pressure: Full Model, Test 2 with
	R450A, condenser model with 30 elements and
	Tune 1, $x_{0,LR} = 0.2$ . 141
Figure 90	Evaporator pressure: Full Model, Test 2 with
	R450A, evaporator model with 20 elements and
<del>.</del>	Tune 1, $x_{0,LR} = 0.2$ . 142
Figure 91	Evaporator pressure:Simplified Model, Test 2
	with R450A, evaporator model with 20 elements
T.	and Tune 1. 142
Figure 92	Condenser pressure: Full Model, Test 2 with
	R450A, condenser model with 30 elements and
T.	Tune $1, x_{0,LR} = 0$ . 143
Figure 93	Evaporator pressure: Full Model, Test 2 with
	R450A, evaporator model with 20 elements and
г.	Tune 1, $x_{0,LR} = 0$ . 144
Figure 94	Condenser saturation and LR temperatures:
	Full Model, Test 2 with R450A, condenser model
T.	with 30 elements and Tune 1. 144
Figure 95	Condenser refrigerant outlet temperatures : Full
	Model, Test 2 with R450A, condenser model
T' (	with 30 elements and Tune 1. 145
Figure 96	Evaporator saturation and SA temperatures:
	Full Model, Test 2 with R450A, evaporator model
T:	with 20 elements and Tune 1. 145
Figure 97	Evaporator refrigerant outlet temperatures : Full
	Model, Test 2 with R450A, evaporator model
	with 20 elements and Tune 1. 146

Figure 98	Condenser pressure:Full Model, Test 1 with R450A, condenser model with 30 elements and
Figure 99	Tune 1, $x_{0,LR} = 0$ . 147 Condenser saturation and LR temperatures: Full Model, Test 1 with R450A, condenser model with 30 elements and Tune 1, $x_{0,LR} = 0$ . 147
Figure 100	Condenser refrigerant outlet temperature: Full Model, Test 1 with R450A, condenser model
Figure 101	with 30 elements and Tune 1, $x_{0,LR} = 0$ . 148 Condenser secondary fluid outlet temperature: Full Model, Test 1 with R450A, condenser model
Figure 102	with 30 elements and Tune 1, $x_{0,LR} = 0$ . 148 Pressures in the hot branch, condenser inlet and outlet and compressor outlet, during Test 1 with
Figure 103	R450A. 150 Pressures in the hot branch, condenser inlet and outlet and compressor outlet, during Test 2 with
Figure 104	R450A. 150 Evaporator pressure:Full Model, Test 1 with R450A, evaporator model with 20 elements and
Figure 105	Tune 1, $x_{0,LR} = 0$ . 151 Evaporator pressure and SA temperatures: Full Model, Test 1 with R450A, evaporator model
Figure 106	with 20 elements and Tune 1, $x_{0,LR} = 0$ . 151 Evaporator refrigerant outlet temperatures: Full Model, Test 1 with R450A, evaporator model
Figure 107	with 20 elements and Tune 1, $x_{0,LR} = 0$ . 152 Evaporator secondary fluid outlet temperatures: Full Model, Test 1 with R450A, evaporator model
Figure 108	with 20 elements and Tune 1, $x_{0,LR} = 0$ . 152 Refrigerant mass flow rate: Simplified Model, Test 1 with R450A,. 154
Figure 109	Refrigerant temperature at the compressor outlet: Simplified Model, Test 1 with R450A. 155
Figure 110	Electric power consumption and power delivered to the fluid by the compressor: Simplified Model, Test 1 with R450A. 155
Figure 111	Refrigerant mass flow rate: Simplified Model, Test 2 with R450A. 156
Figure 112	Refrigerant temperature at the compressor outlet: Simplified Model, Test 2 with R450A. 157
Figure 113	Electric power consumption and power delivered to the fluid by the compressor: Simplified Model, Test 2 with R450A. 158

169

profile.

## LIST OF TABLES

Table 1	Characteristics of the semi-hermetic reciprocat-
	ing compressor D3.13.1Y VS by Frascold. 15
Table 2	HEX data 16
Table 3	Expansion valves data. 17
Table 4	Refrigerant accumulation devices. 17
Table 5	Piping data. 17
Table 6	Mass flow meter, model Proline Promass E300
	by Endress Hauser, Hauser, 2022, 2024. 18
Table 7	Vortex flow meter, model Huba Control 210 Con-
•	trol, 2020. 18
Table 8	Temperature traducer, Carel Pt100, Carel, 2023. 19
Table 9	Pressure traducers by Huba, model Huba Con-
,	trol 520, Control, 2024. In the plant, a sensors
	with two different operative ranges is installed
	for the low and high-pressure branches. 19
Table 10	Electric power transducer CEWE DPT 221-401. 19
Table 11	Measures acquired and employed for the vali-
	dation of the VCS model. 21
Table 12	Refrigerant physical properties tables employed
	in the HEX model. 35
Table 13	Secondary fluid physical properties tables em-
-	ployed in the HEX model. 35
Table 14	Refrigerant physical properties tables employed
	in the compressor physical model. 35
Table 15	Refrigerant physical properties tables employed
	in the accumulator model. 35
Table 16	Limits for the physical properties tables. 39
Table 17	List of the developed versions of the dynamic
	correction of the refrigerant temperature at the
	compressor outlet. 59
Table 18	Conditions for the first (a) and second (b) nu-
	merical test of the accumulators and pipe mod-
	els. 8 <sub>3</sub>
Table 19	Conditions for the third numerical test of the
	accumulators and pipe models. 85
Table 20	Correction gains for the HTC tuning of the re-
	frigerant side in the condenser model. 131
Table 21	Main geometrical employed in the HTC correla-
	tions for BPHEXs. 170

## INTRODUCTION

According to a recent report by the International Institute of Refrigeration, this sector is responsible for one-fifth of the global electric energy demand, and this figure is expected to more than double in the next few years due to the skyrocketing air-conditioning applications. In this sector, the leading technology is the Vapour Compression System (VCS) due to its flexibility, scalability and relative simplicity of layout. Furthermore, this system is also employed in Heat Pump (HP) systems, which are increasingly diffuse in many industrial and civil installations for ambient warming or heat recovery.

For these reasons, the optimization of VCSs should considerably affect global energy consumption and may help reduce the environmental impact of the Heating, Ventilation, Air Conditioning and Refrigeration (HVACR) sector. In this context, numerical modelling has been proven a suitable tool to achieve this goal, being helpful from the engineering to the tuning phase of a new system. Moreover, dynamical models are increasingly employed as Digital Twins in advanced real-time control systems, able to automatically follow the optimal set points, by varying the operating conditions.

This is the background that led to the development of this research project. This work involves a long path in the dynamical modelling of VCSs, with the main goal to contribute to major comprehension of the physical, mathematical and numerical aspects of developing such models oriented to control applications and real-time simulations.

Despite the large diffusion of the moving boundary approach to model the Heat Exchangers (HEXs), the choice fell onto the finite volume scheme, intending to demonstrate its reliability in this application. Since the accumulation devices and the piping are often disregarded, they should be significant and usually are modelled through a lumped-parameter approach.

The work is organized as follows. Chapter 1 introduces the state of the art of VCS modelling with a particular focus on the control-oriented applications that involve the finite volume approach for HEX modelling. The chapter 2 summarises, with no pretence of completeness, some key points about dynamic system theory that will be the underlying principles for developing the dynamical model of the VCS. Then, each of the main components of the VCS is investigated, and the corresponding numerical model is developed: in chapter 6, the compressor; in chapter 7, the pipes; in chapter 8, the expansion device; in chapter 9, the accumulators; and in chapter 10, the heat exchangers.

Then, the complete model of the vapour compression machine is presented in chapter 11 in two versions: the first with no accumulation devices, the latter with a liquid receiver and a suction accumulator. The results of many numerical tests performed are presented in this chapter, starting from the investigation of the grid dependence to the evaluation of the tuning of the Heat Transfer Coefficients to enhance the accuracy of the HEX model. The dynamical models are validated against experimental data obtained from an experimental test rig located at the Polytechnic of Milan, as described in chapter 3, where the facility is described at first, then the collected data are assessed in terms of accuracy and reliability for the investigation of transients. Moreover, chapter 4 describes the method for evaluating the physical properties of the working fluids, which is critical for the dynamical model's performance.

# 1 | VAPOUR COMPRESSION SYSTEMS MODELLING

### 1.1 VAPOUR COMPRESSION SYSTEMS

The Vapour Compression System (VCS) is the leading technology in the refrigeration sector, even if it is also employed in air conditioning applications and Heat Pumps (HPs). This cycle transfers heat from a colder to a warmer environment. This job can be performed by employing a certain amount of work, according to the second principle of thermodynamics; in fig. 1 the schematic of a subcritical VCS is represented, in which all the thermodynamic transformation of the refrigerant take place under the critical pressure and temperature. This is the most diffuse implementation of VCS, but recently the C0<sub>2</sub> transcritical cycles are increasingly employed in particular in the retail sector. In this cycle, the hot branch evolves over the critical point, the condenser is therefore replaced with a gas cooler, while the low-pressure branch remains in the saturated vapour field. In supercritical cycles, both branches evolve over the critical point, and they are employed in higher temperature applications, like, for example, the Organic Rankine Cycle investigated by Y. M. Kim et al., 2012.

Subcritical, transcritical, supercritical cycles

The working fluid, usually called refrigerant, evolves between two heat exchangers, interacting with the two environments; the heat exchangers are maintained at different pressure levels using a compressor and an expansion device. The refrigerant goes through different states, undergoing four thermodynamic transformations. Referring to fig. 1, the refrigerant superheated vapour (1) is sucked into the compressor, in which its volume is reduced and its pressure increased; some irreversibilities inevitably characterize the compression, so the outlet state (2) does not correspond to the isoentropic process. Moreover, when the pressure ratio is too high, the compression is refrigerated to contain the outlet temperature of the refrigerant under safety limits to prevent lubricant depletion and seal deterioration. Then the refrigerant enters the high temperature Heat Exchanger (HEX) where it undergoes condensation (2-3) in subcritical cycles; in transcritical VCS, the refrigerant gas is cooled. The subcooled liquid (3) goes through the expansion device, which can have fixed or adjustable openings to reach the low branch pressure as a two-phase mixture. This process can be considered isoenthalpic because the heat transfer rate in this component can be ignored. Finally, the refrigerant is warmed in the low pressure HEX, where it evaporates to reach the superheated vapour state (1).

Main components and thermodynamic transformations

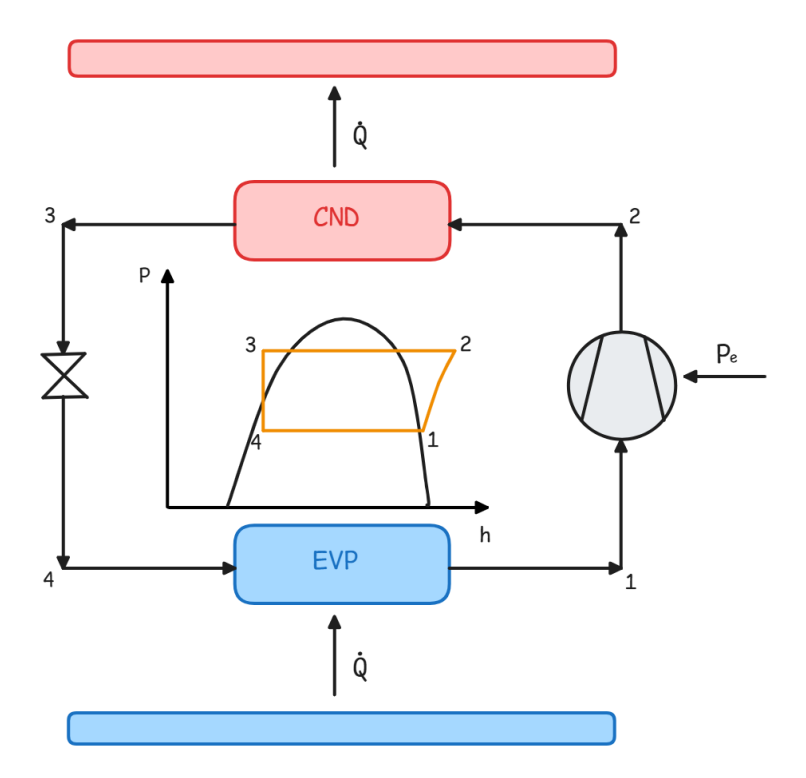


Figure 1: Basic scheme of a subcritical VCS with the corresponding thermodynamic processes represented on the p-h diagram.

Beyond these four main components, the VCS can be equipped with some auxiliaries, depending on the configuration required. Often, accumulation devices are installed in the suction line to avoid liquid infiltration to the compressor or at the condenser outlet to ensure liquid flow through the expansion valve. Furthermore, in larger plants, a vessel called *separator* is employed to decouple the circuit in two portions to enable more suitable conduction strategies; on one hand, the main loop, responsible for the heat rejection, is composed of the compressors, the condensers and the expansion devices, while the user's side involves all the components devoted to the heat removal from the cold rooms, which are usually equipped with aero-refrigerators if a secondary fluid is employed, or aero-evaporators, if the refrigerant is fed directly to them.

The application of VCSs as refrigeration cycles is widespread in the food preservation sector, in which it is possible to distinguish two main categories: the fridge installations, which operate around o °C and the freezing application in which the desired temperature is around -20 °C. To maintain the quality and safety of perishable foods, the cold chain is widely diffused worldwide; it is an uninterrupted delivery system involving temperature-controlled transport and storage from the producers to the final users. The cold chain involves domestic and commercial installations, refrigerated transport and cold storage. The cold chain is estimated to be responsible for about 260 Mt of CO<sub>2</sub> equivalent emission, as reported by Sarr et al., 2021. The refrigeration

**Auxiliary** components

sector also sweeps from the medicine applications, like the Magnetic Resonance Imaging (MRI) machines, to the Liquified Natural Gas (LNG), like regasification terminals or the vessels of the tanker fleet. Furthermore, most air conditioning applications involve VCS in cooling and heating modes. Indeed, the VCS can be used as a refrigeration cycle, in which the desired effect is the heat removed from the cold reservoir, or as HP whose aims to warm the high-temperature environment. The air conditioning applications range from commercial and residential buildings to mobile installations in conditioned vehicles. The refrigeration sector accounts for almost one-fifth of the global electric energy demand, which is expected to more than double in the next few years, in particular, due to the skyrocketing of air conditioning installations, as remarked by Dupont et al., 2019.

From the above considerations, optimising the VCSs can considerably reduce the environmental impact of the Heating, Ventilation, Air Conditioning and Refrigeration (HVACR) sector. The performance of VCSs in refrigeration applications is usually evaluated with the Coefficient of Performance (COP), defined as the ratio between the cooling effect and the compressor power consumption. More precisely, even the electric energy needed to power the ventilators or the pumps that move the secondary fluid should be considered; these contributions become significant in larger plants. On the other hand, when the VCS is employed in HPs, its COP is calculated as the ratio between the heating effect and the power required by the system.

Different approaches can be undertaken to reach a better COP: improving the performance of each component of the system, developing the plant configuration to increase the overall COP and implementing suitable control strategies to drive the operating point of the VCS near optimality as the environmental conditions vary. From the design phase to the real-time conduction, the numerical model has proved to be a valuable tool in supporting the optimisation of these systems. Indeed, as pointed out by B. P. Rasmussen and Shenoy, 2012, the numerical models of VCSs are helpful for system analysis and engineering, model-based control design, in-place tuning during the commissioning or Fault Detection and Diagnosis (FDD) in the operating life.

For these reasons, this work focuses on the numerical modelling of VCSs, with the primary goal of realizing a tool suitable for realtime dynamical simulations to be employed also as a Digital Twin in advanced control systems. Indeed, static models are more appropriate for the initial sizing and selection of the components and the definition of the base configuration to match the project specifications, while the dynamical approach is more suitable for control purposes and FDD, as pointed out by P. Li et al., 2014. The steady-state models can also be employed for FDD comparing the stationary operation of the

actual plant with those predicted by the model, as realized by M. Kim et al., 2008. However, they are not able to conduct stability analysis or transient investigation.

To this aim, a solid foundation in systems theory is important to orient the model design and the simulation set-up. In this context, some general pieces of information about the dynamical systems theory are outlined in chapter 2 to state the reasons for the modelling choices adopted in this work.

In the following, some references describing the dynamical modelling of VCSs are provided.

#### 1.2 LITERATURE OVERVIEW

Research on transient simulation of VCSs can be traced back to more than 40 years ago, and many publications can be found in this field.

The doctoral thesis of Dhar, 1978 is among the first to study the transient analysis of refrigeration systems. The simulation is realized with a fixed time step. The model is very apt for capturing the major transients of the systems.

Chi and Didion, 1982 realized a dynamic model of a complete VCS; the Fortran code is composed of seven components sub-routines that account for the dynamic response of electric motors, compressors, shafts, electric fans, air-refrigerant heat exchangers, accumulators, and thermostatic expansion valves. The model simulates an air-to-air HP and is validated with experimental data. The ordinary differential equations are solved with a first-order Euler method and a time step  $\Delta t$ =0.005 s. A moving boundary approach is adopted for the HEX.

MacArthur, 1984 investigated the transient behaviour of an HP employing a finite volume discretisation for the condenser and the evaporator. The other components, i.e. the accumulator, expansion device, and compressor are modelled with a lumped parameter approach. Further, Grald and MacArthur, 1992 also tested a moving boundary framework for the time-dependent simulation of two-phase flow to realize the dynamic model of an HP.

Willatzen et al., 1998 investigated the behaviour of a VCS under large transients, like compressor on-off, by employing a moving boundary approach to deal with the HEX. The pressure drop is neglected in this work, and the void fraction is assumed to be time-invariant.

A particular focus on the control algorithms development is present in the work of He et al., 1998. The multi-input multi-output (MIMO) framework is employed for the dynamical model of a VCS.

B. P. Rasmussen and Alleyne, 2004 proposed a control-oriented model of a transcritical VCS employing CO2 as refrigerant. Firstly, they developed an 11th-order nonlinear dynamic model of the system

starting from the first principle balance equations. Then, recognizing the presence of different time scales, the model is reduced by applying the singular perturbation technique. The evaporator is treated with a moving boundary approach, while the gas cooler model has a single control volume (lumped parameter model).

McKinley and Alleyne, 2008 developed a dynamical model of VCS, employing the moving boundary scheme; moreover, they extended this technique to large transients simulation, introducing the possibility to switch between modes characterised by the presence of a different number of zones. The model is developed in the Simulink® environment using the Thermosys Toolbox. Likewise, B. Li and Alleyne, 2010 could simulate compressor on-off transients without incurring in numerical failures during the disappearance of one zone.

From this short review, it is clear the presence of an undeclared dispute between the supporters of the moving boundary or switched moving boundary technique and the finite volume approach, ascertain which method is best suited for dynamical models of VCSs.

In general, for control purposes and real-time applications, the lower the order, the better the model. The moving boundary approach requires fewer state variables to be integrated at each time step than the finite volume scheme. Considering two variables to describe the state of the fluid and one for the wall temperature, the moving boundary approach for the condenser requires several state variables equal to 3  $\times$  3 zones. In comparison, the finite volume scheme with n elements leads to  $3 \times n$  states variables.

Bendapudi et al., 2008 realised an in-depth comparison between moving boundary and finite volume formulations, highlighting that the first is less computationally intensive. Still, the latter is more robust, especially in extensive transient simulations. Their accuracy is nearly identical. In a previous job, Bendapudi et al., 2005 realised a finite volume model of a flooded shell-and-tube HEX and carefully analysed it from a numerical point of view, investigating the effect of the mesh size, the solver and the integration time step. It was found that a mesh size of 15 elements is necessary to obtain an acceptable steady-state accuracy.

Desideri et al., 2016 compared the two techniques in realising the evaporator model employed in a small-sized Organic Rankine Cycle. The model is developed in the Modelica® environment. Also, the moving boundary is faster than the finite volume model in this case. Moreover, the minimum number of 20 nodes is recommended to avoid numerical inconsistencies.

Also, Pangborn et al., 2015 took part in this debate. The dynamic models of the HEX of a VCS were realized in Simulink $^{(\!R\!)}$  environment, with the main goals of control design applications. They overcame the conventional trade-off between MB and FV: the FV is usually

MB vs FV in VCS dynamical models

considered more accurate while the MB is faster and computationally lighter. Conversely, they demonstrate that the calculation time and the accuracy of a FV model depends to a large extent on the way the code and the algorithms are realized. The Authors going to suggest different tricks to enhance the stability of the model, reduce the stiffness of the system of differential equations, increase the accuracy and reduce the run time, reaching a performance similar to that of the MB scheme. It was highlighted that the main advantage of a FV formulation is its flexibility; indeed, it can be easily employed in reversible HP as proposed by Salazar-Herran et al., 2020.

#### THE USE OF NUMERICAL MODELS 1.3

In many circumstances, it is helpful to develop mathematical models of physical systems or processes to investigate them and achieve a deeper understanding of the underlying physics. Moreover, the models have proved very useful in the design phase to support selecting and sizing the components most fit the actual application and operating conditions. Finally, models are being increasingly employed to optimise the performance of systems and plants in different ways. With the model, it is possible to investigate the design and the actual operating range to find the points that yield the best value for the performance variable; the system can then be operated at that working point. Since the increased availability of powerful CPUs and the development of information technologies, above all the spreading of machine learning algorithms and artificial intelligence applications, real-time control systems are increasingly adopted in all sectors, using models as digital twins.

In this context, the development of a VCS dynamical model must face different challenges concerning its physical foundation and its numerical robustness.

The fundamental request for the model of a physical system or process is its accuracy in predicting the quantities of interest. However, the level of precision required depends on the application. The same level of accuracy must characterize the experimental data collected for model validation.

Accuracy

The accuracy required influences the approach selected to model the component. Indeed, a lumped-parameter scheme can be employed when the spatial behaviour of the process is not critical. In contrast, the distributed parameter approach is necessary to capture the spatial evolution of the process, which can be crucial, especially for the HEXs. In this context, MB or FV techniques were used to treat two-phase flows.

Lumped vs distributed parameter approach

Another key aspect in VCS modelling is the presence of very different time scales involved in the process. Static or dynamical models can be used for the different components of the plant, depending on the time scale of interest. In this context, components related to the mass flow rate are treated as static. In contrast, components involved in mass accumulation and heat transfer are approached as dynamical systems, as motivated in chapter 2. Also, as investigated in chapter 10, the presence of different time scales leads to increased stiffness of the system of differential equations. This may lead to numerical issues or accuracy reduction if countermeasures are not applied. Finally, the control actions to drive the system to the selected operating point can act only on specific dynamics.

Different time scales

The physical insight the model could provide for the user is no less critical. Although physically based models are more difficult to develop, and often mathematical challenges must be faced, they lead to a deeper understanding of the simulated process. For this reason, they should be beneficial in the design or tuning phase. Furthermore, the physical-based or grey box models allow more confidence when extrapolating outside the validation field. On the opposite side, as widely discussed by B. P. Rasmussen, 2012 and P. Li et al., 2014, the black box model may be more straightforward to develop: indeed, generally, the model is made of a function that correlates inputs and output, whose coefficients need to be determined through regression procedures over a set of experimental data. These models can be very accurate in the validation field but are often prone to considerable errors during extrapolation. Moreover, the model cannot be used to enhance the physical comprehension of the process.

Grey box vs black box modelling approach: physical insight and extrapolation ability

Another critical aspect to evaluate is the numerical robustness of a model; this is important in stand-alone simulations, but even more so when interfacing with other models is required to realise integrated simulations. In this context, some observations about the solver and the corresponding integration time step selection should be made. Indeed, the modern programming languages and simulation environments like Simulink® employed in this work make different solvers available to solve systems of differential equations. The variable step solver can automatically adapt its step size to achieve the prescribed accuracy. This is very useful to combine accuracy and run time. However, the more restrictive requirements are dominant when different subsystems are coupled. For this reason, analysing the numerical behaviour of the solution with a fixed-step solver helps point out the criticalities of the model before employing it in more complex scenarios. Also, the fixed integration step size is helpful during the data processing of the solution. For these reasons, in this work the ode3 fixed-step solver is chosen, and different options for time step are investigated to combine accuracy and run time.

# 2 | THE MODELLING OF DYNAMICAL SYSTEMS

Broadly specking, a system is a way to describe a physical or artificial process, highlighting the way in which specific quantities of interest evolve in time under the influence of their interaction with the environment. Usually, a *system* is defined as an oriented abstract object. In practice, a set of equations, algebraic or differential, is used to reproduce the dependence of the outputs on the inputs; therefore the orientation of the system relies upon the causality principle. In general, the processes of engineering interest evolve in time, so the corresponding dynamical system are composed of a set of differential equations to describe this time dependence. However, under certain circumstances, the dynamical system can be treated through a steady state approach, in which only the equilibrium states of the process are investigated. On the other hand, sometimes evolving processes can be described with static system, without employing any differential equations; indeed, in this case, the behaviour of the output is uniquely determined by that of the inputs. This chapter reports some basic concepts from dynamical system theory, which are used to inform the modelling choices adopted in this work.

### 2.1 DYNAMICAL SYSTEMS

Since a *system* is an oriented abstract object, its causal orientation must be recognized to properly define inputs  $\mathbf{u}$  and outputs  $\mathbf{y}$  and develop the mathematical relations between them. Generally, a dynamical system can be described with a Input-State-Output (ISO) representation, eq. (2.1), where all the quantities involved are vectors (represented in bold). The inputs and the outputs are related by the state  $\mathbf{x}$  of the system, whose time evolution is described by a set of differential equations. The vector function  $\mathbf{f}$  and  $\mathbf{g}$  define the causal relationship between the variables, which can generally be non-linear and time-dependent.

$$\begin{cases} \dot{\mathbf{x}}(t) = \mathbf{f}(\mathbf{x}(t), \mathbf{u}(t), t) \\ \mathbf{y}(t) = \mathbf{g}(\mathbf{x}(t), \mathbf{u}(t), t) \end{cases}$$
(2.1)

However, for engineering applications, it is often assumed that the system is *stationary* or *time invariant* eq. (2.2), so the functions  $\mathbf{f}$  and  $\mathbf{g}$  do not vary in time; this is a reasonable assumption because the process or the component may not vary their configuration during the

Stationary or time-invariant systems

process. Nevertheless, this assumption may have to be dropped if the investigation focuses on processes such as fouling and fault detection during the operating life of the plant.

$$\begin{cases} \dot{\mathbf{x}}(t) = \mathbf{f}(\mathbf{x}(t), \mathbf{u}(t)) \\ \mathbf{y}(t) = \mathbf{g}(\mathbf{x}(t), \mathbf{u}(t)) \end{cases}$$
(2.2)

Despite a linear dependence between inputs is hard to find in actual processes of engineering interest, linear dynamical models, eq. (2.3), are often employed because even a non-linear system can be linearised for studying small variations around a certain *equilibrium point*. This approach is very useful for stability analysis and controller design.

$$\begin{cases} \dot{\mathbf{x}}(t) = \mathbf{A}(t)\mathbf{x}(t) + \mathbf{B}(t)\mathbf{u}(t) \\ \mathbf{y}(t) = \mathbf{C}(t)\mathbf{x}(t) + \mathbf{D}(t)\mathbf{u}(t) \end{cases}$$
(2.3)

Similarly, for the non-linear cases, when all the matrices of the linear models are time-independent, the system can be defined as stationary linear dynamical system, eq. (2.4).

$$\begin{cases} \dot{\mathbf{x}}(t) = \mathbf{A}\mathbf{x}(t) + \mathbf{B}\mathbf{u}(t) \\ \mathbf{y}(t) = \mathbf{C}\mathbf{x}(t) + \mathbf{D}\mathbf{u}(t) \end{cases}$$
(2.4)

The equilibrium point or steady state of the system  $\mathbf{x}_e$  is defined by Steady state eq. (2.5).

$$\dot{\mathbf{x}}_e(t) = \mathbf{f}(\mathbf{x}_e(t), \mathbf{u}(t)) = 0 \tag{2.5}$$

When the evolution of the outputs of a system does not depend on the inputs, the system is called *autonomous*, and is described by eq. (2.6) for the *stationary* case.

$$\begin{cases} \dot{\mathbf{x}}(t) = \mathbf{f}(\mathbf{x}(t)) \\ \mathbf{y}(t) = \mathbf{g}(\mathbf{x}(t)) \end{cases}$$
 (2.6)

#### System response and stability 2.1.1

The response of dynamical systems that is the time evolution of their outputs, is generally a combination of two parts: the free and the forced response. The system produces the free response when it is not subjected to any inputs, so it is also the response of an autonomous system; the normal modes characterise the free response, which is the basic pattern of motion of the system. On the other hand, the forced response considers the inputs, but it also relies on the normal modes. So, the investigation of the free response is of paramount importance for the description of the dynamical system.

In a linear dynamical model, the normal modes are determined by the eigenvalues,  $\lambda$ , of the matrix **A**, eq. (2.4). In the particular case of Free and forced response

the diagonal matrix  $\mathbf{A}$ , the eigenvalues are the diagonal elements, and the time behaviour of the states correspond directly to each normal mode. Moreover, the time constant,  $\tau$ , of each mode is defined by the corresponding eigenvalue  $\tau = 1/\lambda$ . For example, in a first-order mode, the time constant represents the time necessary to reach 63.2% of the mean value of the steady state in response to a step variation of the input. As a consequence, the eigenvalues are indicative of the speed of the associated normal modes and, in some conditions, may be related directly to the states of the dynamical system.

The concept of stability is of paramount interest in studying dynamical systems. Stability is a property of the system around a particular equilibrium state. In loose words, a system is stable in a certain equilibrium state if, after being subjected to disturbances, it returns to its primitive position or remains in a small area around it. The linear dynamical system has only one equilibrium point  $\mathbf{x}_e = 0$ . The investigation of its stability is therefore straightforward using the eigenvalues of the matrix **A**. Indeed if the real part of  $\lambda$  is negative Re( $\lambda$ ) < 0 the trend of the mode is decreasing, so the free response goes to zero in a certain time depending on the corresponding time constant. This trend is damped and stable. In contrast, if the real part of  $\lambda$  is positive  $Re(\lambda) > 0$ , the mode diverges to infinity, and it contributes to instability. In the case of non-linear dynamical system, the above consideration can be extended to the system linearized around the steady state.

Stability

#### STATIC SYSTEMS 2.2

The system is called *static* or *non-dynamical*, if the outputs depends on the inputs only and it is described mathematically by a set of algebraic equations, like in eq. (2.7) for the stationary case.

$$\mathbf{y}(t) = \mathbf{g}(\mathbf{u}(t)) \tag{2.7}$$

### When can a physical system be treated as non-dynamical?

The state variables are physically associated with the variation of mass, energy and momentum inside the system under investigation. If it could not store these quantities, it would be modelled without states.

Although the system allows storing these quantities, in certain cases it can be treated as non-dynamical. Indeed, if the states do not affect the monitored outputs in a certain process, or their effect is negligible, it can be modelled with a static system employing only algebraic equations. This is the case for the expansion valve in the present work: indeed, since the casing can vary its temperature in

Physical interpretation of state variables

Independence of outputs from the states

time, so a state related to the internal energy of the valve body would be present, yet this does not affect the mass flow rate that pass thought the orifice.

Another aspect to consider in selecting the proper model for a physical system is the time scale of interest. For example, if the time horizon of the investigation is in the order of hours, the contributions that can be assumed to be exhausted in the time of minutes or seconds are likely to be be of no consequence. In this context, evaluating the time constant of the modes associated with the systems may be very useful in reducing the order of the model, while focusing on those state variables that significantly affected the process. In the modelling of VCS the time scale of 1 s seems appropriate to capture the main dynamics and investigate suitable control strategies. This assumption will be reviewed in the following section in the light of the achieved results. For the above reasons, the model of the compressor can be approached statically. Indeed, the characteristic time of the compressor is related to its rotational speed; the mass and the temperature of the refrigerant change considerably during a cycle, but this variation repeats cyclically, so it can be assumed that its effect is irrelevant over the cycle time. When investigating the compressor with a time scale of 1 s, the state variables related to the refrigerant evolving inside can be neglected, and a static model can be employed; conversely, the case temperature will be treated as a state variable, because its time constant is much larger than of the time scale adopted and its behaviour affects the outlet refrigerant temperature, which is one of the monitored outputs of the model.

Different time scales

#### 2.3 STIFFNESS

Let's consider a linear system of differential equations in the implicit form eq. (2.8)

$$\mathbf{Z}\dot{\mathbf{x}} = \mathbf{R} \tag{2.8}$$

This implicit formulation can be led back to the explicit form eq. (2.6) by calculating the coefficient matrix inverse  $\mathbf{Z}^{-1}$ . The numerical accuracy of this process depends on the conditioning number defined as the ratio between the maximum and minimum singular value of the matrix **Z**. If **Z** is a normal matrix, the conditioning number  $k(\mathbf{Z})$  is the modulus of the ratio between the maximum and minimum eigenvalue.

Conditioning number

$$k(\mathbf{Z}) = \frac{|\lambda_{\text{max}}|}{|\lambda_{\text{min}}|} \tag{2.9}$$

The bigger the conditioning number, the less accurate the matrix inversion calculation will be.

When considering a linear autonomous dynamical system in the form eq. (2.6), the solution of the set of differential equations can be formulated as

$$\mathbf{x}(t) = \sum_{i=1}^{n} K_i e^{\lambda_i t} \mathbf{c}_i$$
 (2.10)

where  $\mathbf{c}_i$  is the eigenvector associated with the i-th eigenvalue, and K<sub>i</sub> is an arbitrary constant. The stiffness of a differential equation problem is related to the accuracy of the solution; stiff problems need a very small integration step to achieve the prescribed accuracy. The evaluation of the stiffness of the problem is made employing the stiffness ratio, defined as the ratio between the absolute value of the eigenvalue with the highest real part and the absolute value of that with the lowest real part.

Stiffness ratio

$$SR = \frac{|Re\{\lambda_{max}\}|}{|Re\{\lambda_{min}\}|}$$
 (2.11)

This parameter describes the ratio between the magnitudes of the extreme time scales involved in the dynamical system; the combination of normal modes with very different time scales could lead to a reduction in accuracy and needs careful attention in the selection of the numerical algorithm employed for the solution. The higher the stiffness ratio, the stiffer the problem, and the solution becomes if no suitable algorithm is used. With very stiff problems, the solution procedure fails unless a proper algorithm and a suitable integration step size are adopted.

Stiffness and time

In conclusion, the concepts of conditioning number and stiffness ratio are very similar when employed to characterise the numerical properties of linear dynamical systems. The larger these parameters are, the less accurate the numerical problem solution may be; the conditioning numbers concern the matrix inversion algorithm, whereas the stiffness is related to the accuracy of the transient solution of linear differential equations involving time scales very different in magnitude.

# 3 | EXPERIMENTAL FACILITY AND DATA PROCESSING

The data available for validation and testing are collected in two different experimental campaigns carried out at a facility located at the Energy Department of the Polytechnic of Milan. The experimental facility and the first measurement campaign are described in detail in Lucchi, 2020. The test rig comprises the VCS and some auxiliary circuits that allow plant operation. The system is designed mainly for the steady-state investigation of the performance of new low Global Warming Potential (GWP) refrigerants. During the second experimental campaign, the configuration of the auxiliaries differed slightly from the first, but the equipment on the refrigerant side remained the same. In the following, some pieces of information about the plant and the experimental campaigns are reported; further details can be found in Lucchi, 2020 and Roberti, 2020.

### 3.1 TEST APPARATUS

The actual configuration of the experimental rig is shown in fig. 2. The core is the VCS composed of a reciprocating compressor, an electronic expansion valve, and two Brazed Plate Heat Exchangers (BPHEXs). Beyond these key components, the main loop is also equipped with some auxiliaries that allow the safe operation of the system. Downstream the compressor, an oil separator prevents lubricant from circulating through the other components, reducing the heat transfer performance; moreover, a compensation line recirculates the collected lubricant to the compressor case and enables pressure equalisation when the compressor is off and the valve is completely closed. Furthermore, a liquid receiver is placed downstream of the condenser to collect the liquid refrigerant and prevent a two-phase mixture from entering the valve. Finally, upstream of the compressor, a suction accumulator prevents liquid bubbles from flowing into the compression chamber causing damage.

Beside the main loop, two auxiliary circuits are needed to operate the system. The hot side is filled with water while the cold with a mixture of water and glycol ethylene with a volume concentration of 25.4% and a freezing temperature of -12.6 °C. In the actual configuration, the secondary loops are totally independent. Indeed, the recuperator is removed to enhance the degree of freedom in defining the operating conditions, Lucchi, 2020. Both secondary circuits are still

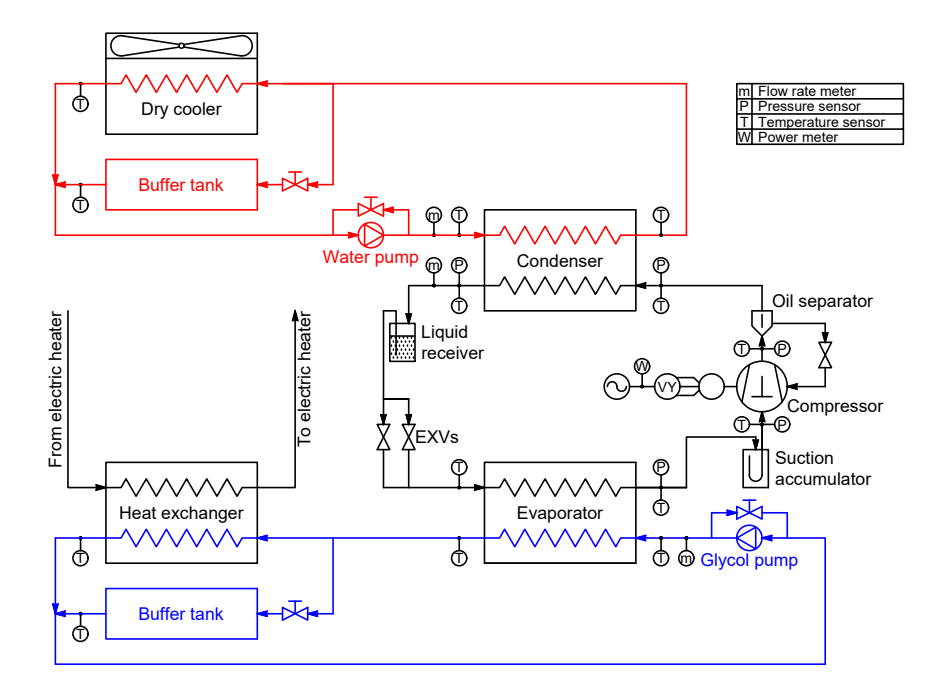


**Figure 2**: Layout of the experimental facility at the Milan Polytechnic.

equipped with a 500-litre tank, but an HEX is added in parallel. On the hot side, an air-to-water finned tube HEX ensures heat rejection from the VCS. The cold secondary circuit is connected by a BPHEX to another loop equipped with an electrical heater, which is composed of three thermoresistors of about 2.5 kW of power, one of which is controlled by Pulse-Width Modulation (PWM), to ensure an accurate definition of the power provided to the coolant; the heater circuit is filled with water to avoid the chemical incompatibility between the glycol ethylene and the components of the heater itself.

More data about the components are given below, since they will be employed to define the numerical model.

#### Compressor 3.1.1

The compressor is a semi-hermetic reciprocating Frascold D<sub>3</sub>-1<sub>3</sub>.1Y VS coupled with an inverter; the supply frequency can vary in the range 30-87 Hz. The company publishes the main characteristics of the machine (geometrical and performance data) through its selection software Frascold Selection Software 1; some useful data for the realization of the model are listed in table 1. Moreover, the selection software also made the polynomial coefficients available for evaluating the main performance indicators according to the reference standards EN 12900, 2013 and AHRI 540, 2020.

<sup>&</sup>lt;sup>1</sup> Frascold Selection Software 3 v1.24.2

Physical quantity	Value	UoM
Cylinders	2	-
Nominal motor power	2.2	kW
Max power consumption	4.8	kW
Frequency min	30	Hz
Frequency max	87	Hz
Motor voltage at 50 Hz	220-240	V
Displacement 50 Hz	13.2	${\rm m}^3{\rm h}^{-1}$
Displacement 60 Hz	15.8	${\rm m}^3{\rm h}^{-1}$
Nominal operating frequency	50	Hz
Nominal Compressor speed	1450	rpm

Table 1: Characteristics of the semi-hermetic reciprocating compressor D<sub>3</sub>.1<sub>3</sub>.1<sub>Y</sub> VS by Frascold.

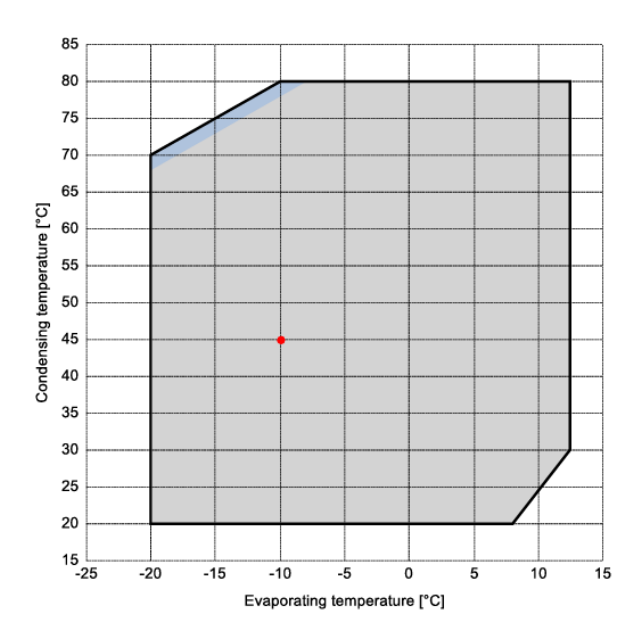


Figure 3: Operating envelope of compressor Frascold D3.13.1Y.

## Evaluation of the single stroke nominal displacement

The manufacturer provides a nominal displacement in m<sup>3</sup> h<sup>-1</sup> for two different operating frequencies, so it is possible to trace beck the singlestroke nominal displacement. Furthermore, from the available data is possible to derive that the number of polar pairs  $(n_p)$  of the driver is two, so the relation between electric current frequency ( $\omega$ ) and the number of revolutions of the crankshaft  $(\Omega)$  is:

$$\Omega = \frac{f}{n_{p}} \tag{3.1}$$

So the single stroke displacement is:

$$V_0 (cm^3) = \frac{V_0}{\Omega} \left( \frac{m^3 h^{-1}}{Hz} \right) \frac{10^6}{3600}$$
 (3.2)

Symbol	Value	UoM		Symbol	Value	UoN
L	348	mm	-	L	266	mm
В	91	mm		В	95.5	mm
b	2.6	mm		b	2.4	mm
β	60	deg		β	50	deg
ф	1.21	-		ф	1.19	_
$n_{ch,r}$	15	-		$n_{ch,r}$	20	_
$n_{ch,s}$	15	-		$n_{ch,s}$	20	_
n <sub>plates</sub>	30	-	_	n <sub>plates</sub>	40	-
•						

(a) Evaporator data.

(b) Condenser data.

Table 2: HEX data

According to this consideration, the single stroke nominal displacement can be assumed  $V_0 \simeq 146 \text{ cm}^3$ .

## 3.1.2 Brazed plate heat exchanger

The evaporator and the condenser are brazed plate heat exchangers provided by Swep. Their main geometrical characteristics, employed for realising the HEX models, are listed in table 2. The evaluation of the reference plate dimensions L and B is described in detail in Roberti, 2020.

## Expansion valve

As reflected in fig. 2, the VCS is equipped with two expansion valves, both manufactured by Carel. The reason behind this choice is to guarantee the controllability of the cycle, even for a small mass flow rate. Suppose the desired operating point corresponds to a certain pressure drop and mass flow rate near the lower end of the valve regulating range. In that case, the regulated point of the valve may sway between the totally closed position and the minimum opening, which could be too much for the desired mass flow rate, leading to oscillating conditions in the whole plant. To avoid this phenomenon, two valves of different sizes are installed, EV205 and E2V24; in table 3, the flow coefficients from the Carel data-sheet Carel, 2018 are reported. The manufacturer also provides the nominal cooling capacity for each valve; this piece of information depends on the refrigerant employed and the operating conditions, for example, working with R134A at condensation temperature of 38 °C and evaporation temperature of 4.4 °C, the nominal cooling capacity of the two valves are respectively 1.5 kW and 15.1 kW, Carel, 2010.

Valve	kv (m <sup>3</sup> h <sup>-1</sup> @ 1 bar)
E2V05	0.019
E2V24	0.20

Table 3: Expansion valves data.

	V (dm <sup>3</sup> )	Manufacturer
Suction accumulator Liquid receiver Hermetic oil separator	2.33 2.8 2.8	Emerson Frigomec Copeland

 Table 4: Refrigerant accumulation devices.

In this experimental campaign, only the E2V24 was employed because it could cover all the operating conditions during the tests.

#### Refrigerant accumulators 3.1.4

Three devices in the VCS under examination accomplish the function of refrigerant accumulation: the suction accumulator, the liquid receiver and the hermetic oil separator. In table 4, the volumes of the devices are reported.

## 3.1.5 Pipes

The pipe dimensions employed in the refrigerant circuit are reported in table 5. Standard copper tube for refrigeration applications are installed with a thickness s=1 mm.

#### MEASUREMENT INSTRUMENTATION 3.2

The experimental facility is equipped with measurement instruments to monitor the behaviour of the working fluids during plant operations. Four kinds of measurements are available: mass flow rate, temperature, pressure, and electric power consumption.

Phase	D <sub>ext</sub> mm	D <sub>ext</sub> inch
Vapour	19.05	1/2
Liquid	12.7	3/4

Table 5: Piping data.

Range kg h <sup>-1</sup>	Phase	Uncertainty	Resp. time
0-2000	_	± 0.15% rv	1
0-2000		± 0.5% rv	1

Table 6: Mass flow meter, model Proline Promass E300 by Endress Hauser, Hauser, 2022, 2024.

Range dm <sup>3</sup> s <sup>-1</sup>	Uncertainty	Resp. time ms	Delay s
9 9	± 1% fs at <50% fs ± 2% fs at >50% fs	9	<2 <2

Table 7: Vortex flow meter, model Huba Control 210 Control, 2020.

#### 3.2.1 Mass flow rate

## Refrigerant

The refrigerant mass flow rate is measured at the condenser outlet with an Endress-Hauser Proline Promass E300. The measure is based on the Coriolis effect. The sensor's location is chosen to prevent accuracy reduction when crossed by two-phase mixtures and prevent the instrument from coming into contact with lubricant and very hot vapour refrigerant at the compressor outlet. The high temperature could damage the electronic components inside the instrument. Another possible location for this measurement would be the compressor inlet downstream of the suction accumulator to avoid liquid bubbles. The instrument's accuracy is enhanced with single-phase flow, even if it can also measure liquid-vapour mixture flows. In table 6 some information about the mass flow meter employed are collected.

## Secondary fluid

On the two secondary circuits another kind of flow sensor is employed. A vortex flow meter provided by Huba is installed at the discharge section of each pump. This sensor uses the principle of the oscillating vortices described by von Karman; by measuring the frequency of the oscillation downstream a calibrated obstacle posed in the measurement section, it is possible to estimate the flow rate. Some data are gathered in table 7.

Range °C	Uncertainty	Time constant
-50 - 250	$\pm (0.005 \times T) + 0.3$	20

**Table 8:** Temperature traducer, Carel Pt100, Carel, 2023.

Level	Range bar	Uncertainty	Resolution	Resp. time ms
High	•	±0.3% fs	0.1% fs	<2
Low		±0.3% fs	0.1% fs	<2

Table 9: Pressure traducers by Huba, model Huba Control 520, Control, 2024. In the plant, a sensors with two different operative ranges is installed for the low and high-pressure branches.

#### 3.2.2 Temperature

Temperature measurements are gathered at the inlet and outlet section of each heat exchanger, both on the refrigerant and secondary fluid, and at the suction and discharge section of the compressor. The sensors employed are installed are Resistence Temperature Detector (RTD) Pt100 class B, produced by Carel and calibrated through a thermostatic bath. In table 8 the main characteristics of the temperature sensors are reported.

## 3.2.3 Pressure

The pressure is measured only on the refrigerant side, at the suction and discharge section of the compressor and at the inlet and outlet section of the condenser. The pressure transducers employed are the Huba Control 520 sensors, whose data are summarised in table 9.

#### 3.2.4 Electric power consumption

The electric power consumption of the compressor is measured with a programmable by CEWE transducer, table 10

Range kW	Uncertainty	Resp. time ms
0-4	$\pm$ 0.2% fs	300

**Table 10**: Electric power transducer CEWE DPT 221-401.

#### DATA PROCESSING 3.3

#### Data acquisition 3.3.1

The data are collected with a data acquisition board realised by National Instrument. The sample time chosen for the data acquisition campaign is 1 s. This is compatible with all the instruments installed in the rig. The only exception would be the temperature measurement: the transducer has a time constant of about 20 s that leads to a response time of about 100 s. The reliability of this measurement will be discussed next.

## Measurements employed and calculated quantities

Among the data acquired, the measurements employed to validate the VCS model are shown in table 11.

On the low-pressure branch, despite the refrigerant pressure at the evaporator outlet section being measured by the expansion valve microcontroller, the values are not available for data acquisition due to compatibility issues. So, for the validation, the pressure at the evaporator outlet is assumed to be the same as that measured at the compressor inlet.

Refrigerant pressure at the evaporator outlet

The refrigerant pressure at the evaporator inlet is not directly measured. Still, it is calculated, assuming an isoenthalpic processes between the condenser outlet and the evaporator inlet. It can be assumed that the refrigerant enters the Expansion Valve (EXV) as saturated liquid, due to the presence of the Liquid Receiver (LR), which during normal operations contains a two-phase mixture. Once the enthalpy is determined utilizing the state equation, the pressure at the evaporator inlet can be evaluated from the calculated enthalpy and the measured temperature.

Refrigerant pressure at the evaporator inlet

During the validation of the HEX models, also the saturation temperature is analysed, although it is directly related to the pressure levels. The calculated saturation temperature is compared with the experimental values that are calculated from the inlet and outlet pressure measurements. In the case of zeotropic mixtures, the saturation temperatures are slightly different between the vapour and the liquid. Despite this difference being negligible, the methodology employed for the calculations is reported for completeness. The vapour saturation temperature is employed for the condenser inlet and the evaporator outlet, where refrigerant vapour is present. In contrast, the liquid saturation temperature is used for the condenser outlet and evaporator inlet.

Saturation temperature corresponding to the pressure measurements

Fluid	Quantity	Location
	Mass flow rate	Downstream of the condenser
		Condenser inlet
	Pressure	Condenser outlet
	Tiessure	Compressor inlet
Pofricarant		Compressor outlet
Refrigerant		Condenser inlet
		Condenser outlet
	Tomporatura	Compressor inlet
	Temperature	Compressor outlet
		Evaporator inlet
		Evaporator outlet
	Mass flow rate	Upstream of the condenser
Water	Tomporaturo	Condenser inlet
	Temperature	Condenser outlet
	Mass flow rate	Upstream of the evaporator
Water glycol ethylene	Tomporaturo	Evaporator inlet
	Temperature	Evaporator outlet

Table 11: Measures acquired and employed for the validation of the VCS model.

#### Data analysis 3.3.3

In the following some plots of the data collected are shown to demonstrate the reliability of the available measurements, comparing the data with the accuracy of the correspondent transducer. As described before, four kinds of measurements are taken. Still, the transducers can be grouped into six categories according to their accuracy: refrigerant mass flow rate, secondary fluid mass flow rate, high pressure, low pressure, temperature and electric power. The plots in figs. 4 to 10 represent 50 s of Test 1 with R450A during which the compressor frequency undergoes a step variation from 50 to 60 Hz.

The most accurate measurement in the test range is relative to the refrigerant mass flow rate, obtained with the Coriolis transducer fig. 4. Likewise, the electric power measurement is very reliable. Moreover, their dynamic response is compatible with the acquisition sample time even for dynamic analysis of the system. The pressure accuracy of the transducer is within norm; since it is rated with reference to the full scale (fs), it is different for the measurements on the low-pressure and high-pressure sides. The response time is suitable for dynamic behaviour investigation, table 9. On the other hand, the secondary flow rate meter introduces a consistent uncertainty around 1% of the full scale, table 7, that affects the reliability of the collected data fig. 5. Even

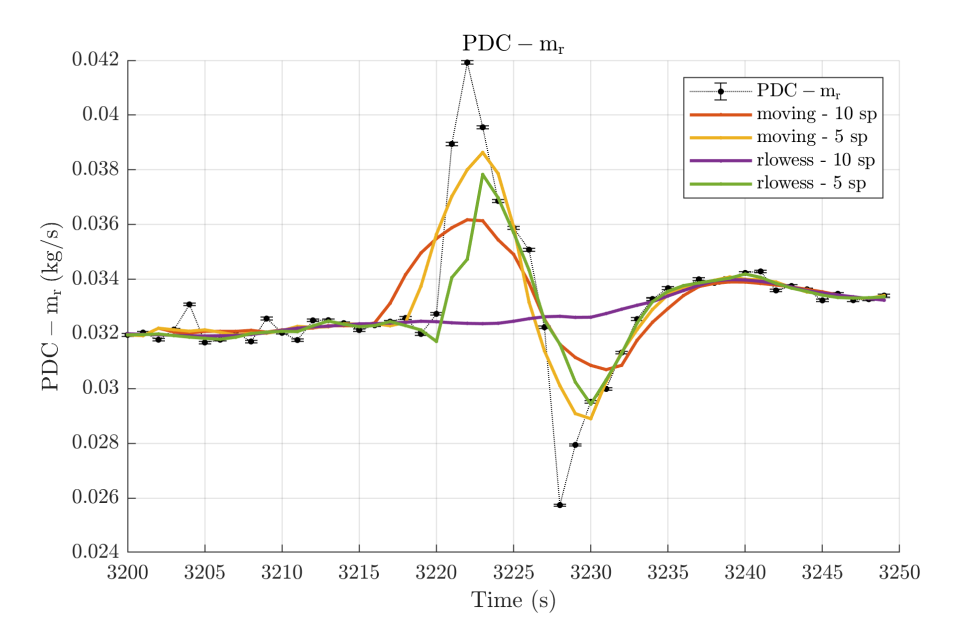


Figure 4: Accuracy evaluation of the refrigerant mass flow rate measurements and smoothing solutions comparison.

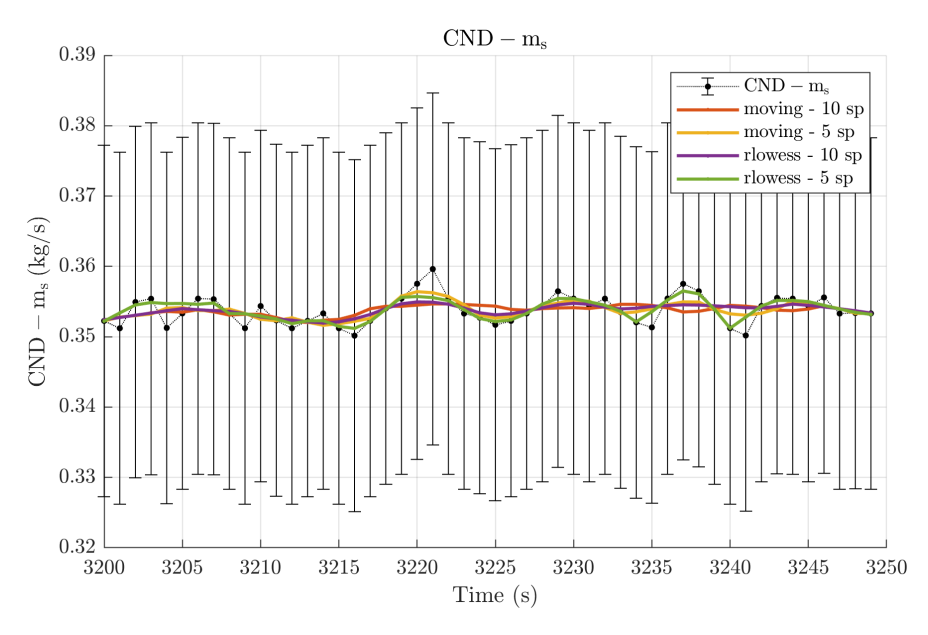


Figure 5: Accuracy evaluation of the water mass flow rate measurements in the hot secondary circuit and smoothing solutions comparison.

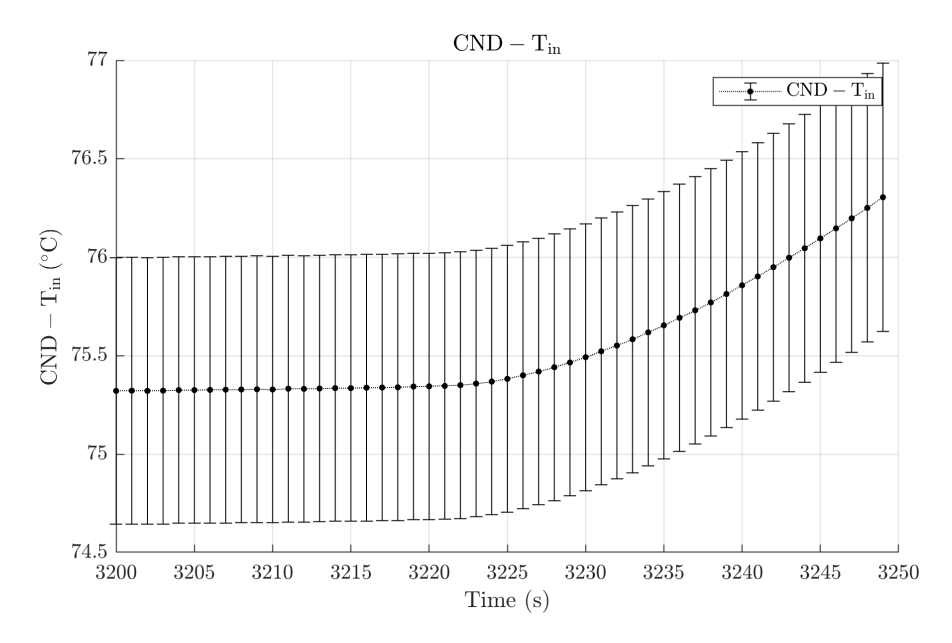


Figure 6: Accuracy evaluation of the refrigerant temperature measurements at the condenser inlet.

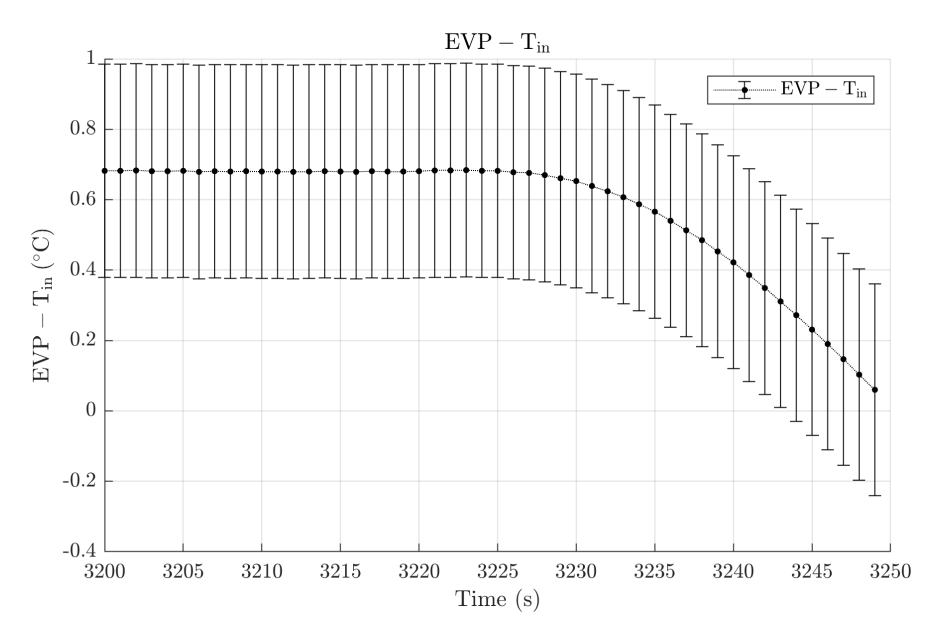


Figure 7: Accuracy evaluation of the refrigerant temperature measurements at the condenser inlet.

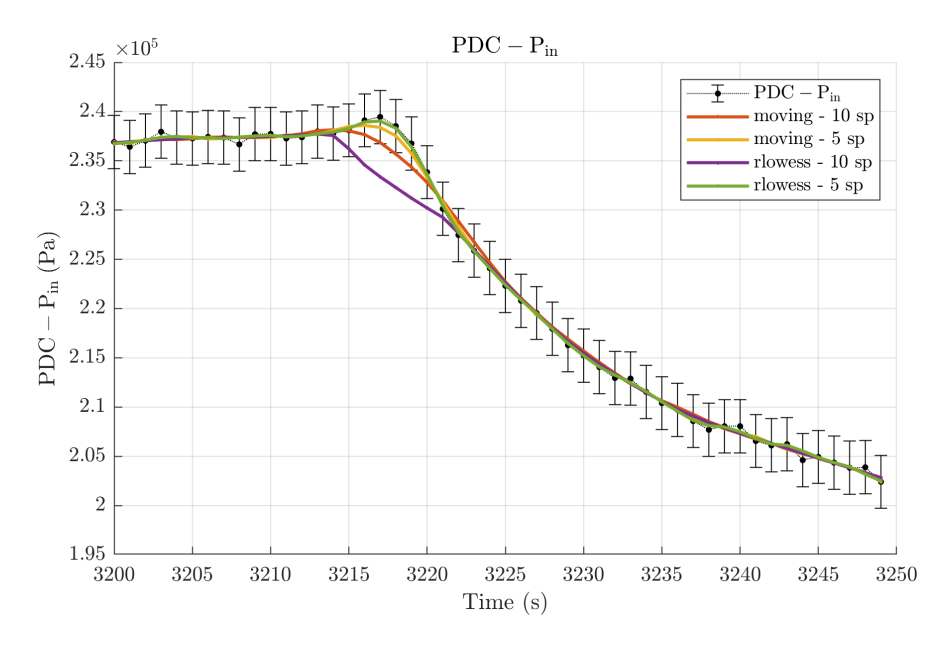


Figure 8: Accuracy evaluation of the refrigerant pressure measurements at the compressor inlet and smoothing solutions comparison.

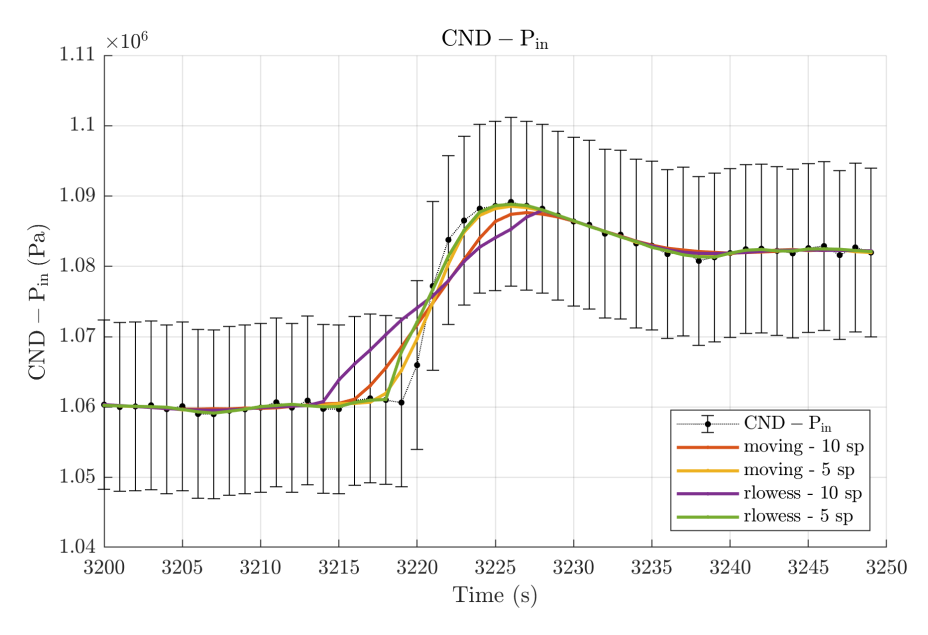


Figure 9: Accuracy evaluation of the refrigerant pressure measurements at the condenser inlet and smoothing solutions comparison.

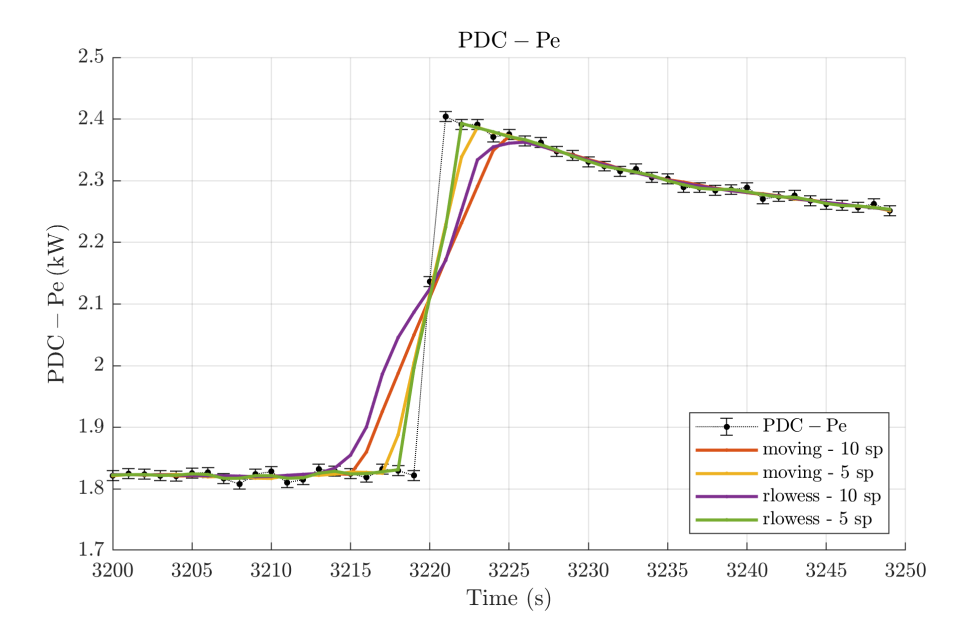


Figure 10: Accuracy evaluation of the comparison of compressor electric power measurements and smoothing solutions.

if the full performance investigation of the VCS can be realized with the refrigerant side measurements, which are more accurate, some inaccuracies may arise during the investigation of the heat transfer of the secondary fluid, which is the main goal of the system, be it the cold side for refrigeration plants or the hot side for heat pumps. The dynamic response is satisfactory but affected by a small delay to the analogic acquisition. Finally, the RTDs installed in the test rig are employed to evaluate the temperature of both fluids and the environmental air in the neighbourhood of the compressor. Their accuracy is class B, so in the range of interest for these test, is within  $\pm$  o.8 °C.

The test rig is designed chiefly for the steady state investigation of the VCS performance. However, the kind of measurements available allow its use for transients analysis too. Indeed, the response time of the installed transducers is compatible with the sampling time.

Although the experimental facility is realized according to the highest standards, the available data are subjected to some small oscillations brought by the measurement apparatus or the flow conditions inside the circuits.

#### Dynamic behaviour of the temperature sensor 3.3.4

The temperature transducers installed in the experimental facility are RTDs. The working principle of the sensor is based on the deviation of the electric resistance of a material with the temperature. The RTD Pt100 by Carel in fig. 11 is placed inside a small case made of stainless



Figure 11: Temperature transducer RTD Pt100 by Carel Carel, 2023.

steel in order to achieve the IP65 index of protection for the electronic instruments (according to EN 60529). The sensor housing leads to a slower dynamic response of the transducer, indeed its time constant is about 20 s in air, Carel, 2023.

This sensor's dynamic response may interfere with the measurement's reliability during transients. Indeed, in steady-state conditions, the instrument's accuracy is the parameter used to evaluate the reliability of the measured value. The dynamic behaviour of the sensor can be simulated as a filter with a first-order transfer function; the damping effect is related to the time constant of the input signal. In this case, if the dynamic behaviour of the variable to be measured is slower than that of the temperature transducer, the sensor marginally affects the measurement. On the other hand, if the system dynamic to be evaluated is faster than the sensor, it cannot follow its behaviour, and it produces a damped signal.

Two possible solutions can be adopted during the validation process. The first applies the signal reconstruction of the temperature measured value to estimate its real value, which is employed for comparison with model prediction. In the second case, the calculated temperature is processed with a low-pass filter with the same time constant of the transducer to emulate its effect, and then this value is used for comparison with the measured data.

In this work, the latter approach is followed to evaluate the influence of the sensor on the calculated values. A simple first-order dynamic system is realized to simulate the sensor's behaviour. The first transfer function is in the form of eq. (3.3):

Modelling of the sensor dynamic

$$F(s) = \frac{1}{\tau s + 1} \tag{3.3}$$

where  $\tau$  indicates the sensor time constant in s. The Simulink<sup>®</sup> model is shown in fig. 12. The user must provide two user-defined parameters: the time constant of the sensor  $\tau$  and the initial value of the temperature.

In order to evaluate the effect of the sensor on the temperature calculated by the compressor physical model, a comparison between the experimental data, the calculated values and the output of the sensor model is carried out during a frequency transient. From fig. 13, it is possible to appreciate that the effect of the transducer time constant is negligible, showing a peak absolute deviation of about 4%; which is



Figure 12: Simulink® scheme of the temperature transducer model.

less than one half of the deviation imputable to the compressor model with respect to the experimental data during transients, indeed the steady state evaluation is not influenced by the sensor response time.

Finally, given that the temperature dynamic to be investigated is much slower than that of the sensor, the effect of the time constant of the temperature transducer is neglected in the validation, both for the inputs and for the outputs calculated.

#### 3.3.5 Data smoothing

The measured data are employed to validate the numerical model of the VCS and each one of its components. To this aim, the experimental data are employed to compare the model outputs with the real values and inputs for each model to compare the physical and digital twins in the same operating conditions. In this context, the input data must be as smooth as possible to avoid introducing undesirable oscillating behaviour in the numerical model. This problem is especially felt by the HEX dynamical model, which requires the solution of a system of differential equations that leads to an ill-conditioned matrix or stiff numerical problem, see chapter 10.

In this context, the data to be fed as input to the models are smoothed to remove the non-significant oscillations while retaining the dynamic behaviour during the transients investigated. To this aim the Matlab® function Smooth is employed, see MathWorks, 2024b; two different algorithm were tested, the moving average and the robust local regression using weighted linear least squares and a 1st degree polynomial mode, with different number of samples involved (5 or 10). From the plots in figs. 4, 5 and 8 to 10 is possible to evaluate the effect of the smoothing of the experimental data; the temperature measurements were not smoothed because the dynamic response of the sensor leads to very plain trends. The regression algorithm offers to a faithful approximation of the original data and also captures the transient behaviour with good accuracy; this is evident from the pressure and refrigerant mass flow rate measurements figs. 4, 8 and 9: increasing the number of points involved in the regression or in the average calculation, reduces the oscillations of smoothed data, but also reduces their capability of capturing the dynamic behaviour of the physical variable.

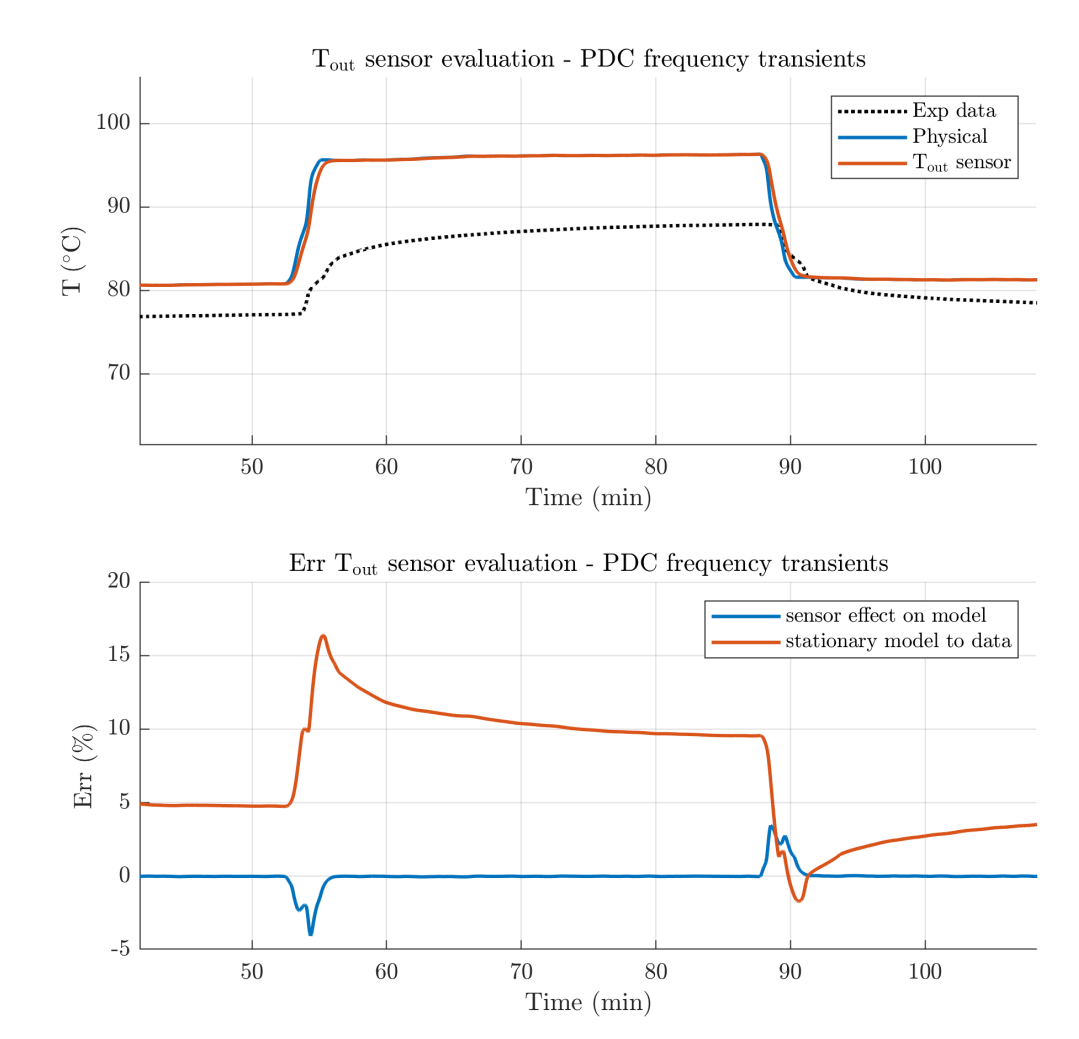


Figure 13: Verification of the effect of the transducer dynamics on the refrigerant outlet temperature evaluated by the compressor physical model. The experimental data (Exp data) are compared with the values calculated using the physical model of the compressor (Physical) and with the same values filtered by the sensor model (Tout sensor).

For this reason, to smooth the experimental data in order to create reliable inputs for the numerical model validation, the robust local regression algorithm is chosen, with a moving window of 5 samples, which corresponds in this case to 5 s. However, the secondary flow mass flow rate needs different processing because, in some conditions, the signal is affected by a large amount of noise, which entails unrealistic oscillations of the values around their mean. Given this time vector must be provided as input directly to the model, stronger filtering is necessary to avoid numerical failures. So the e robust local regression algorithm with a moving window of 30 samples, which corresponds in this case to 30 s, is applied.

Smoothing algorithm chosen: robust local regression

#### TEST PERFORMED 3.4

Some experimental data were carried out employing the R450A refrigerant.

- 1. Test 1 with R450A This test is conducted at a fixed compressor frequency equal to 50 Hz. The valve opening varies during the test, as reported in the corresponding time vector. The controlled inputs during the central portion of the test employed in the full machine validation are represented in fig. 14.
- 2. Test 2 with R450A This test is performed at fixed valve opening, and the compressor frequency undergoes a step variation from 50 Hz to 65 Hz and return. A complete shutdown-restart compressor transient is investigated at the end of the test. The controlled inputs during the central portion of the test employed in the full machine validation are represented in fig. 15.

The behaviour of the secondary fluids during the same interval of the two experimental tests is represented in figs. 16 and 17, to offer a general idea of the operating point of the plant. The refrigerant side will be addressed extensively in chapter 11.

In the full machine validation, chapter 11, only the central portion of the two tests is employed, while for the compressor a larger window is preferred, chapter 6.

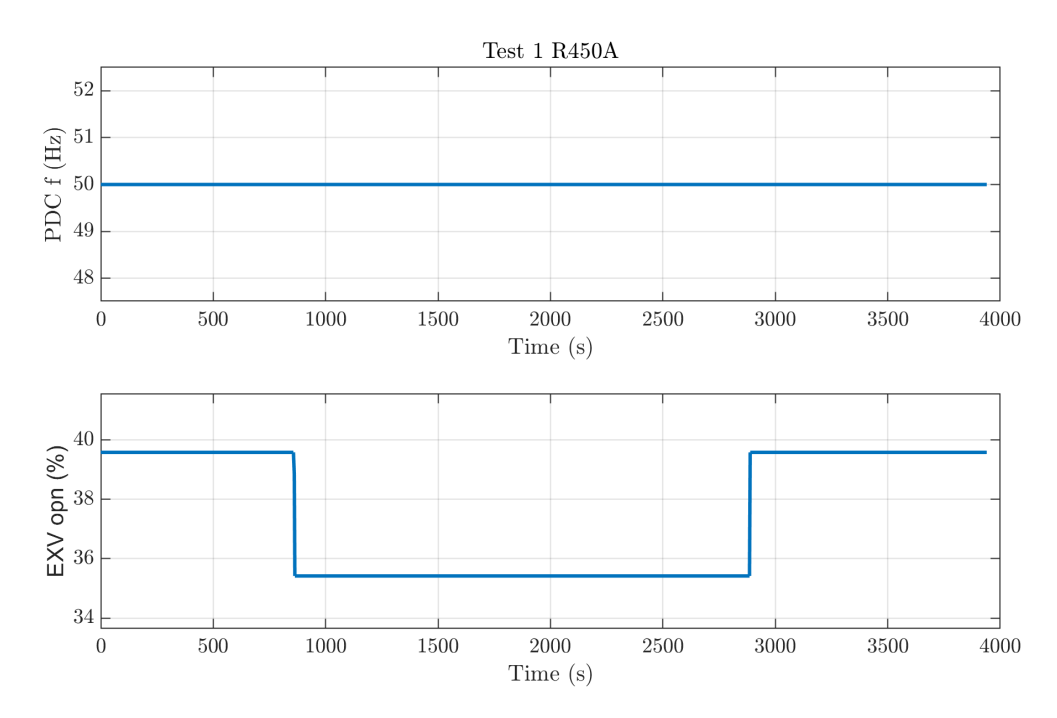


Figure 14: Controlled input during the Test 1 with R450A.

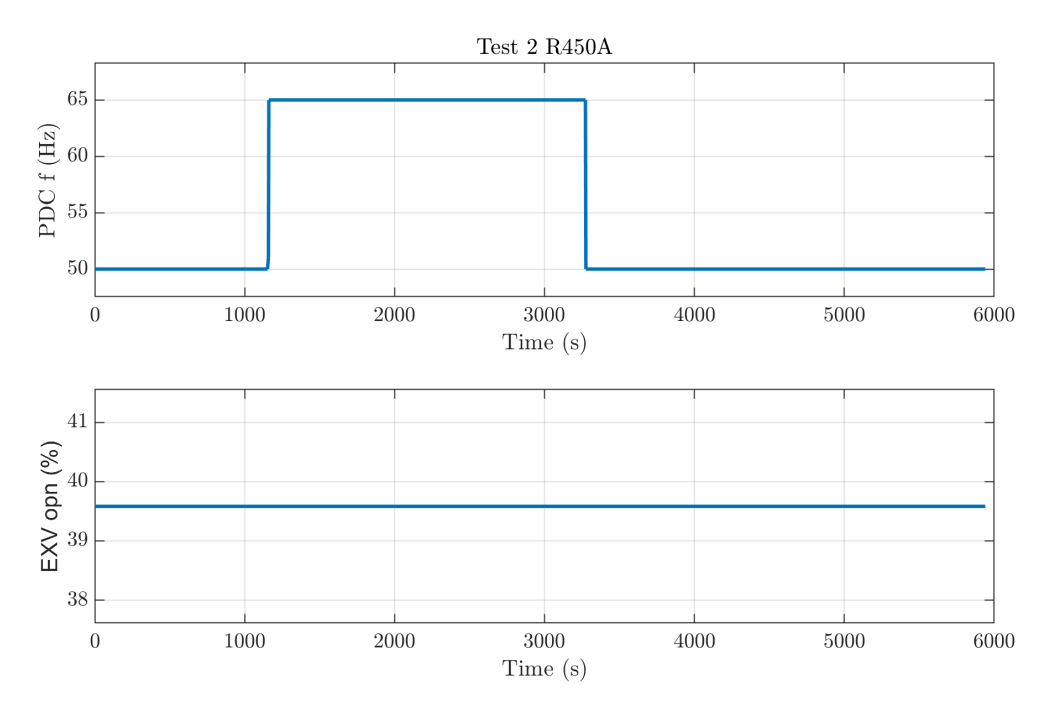


Figure 15: Controlled input during the Test 2 with R450A.

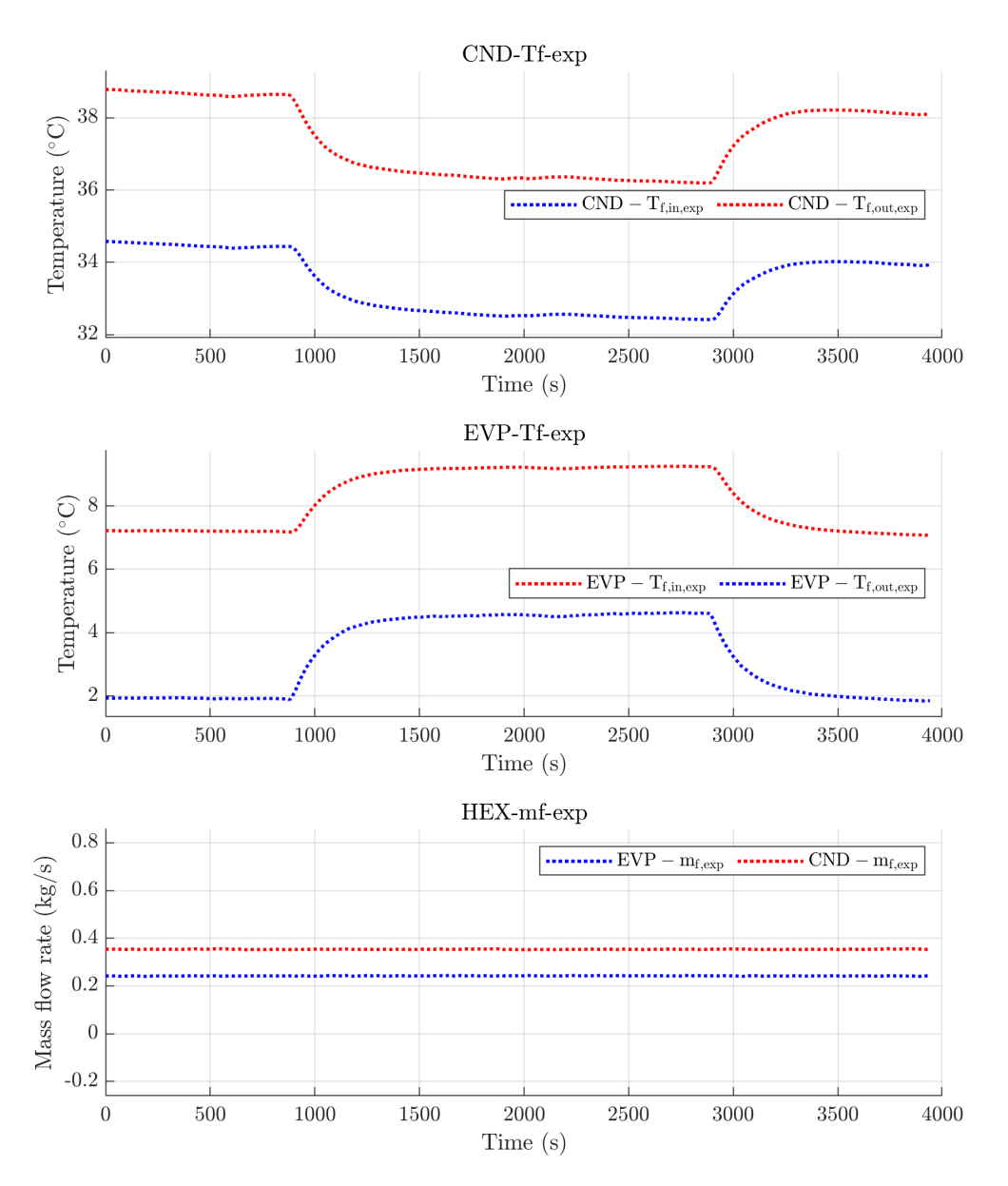


Figure 16: Experimental behaviour of secondary fluids during Test 1 with R450A. From the top: inlet and outlet temperature of the secondary fluids in the condenser and in the evaporator, and their mass flow rate.

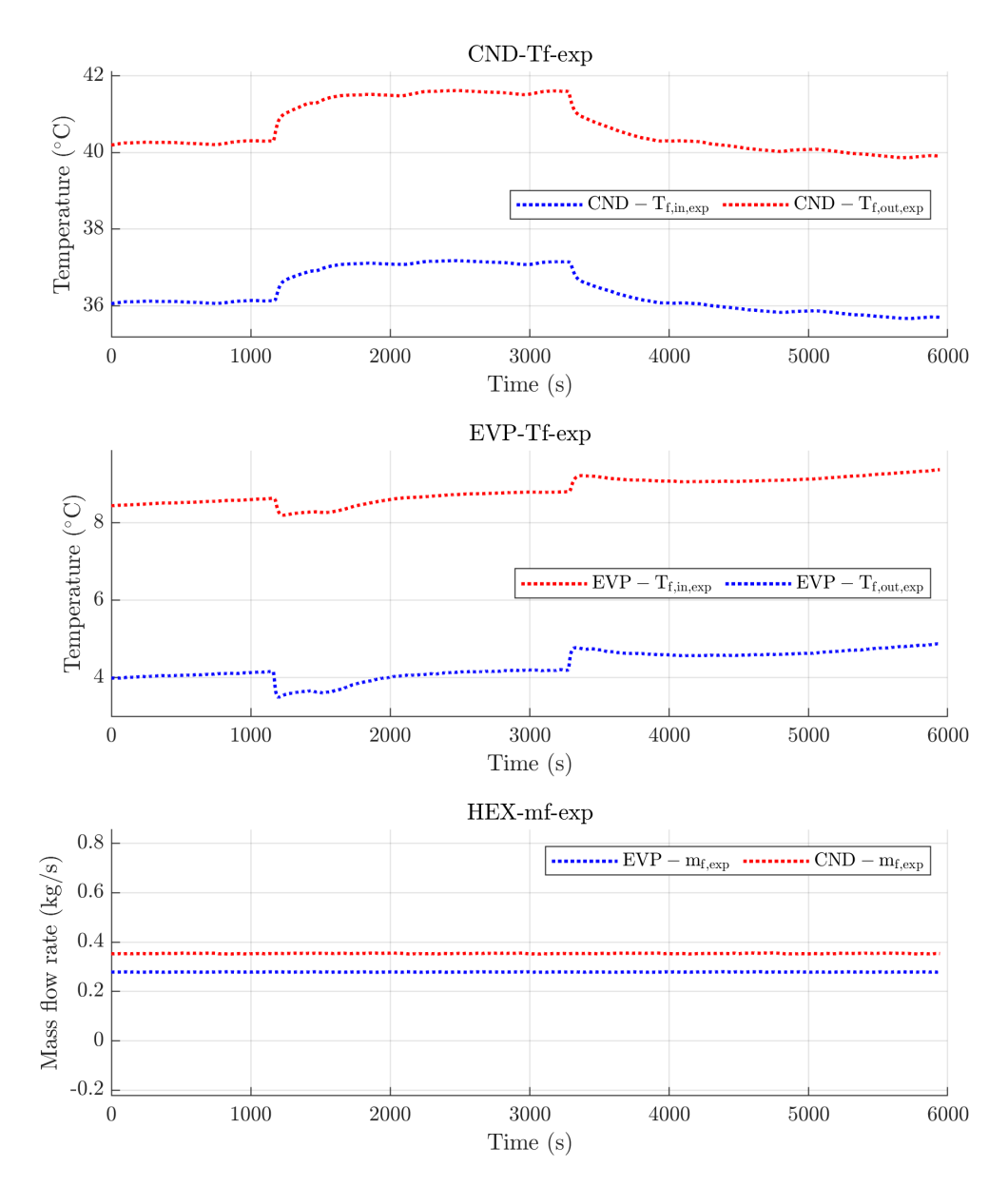


Figure 17: Experimental behaviour of secondary fluids during Test 2 with R450A. From the top: inlet and outlet temperature of the secondary fluids in the condenser and in the evaporator, and their mass flow rate.

# 4 PHYSICAL PROPERTIES OF THE WORKING FLUIDS

## 4.1 PHYSICAL PROPERTIES OF THE FLUIDS

In the context of numerical modelling of processes involving fluids, the evaluation of their physical properties when varying the operating conditions is a key factor that affects both the accuracy and the calculation speed of the model. The most precise way to evaluate the physical properties is by directly employing the state equations for pure substances or mixtures. Different libraries make available the solutions of the equations of state for many fluids of interest, like CoolProp by Bell et al., 2014 and RefProp by Huber et al., 2018. They are very similar in use and accuracy; the main differences are that CoolProp is open-source software, while RefProp usage is limited by license, and RefProp has a more extensive library of pure substances and mixtures. In this work, the Refprop libraries are employed when the refrigerant is unavailable in CoolProp. Both these libraries can easily be called in Matlab<sup>®</sup> script or a Simulink<sup>®</sup> block function. Although this libraries are coded to guarantee the best performance in terms of calculation speed, the direct calls to them slow down the simulation in Simulink® considerably. Moreover, from the coding point of view, introducing frequent function calls to an external library without complete control may lead to unexpected problems during the execution. For these reasons, the physical properties are evaluated during the simulation by employing tabulated data generated with these libraries to avoid external calls. The physical properties are pre-calculated by applying the state equations, collected into tables, and saved in data files; during the initialization of the simulation, the data are uploaded into the workspace and linked to a specific Lookup Table block, which can evaluate the desired variable by performing a linear interpolation over the available data starting from the inputs provided. In this way, the coding of the block function for the evaluation of the physical properties of the working fluids becomes very easy thanks to the capabilities of the Simulink® environment; on the other hand, more effort must be devoted during preprocessing for the creation of a suitable data table. In the following, more details are provided about this phase.

#### Simulink® Lookup Tables 4.1.1

As reported in the Mathworks Help Center, MathWorks, 2024a, the Lookup Tables are designed to model the non-linearity of a process by approximating a mathematical function with sample tabulated data, which map the inputs to the output. In this work, both onedimensional and bidimensional Lookup Tables are employed: in general, the n-D Lookup Table block evaluates a sampled representation of a function F in n variables.

$$y = F(x_1, x_2, ..., x_n)$$

The block produces a y value by looking up or interpolating a ndimensional data table provided as a block parameter. The other parameters of the block are the so-called breakpoints, which are the vectors employed during table construction to individuate the points in the table; so, each dimension of the data table corresponds to a breakpoint vector. Summarizing, for the definition of a Lookup Table block is needed: a n-dimensional table that gathers the values of y for each value of the breakpoints vectors,  $tb = (d_1, d_3, ..., d_n)$ , and the n breakpoints vectors with dimension equal to  $d_1, d_2, ..., d_n$ respectively. The block produces only one output y and receives n inputs corresponding to the number of dependant variables of the function F. In Matlab® environment, by convention, the first input identifies the first dimension (row) breakpoints, and the second input identifies the second dimension (column) breakpoints.

## Required tables

In each numerical model, the evaluation of the physical properties of the working fluid is needed. It is possible to fully define a thermodynamic state by knowing two intensive and one extensive variables. Given the control volume, only two intensive quantities are needed to calculate all the other physical properties of the substance by applying the suitable state equation. Likewise, employing the Lookup Table, it is possible to calculate the variable of interest by providing intensive quantities as inputs. The input values for the Lookup Tables coincide with the state variables selected in the model. On the other hand, for the compressor physical model, which has no state variables, the inputs of the tables are related to the equations employed. For these reasons, two-dimensional Lookup Tables are used for most physical property evaluations. In contrast, one-dimensional Lookup Tables evaluate the saturation conditions where only one intensive variable is needed. In tables 12 to 15 the physical properties tables employed for each model are reported.

Output	Input	State
$\frac{\partial \rho_{r,j}}{\partial p}\Big _{h}$	p, h	SC-TP-SH
$\frac{\partial \rho}{\partial p} \Big _{h}$	p, h	SC-TP-SH
T	p, h	SC-TP-SH
ρ	p, h	SC-TP-SH
$T_{sat}$	p	TP
h <sub>l,sat</sub>	p	TP
$h_{v,sat}$	p	TP

Table 12: Refrigerant physical properties tables employed in the HEX model.

Output	Input	State
ρ	T	SC
$c_p$	T	SC
c <sub>p</sub> μ	T	SC
λ	T	SC

Table 13: Secondary fluid physical properties tables employed in the HEX model.

Output	Input	State
ρ	T, p	SH
h	s, p	SH
T	h, p	SH
S	T, p	SH
h	T, p	SH
$T_{sat}$	p	TP

Table 14: Refrigerant physical properties tables employed in the compressor physical model.

Output	Input	State
р	ρ, u	SC-TP-SH

Table 15: Refrigerant physical properties tables employed in the accumulator model.

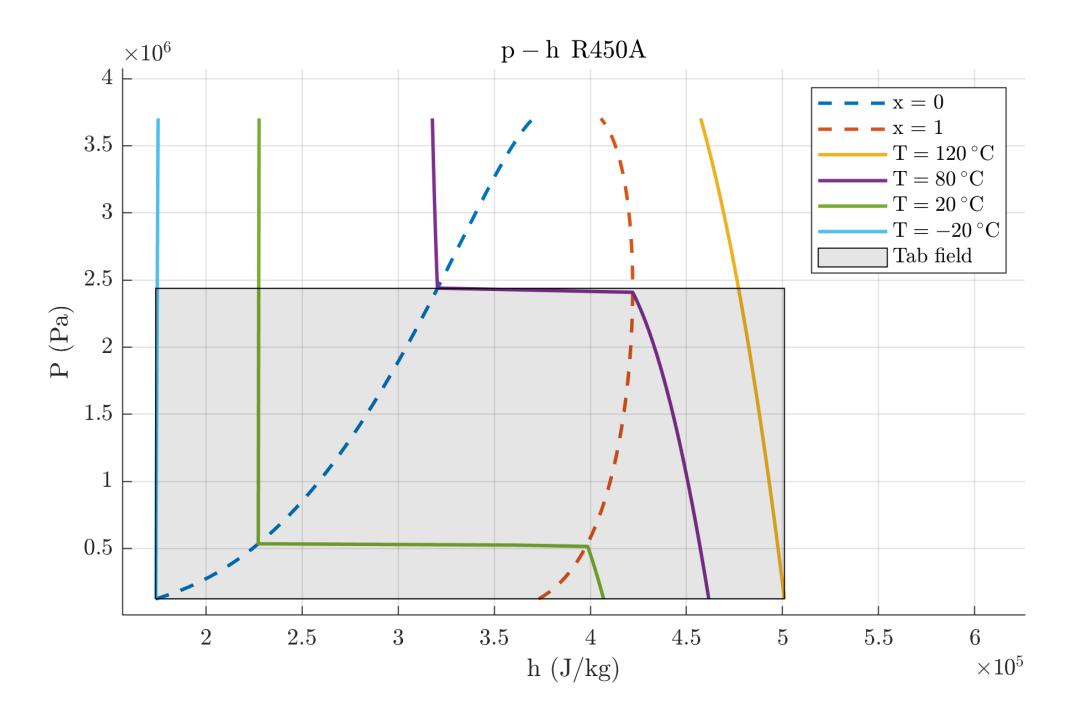


**Figure 18**: P-h diagram for R450A.

## Operating limits

The operating limits of a refrigerant involved in a VCS are usually defined in terms of maximum and minimum pressure and maximum temperature. These limits are mainly related to the compressor characteristics, particularly the sealing element and operating limits of the lubricant. The maximum refrigerant temperature is reached at the end of the compression phase; for high-pressure ratios, extra cooling is needed. The maximum temperature for the refrigerant is around 120 °C to avoid oil depletion and seal deterioration.

As an example, in fig. 3, the operating envelope of the compressor D<sub>3</sub>-1<sub>3</sub>.1Y VS by Frascold employed in the experimental facility is shown. However, these limits are common for VCS applications. The corresponding saturation temperature represents the maximum and minimum pressure levels for condensation and evaporation. The blue field in the top left corner represents the region where additional cooling is required because, in these conditions, the refrigerant leaves the compressor at a temperature higher than the prescribed limit.

To calculate the physical property tables, the evaluation field must be defined in terms of the input variables employed. So, starting from the saturation temperature limits, which correspond to the pressure limitation and the maximum temperature allowable, the range of the other variables must be derived. Starting from the thermodynamic diagram p-h fig. 18, T-s fig. 19 and p-u fig. 20 is possible to define the suitable limits, which are listed in table 16. The same argument can be applied to all refrigerants.

Operating envelope of the compressor

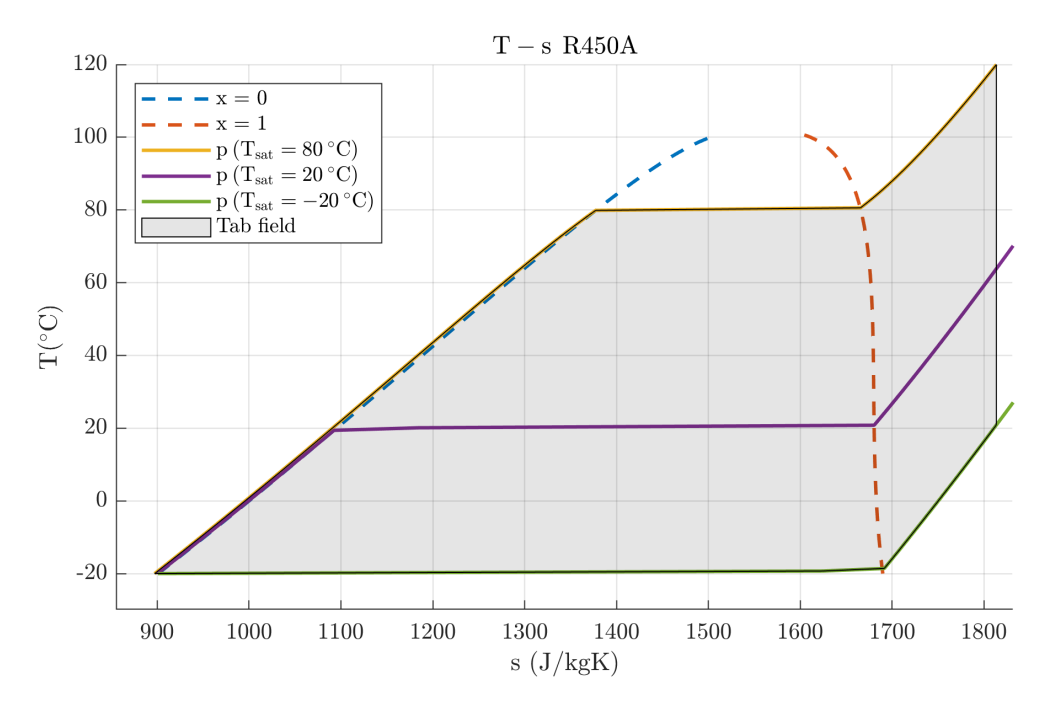


Figure 19: T-s diagram for R450A.

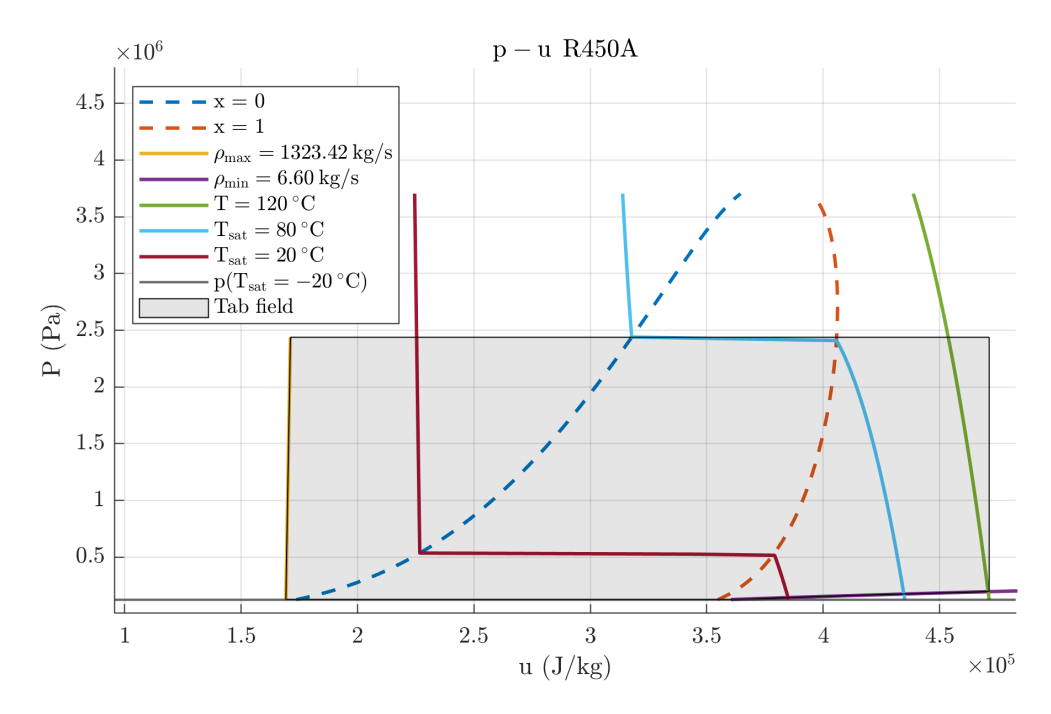


Figure 20: P-u diagram for R450A.

The lower limit for the specific enthalpy, internal energy, and entropy is assumed to correspond to the saturated liquid state at the minimum pressure. On the other hand, the upper limit for the specific enthalpy, internal energy, and entropy is identified with the conditions of maximum temperature allowable and minimum pressure, even if these conditions are not achieved during normal operation. Concerning the density, the maximum and the minimum values in the operating envelope occur at the maximum pressure and minimum temperature and the minimum pressure and maximum temperature, respectively. However, these limits are too conservative because they consider states unreachable during regular operations. The density range is therefore as follows: the maximum value corresponds to saturated liquid condition at the minimum pressure, the minimum value corresponds to the saturated vapour at the same pressure. The reliability of this selection can be appreciated in fig. 20.

## Table calculation: troubleshooting

For certain refrigerants, like the zeotropic mixture R450A, some routines contained inside the physical library RefProp can fail close to the critical point; this issue was encountered looking for T and ρ from T and p and looking for p starting from  $\rho$  and u. The error is motivated by the lack of some coefficients for evaluating the critical line. The evaluating field must therefore be far from the critical point. This restriction is compatible with the operating envelope. In the p-pu table, other errors may arise, some related to the overstepping of the acceptable range of the physical variable employed and some related to the discontinuity of the density curve when crossing the lower limit curve. To overcome the first criticality, suitable pressure and internal energy limitations are imposed; for the latter, a more careful procedure is needed: after detecting the unexpected values, these are substituted with a linearly interpolated value along the same isochoric line.

Another aspect to mention is the definition of the vectors for creating the data tables, the so-called breakpoints vectors MathWorks, 2024a. A more accurate interpolation is reached with a finer grid. The breakpoints are equispaced between the maximum and the minimum allowable value. Yet, the density vector needs a different approach because the limits differ by about three orders of magnitude. In this case, an equispaced vector is not suitable. A logarithmic distribution is chosen instead: the values in this vector are logarithmically spaced between the selected decades, from 10<sup>0</sup> to 10<sup>4</sup>. Then, values at the ends are selected to be in the previously defined density limits. Finally, the vector may be refined if need be.

Quantity	Value
$T_{max}$	120 °C
$T_{sat,max}$	8o °C
$T_{\text{sat,min}}$	-20 °C
$p_{max}$	$p(T_{sat,max})$
$P_{min}$	$p(T_{sat,min})$
$h_{max}$	$h(T_{max}, p_{min})$
$h_{min}$	$h(T_{\min}, x = 0)$
$\mathfrak{u}_{max}$	$u(T_{max}, p_{min})$
$\mathfrak{u}_{min}$	$u(T_{\min}, x = 0)$
$\rho_{max}$	$\rho(p_{\min}, x = 1)$
$\rho_{\text{min}}$	$\rho(p_{\min}, T_{\max})$

**Table 16:** Limits for the physical properties tables.

## Evaluation of the partial derivatives

As mentioned before, the thermodynamic state of a fluid is completely defined by an extensive variable and two intensive variables. In this case, the average pressure and the enthalpy of the refrigerant are chosen as state variables to be integrated over time. From their, it is possible to calculate all the fluid properties employing a suitable equation of state.

To implement the model, the partial derivatives of density respect to the state variables need to be calculated, as discussed in chapter 10. Indeed, the time variation of the density can be estimated from that of the pressure and enthalpy employing the partial derivatives, eq. (4.1).

$$\frac{d\rho}{dt} = \frac{\partial\rho}{\partial\rho}\bigg|_{h} \frac{d\rho}{dt} + \frac{\partial\rho}{\partial h}\bigg|_{p} \frac{dh}{dt}$$
(4.1)

At each time step, the following derivatives need to be evaluated in each element of the grid.

$$\frac{\partial \rho_{r,j}}{\partial p}\bigg|_{h} \qquad \frac{\partial \rho_{r,j}}{\partial h_{r,j}}\bigg|_{p} \tag{4.2}$$

The partial derivatives are evaluated employing the suitable fluid properties library. The density value is calculated for a feasible operating envelope defined by the pressure and enthalpy vectors. The partial derivatives are evaluated with a central difference method, maintaining the pressure or enthalpy fixed and varying the other variable to calculate the desired partial derivative. For the values at the boundary of the table, a forward difference or a backward difference scheme is employed. The calculated values are stored in a table and saved in the file, with the corresponding pressure and enthalpy vector employed

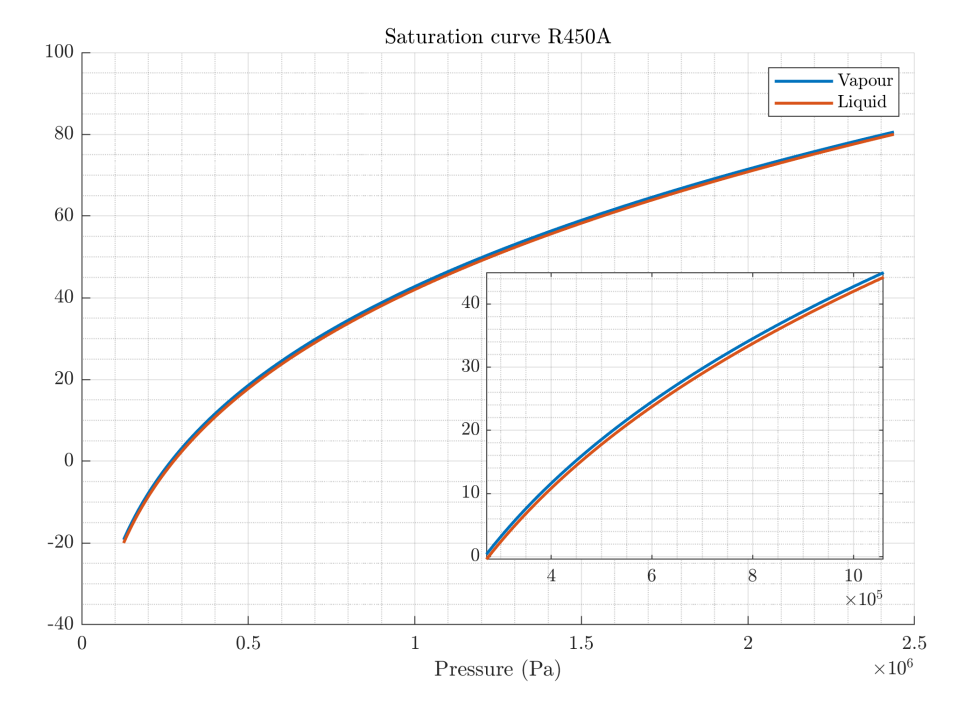


Figure 21: Saturation curve relative to R450A refrigerant.

as indices. In the Simulink® environment, the table and the vector are loaded in the workspace and employing the Lookup Table block, it is possible to extract a linear interpolated value for the given input in terms of pressure and enthalpy.

#### Saturation curve 4.1.5

From fig. 21 it is possible to appreciate that a small saturation temperature glide, typical of zeotropic mixtures, characterizes the R450A.

Moreover, for the R450A refrigerant a variation of the saturation temperature of 1 °C correspond to a pressure drop of about 20 kPa. This can be helpful information to evaluate the reliability of the simulation test performed and the comparison with the experimental measurements. Indeed, the temperature sensors have an accuracy in the order of  $\pm 0.5$  °C, while the pressure measures have a reliable range of about 5 kPa at the low-pressure side and 20 kPa at the high-pressure side. This uncertainty corresponds to a variation of almost 1 °C in the saturation temperature.

## 5 | THE GOVERNING EQUATION

## 5.1 BALANCE EQUATIONS

Generally, in most HEXs, two working fluids interact, separated by a wall. Given a generic portion of the HEX, three zones can be recognized: the refrigerant, the secondary fluid, and the HEX wall. The process can thus be investigated by employing the mass and energy balance for both fluids and the HEX wall and evaluating the heat transfer rate between the fluids and the HEX wall in a suitable way.

## 5.1.1 Mass balance equation

The mass balance equation to be applied to both working fluids can be written in the following general form:

$$\frac{\mathrm{d}(\rho V)}{\mathrm{d}\tau} = \dot{m}_{i} - \dot{m}_{o} \tag{5.1}$$

While the refrigerant density varies considerably during the process due to the phase change and the pressure variation during transients, the secondary fluid's density in most applications can be considered constant because the operating pressure and temperature do not vary significantly. In the case of incompressible flow, the mass balance equation reduces to:

$$\frac{d(\rho V)}{d\tau} = \dot{m}_i - \dot{m}_o = 0 \tag{5.2}$$

## 5.1.2 Energy balance equation

The energy balance equation for the generic fluid contained in the control volume can be written as:

$$\frac{dU}{d\tau} = \frac{d(\rho uV)}{d\tau} = \dot{m}_i h_i - \dot{m}_o h_o + \dot{Q}$$
 (5.3)

In case of incompressible flow in an equispaced grid the energy balance reduces to

$$\rho V \frac{du}{d\tau} = \dot{m}_i h_i - \dot{m}_o h_o + \dot{Q}$$
 (5.4)

The term  $\dot{Q}$  represents the net thermal power that enters the control volume. The energy balance equation can also be employed for the heat exchanger wall in the following form:

$$m_w \frac{du_w}{d\tau} = m_w c_w \frac{dT_w}{d\tau} = \dot{Q}_i - \dot{Q}_o$$
 (5.5)

#### **HEAT TRANSFER** 5.2

The evaluation of the heat transfer rate should be carried out by employing the  $\varepsilon-NTU$  technique because only the inlet condition of working fluids in the control volume is known.

$$\dot{Q} = \epsilon C_{\min} (T_{\text{hot.i}} - T_{\text{cold.i}})$$
 (5.6)

## 6 compressor

Positive displacement compressors are the most commonly used in VCS, be it for refrigeration or air conditioning applications or heat pumps because they guarantee the set flow rate regardless of the operating pressure levels. Indeed, positive displacement compressors work by trapping a fixed volume of gas from the suction line and mechanically reducing its volume to increase the pressure. In contrast, a dynamic compressor increases the working fluid's kinetic energy, employing rotating blades or impellers; a diffuser then converts it into pressure. The most diffuse types in VCS are the reciprocating, both hermetic ore semi-hermetic, the rolling piston, the scroll and the screw compressors.

The compressor's main function is to generate a refrigerant mass flow rate from a low-pressure to a high-pressure reservoir.

## 6.1 COMPRESSOR MODELLING

The modelling of compressors plays an important role in the simulation of VCSs, whether for refrigeration, air conditioning applications or heat pumps. Indeed, an accurate estimation of the refrigerant outlet conditions positively affects the accuracy of the whole cycle simulation, and the electric energy consumed by the VCS for the most part is absorbed by the electric motor which powers the compressor; indeed, fans and pumps for the handling of the secondary fluid are often less energy consuming.

The modelling of compressors employed in VCSs has been addressed by several works with different approaches. According to Negrão et al., 2011 the mathematical models can be grouped into three main categories: polynomial fits, semi-empirical and detailed models.

The reference standards for the manufacturers' certification of the compressor performance adopt the polynomial fits. These models employ a third-order polynomial to correlate the performance variable to the suction and discharge line saturation temperatures, *AHRI 540*, 2020; *EN 12900*, 2013. Since this approach is considered not to have physical meaning, it is suggested not to employ out of the test range W. Li, 2012; Negrão et al., 2011

At the other end, the third category gathers more complex approaches to compressor modelling which aim to describe the different

Polynomial models

Detailed models

physical processes involved in the system, Giuffrida, 2016; Molinaroli et al., 2017; Navarro et al., 2007. In the case of positive displacement compressors the evolution of the refrigerant through the machinery can be divided into the following sequence of effects:

- 1. isobaric heat transfer to the sucked refrigerant at the suction, due to motor cooling and friction;
- 2. isobaric mixing of the sucked refrigerant with internal leakages
- 3. vapour heating due to the heat transferred from the hot side of the compressor (discharge) to the inlet flow and to the leaks;
- 4. isoenthalpic pressure loss at the suction valve;
- 5. isentropic compression from the suction pressure up to the internal discharge pressure;
- 6. isoenthalpic expansion from the internal discharge pressure to the actual discharge pressure through the discharge valve
- 7. isobaric heat transfer at compressor discharge.

Accounting for all effects leads to a detailed model of the refrigerant behaviour through the compressor. However, some parameters must be identified with an objective function minimization procedure based on the deviation of the predicted performance from their rated values, Duprez et al., 2007; Giuffrida, 2016; Molinaroli et al., 2017. As an alternative, the identification procedure can be realized employing measurement data, which must be collected from elaborated experimental campaigns, Longo and Gasparella, 2003; Winandy et al., 2002.

Between the two extremes, the so-called semi-empirical models start from basic fluid dynamic and thermodynamic relations to describe the behaviour of the compressor, such as those proposed by W. Li, 2012, 2013 and Negrão et al., 2011. These approaches fall into the category of grey-box models, B. D. Rasmussen and Jakobsen, 2000, because, although the main physics of the process are well captured, some parameters need to be defined to achieve the desired accuracy for the model. A key role is played by determining the efficiencies, which assess the distance between the ideal and the actual process. Also, in this case, performance data are needed to evaluate these efficiencies using a minimization procedure.

The models can be classified according to their ability to evaluate the process out of the test range accurately. Often, the available data cover only a portion of the operating conditions, so extrapolation accuracy is a very important feature during any complex simulation. In general, the black-box approach, like the polynomials, is unsuitable for Semi-empirical models

Extrapolation capability

extrapolation because the accuracy of the predicted values can have an unphysical outcome. The third-order polynomial can fit the available data very precisely. Yet, its trend has no physical meaning, as pointed out by Reindl and Klein, 2000, which leads to significant errors during extrapolation. The *grey-box* model is more suitable for extrapolation W. Li, 2012 because the main behaviour of the process is described by physical correlations; the tuning parameters affect the accuracy of the model, not its general trend. To employ the extrapolation capability of the grey-box models, neural network approaches can be used Yang et al., 2009.

The models of the compressors can be categorized according to their ability to capture the transient behaviour of the process. For the most part, the approaches mentioned above are validated in stationary conditions, but this is not strictly equivalent to rate them as unsuitable for transient simulations. The models presented by Longo and Gasparella, 2003 and Rigola et al., 2001 can capture the dynamic behaviour of the refrigerant inside the compressor during the cycle as function of the crank angle. Yet, this implies that the test rig must be apt to measure with a sampling frequency higher than twice the rotational frequency of the crankshaft (Nyquist-Shannon sampling theorem).

For this work, the compressor can be treated as a static system; so a set of algebraic equations suffices to describe the behaviour of this component. The model must provide the outlet state of the refrigerant starting from its inlet state and the operating pressure levels on both sides. The available pressure and temperature measurements can define the inlet thermodynamic state of the refrigerant. The model inputs are thus the operating pressure levels and the inlet refrigerant temperature. Moreover, if the compressor rotational speed can change during operation, this should be considered as controlled input for the model. The main outputs are the refrigerant mass flow rate and outlet temperature. The electric power consumption should be also computed for performance investigation.

The compressor model is developed following two approaches:

- 1. the physically-based correlations implementing the volumetric and isoentropic efficiency maps;
- 2. the third-order polynomial correlations defined according to the reference standards.

#### 6.2PHYSICALLY-BASED MODEL

Given a compressor with a particular geometrical characteristic, in terms of nominal displacement  $V_n$  for each revolution, the mass flow

Modelling approaches selected rate elaborated can be evaluated as a function of the operating pressure levels and of the rotational speed, according to eq. (6.1)

Mass flow rate

$$\dot{m}_{\rm r} = \eta_{\rm vol} \, \Omega \, \rho_{\rm r.i} \, V_{\rm n} \tag{6.1}$$

where  $\Omega$  is for the rotational frequency (Hz),  $\rho_{r,i}$  is the refrigerant density at the inlet section (kg m<sup>-3</sup>),  $V_n$  is the nominal displacement and  $\eta_{vol}$  is the volumetric efficiency of the machine, which is, in general, a function of the operating pressure levels, the refrigerant density at the inlet and the rotational speed,  $\eta_{vol} = f(p_i, p_o, \rho_i, \Omega)$ . The volumetric efficiency is, for the most part, influenced by the physical characteristics of the compressor.

The refrigerant outlet conditions can be evaluated considering that the enthalpy variation corresponding to the isoentropic transformation between the operating pressure levels must be according to the isoentropic efficiency,  $\eta_{is}$  which is, in general, a function of the operating pressure levels, the inlet refrigerant density and the rotational speed,  $\eta_{is} = f(p_i, p_o, \rho_i, \Omega)$ . The isoentropic efficiency is related to the characteristics of the machine and the physical properties of the refrigerant.

Outlet enthalpy

$$h_{r,o} = h_i + \frac{h_{r,o,is} - h_{r,i}}{\eta_{is}}$$
 (6.2)

The outlet enthalpy corresponding to the isoentropic transformation h<sub>r.o.is</sub> is evaluated using the equation of state for the refrigerant, implemented in the fluid properties library. Indeed, assuming superheated vapour at the inlet, from the knowledge of  $p_{r,i}$  and  $T_{r,i}$  the thermodynamic state is fully defined, so its entropy. Then, the isoentropic outlet state of the refrigerant which include its enthalpy h<sub>r,o,is</sub> can be evaluated from  $p_{r,o}$  and  $s_{r,o} \equiv s_{r,i}$ .

All the refrigerant physical properties needed by the model are evaluated by linearly interpolating tabulated values, employing the Simulink<sup>®</sup> Lookup Tables. The tables of the refrigerant properties are realized using a suitable fluid properties library, and the data are stored in a .mat file which is loaded into the workspace before the simulation starts.

In fig. 22, the realization in the Simulink® environment of the physical-based model of the compressor is sketched. The two 4D Lookup Table evaluate the efficiencies, as described in the following, while the other Lookup Tables are used to determine the physical properties of the refrigerant.

#### Efficiencies evaluation 6.2.1

A crucial point in the realization of the physically-based model is the evaluation of the efficiencies. Volumetric efficiency is a characteristic

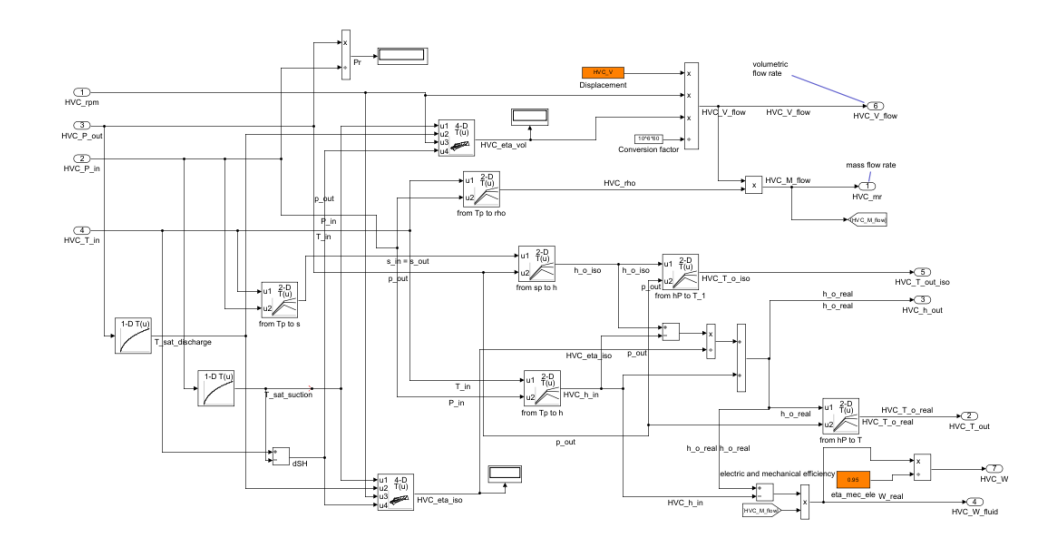


Figure 22: Physically-based model of the compressor realized in the Simulink® environment.

of the machine and is influenced by a dead volume or leakages from sealing elements, whereas, the isoentropic efficiency is more dependent on the refrigerant. Compressor efficiencies can be measured during an experimental campaign or derived from the polynomial correlations provided by the manufacturer. This work chooses the latter approach. In both cases, the efficiencies should be related to some operating parameter, based on experimental data or calculated performance indicators, to elaborate some correlations. In Fasl, 2013 they are related to the outlet pressure, the density ratio and the rotational speed, eq. (6.3).

$$\eta_{\text{vol}}, \eta_{\text{is}} = f\left(\omega, \frac{\rho_{\text{o}}}{\rho_{\text{i}}}, P_{\text{o}}\right)$$
(6.3)

In this work, since the efficiencies are determined using the compressor polynomials, the same independent variables are selected: the saturation temperature at the suction and discharge, the rotational speed and the degree of superheating at the compressor inlet eq. (6.4).

$$\eta_{\text{vol}}, \eta_{\text{is}} = f(T_S, T_D, \omega, \Delta T_{\text{sh}})$$
(6.4)

The values of mass flow rate and outlet temperature are calculated with the polynomial correlations for different values of  $T_S$ ,  $T_D$ ,  $\omega$  and  $\Delta T_{sh}$ , selected within the operating envelope of the compressor.

The volumetric efficiency can be evaluated as:

Volumetric efficiency

$$\eta_{\text{vol}} = \frac{\dot{m}_{\text{r}}}{\rho_{\text{r,i}} V_{\text{n}} \Omega} \tag{6.5}$$

where  $\rho_{r,i}$  is calculated with the physical properties library, knowing the inlet pressure (corresponding to the suction saturation temperature  $T_S$ ) and the degree of superheating  $\Delta T_{SH}$ . The single stroke displacement  $V_n$  is stated in the manufacturer's data-sheet. The rotational speed  $\Omega$  is the compressor speed, which is related to the frequency  $\omega$ using the number of pole pairs  $n_p$ .

$$\Omega = \frac{\omega}{n_p} \tag{6.6}$$

The isoentropic efficiency is calculated with

Isoentropic efficiency

$$\eta_{is} = \frac{h_{r,o,is} - h_{r,i}}{h_{r,o} - h_{r,i}}$$
(6.7)

where h<sub>o</sub> is obtained using the polynomials, from the knowledge of the outlet pressure also  $h_{r,o}$  is determined from the equation of state. The other states ( $h_{r,i}$  and  $h_{r,o,is}$ ) are fully identified by the operating pressure and the degree of superheating  $\Delta T_{SH}$ .

The calculated efficiencies are collected in a four-dimensional array and stored in a .mat file. The two maps are employed in the 4D Lookup Table to evaluate the efficiencies by linearly interpolating the tabulated data.

### 6.3 POLYNOMIAL APPROACH

Manufacturers usually states the performance of their compressors according to reference standards, such as the EN 12900, 2013 and AHRI 540, 2020. These documents prescribe evaluating the main performance indicators of a compressor, X with third-degree polynomials in the form

$$X = a_1 + a_2 T_S + a_3 T_D + a_4 T_S^2 + a_5 T_S T_D + a_6 T_D^2 + a_7 T_S^3 + a_8 T_S^2 T_D + a_9 T_S T_D^2 + a_{10} T_D^3$$

$$(6.8)$$

where T<sub>S</sub> and T<sub>D</sub> are the saturation temperature (°C) in the suction and in the discharge line, respectively, and  $\bar{\alpha} = \{\alpha_1, ... \alpha_{10}\}$  is a set of coefficients depending on the supply frequency w and the degree of superheat at the compressor inlet  $\Delta T_{SH}$ . For each process variable, therefore,  $\bar{a}_X = f(\omega, \Delta T_{SH})$ . The process variables of interest for the development of the model are the refrigerant mass flow rate  $\dot{m}_r$ , its outlet temperature  $T_{r,out}$  and the electric power consumption  $P_e$  as a function of the pressure levels in the suction line and in the discharge lines; the manufacturer can also provide the coefficients for other performance indicators like the cooling capacity, which is useful in the design phase.

The model reduces to a set of three algebraic equations that provide the values of the desired process variables under varying the operating conditions.

$$\begin{cases} m_r = \Phi \left( T_S, T_D, \Delta T_{SH}, \omega \right) \\ T_o = \Phi \left( T_S, T_D, \Delta T_{SH}, \omega \right) \\ P_e = \Phi \left( T_S, T_D, \omega \right) \end{cases} \tag{6.9}$$

The eq. (6.9) are coded in the Simulink® environment fig. 23

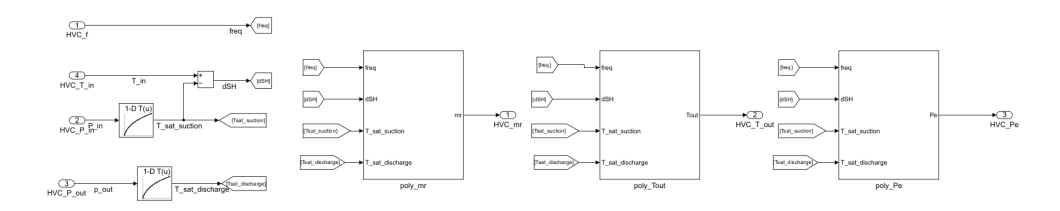


Figure 23: Simulink® scheme of the compressor model according the polynomial approach. Each block evaluates one polynomial corresponding to one process variable: the mass flow rate m<sub>r</sub>, the outlet temperature T<sub>r,out</sub> and the electric power consumption  $P_e$ .

The experimental facility is equipped with a reciprocating compressor by Frascold (model D3-12.1Y VS), and the corresponding polynomial coefficients are obtainable from the Frascold Selection Software 1. The polynomial coefficients are provided in the form  $\bar{a}_X = f(\omega, \Delta T_{SH})$ . So, for each process variable, the vectors ā are gathered varying the rotational speed  $\omega$  and the degree of superheat  $\Delta T_{SH}$ .

For the compressor, the range of frequencies taken into account is 30-80 Hz with a step of 10 Hz, while the range of superheating is o-40 °C with a step of 10 °C. The coefficients obtained were rearranged to create a bi-dimensional array for each component  $a_i$  of the vector  $\bar{a}$ ; the values at different positions in the matrix correspond to a degree of superheat and speed of revolution. These arrays are stored in a .mat file and loaded into the workspace before the simulation starts. For the actual value of superheating and speed of revolution the coefficient are evaluated by a 2D linear interpolation using the Lookup Table block. An example of the code realization for the mass flow rate polynomial is presented in fig. 24.

### VALIDATION OF THE COMPRESSOR MODELS 6.4

The compressor models are validated by employing the available experimental data, which involve the refrigerant R450A in two different

<sup>&</sup>lt;sup>1</sup> Frascold Selection Software 3 v1.24.2 - 09/07/2024

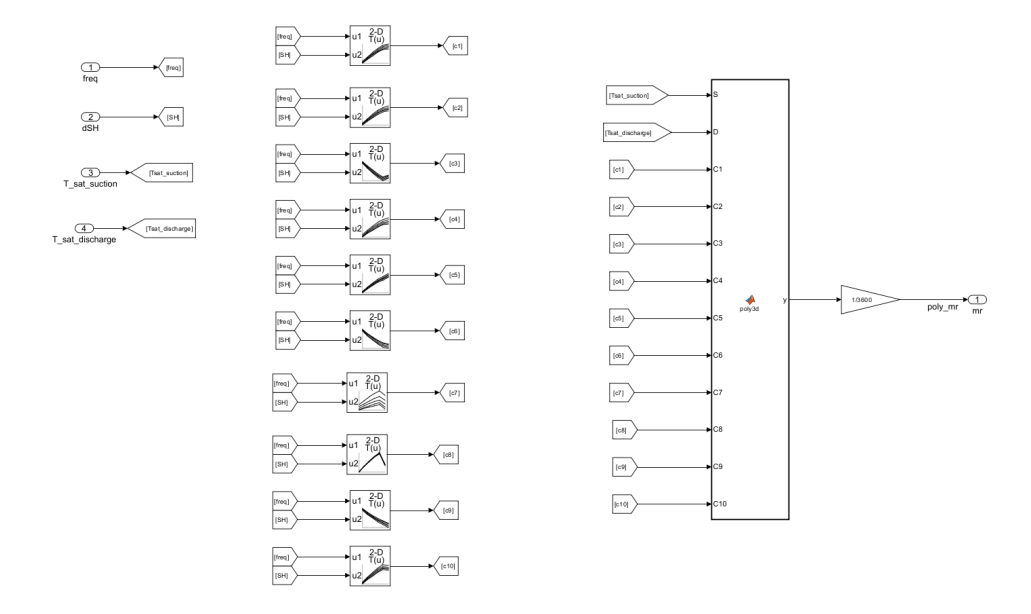
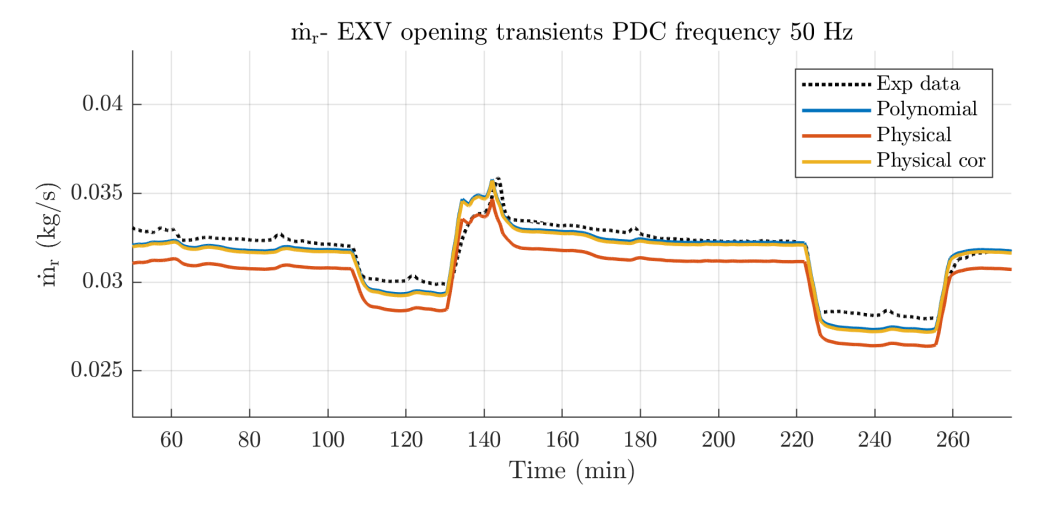


Figure 24: The Simulink® code of the mass flow rate polynomial of the compressor model; each 2D Lookup Table evaluates the coefficients ai by linear interpolating the tabulated data.

tests, see section 3.4. For the validation of the compressor a larger window of experimental data is employed; for this reason, in all the plots represented in this chapter, the reference time correspond to the moment when the machine is turned on and the data acquisitions starts. The experimental data are used to provide the inputs to the model and to compare the calculated outputs.

#### Mass flow rate 6.4.1

From figs. 25 and 26 it is possible to appreciate that both models agree well with the experimental mass flow rate. However, the physical model underestimates the mass flow rate more than the polynomial one. The polynomial model shows an absolute average error below 1%, while the physical model reaches an underestimation of about 5%. This may be related to an incorrect estimation of the single stroke displacement  $V_n$ , which is assumed  $V_n \simeq 146 \text{ cm}^3$ , as described in section 3.1.1. However, the results do not change when a different value for  $V_n$  is chosen, both in the model and in the efficiencies evaluation algorithm. This error may be related to the liner interpolation mechanism involved in the calculation of the volumetric efficiency. In summary, although the global trend of the mass flow rate is captured well also by the physical model, a simple tuning coefficient on the mass flow rate can increase the accuracy and reduce the error, eq. (6.10). In this case, tuning the mass flow rate prediction using a correction of



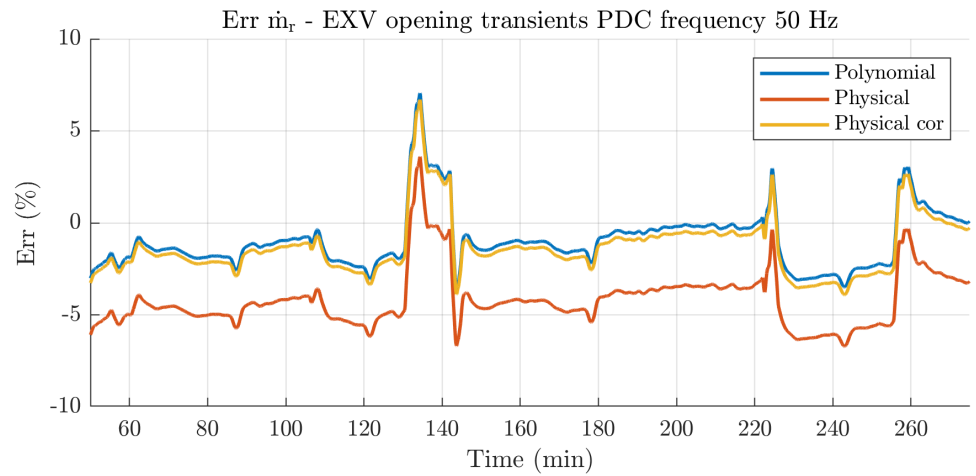


Figure 25: Compressor mass flow rate validation during Test 1 with R450A.

3%,  $C_{PH} = 1.03$ , the model achieves a satisfactory accuracy for both tests, figs. 25 and 26.

$$\dot{\mathbf{m}}_{r,PH,cor} = \mathbf{C}_{PH} \, \dot{\mathbf{m}}_{r,PH} \tag{6.10}$$

#### Power consumption 6.4.2

Both models provide the prediction of the electric power required by the compressor. The comparison with the experimental data shows a good agreement for all the trends of the calculated variables, but a negligible deviation from the experimental data is present for both models in both test cases. During Test 1 with R450A, fig. 27, the polynomial prediction deviates of about 4.5% while the physicallybased evaluation of only 3%. In the second test case, both the errors shrink to 2-4%, fig. 28; it is to be remarked the energy consumption predicted becomes more accurate during the valve opening reduction.

If evaluating the power demand using the physical model a feasible value for the electromechanical efficiency of the motor must be

Electromechanical efficiency

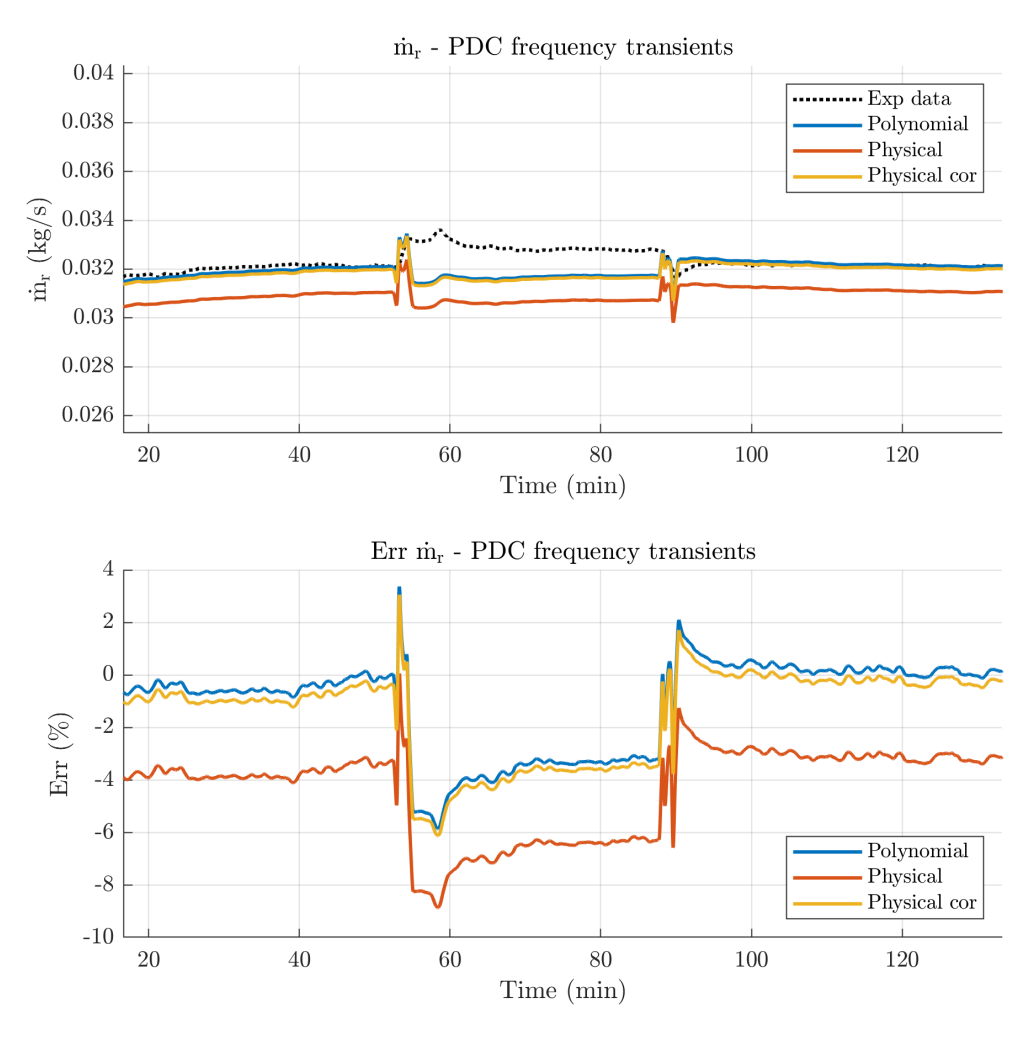


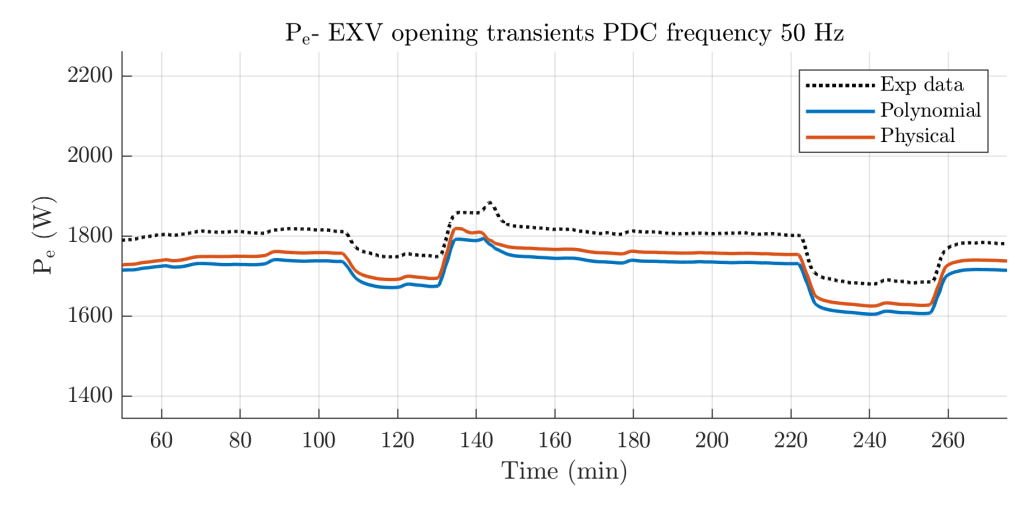
Figure 26: Compressor mass flow rate validation during Test 2 with R450A.

assumed; for these tests  $\eta_{em} = 0.95$ . By tuning this parameter, it is possible to further increase the accuracy of the prediction for most of the experimental data.

## Refrigerant outlet temperature

As for the previous investigation, also the general trend of the refrigerant outlet temperature is captured well by both the models, see figs. 29 and 30. However, in this case, besides a deviation from the steady state conditions, during the transients, the error increases before stabilizing after a certain time. This behaviour may be related to specific dynamics in the refrigerant outlet temperature, which the models are unable to capture. The steady-state deviation settles around 5% for both models in both test cases, except for the transients, where the error peaks at over 15%.

A suitable block function was developed to correct the so-called static evaluation of the refrigerant outlet conditions, introducing a first-order dynamic to resolve this issue.



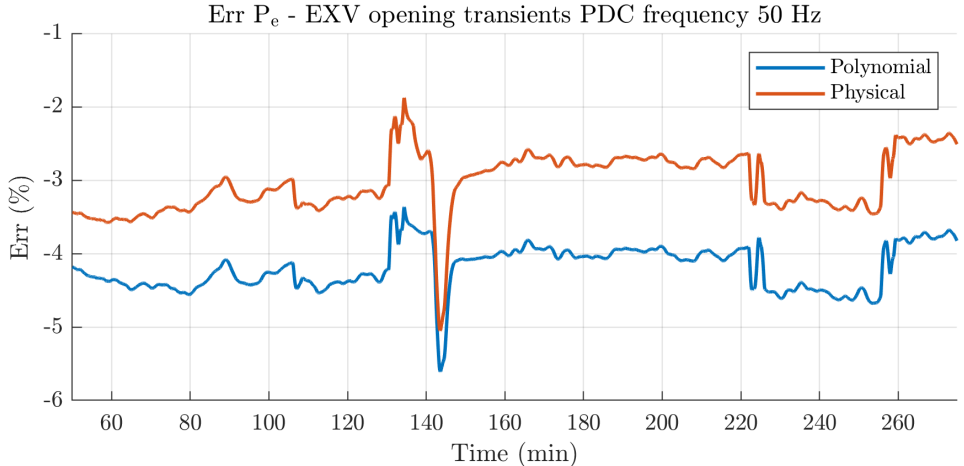


Figure 27: Validation of the electric power consumption of the compressor during Test 1 with R450A.

## Dynamic outlet refrigerant conditions

## First order dynamic

A possible way to consider the dynamic behaviour of the refrigerant at the compressor is proposed by Fasl, 2013, who introduced first-order dynamic for the refrigerant enthalpy.

$$\frac{dh_{r,o}}{d\tau} = \frac{1}{\Delta\tau}(h_{r,o,stat} - h_{r,o}) \tag{6.11}$$

However, it is more convenient to evaluate the same dynamic in terms of temperature because this quantity is measured and therefore directly available for comparison.

$$\frac{dT_{r,o}}{d\tau} = \frac{1}{\Delta \tau} (T_{r,o,stat} - T_{r,o}) \tag{6.12}$$

Equation (6.12) evaluates the delay required by the refrigerant to reach the outlet conditions estimated with the polynomial or physicallybased stationary model. After a certain time, the refrigerant temperaFirst order dynamic for refrigerant enthalpy or temperature

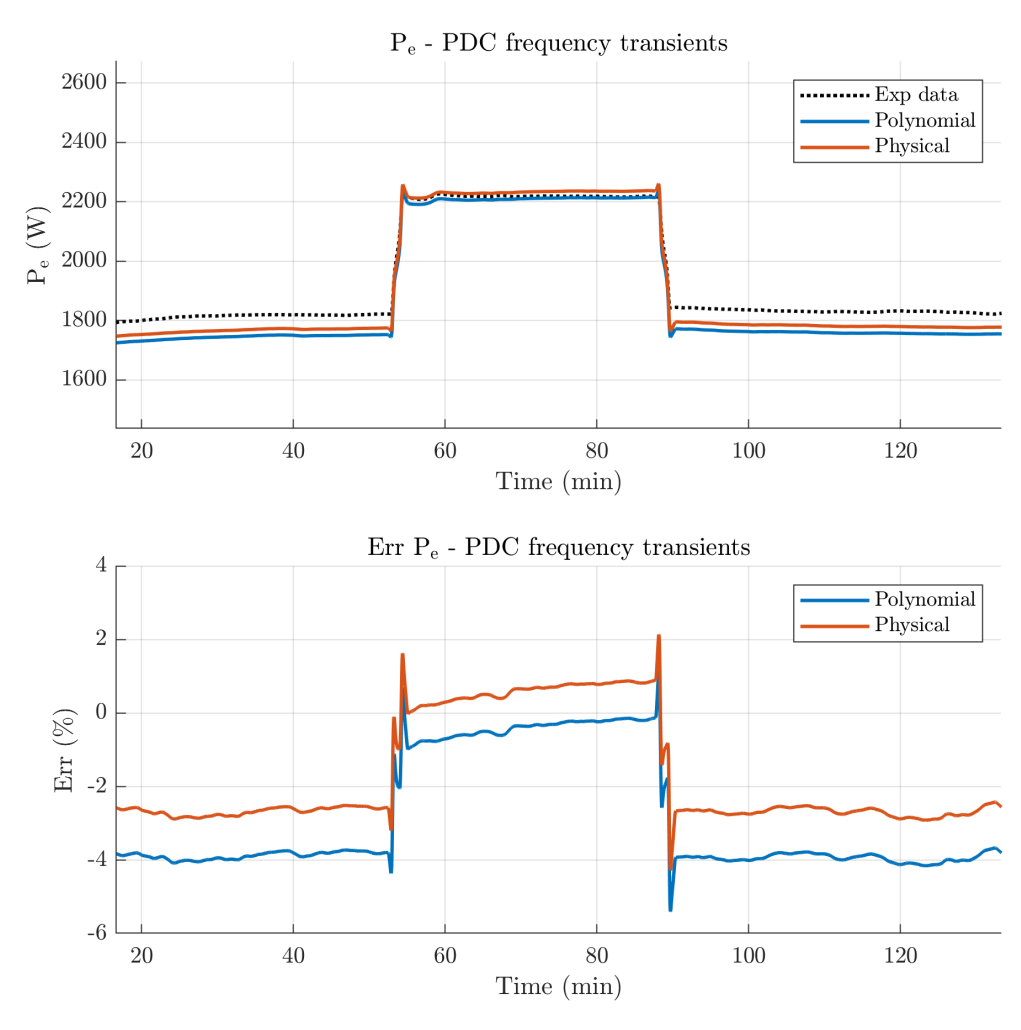
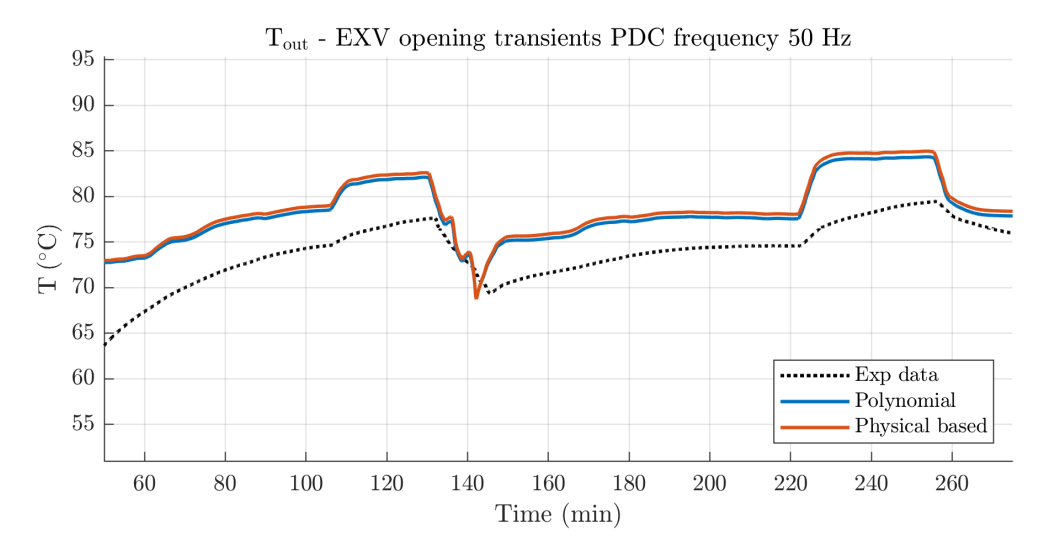


Figure 28: Validation of the electric power consumption of the compressor during Test 2 with R450A.

ture becomes equal to the steady state value predicted by the stationary model. Tweaking the time constant  $\Delta \tau$  captures the transient behaviour of the temperature. However, the steady state conditions are insensitive to this kind of correction. In fig. 31, the Simulink® code for the dynamic correction of the outlet refrigerant temperature is shown. In figs. 35 and 36 the different versions of the dynamic correction of the refrigerant temperature at the compressor outlet are compared employing the data from both experimental tests. The different dynamic corrections are enumerated from o to 4. Version o is the first order dynamic described by eq. (6.12); the other versions are presented in the following and summarized in table 17.

From figs. 35 and 36, it is possible to appreciate that with a suitable selection of the time constant  $\Delta \tau$  the transients are well captured, but no benefits are experienced in the evaluation of the steady state conditions.



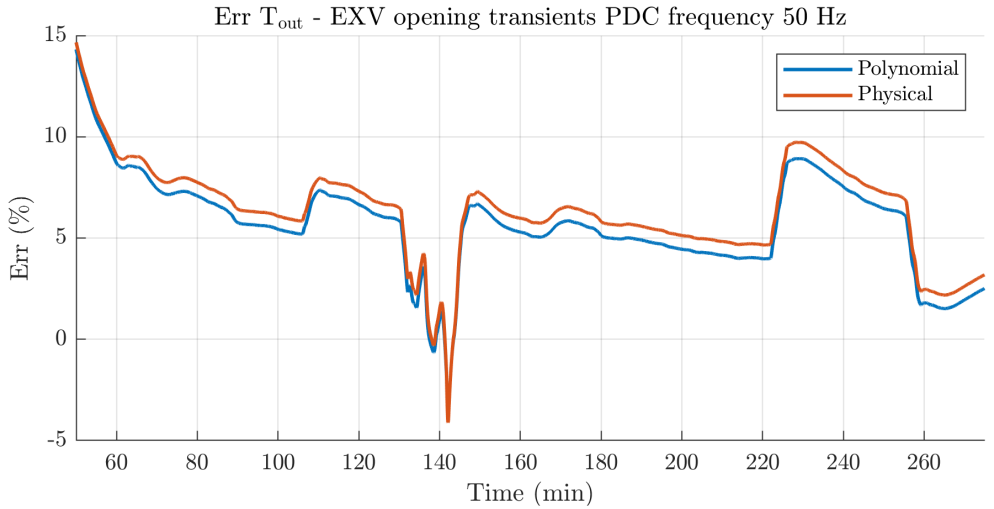


Figure 29: Refrigerant outlet temperature validation during Test 1 with R450A.

From fig. 30, it is evident that the stationary outlet temperature is not well captured by the static system either. So, in addition to a dynamic correction, a steady state correction is necessary.

## Evaluation of the heat transfer from the compressor case

The problem discussed at the end of the last section may be tackled starting from the consideration that the heat transfer to the environments through the compressor case influences the outlet refrigerant temperature. Moreover, as a first approximation, it is possible to assume that the refrigerant temperature at the outlet is equal to that of the portion of the shell involved in the heat transfer process. The compressor shell has a certain heat capacity that leads to thermal inertia,

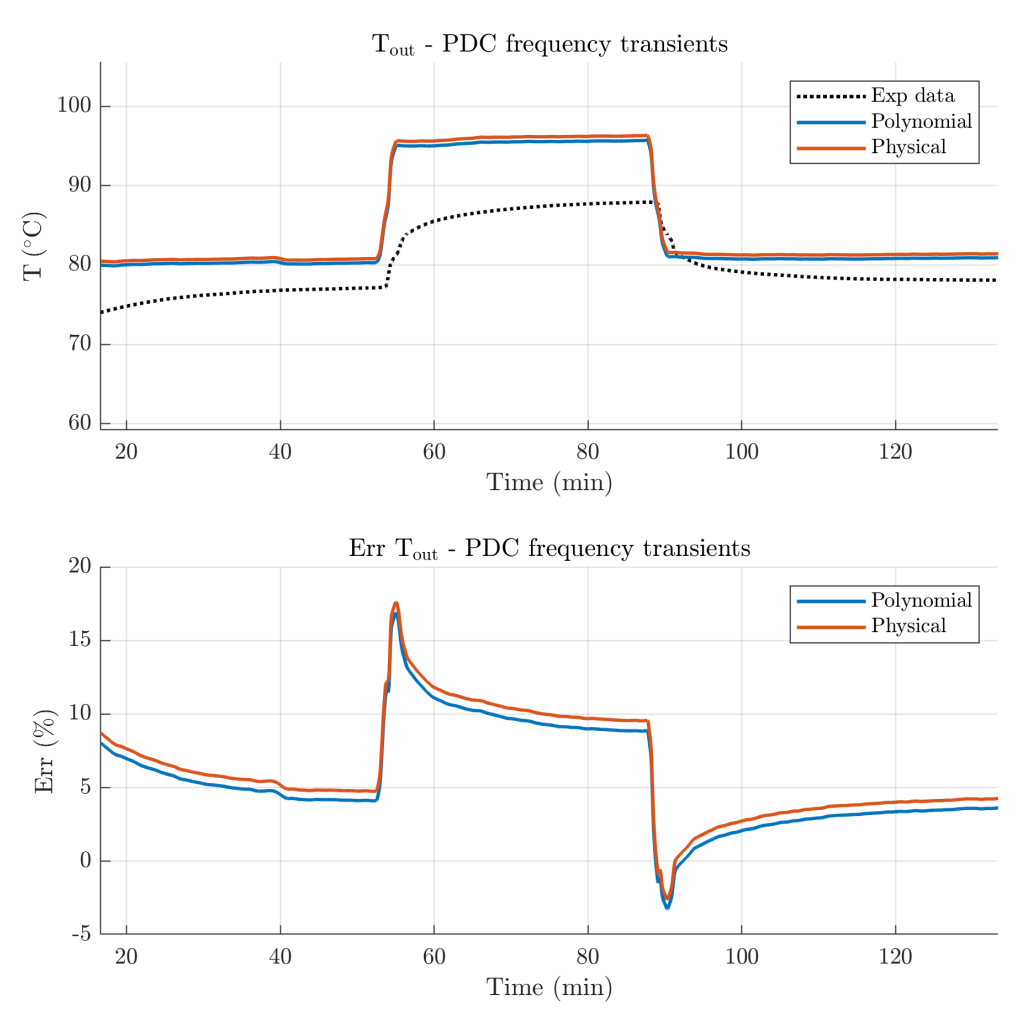


Figure 30: Refrigerant outlet temperature validation during Test 2 with R450A.

and exchanges heat with the air on the outer side and the refrigerant on the inner side. The governing equations can be written as follows:

$$\begin{cases} \frac{dT_{r,o}}{d\tau} \simeq \frac{dT_w}{d\tau} = \frac{1}{C_w} (\dot{Q}_a - \dot{Q}_r) \\ \dot{Q}_a = \alpha_a A_{w,o} (T_a - T_w) \\ \dot{Q}_r = \alpha_r A_{w,i} (T_w - T_r) \end{cases} \tag{6.13}$$

where  $T_a$  is the temperature of the air close to the compressor shell,  $T_r$ is the outlet temperature of the refrigerant from the static model, C<sub>w</sub> is the thermal capacity of the shell,  $\alpha_a$  and  $\alpha_r$  are the convective heat transfer coefficients on the outer and inner side respectively,  $A_{w,o}$  and  $A_{w,i}$  are the corresponding heat transfer area. It is quite challenging to evaluate the dimension of the portion of shell involved in the process and, even harder, to determine the heat transfer coefficients. Free convection is assumed on the outer side and forced convection on the inner side. Ultimately, there are three parameters which can be tuned to develop this additional model,  $C_w$ ,  $(\alpha_a A_{w,e})$ , and  $(\alpha_r A_{w,i})$ ;

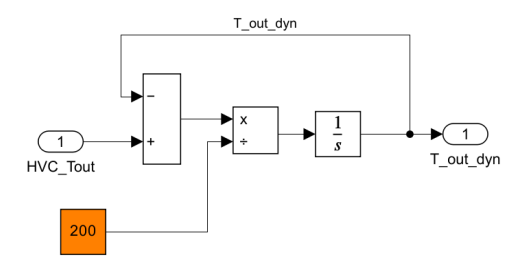


Figure 31: Block for evaluating the dynamic behaviour of the refrigerant outlet temperature, with only the thermal capacity effect, named version o.

moreover, as a first estimate, is possible to assume the same value for the heat transfer areas on both sides of the shell. This procedure to evaluate the dynamic behaviour of the temperature is named version 1 in the following analysis, see table 17.

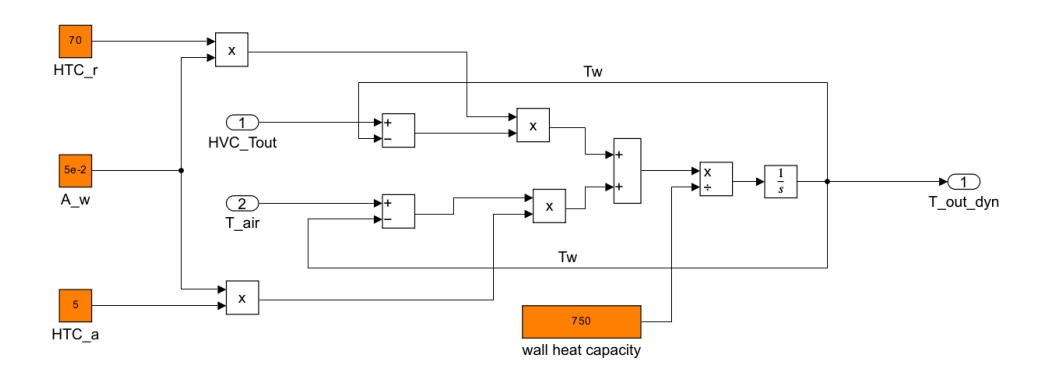


Figure 32: Block for evaluating the dynamic behaviour of the refrigerant outlet temperature, which is assumed equal to the temperature of the shell, second approach, named version 1.

By comparing the numerical results with the experimental data from Test 2 with R450A in fig. 36 it can be recognized that the predictions are quite accurate when the compressor runs at 50 Hz, but when the compressor speeds up the evaluation of the steady state temperature is not so accurate. In other words, the model is well-tuned for the first stationary condition but not enough for the other stationary operating point. This may lead back to the dependence of the refrigerant side heat transfer coefficient on the inner side the compressor regime or, more precisely, with the refrigerant flow rate. To account for this phenomenon, a linear dependence on the working pressure ratio, employing a 1D Lookup Table is given to the heat transfer coefficient on the refrigerant side, as shown in fig. 33. This third realization is named version 2 in the next.

A more sound physical foundation for tuning the heat transfer coefficient may be obtained by assuming a linear dependence on the refrigerant volumetric flow rate. This development is named version

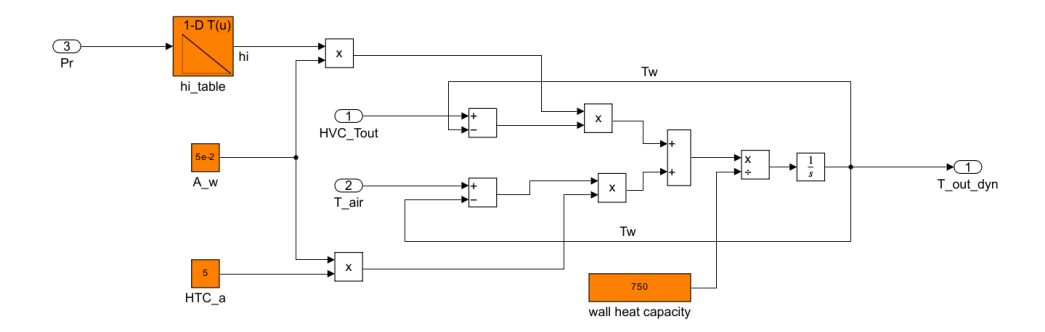


Figure 33: Enhanced version of the block for evaluating the dynamic behaviour of the refrigerant outlet temperature, with a linear interpolation tuning on the heat transfer coefficient on the refrigerant side, named version 2.

3. After tuning, the resulting trend of the Heat Transfer Coefficient is decreasing with the volumetric flow rate; the same behaviour was encountered for the pressure ratio.

Introducing a linear dependence of the refrigerant-side heat transfer coefficient allows an augmented accuracy in the prediction of the outlet temperature during all the phases of Test 2 with R450A, which is characterized by the variation of the compressor frequency. The absolute error is contained within about 3%. The dependence of the heat transfer coefficient on the flow conditions seems realistic and reliable. However, the plots in fig. 35 show that although during the most part of the test, the outlet temperature is predicted with a deviation below 3%, during the valve opening transient, the error becomes larger than 4%, and the dynamic behaviour of the temperature is captured less satisfactorily.

## Decoupling with wall temperature

Finally, to enhance the accuracy and physical grounding of the model, the evaluation of  $T_{r,o}$  is separate from  $T_w$ . In this case, the dynamic behaviour of the refrigerant outlet temperature is described as that of a flow inside a pipe whose wall, provided with a certain heat capacity, exchanges heat with the external air and the refrigerant itself. The wall temperature is calculated with eq. (6.13), but the outlet temperature is evaluated assuming a logarithmic profile of the refrigerant flowing on a wall at constant temperature T<sub>w</sub>. In fig. 34, the Simulink<sup>®</sup> code of the version 4 of the dynamic outlet temperature block is shown. Besides evaluating the shell temperature due to the heat transfer process with the air on the outside and the refrigerant on the inside, the outlet temperature is evaluated assuming an exponential profile. Downstream of the block for the temperature profile calculation, a

Version	Description
0	First order dynamic
1	First order dynamic integrated with the estimation of
	the heat transfer, assuming $T_{r,o} \equiv T_w$ , see eq. (6.13)
2	Same as version 1 except for the linear dependence of
	HTC on the pressure ratio
2	Same as version 1 except for the linear dependence of
	HTC on the volumetric flow rate
4	$T_{r,o}$ is decoupled from $T_w$ using a the pipe model to
	estimate the heat transfer
5	Same as version 4 except for the linear dependence of
	HTC on the number of revolutions per minute

Table 17: List of the developed versions of the dynamic correction of the refrigerant temperature at the compressor outlet.

numerical check is carried out with a switch block to avoid simulation crash when the mass flow rate and, as a consequence, the NTU, goes to zero.

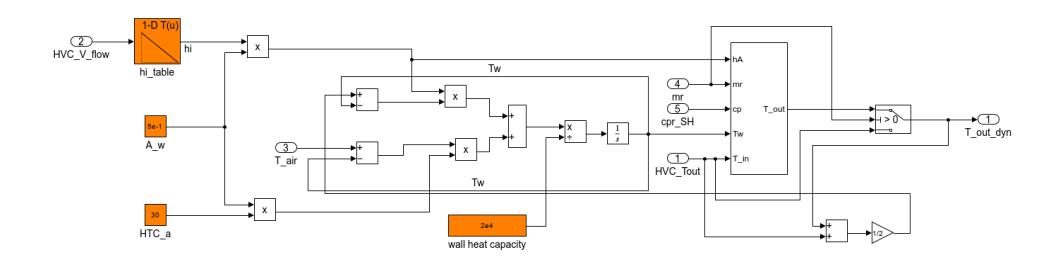
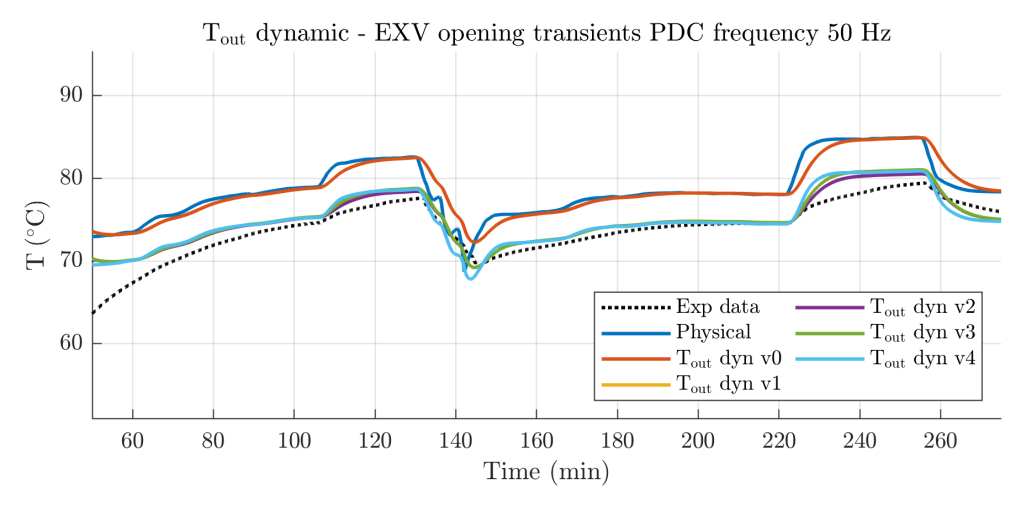


Figure 34: Function block for evaluating the dynamic behaviour of the refrigerant outlet temperature, which is decoupled from that of the wall, version 4.

## Final improvement of the dynamic correction

After some tests, a slightly different configuration is selected for the dynamic correction of the refrigerant temperature at the condenser outlet. Indeed, the variation of the HTC on the refrigerant side is associated with a linear dependence on the rotational speed of the compressor,  $\Omega$ . This choice is proven helpful in the tuning phase, because is easier to measure the rotational speed respect to the volumetric flow rate. The resulting model, the fifth version, is employed in the full machine tests described in chapter 11.



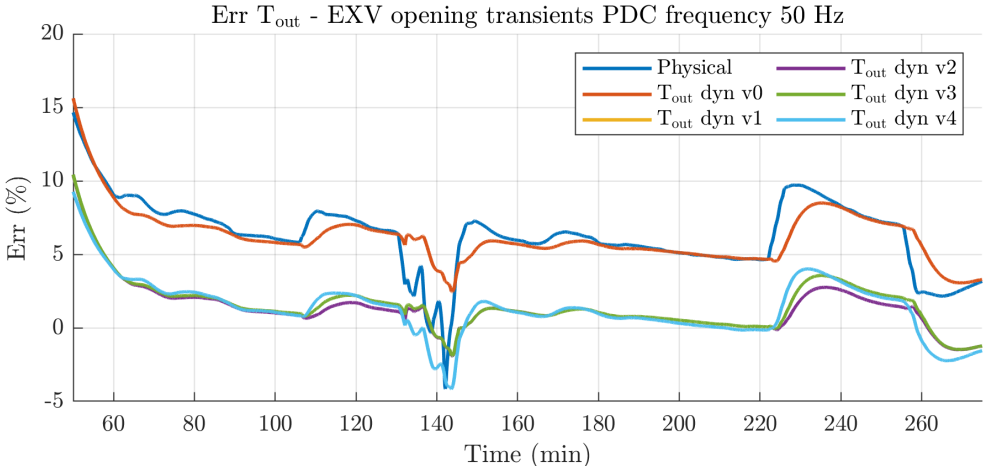


Figure 35: Validation of the dynamic prediction of the compressor refrigerant outlet temperature during Test 1 with R450A. The different versions of the dynamic correction of the outlet temperature are compared, see table 17.

#### 6.4.5 Concluding remarks on the dynamic correction of the temperature

Introducing a dynamic correction in the evaluation of the static outlet temperature increases the model accuracy. The solution that combines the wall's dynamic with the heat transfer estimation is more accurate than a simple first-order dynamics. Indeed, the first version, which ignores the heat transfer rate is not sufficiently accurate in the steady state evaluation of the outlet temperature, even if the transient is fully captured. The other versions combine a good accuracy in the stationary conditions and during the transients. In terms of physical insight, the last approaches (versions 4 and 5) are more reliable, although the accuracy is not enhanced appreciably in comparison with the others (versions 1 and 2).

It should be considered that introducing more detailed models requires the assessment of more parameters; even though they allow

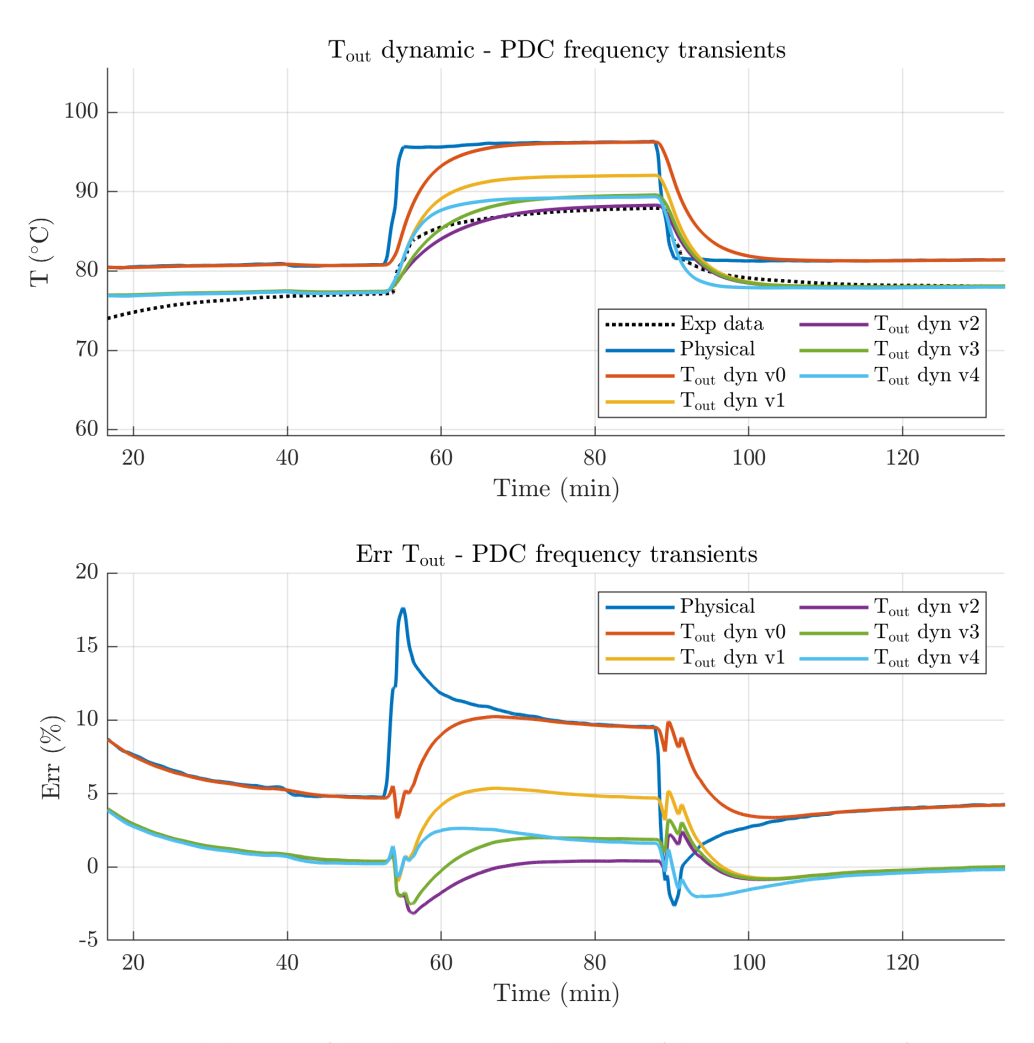


Figure 36: Validation of the dynamic prediction of the compressor refrigerant outlet temperature during Test 2 with R450A. The different versions of the dynamic correction of the outlet temperature are compared, see table 17.

a physical understanding of the process, their definition may become very challenging. In this context, it can be concluded that to achieve an adequate accuracy of the outlet temperature prediction in stationary and transient conditions, the evaluation of the heat transfer rate between the refrigerant and the environment should be combined with the first order dynamic of the temperature of the case. Depending on the actual application and the data available for the definition of the model different approaches can be chosen among the proposed versions 1 to 5.

## 7 PIPING

Piping is the most diffuse component in VCS, and in general, in all processes involving flowing fluids, the tubes are necessary to connect the system's main components and allow the fluids to move to different parts of the plant even at a considerable distance. The pipelines are probably the first component in terms of the mass of material employed in the larger refrigerated warehouses. However, pipes are usually ignored from a modelling point of view, particularly in smaller applications, because their contribution to pressure variation and heat transfer is negligible. Indeed, pipes are designed to guarantee the nominal flow rate with the minimum acceptable pressure losses, and they are often insulated when the heat rejection could reduce the efficiency of the plant, in particular on the cold side. Moreover, from a modelling point of view, their effect can be easily accommodated into other components; for example, the pressure losses occurring in all the piping from the condenser to the evaporator are usually ascribed to the expansion device without considerable reduction in accuracy. Similarly, the possible heat transfer rate, both on the hot or on the cold side, can be assigned to the corresponding HEX. Finally, given the small dimension of the pipes, mass and energy storage can be neglected, especially in smaller plants or ascribed to the accumulation device in the larger ones.

When to ignore pipes

Nonetheless, as pointed out by Fasl (2013) in dynamical models of systems involving mass accumulators, the pipe model becomes necessary to evaluate the mass flow rate in a certain portion of the circuit. Indeed, in the numerical modelling of systems involving fluids, the dynamical components, designed to describe the time evolution of mass and energy, need information about the mass flow rate at boundaries as an input; for this reason, the dynamical component (more precisely those for which the mass balance equation is required) must be connected by components able to evaluate the mass flow rate between them. For example, in simple VCS without any additional vessels, the two HEXs are connected through the compressor and the expansion device, which determine the mass flow rate they exchange. Conversely, if additional vessels are employed, is not possible to link them to the HEXs without employing an element that evaluates the mass flow rate, i.e. the model of the pipe.

Need for a pipe model

In very general terms a fluid flowing inside a duct is subjected to shear force and can exchange heat with the wall. Two processes are thus involved: the pressure losses due to friction and the heat transfer due to temperature difference. In the context presented above, the main goal of the pipe model is to allow the estimation of a mass flow rate between two reservoirs kept at different pressure levels, such as between the condenser and the LR or the evaporator and the Suction Accumulator (SA). The pipe model focuses on determining the pressure losses due to friction, while the heat transfer rate is currently ignored.

#### PRESSURE LOSSES DUE TO FRICTION 7.1

The problem of determining the pressure drop needed to sustain an internal flow is frequently encountered in engineering applications. The pressure losses in these flows are mainly related to friction between the fluid and the inner wall, and are called distributed. Other sources of dissipation are obstacles along the fluid path, like fittings, bends, elbows, tees, inlets, exits, expansions, and contractions, which produce a *localised* pressure drop. In long pipelines, the first is usually the most important, but in smaller plants, the contribution of localised pressure losses cannot be disregarded.

#### Distributed pressure losses 7.1.1

The distributed pressure losses in an internal flow are usually calculated with eq. (7.1), which relates them to the *dynamic pressure* of the flowing fluid through a coefficient called Darcy-Weisbach friction factor f.

$$\Delta p = f \frac{L}{D} \frac{\rho u_{\rm m}^2}{2} \tag{7.1}$$

where  $\rho$  is the density, L is the length of the tube, D its diameter, u<sub>m</sub> the mean velocity defined as that uniform velocity over the cross sectional area  $A_c$  that provides the same mass flow rate.

$$u_{\mathfrak{m}} \equiv \frac{\dot{\mathfrak{m}}}{\rho A_{c}} \tag{7.2}$$

The Darcy-Weisbach equation can be rearranged to highlight the mass flow rate and assume a tube with a circular cross-section.

$$\Delta p = f \frac{8}{\pi^2} \frac{L}{D^5} \frac{\dot{m}^2}{\rho} \tag{7.3}$$

The mass flow rate can be obtained from the eq. (7.3). However, the friction factor conceals a dependence on the mass flow rate, so the problem becomes implicit and, in general, requires an iterative procedure to be solved.

Darcy-Weisbach relation

In conclusion, the pipe model described by eq. (7.4) needs as inputs the pressure levels p<sub>i</sub> and p<sub>o</sub> at the inlet and outlet and the density ρ of the working fluid. The geometrical characteristics of the tube (diameter and lenght) are constant parameters.

Obtaining the mass flow rate is an implicit problem

$$\dot{m} = \sqrt{\rho_i(p_i - p_o) \frac{1}{f(\dot{m})} \frac{\pi^2}{8} \frac{D^5}{L}}$$
 (7.4)

#### FRICTION FACTOR 7.2

The friction between wall and fluid depends on the kind of fluid and its phase, the volume flow rate and the geometrical characteristics of the pipe (cross-section, hydraulic diameter and lenght). In general for internal flows,  $f = f(Re, D_h)$  where  $D_h$  is the hydraulic diameter of the pipe (which for circular tubes coincides with the diameter) and the Re is the Reynolds number, that can be expressed as a function of the mass flow rate, eq. (7.5).

$$Re = \frac{\dot{m}D}{\mu A_c} = \frac{4\dot{m}}{\pi \mu D} \tag{7.5}$$

The friction factor can be evaluated employing the Colebrook equation which can be used for liquid or gaseous flows, Colebrook, 1937.

Colebrook

Blasius

$$\frac{1}{\sqrt{\mathfrak{f}}} = -2\log_{10}\left(\frac{\epsilon}{3.7D} + \frac{2.51}{\text{Re}\sqrt{\mathfrak{f}}}\right) \tag{7.6}$$

Despite the accuracy of eq. (7.6) in the estimation of the friction factor over a wide range of flow regimes and roughness values, its main disadvantages are the non-linearity and implicit form; the solution must be retrieved iteratively. To overcome this issue, many explicit approximations have been proposed, Brkić, 2011, but often, these formulations are apt to specific conditions.

For example, the Blasius equation, eq. (7.7) is a straightforward relation applicable to flows in smooth pipes, corresponding to the lower portion of the Moody diagram. The smooth pipe conditions can be assumed when the relative roughness is small; the lower the Re larger the relative roughness which can be approximated by the smooth tube assumption.

$$f = 0.316 Re^{-\frac{1}{4}} \tag{7.7}$$

An explicit formulation of the Colebrook equation is due to Haaland (1983), eq. (7.8). According to the Author, it can be employed with the same limitations of the Colebrook equation; moreover, it has been proven very accurate, especially in the fully turbulent regime

Halland

Brkić (2011). It is still suitable for liquid and gaseous flows, but the coefficient n must be chosen; according to Haaland, 1983, with n = 1, the equation can be applied to liquid flows, while with n = 3 to gaseous transmission lines.

$$\mathfrak{f} = \left\{ -\frac{1.8}{n} \log_{10} \left[ \left( \frac{6.9}{Re} \right)^n + \left( \frac{\epsilon}{3.7D} \right)^{1.11n} \right] \right\}^{-2} \tag{7.8}$$

Another approximation applicable to the full range of turbulence and laminar flow, is proposed by Churchill (1977), eq. (7.9). According to Brkić, 2011, it is accurate with respect to the Colebrook equation in all the range, especially in the turbulent regime.

Churchill

$$f = 8 \left[ \left( \frac{8}{Re} \right)^{12} + \frac{1}{(A^{16} + B^{16})^{3/2}} \right]^{1/12}$$

$$A = -2.457 \ln \left[ \left( \frac{7}{Re} \right)^{0.9} + 0.27 \frac{\epsilon}{D} \right]$$

$$B = \frac{37530}{Re}$$
(7.9)

#### Friction factor in two-phase flow 7.2.1

In two-phase flows, the direct approach to the friction factor calculation is not possible because complex dissipation mechanisms occur. Twophase pressure drop models have traditionally been divided into homogeneous flow and separated flow models, Field and Hrnjak, 2007. In the first category the liquid and vapour phases are considered flowing at the same velocity, so they are treated as a homogeneous fluid whose physical properties, like density and viscosity, can be evaluated as an average. This assumption is compatible with flow regimes such as mist or bubbly flow where one phase is evenly dispersed into the other, so the flowing fluid's behaviour can be investigated by evaluating its physical properties as an average over the control volume. However, in slug-plug or annular flow regimes, the liquid and vapour phases evolve with a non-negligible slip ratio, that is, the ratio between the velocity of the vapour and that of the liquid phase. In this context, the separated flow models, which consider the two phases separately and investigate their interaction, are more suitable. The latter approach provides a more physical insight into the process, is probably more accurate, but is also more complex, indeed a flow regime must be recognized or assumed and a larger number parameters must be provided.

Homogeneous vs separated flow models

## Homogeneous flow model

According to the homogeneous assumption, the Reynolds number (Re) is evaluated employing the averaged properties of the fluid. The Reynolds number can be expressed in terms of mass flow rate (m), eq. (7.5). Since the two phases are flowing together, the density of the mixture is estimated in any section of the channel with a mass average; so the mean density can be evaluated with eq. (7.10), eq. (7.10).

$$\frac{1}{\rho_{\rm m}} = \frac{x}{\rho_{\rm v}} + \frac{1 - x}{\rho_{\rm l}} \tag{7.10}$$

where x is the vapour quality.

Conversely, different ways are employed to evaluate of the viscosity of the mixture. An interesting helpful framework to classify the approaches, Field and Hrnjak, 2007, employs the concept of idealdamping elements typical of dynamical systems. Indeed, viscous dissipation is related to shear force in a fluid moving along a wall. In this case the reciprocal disposition of the phases can affect the total shear experienced by the moving fluid. For example, the liquid portion flows along the wall in annular flow, whilst the vapour flows in contact with the liquid. The total shear can be interpreted as the effect of two dampers in series. Likewise, for slug-plug flows, the two phases run one behind the other, so the total dissipation can be understood as the effect of two dampers in parallel.

Damper net interpretation of two-phase viscosity

The first approach is traditionally attributed to McAdams et al., 1942, and can be seen as a series combination of the two-phase viscosities, weighted by the mass.

McAdams et al.

$$\frac{1}{\mu_{\rm m}} = \frac{x}{\mu_{\rm v}} + \frac{1 - x}{\mu_{\rm l}} \tag{7.11}$$

A similar approach is that by Dukler et al., 1964. This represents the averaged viscosity as the series combination of the single phases weighted by volume, so the void fraction ( $\gamma$ ) is employed.

Dukler et al.

$$\mu_{\rm m} = \gamma \mu_{\rm v} + (1 - \gamma) \mu_{\rm l} \tag{7.12}$$

The void fraction can be evaluated as:

$$\gamma = \left(1 + S\left(\frac{1 - x}{x}\frac{\rho_{\nu}}{\rho_{1}}\right)\right)^{-1} \tag{7.13}$$

where the slip ratio (S) is defined as  $S = u_v/u_l$ . Considering the homogeneous flow assumption, S = 1 so the averaged viscosity can be evaluated as

$$\mu_{\mathfrak{m}} = \rho_{\mathfrak{m}} \left( \frac{x}{\rho_{\mathfrak{v}}} \mu_{\mathfrak{v}} + \frac{1 - x}{\rho_{\mathfrak{l}}} \mu_{\mathfrak{l}} \right) \tag{7.14}$$

A parallel combination of the liquid and vapour viscosity averaged by mass is proposed by Cicchitti et al., 1959.

Cicchitti et al.

$$\mu_{\rm m} = x\mu_{\rm v} + (1-x)\mu_{\rm l} \tag{7.15}$$

The same parallel arrangement can be averaged over the volume, employing the void fraction, as shown in Field and Hrnjak, 2007.

$$\frac{1}{\mu_{\rm m}} = \frac{\gamma}{\mu_{\rm v}} + \frac{1 - \gamma}{\mu_{\rm l}} \tag{7.16}$$

## Separated flow model

The homogeneous models can inaccurately estimate the pressure drop in two-phase flows, especially in certain flow regimes. To overcome their restrictive assumptions, separated flow models are proposed. They allow a slip velocity between the phases and can deal with different physical properties and investigate their interaction. In this approach, the two-phase pressure drop is generally related to that of the single phase, whether liquid or vapour, using the corresponding two-phase multiplier  $\Phi^2$ . Two different multipliers can be defined depending on the reference phase considered.

Two-phase multiplier

$$\Phi_{l}^{2} = \frac{\frac{dp}{dx}\Big|_{tp}}{\frac{dp}{dx}\Big|_{l}} \qquad \Phi_{v}^{2} = \frac{\frac{dp}{dx}\Big|_{tp}}{\frac{dp}{dx}\Big|_{v}}$$
(7.17)

In eq. (7.17), the reference is the actual single-phase flow in the tube; however, it is possible to define different multipliers assuming that the entire flow is liquid or vapour; in this case, the flow regime is evaluated with  $Re_{l,a}$  if all the fluid flow is considered liquid or conversely  $Re_{\nu,a}$ if it is assumed as vapour. The corresponding multipliers are  $\Phi_{l,a}^2$ e  $\Phi_{\nu,a}^2$ . The latter approach is very suitable when the correlation for the two-phase multiplier is developed starting from experimental measurements. A correlation to calculate the two-phase multiplier referred to the liquid flow is that those proposed in Friedel et al., 1980.

$$\begin{split} & \varphi_{l,a}^2 = C_1 + \frac{3.24C_2}{F_m^{0.045}W_m^{0.035}} \\ & C_1 = (1-x)^2 + x^2 \frac{\rho_l f_{\nu,a}}{\rho_{\nu} f_{l,a}} \\ & C_2 = x^{0.78}(1-x)^{0.24} \left(\frac{\rho_l}{\rho_{\nu}}\right)^{0.91} \left(\frac{\mu_{\nu}}{\mu_l}\right)^{0.19} \left(1 - \frac{\mu_{\nu}}{\mu_l}\right)^{0.7} \\ & Fr_m = \frac{G^2}{g d_h \rho_m^2} \\ & We_m = \frac{G^2 d_h}{g \sigma_m} \end{split}$$

Also the Lockhart-Martinelli  $\chi$  parameter is widely employed to obtain the pressure drop in two-phase flows. It is defined as the ratio between the liquid phase pressure drop of the liquid phase and of the the vapour, Lockhart and Martinelli, 1949.

Loackhart-Martinelli parameter

$$\chi^2 = \frac{\frac{\mathrm{dp}}{\mathrm{dx}}\Big|_{1}}{\frac{\mathrm{dp}}{\mathrm{dx}}\Big|_{y}} \tag{7.19}$$

The Authors originally employed this parameter to correlate the pressure drop and the void fraction in two-phase flows. Since then, many efforts have been made to correlate the void fraction and the pressure drop in different flow regimes.

## The approach selected

In conclusion, in this work the homogeneous flow model is selected for the evaluation of the friction factor. Indeed, this assumption is compatible with the pipe diameter employed in this kind of applications, and with the most likely flow regimes in these configurations. During normal operations, in the line downstream of the condenser, the refrigerant is subcooled liquid or saturated vapour with very low quality. At the other end, in the line downstream of the evaporator, refrigerant superheated vapour is present or very high quality vapour with a few drops dispersed at most. In these flow conditions the homogeneous assumption combines good capability in capturing the process and relative simplicity.

## Localised pressure losses

The localised pressure losses in a pipeline are usually evaluated referring to the dynamic pressure and employing a loss coefficient K<sub>L</sub>, eq. (7.20)

$$\Delta p = K_L \frac{\rho u_m^2}{2} = K_L \frac{8}{\pi^2} \frac{\dot{m}^2}{\rho D^4}$$
 (7.20)

The loss coefficient accounts for the different localised pressure losses that can occur in a pipeline, such as bends, section variation, inlets, exits, or fittings. For each of them, tabulated values are available, obtained from experimental measurements.

The localised pressure losses can be expressed through the equivalent length. This approach is more suitable for this application. Indeed, in this way, the evaluation of the localised pressure losses can be easily integrated into eq. (7.4) by acting on the length of the tube. The equivalent length can be evaluated with:

$$L_{eq} = \frac{D}{f} K_{L} \tag{7.21}$$

## The order of magnitude of the pressure losses

The different two-phase models for evaluating the friction losses are compared in a realistic application; under the same conditions, the order of magnitude of the localised pressure drop is also examined.

Consider the case of a typical copper connection line between the condenser and the expansion valve or accumulation vessel, if present, in a small VCS. It is assumed a standard external diameter of 12.7 mm (1/2 in) and a thickness of 1 mm. The refrigerant employed is R450A; a mass flow rate  $\dot{m} = 0.035 \text{ kg s}^{-1}$  is assumed. The friction factor is evaluated with the Blasius equation because the smooth tube approximation is compatible with the actual roughness ( $\epsilon$ =0.1 µm in Silmet, 2024).

As shown in fig. 37, despite the average viscosity and, as a consequence, the Reynolds number, differ quite significantly when evaluated with the different relations, the friction factor and the pressure losses are very similar: the maximum deviation between them is around 0.5 kPa m<sup>-1</sup>. To summarise, the pressure variation per meter of pipe is comparable with the dynamic pressure. Likewise, the localised pressure drop in the same test case can be evaluated with eq. (7.20). They have the same order of magnitude of the dynamic pressure, while in this case the loss coefficient of the obstacles and their number plays a key role. The effect of bend in the pipe can be evaluated by applying a factor  $K_L = 0.3$  (taken from Çengel and Cimbala, 2014, p. 378) to the value of the dynamic pressure.

In conclusion the two source of pressure losses in a flowing fluid are almost of the same order of magnitude; both must be carefully evaluated in the actual applications.

#### 7.3 MODEL REALIZATION

In fig. 38, the Simulink® realisation of the model of the pipe is shown. As mentioned before, the solution of eq. (7.4) must be reached iteratively because the formulation is implicit and non-linear. However, rather than applying an algorithm to find the zeros of the non-linear equation, like fzero in Matlab®, which can be computationally intensive, in the Simulink® model, the friction factor is calculated employing the mass flow rate values corresponding to a previous time step, which can be stored in a Memory block. This block provides a *sort of state* of the system, which is directly associated with the value of the output variable at the previous time step. For this reason, the model cannot be defined as static anymore.

In this context, to achieve more control over the dynamic behaviour of this model, the Memory block is substituted with a transfer function,

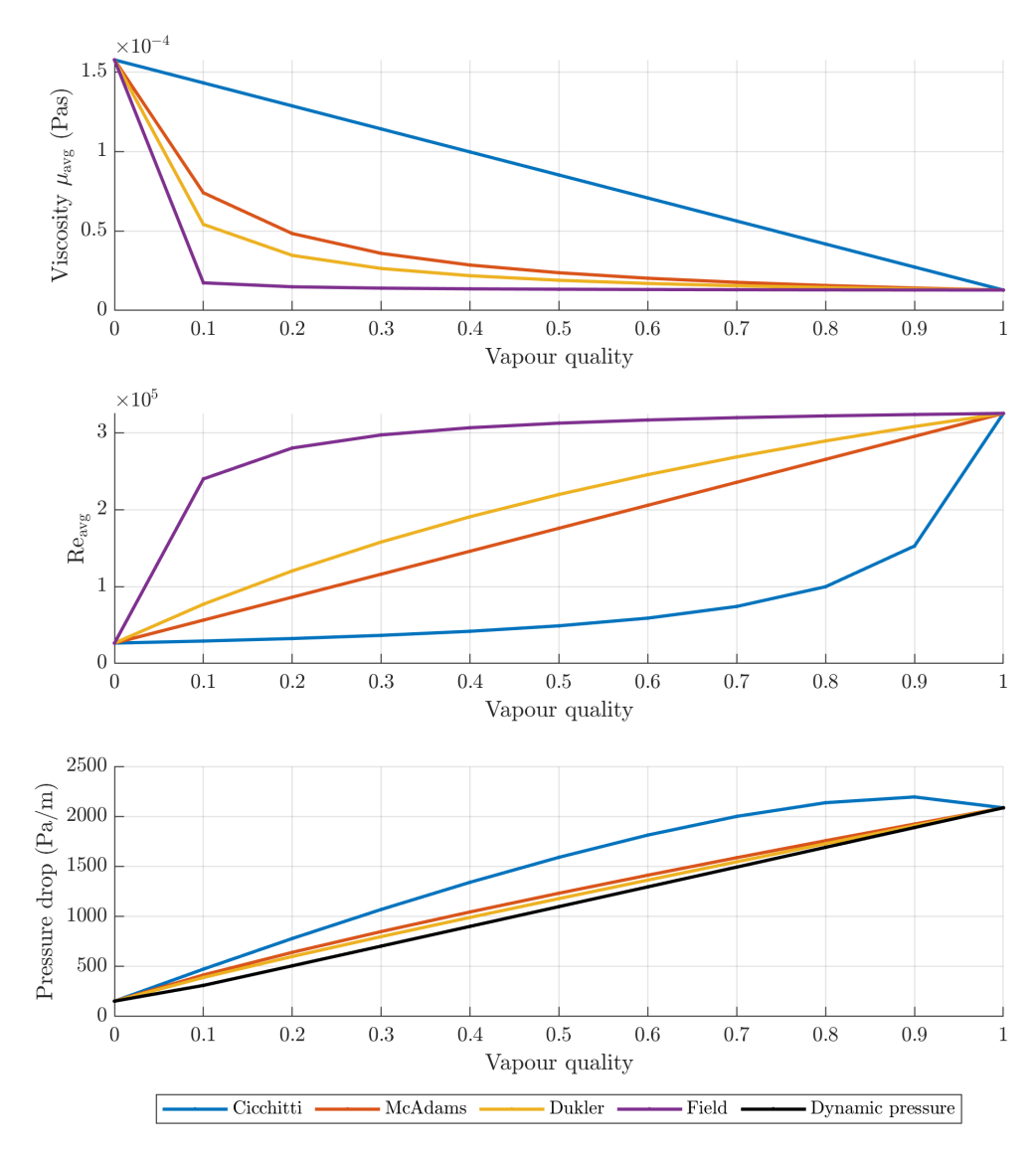


Figure 37: Comparison between the homogeneous models for the pressure drop evaluation in a circular tube with R450A.

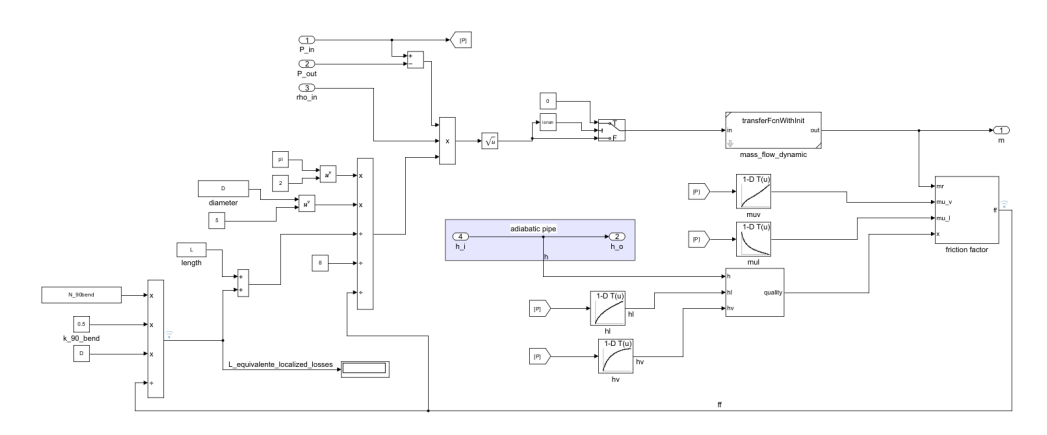


Figure 38: Model of the pipe realized in Simulink®

which provides the first-order dynamics. The block developed is integrated with the possibility to define user-defined initial conditions. The first order transfer function is characterized by a time constant. The flow change in the pipe is not instantaneous, and it characterised by a certain dynamic behaviour. A faster dynamic can be associated with the speed of the pressure perturbation along the pipe (i.e. speed of sound) and a slower one is related to the time needed by the fluid particles to flow from the inlet to the outlet section. However, the model developed does not account for these physical phenomena, but the time constant has only the numerical function of allowing the solution of the implicit equation for the friction factor. It is also possible to tune it to improve the time step, as described in section 9.2.

For completeness, the pipe can be modelled as fully static system if the friction factor is assumed to be known or determined without any relation with the flow regime, which has no physical meaning. This approach can be useful for evaluating the system without the contribution of artificial dynamics. The dynamic trend is captured similarly with both approaches. However, too fast time constant or even worst, static systems negatively impact the time step of the solution algorithm. When a variable step solver is employed, it defines the step size according to the prescribed relative tolerance. In contrast, in a fixed-step simulation, attention must be paid to the amplitude of the integration step to avoid anomalies of the solution.

In section 9.2, numerical tests of the pipe model coupled with the models of the accumulation device are described.

# 8 EXPANSION VALVE

As for other expansion devices, the main function of the expansion valve is reducing the pressure level of the refrigerant from the hot to the cold side of the cycle. With respect to fixed geometry component, like capillary tubes or short-tube restrictors, valves allow control of the operating point of the system by acting on the opening. This is obtained by varying the orifice cross sectional area with the controlled movement of a popper (plug).

## 8.1 EXPANSION VALVE OPERATION

Varying the valve opening the flow rate is modulated up to a maximum value. The relation between the position of the plug and the cross sectional area available for the fluid flow depends on the shape of both. This relation is provided by the manufacturer and is an important information for controlling purposes. Two main characteristics are employed: linear and equal percentage. Often the control valves are designed with an equal percentage characteristic that allows a more precise control capacity in the low range of operation.

The valve opening, thus the movement of the valve plug, can be steered by means of a mechanical or electrical actuators, American Society of Heating and Engineers, 2018.

## 8.1.1 Thermostatic valve

In the thermostatic valve the movement of the plug is caused by the interaction of the pressure and elastic forces. This valve modulates the refrigerant flow entering the evaporator in response to the superheat of the vapour at its outlet. In a typical arrangement, the valve stem is subjected to the opposing actions of the elastic force produced by a spring and a pressure acting on a diaphragm. The thermostatic element is connected to a bulb positioned in contact with the manifold at the evaporator outlet and filled with a fluid. A temperature variation on the bulb corresponds to a pressure variation over the diaphragm. So, adjusting the force of the spring it is possible to regulate the desired superheat, which corresponds to a certain pressure inside the thermostatic element, dependent on the kind of fluid employed in the bulb. Indeed, different thermostatic charges are used: gas or liquid

charge, which employ the same refrigerant of the system, or liquid cross-charge that use a volatile liquid different from the refrigerant.

The mathematical modelling of the mechanical actuation is quite challenging, even more so if the dynamic response is the focus. Basically, the position of the popper corresponds to the equilibrium point between the elastic force of the spring, and the resulting pressure force over the diaphragm caused by the interaction between the saturation pressure in the lower side and the thermostatic fluid pressure in the upper side. Many geometrical characteristics of the valve body are therefore necessary, like the volume available for the trapped fluid in the bulb and in the thermostatic element, the surface of the popper on which the refrigerant pressure acts, the shape of the orifice, the length of the spring; moreover, physical parameters are needed like the elastic constant of the spring or the equation of state for the fluid. All these pieces of information parameter are normally unavailable, so detailed model for practical engineering application is hard to set up. However, very accurate dynamic model of a thermostatic valve is proposed by Eames et al., 2014.

Consideration on modelling

## Electrically actuated valve

The electrically actuated expansion valves can be operated with four basic modes:

- 1. Thermally operated
- 2. Magnetically modulated
- 3. Pulse-width-modulated
- 4. Step motor driven

The first category comprises the valves where the shaft is actuated by a bimetallic element electrically heated or by a force acting over a diaphragm, like in the thermostatic valves, but, in this case, the fluid contained in the chamber is electrically heated to achieve the desired pressure.

In the magnetically modulated valves the positioning of the shaft is obtained by the equilibrium between the elastic force of a spring, a magnetic force produced by a solenoid, and the pressure of the refrigerant over the poppet. Modulating the current in the solenoid it is possible to define different operating points.

The pulse-width-modulated valves are simple on/off solenoid valves equipped with a special controller which defines the opening time as a fraction of the duty cycle.

Finally the valve can be equipped with a step-motor designed to rotate in discrete fractions of a revolution. This actuator is very precise in positioning the shaft and ensures good repeatability.

All electric expansion valves need a suitable electronic controller which determines the position of the shaft by adjusting the electric inputs required by the actuator. Electronic controllers allow more flexibility and accuracy than the mechanically actuated valves. In fact, the thermostatic actuation has the superheat as the only controlled variable; moreover their response is dependent on the fluid, non-linear and limited to the design operating range. Electronic controllers can operate in a wide range, can respond to a variety of input parameters and allow control strategies not possible for mechanically actuated valves.

Electronic controller

From a modelling point of view, this controller may be simpler to implement; indeed the algorithm implemented in the programmable controller must be translated into a different programming language. Considering as control variable only the superheat at the evaporator outlet, reproducing a thermostatic expansion valve, the target value is followed employing a PID controller. More complex control logics can be implemented employing multiple input variables.

Consideration on modelling

## 8.2 NUMERICAL MODELLING

The modelling of the expansion valve is carried out as for a static system, because, as discussed in chapter 2, no mass or energy accumulation occurs in this component during normal operations. Moreover, the heat transfer between the refrigerant and the environment during the expansion can be ignored, so the process is considered as isoenthalpic.

In this context, the characteristic of an expansion valve for refrigeration applications is usually provided in the form of the cooling capacity ( $\dot{Q}_{evp}$ ):

$$\dot{Q}_{evp} = C_0 \sqrt{\rho_{r,l,v,i} \Delta p} [h_{r,evp,o} - h_{r,evp,i}]$$
(8.1)

The mass flow rate through the valve can be calculated with eq. (8.2)

$$\dot{m}_{\rm r} = C_0 \sqrt{\rho_{\rm r,l,\nu,in} \Delta p} \tag{8.2}$$

where  $C_0$  is the valve flow constant and the  $\Delta p$  is the pressure drop in the valve.

### 8.2.1 The manufacturer correlation

In the plant an expansion valve from Carel with an equal percentage characteristic is installed. The electric valve is actuated with a step motor driven by a programmable microcontroller. The manufacturer provides an equation to evaluate the volumetric flow rate obtained varying the pressure difference and the opening

$$\dot{V} = \frac{k_{\nu}(0.1)^{\frac{90 - (y - 10)}{90}} \sqrt{\rho \Delta p \cdot 1000}}{3600^2}$$
(8.3)

where  $\dot{V}$  is volumetric flow rate,  $k_{\nu}$  is the valve flow coefficient  $(k_v=0.25)$ , y is the actual opening of the valve (expressed in % of the maximum opening), (y = 100 corresponds to the maximum value)of the flow rate, while y = 10 corresponds to the minimum value before the shut-off),  $\rho$  is the refrigerant density at the inlet, and  $\Delta p$  is the pressure difference straddling the valve (bar) The position of the poppet is defined in terms of steps of the electric motor, in a range o-400, corresponding to o-100% of opening (y).

#### The valve block 8.2.2

The valve block interfaces with the VCS model by means of inputs and outputs. The main inputs of the EXV block are listed below:

- refrigerant pressure at the inlet
- refrigerant pressure at the outlet
- refrigerant density at the inlet
- refrigerant enthalpy at the inlet

The outputs are

- refrigerant mass flow rate
- refrigerant enthalpy at the outlet

The valve block has also a control input, the valve opening. This can be established manually ore provided by a valve controller block. The evaluation of the refrigerant enthalpy is trivial because it is simply

$$h_{r,i} = h_{r,o}$$
 (8.4)

According to the selection of the system metric, eq. (8.3) can be rearranged to evidence the mass flow rate  $(kg s^{-1})$ ; to evaluate the pressure drop the values are converted from Pascals to bars.

$$\begin{split} \dot{m}_r &= \frac{k_{\nu}(0.1)^{\frac{L-(y-10)}{L}} \rho_{r,i} \sqrt{\rho_{r,i} \Delta p \cdot 1000}}{3600^2} & y \in [0.1,1] \\ \dot{m}_r &= 0 & y \in [0,0.1] \end{split} \tag{8.5}$$

For valve opening below 0.1 the valve is considered closed. In fig. 39 the realization of the model of the expansion valve in the Simulink® environment is shown.

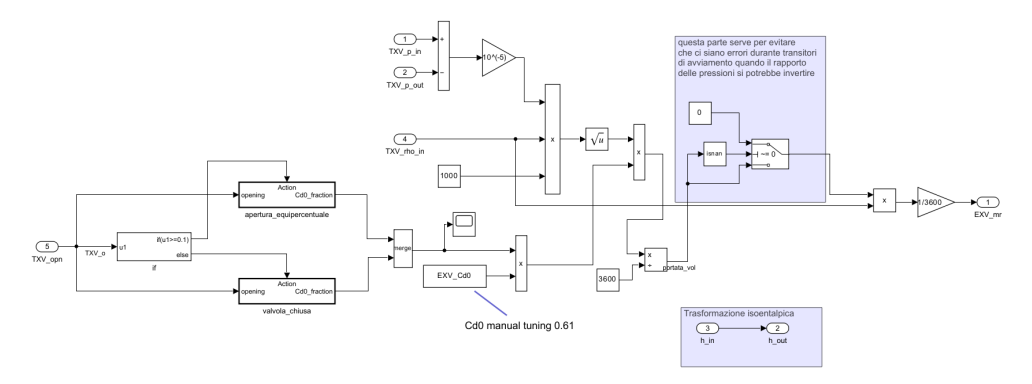


Figure 39: Simulink® scheme of the expansion valve.

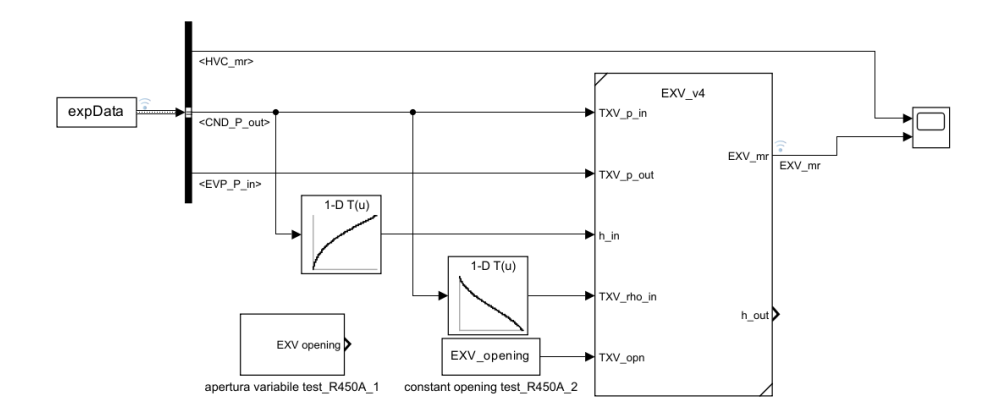


Figure 40: Simulink® scheme of the numerical test rig employed for the validation of the EXV model.

#### 8.3 VALIDATION AND TUNING

The model of the expansion valve is tuned employing the first set of data available (Test 2 with R450A) in which the valve opening is maintained constant for all the test, (see section 3.4). The validation and tuning procedures are realized directly connecting the EXV block to the experimental data available, see fig. 40. The flow coefficient is adjusted manually, because the flow coefficient for the refrigerant employed is not provided by the manufacturer. The results of the tuning are shown in fig. 41

The model is validated employing the remaining test data available, Test 1 with R450A in which the valve opening varies.

Figure 42 shows that the model is able to capture the steady state operating point of the valve when the opening changes with good accuracy. On the other hand, the transient behaviour exhibits more deviation compared to the experimental data. Indeed, with the available measurements, it is difficult to evaluate this behaviour properly, because the liquid receiver is located between the transducer and the valve, fig. 2.

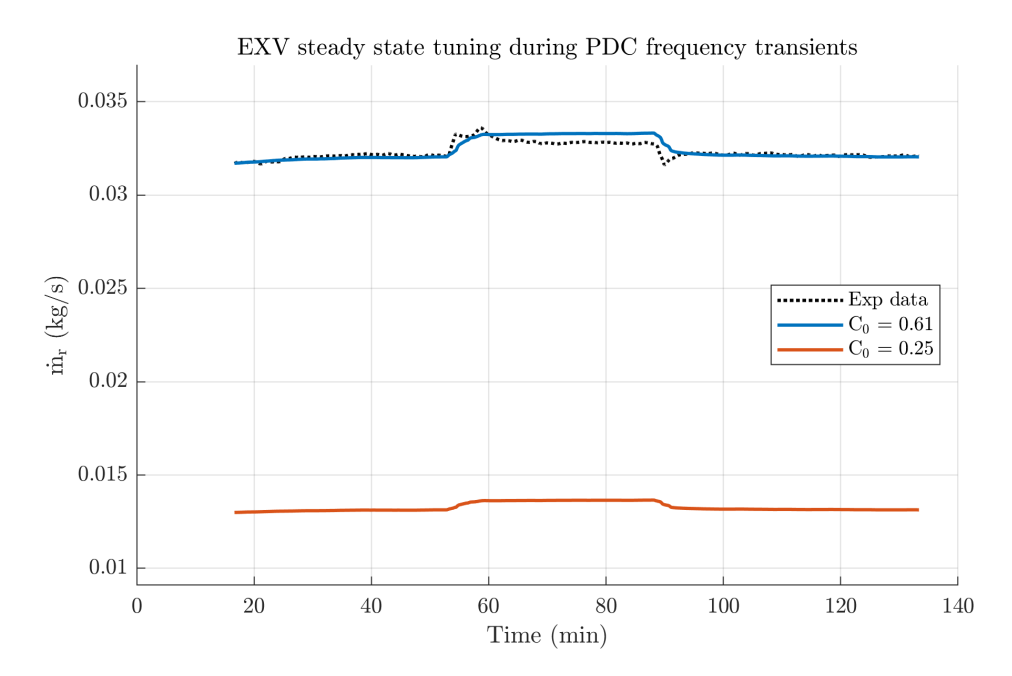


Figure 41: Tuning of the EXV flow coefficient with experimental data under Test 2 with R450A, see section 3.4.

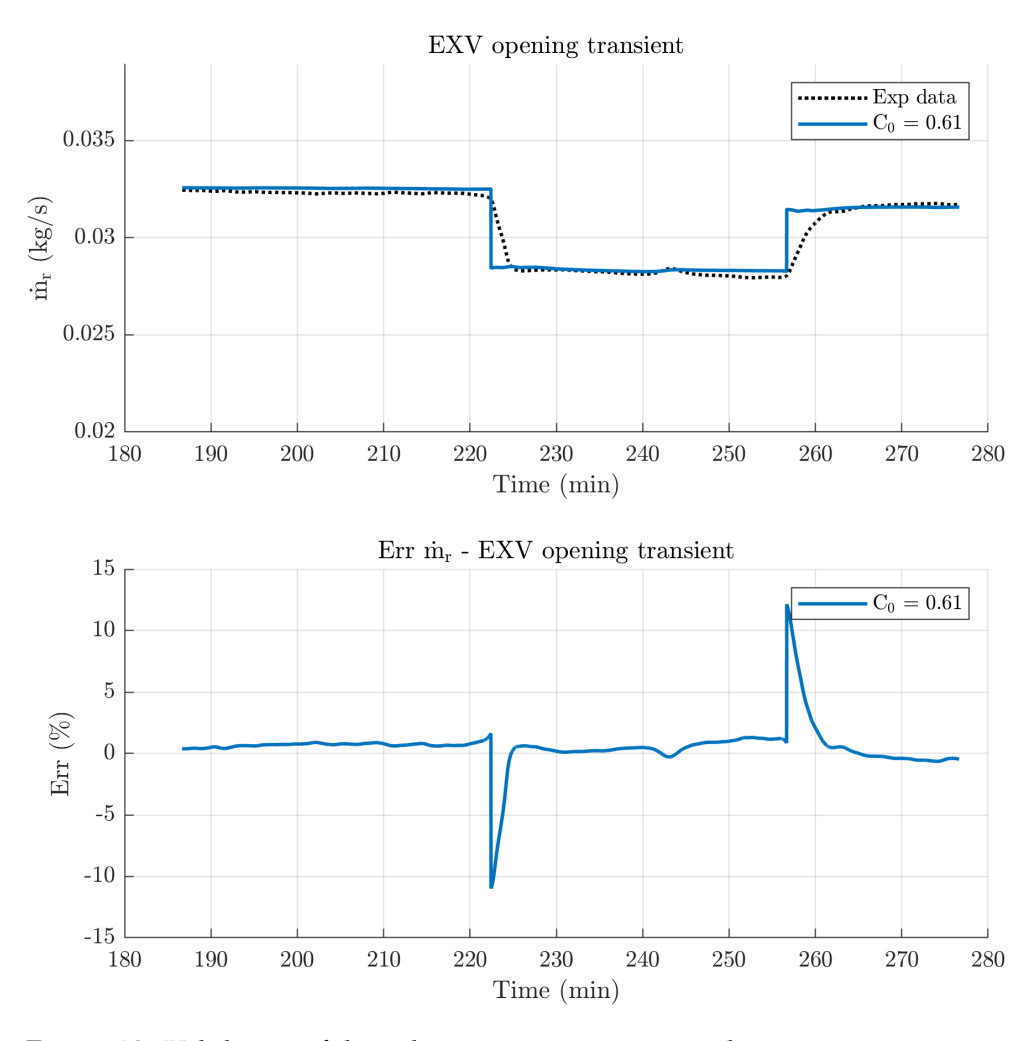


Figure 42: Validation of the valve tuning against two valve opening transients, from Test 1 with R450A, see section 3.4.

# 9 | FLUID STORAGE VESSELS

The VCS are equipped with accumulation devices, which have the main role of disconnecting part of the loop to allow safe operation of the components and protect them from damage. Moreover, in the case of larger plants, their presence may increase the performance, enabling independent control strategies for each portion. A generic reservoir can be filled with either a single-phase fluid or vapour-liquid mixture. The fluid condition is assumed to be of thermodynamic equilibrium in both cases.

## **9.1 NUMERICAL MODEL**

The reservoir is modelled as a fixed volume containing a certain amount of fluid ( $\mathfrak{m} = V\rho$ ) to which the mass and energy balance are applied, eqs. (9.1) and (9.2).

$$V\frac{d\rho}{d\tau} = \dot{m}_i - \dot{m}_o \tag{9.1}$$

$$\frac{dU}{d\tau} = V \frac{d(\rho u)}{d\tau} = \dot{m}_i h_i - \dot{m}_o h_o + \dot{Q}$$
 (9.2)

Rearranging the above equation to highlight the state variables  $\rho$  and u, the final system of differential equations employed to model the accumulation device, eq. (9.3), is obtained:

$$\begin{cases} V \frac{d\rho}{d\tau} = \dot{m}_i - \dot{m}_o \\ V \left( \rho \frac{du}{d\tau} + u \frac{d\rho}{d\tau} \right) = \dot{m}_i h_i - \dot{m}_o h_o + \dot{Q} \end{cases} \tag{9.3}$$

## 9.1.1 Solution algorithm

The system of eq. (9.3) can be implemented in the Simulink<sup>®</sup> environment in two ways. In fact, given that Simulink<sup>®</sup> automatically calculates the solution of a time differential equation in explicit form, eq. (9.3) is rearranged as eq. (9.4) and solved sequentially. The Simulink<sup>®</sup> scheme of the accumulator is sketched in fig. 43.

$$\begin{cases} \frac{d\rho}{d\tau} = \frac{1}{V}(\dot{m}_i - \dot{m}_o) \\ \frac{du}{d\tau} = \frac{1}{\rho} \left[ \frac{1}{V}(\dot{m}_i h_i - \dot{m}_o h_o + \dot{Q}) - u \frac{d\rho}{d\tau} \right] \end{cases} \tag{9.4}$$

For those systems which cannot be directly expressed in explicit form, the matrix formulation is allowable, as  $\mathbf{ZX} = \mathbf{F}$  where the matrix Z is

$$\mathbf{Z} = \begin{bmatrix} V & 0 \\ Vu & V\rho \end{bmatrix} \tag{9.5}$$

The vector of the unknowns  $\dot{\mathbf{X}}$  is:

$$\dot{\mathbf{X}} = \begin{bmatrix} \frac{\mathrm{d}\rho}{\mathrm{d}\tau} & \frac{\mathrm{d}u}{\mathrm{d}\tau} \end{bmatrix}^{\mathrm{T}} \tag{9.6}$$

and the right-hand side is

$$\mathbf{F} = \begin{bmatrix} \dot{\mathbf{m}}_{i} - \dot{\mathbf{m}}_{o} & \dot{\mathbf{m}}_{i} \mathbf{h}_{i} - \dot{\mathbf{m}}_{o} \mathbf{h}_{o} + \dot{\mathbf{Q}} \end{bmatrix}^{\mathsf{T}}$$
(9.7)

The time derivatives can be calculated by inverting the matrix **Z** to obtain the explicit form. Then, they are submitted to the Integrator blocks for the calculation of the solution.

In this form, it is easier to evaluate the eigenvalue of the dynamical system which corresponds to the eigenvalues of the inverse matrix.

$$\lambda_1 = \frac{1}{V}$$

$$\lambda_2 = \frac{1}{\rho V}$$
(9.8)

The fastest mode corresponds to the state of density and is characterized by the largest eigenvalue, which leads to the smallest time constant  $\tau_1 = V$ . This is an interesting result, useful for the definition of the solver parameter, particularly the integration time step, as discussed in section 9.2.

## Function block structure

The structure of the function block of the accumulator is described next. Beside the inlet and outlet mass flow rate, the thermodynamic state of the incoming fluid must be provided to the model in terms of an intensive variable. Indeed, the pressure is determined by the conditions occurring in the vessel, so to define the state of the fluid at the inlet section the specific enthalpy or the internal energy are sufficient; on the other hand, although the temperature can be used for non-azeotropic mixtures because the pressure and the temperature are not coupled in the saturation conditions, in case of pure substances or azeotropic mixtures, this information is inadequate for the evaluation of the thermodynamic state. So, to guarantee a general application of the function block, the inlet condition required is the specific enthalpy hi.

At each time step the model calculates the state variables  $\rho$  and Model algorithm

Inputs

u solving eq. (9.4). The enthalpy of the outlet flow is needed for the energy balance of the vessel, but it is also a consequence of the thermodynamic conditions inside it. To account for this coupling and maintain the explicit formulation of the problem, the value of the previous time step is employed in eq. (9.4). Knowing two state variables, all the other thermodynamic quantities can be evaluated using the state equation that in this work is implemented through the Lookup Tables. More in detail, the saturation pressure and temperature are evaluated with two 2D Lookup Tables, and then the average enthalpy is determined knowing  $\rho$ , u and V. Finally, the quality can be calculated after having evaluated the saturated vapour and liquid enthalpy with a suitable 1D Lookup Table. More details about the creation of these blocs are provided in chapter 4.

The main outputs of the model are the pressure p inside the vessel and, if required, other averaged thermodynamic properties, like the temperature or the quality, which can be useful for the evaluation of the fill level. An important output to provide in the downstream component is the outlet enthalpy h<sub>o</sub>. Special care must be devoted to its evaluation because it is the piece of information necessary for the energy balance over the control volume. This depends on the characteristics of the vessels, i.e. on the position of the ports and on the conditions of the fluid within. So, each kind of accumulator employed in the system will be discussed separately.

The LR, located between the condenser and the expansion valve, is designed to ensure the separation of the liquid from the vapour phase so that the expansion valve is fed only with the former. For this reason, during normal operation, this vessel is filled with two-phase fluid in saturation conditions. The outlet port is located at bottom part to ensure that only liquid leaves the vessel. The inlet port is located at the top and can receive both two-phase, saturated or subcooled liquid. During normal operation, the saturated liquid is present at the outlet port of the vessel, except if the entire vessel is depleted of liquid.

The SA has a different behaviour because the outlet port is positioned in the upper part to ensure vapour conditions at the outlet. Indeed, its main function is to avoid liquid droplets refrigerant entering the compressor. Since it is located downstream of the evaporator, during normal operation, it receives superheated vapour; therefore, when it is filled up with superheated vapour, its effect is that of a lumped pressure drop in the suction line. If some liquid enters from the evaporator, for example, during the start-up or shut-down operations, it is collected in the bottom of the vessel, and saturation conditions set in it, which affect the behaviour of the vessel.

The oil separator, positioned downstream of the compressor, is streamed by superheated vapour, which crosses a mesh filter to remove the oil. Since it operates in single-phase conditions, it can be modelled

Outputs

Outlet enthalpy

Liquid receiver

Suction accumulator

Oil separator

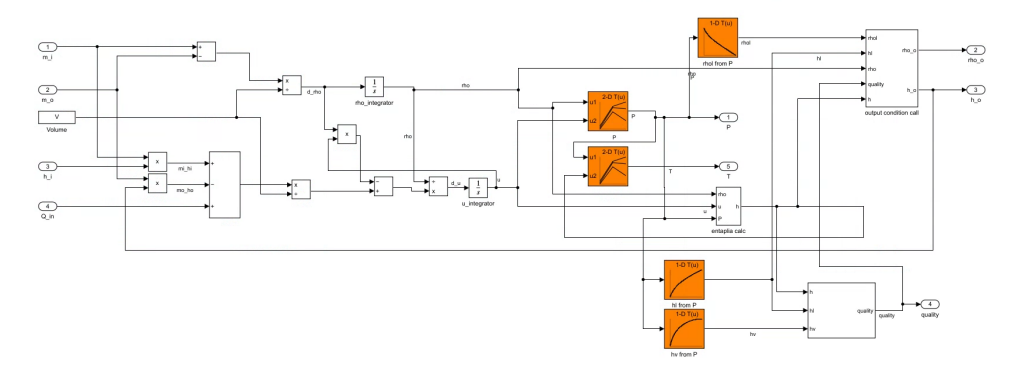


Figure 43: Model of the accumulator realized in Simulink<sup>®</sup>.

simply by a lumped pressure drop, to be estimated based on the filter characteristics.

From the above considerations, the effect of the liquid accumulator, which normally works in saturated conditions, must be considered with a dynamic accumulator model, while the other vessels can be handled in a simplified way as a lumped pressure drop.

#### NUMERICAL TESTS FOR THE ACCUMULATOR 9.2

To verify the behaviour of the models of the accumulation devices and of the pipe in a realistic scenario while having full control over the simulation parameters, a basic numerical set-up is developed. Two vessels, filled with refrigerant R450A in saturation conditions at different pressures are connected using a length of copper tube; the two vessels are assumed adiabatic,  $\dot{Q} = 0$ . In the first half of the simulation (150 s), the whole system composed by the two vessels and the pipe is isolated from the environment (neither mass nor heat transfer occur), and evolves as autonomous system, expressing a free response. The second vessel receives as input the mass flow rate drained from the upstream one through the pipe. After a certain time, the system reaches a steady state condition, when the pressures inside the vessels equalise. At time t=150 s a step variation of the inlet mass flow rate is imposed to the upstream vessel; a fixed flow rate of saturated liquid is assumed. The incoming refrigerant turn the system from the steady state into a forced response which is a dynamical behaviour caused by the presence of the input. In this set-up the system cannot reach a new steady state because no outlet flow rate are allowed for the downstream vessel. The Simulink® realization of the numerical test is sketched in fig. 44.

A second test is carried out with the same set-up of fig. 44, reducing the volume of the upstream vessel to a value compatible with those

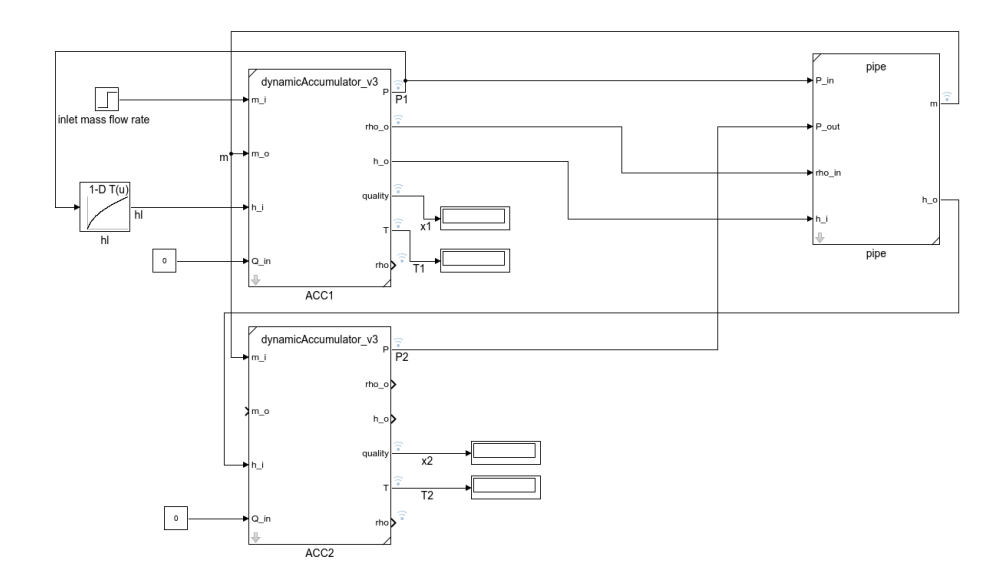


Figure 44: Numerical test set-up with two accumulation devices and one pipe, in Simulink<sup>®</sup>.

employed in the test facility, described in section 3.1, using the same procedure. Only the upstream vessel is reduced to have appreciable transients in the second part of the simulation. The conditions for the tests are summarised in table 18.

A second numerical set-up is realized employing two vessels and two pipes, one connecting the two vessels and one connected to the outlet of the downstream vessel, as sketched in fig. 45. In this way is possible to provide a mass flow rate boundary condition at the inlet of the whole system and a pressure boundary conditions at its outlet. Employing this set-up a third test is carried oud, whose parameters are gathered in table 19. The back pressure is defined in terms of saturation temperature.

#### Results and discussion 9.2.1

In the following, the results of the numerical tests realised are discussed.

In fig. 46 the time behaviour of the mass flow rate and the pressures inside the two vessels are shown. When the pressures equalize, the fluid flow rate between the two vessels ceases. When new refrigerant is injected, the mass flow rate reaches a new steady state value after a small transient. In this second phase, a pressure drop between the two vessels ensures the mass flow rate through the pipe.

In fig. 47 the trends of refrigerant conditions inside the vessels are provided. Despite the fact the same pressure is reached at steady state conditions, the saturation temperature is not the same in the two accumulators because the refrigerant employed is a zeotropic

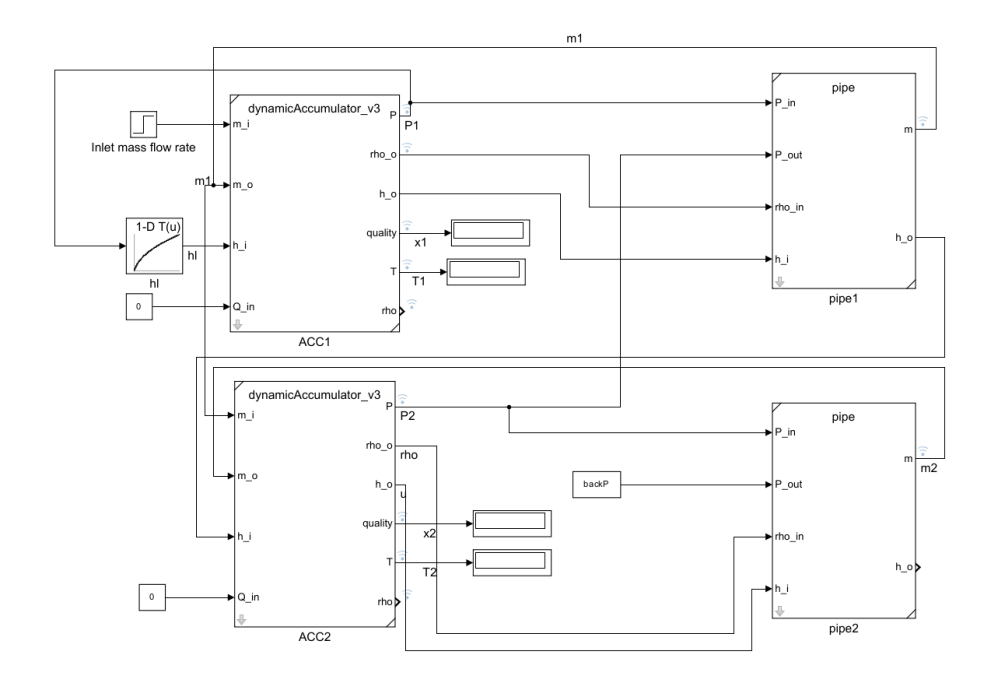


Figure 45: Numerical test rig with two accumulations device and two pipes models, in Simulink®.

Quantity	Value	UoM	Quantity	Value	UoM
$\overline{V_1}$	0.5	$m^3$	$V_1$	2.8	$dm^3$
$V_2$	0.5	$m^3$	$V_2$	0.5	$m^3$
$T_{sat,1}$	25.5	°C	$T_{sat,1}$	25.5	°C
$T_{sat,2}$	25	$^{\circ}\mathrm{C}$	$T_{\text{sat,2}}$	25	°C
$D_{ext}$	9.52	mm	$D_{ext}$	9.52	mm
S	1	mm	S	1	mm
L	1	m	L	1	m
ṁ (t=150 s)	0.1	${\rm kg}{\rm m}^{-3}$	ṁ (t=150 s)	0.1	$kg m^{-3}$
run time	300	S	run time	300	S
	(a)			(b)	

Table 18: Conditions for the first (a) and second (b) numerical test of the accumulators and pipe models.

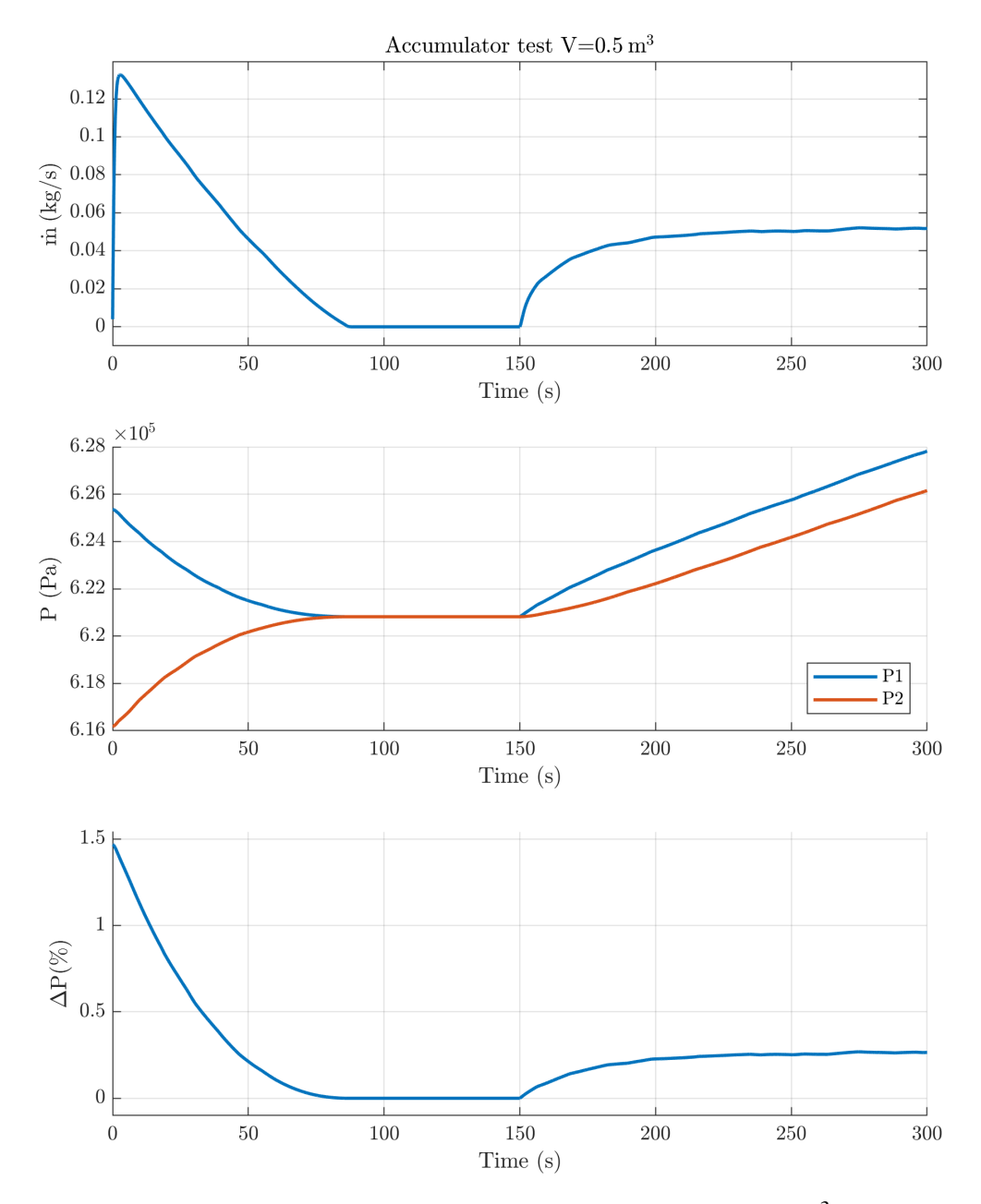


Figure 46: First numerical test with two accumulators (V=0.5 m<sup>3</sup> for both) and a pipe. Starting from the top, mass flow rate through the pipe, pressure in the two vessels and deviation between them normalised by the pressure in the upstream vessel.

Quantity	Value	UoM
$V_1$	2.8	$dm^3$
$V_2$	2.8	$dm^3$
$T_{sat,1}$	25.5	$^{\circ}C$
$T_{sat,2}$	25	°C
$D_{ext}$	9.52	mm
S	1	mm
L	1	m
m (t=50s)	0.05	$kg m^{-3}$
$T_{sat,out}$	27	°C
run time	100	S

Table 19: Conditions for the third numerical test of the accumulators and pipe models.

mixture (R450A), so at the same saturation pressure, the temperature is characterized by a glide. The saturation temperatures vary consistently with the vapour quality and the average density inside the vessels.

Figure 48 shows the behaviour of the mass flow rate and pressures in the second test with a smaller upstream vessel. The transients in this case are faster due to the smaller volume of the vessel. The mass flow rate through the pipe after the transient is almost equal to the forced input at the upstream accumulator  $\dot{m}$ =0.1 kg s<sup>-1</sup>, because only a very small part of the incoming mass flow rate contributes to increase the pressure of the first vessel. During the forced response of the system, the pressure drop in the pipe is therefore larger than the first case, corresponding to the increased mass flow rate.

In the third test, the behaviour of the system under a pressure boundary condition is verified. The trend of the main process variables can be appreciated in fig. 50. After a first transient, the system reaches the steady state when the pressure in the two vessels become equal; then the incoming mass flow rate causes a perturbation that leads the system to a new operating point determined by the back pressure imposed with the second pipe. After a transient, the upstream vessel reaches a steady state under these conditions, but in the downstream accumulator, the thermodynamic conditions are still changing until the end of the simulation.

## Numerical considerations

Further tests have been carried out to evaluate the numerical performance of the model, with a particular focus on the suitable fixed time step to be selected in different scenarios.

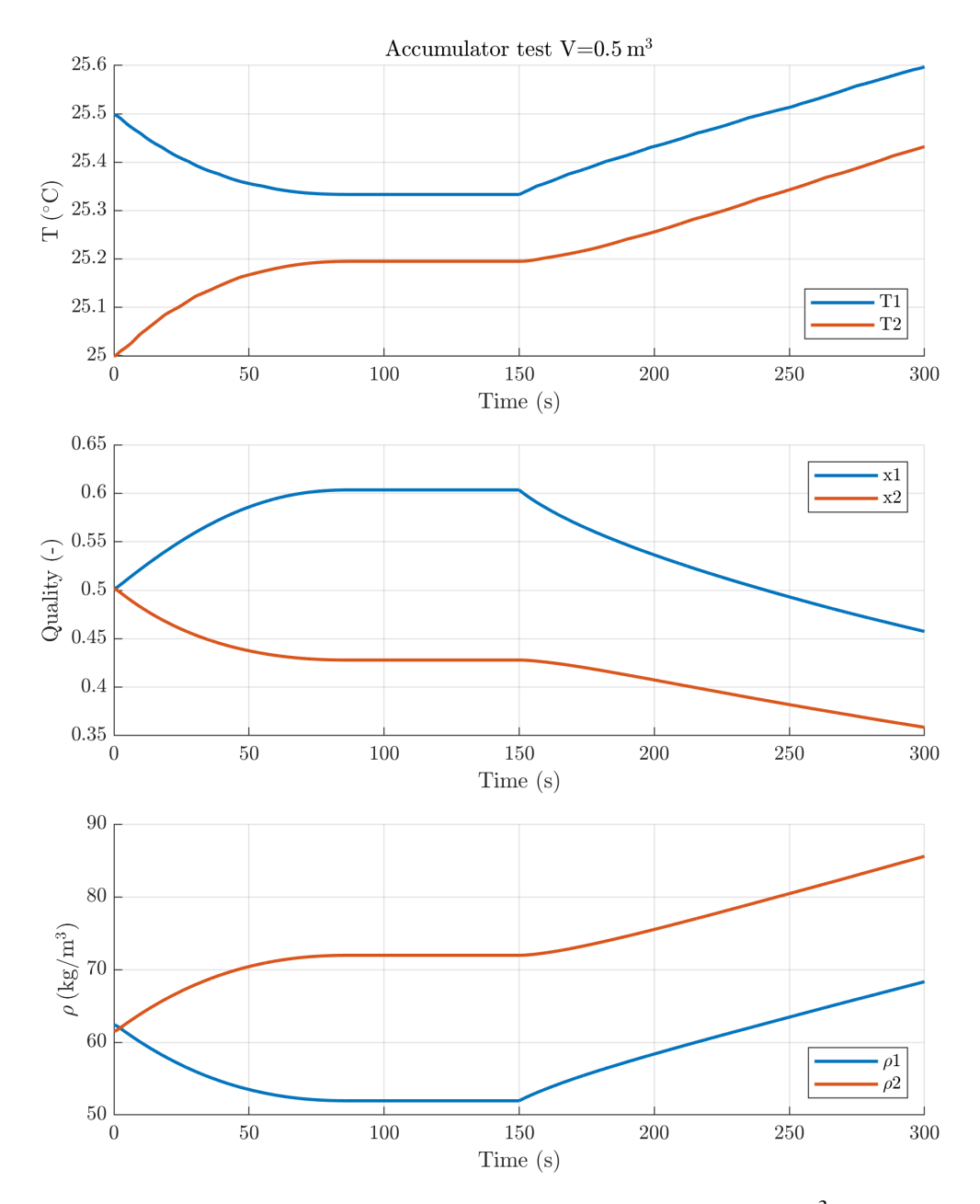


Figure 47: First numerical test with two accumulators (V=0.5 m<sup>3</sup> for both) and a pipe. Starting from the top: temperatures, vapour quality and mean density in the two vessel.

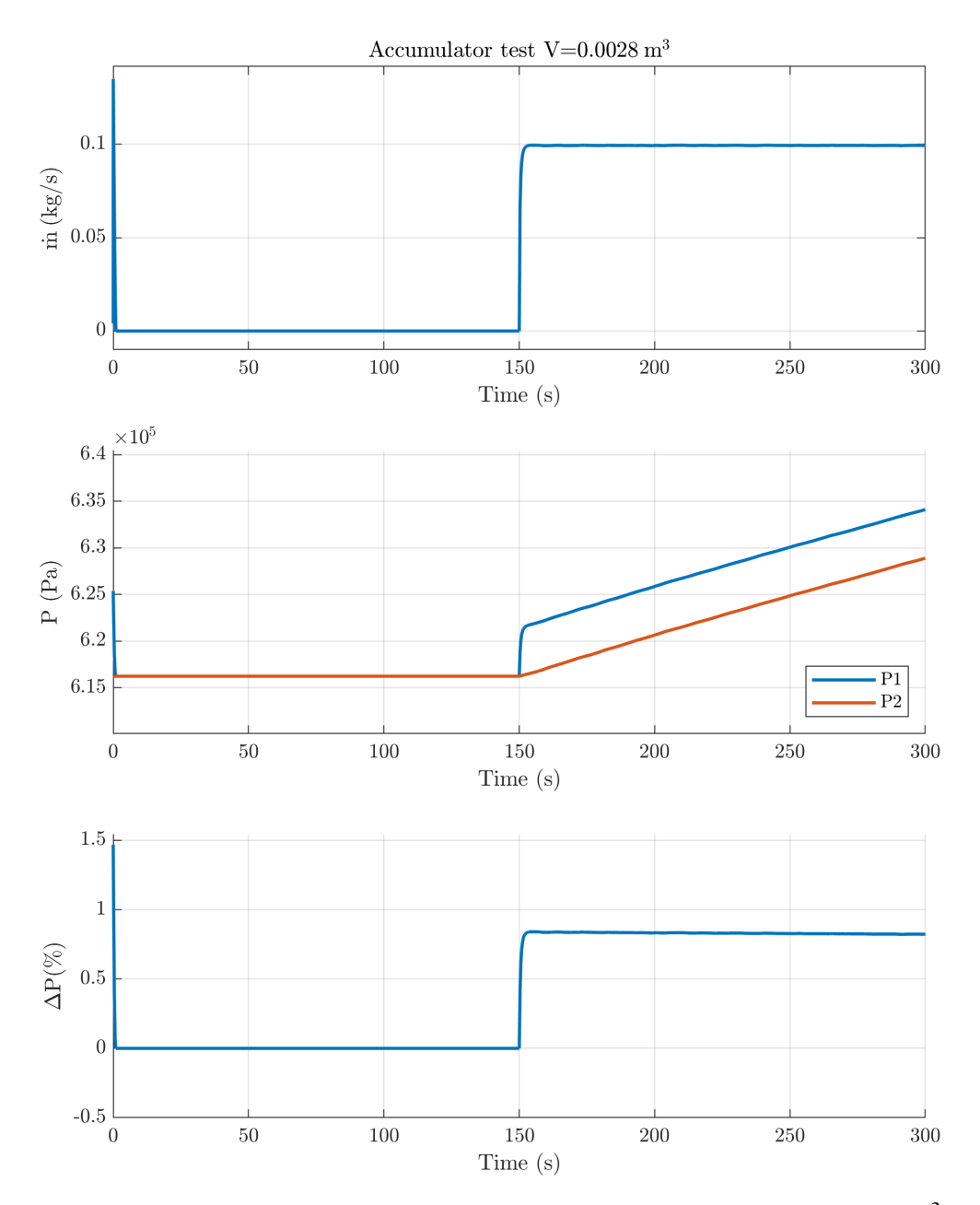


Figure 48: Second numerical test with two accumulators ( $V_1=2.8~\text{dm}^3$  $V_2$ =0.5 m<sup>3</sup>) and a pipe. Starting from the top, mass flow rate through the pipe, pressure in the two vessels and deviation between them normalised by the pressure in the upstream vessel.

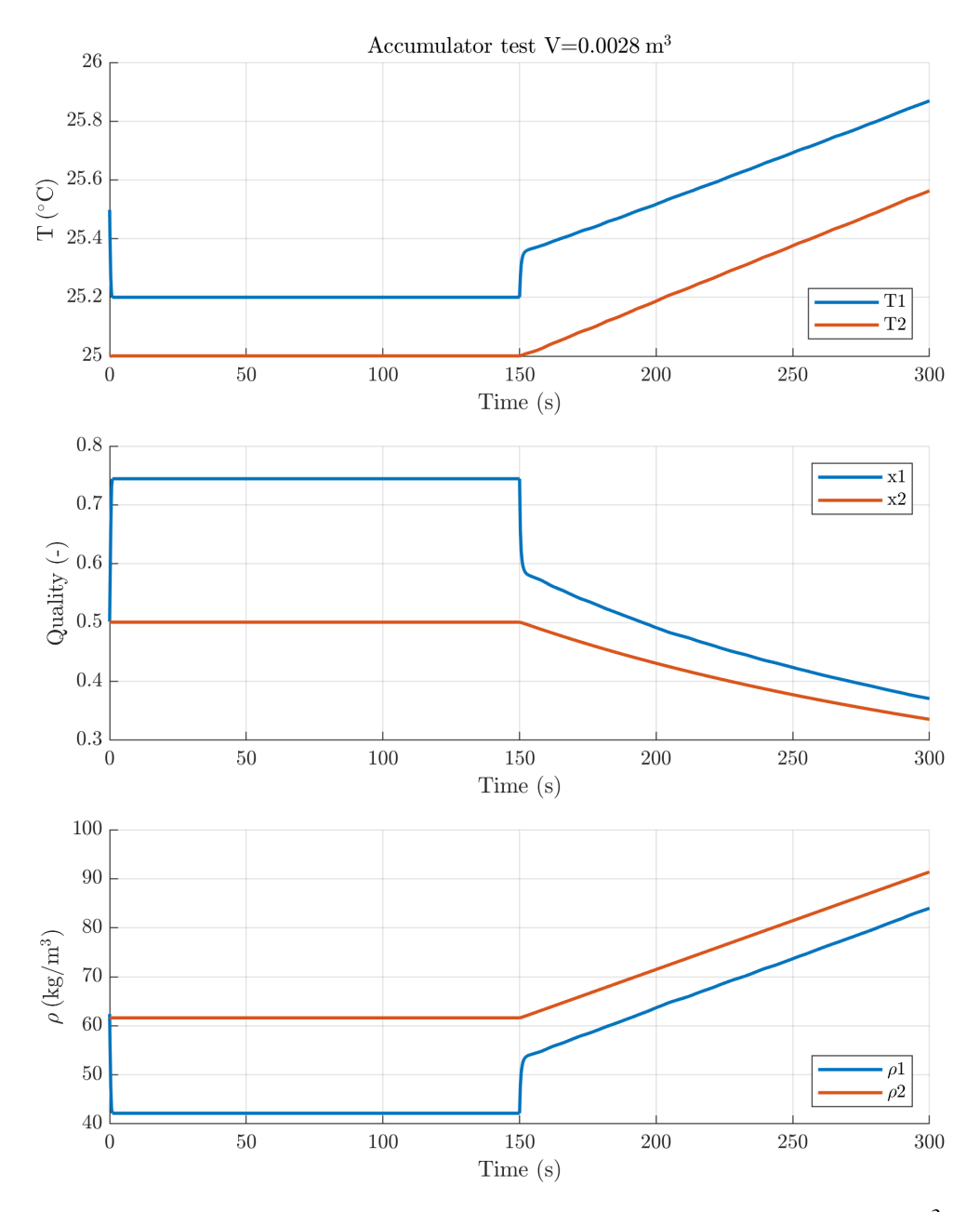


Figure 49: Second numerical test with two accumulators ( $V_1$ =2.8 dm<sup>3</sup>, V<sub>2</sub>=0.5 m<sup>3</sup>) and a pipe. Starting from the top: temperatures, vapour quality and mean density in the two vessels.

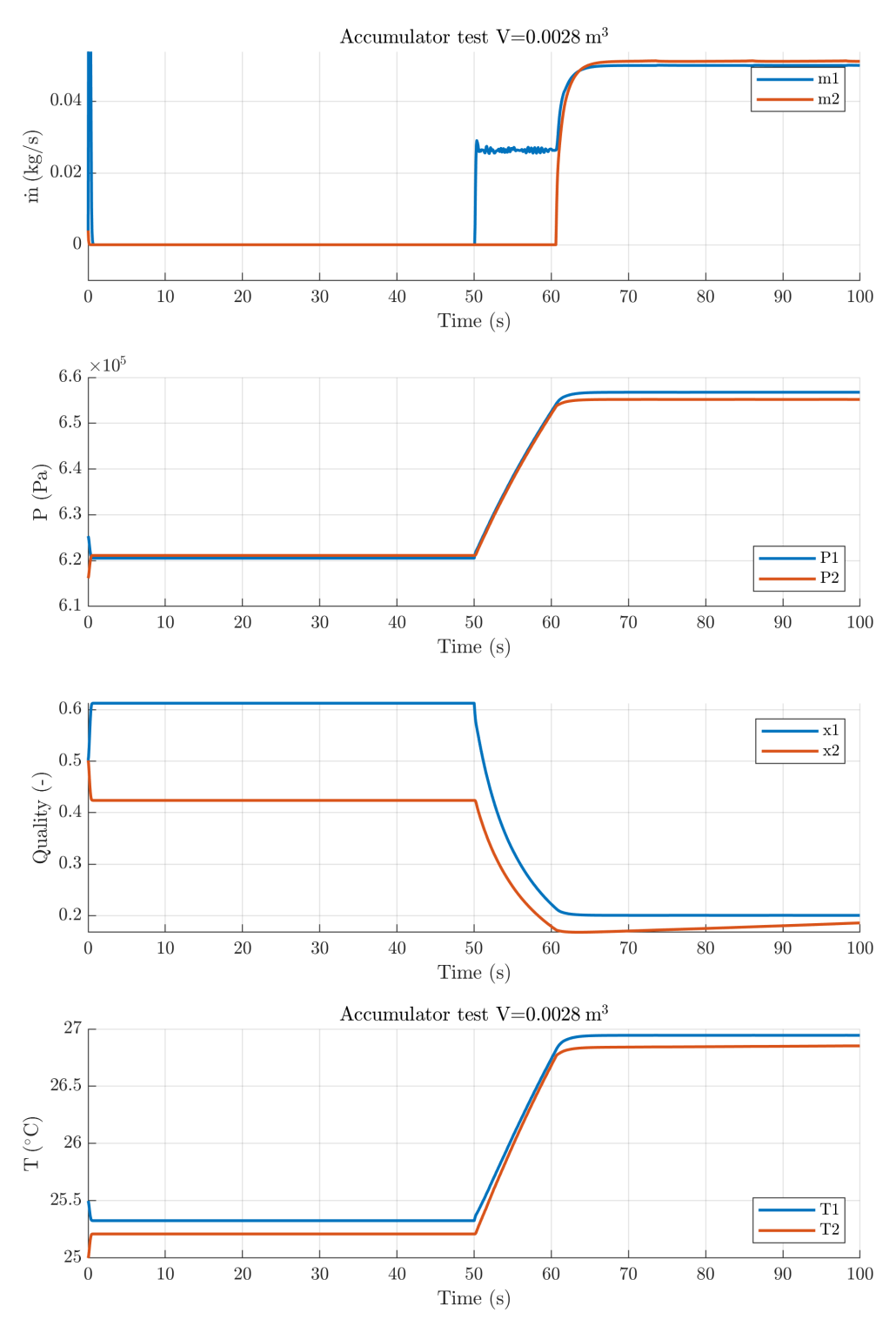


Figure 50: Third numerical test with two accumulators (both V=2.8 dm<sup>3</sup>) and two pipes. Starting from the top, mass flow rate through the two pipes, pressure, the vapour quality and temperature in each vessel.

The first numerical experiment is carried out with the larger vessel by increasing the time constant of the pipe to 25 times the time step of the upstream vessel, fig. 51. If the time constant of the pipe is too large in comparison to that of the upstream vessel, the evaluation of the pressure becomes inaccurate. The integration is performed with ode3 with a time step equal to the smaller  $\tau$  of the upstream vessel; the same results are obtained with smaller steps  $\Delta t$ =0.1 s without an appreciable difference, demonstrating that this deviation in the estimation of the pressure in the steady state conditions is caused by an inadequate time constant for the pipe. A similar behaviour can be found with different fixed time steps and also with a variable step solver like ode45.

On the other hand the results in figs. 46 and 47 were carried out imposing the time constant of the pipe equal to the smallest  $\tau$  of the upstream vessels, that is simply the volume of the accumulator, and the fixed time step is fixed equal to this time constant. So, for V=0.5 m<sup>3</sup> the integration step size is 0.5 s. The solution accuracy remains the same for time step in the range 0.01-1 s; smaller values are not significant for this application, while larger ones lead to simulation breakdown.

The same strategy to determine the pipe time constant and the integration time step can be employed in the second test case with a smaller upstream vessel. The solution represented in figs. 48 and 49 testify a good accuracy. But in this case the step size is of the same entity of the time constant, so equal to 0.0028 s, too small for the aims of this work.

To solve this issue two possible strategies were investigated. The first is simply to increase the time step of the solver; this is possible but the maximum increment is less of one order of magnitude; over this limit, the simulation fails. The second approach is to increase the time constant of the pipe and to fix the time step accordingly. The numerical test shows a good accuracy reached with a 25-fold increase of the time constant and as a consequence of the time step; in fig. 52, a maximum deviation of less than 0.05% of the pressure in the upstream vessel can be appreciated in the steady state condition, when the mass flow between the vessels ceases. When the time constant of the tube increases even more, like in fig. 53, the accuracy reduces, leading to a steady state absolute deviation of the pressure in the order of 0.2%; for an increase of 75 times the deviation is around the 0.5% and the trends shows some unexpected spikes in the mass flow rate and pressure. For larger increment of the time constant and of the integration time step, the simulation accuracy becomes rapidly unacceptable, failing to capture even the main trend of the variables.

The small absolute deviation that would be made even the 75-fold relaxation acceptable must nevertheless be compared with the operating conditions. For example, in the test with a time step relaxation of 50 times fig. 53, the pressure difference that maintains the mass flow

Effects of the pipe time constant on the solver time

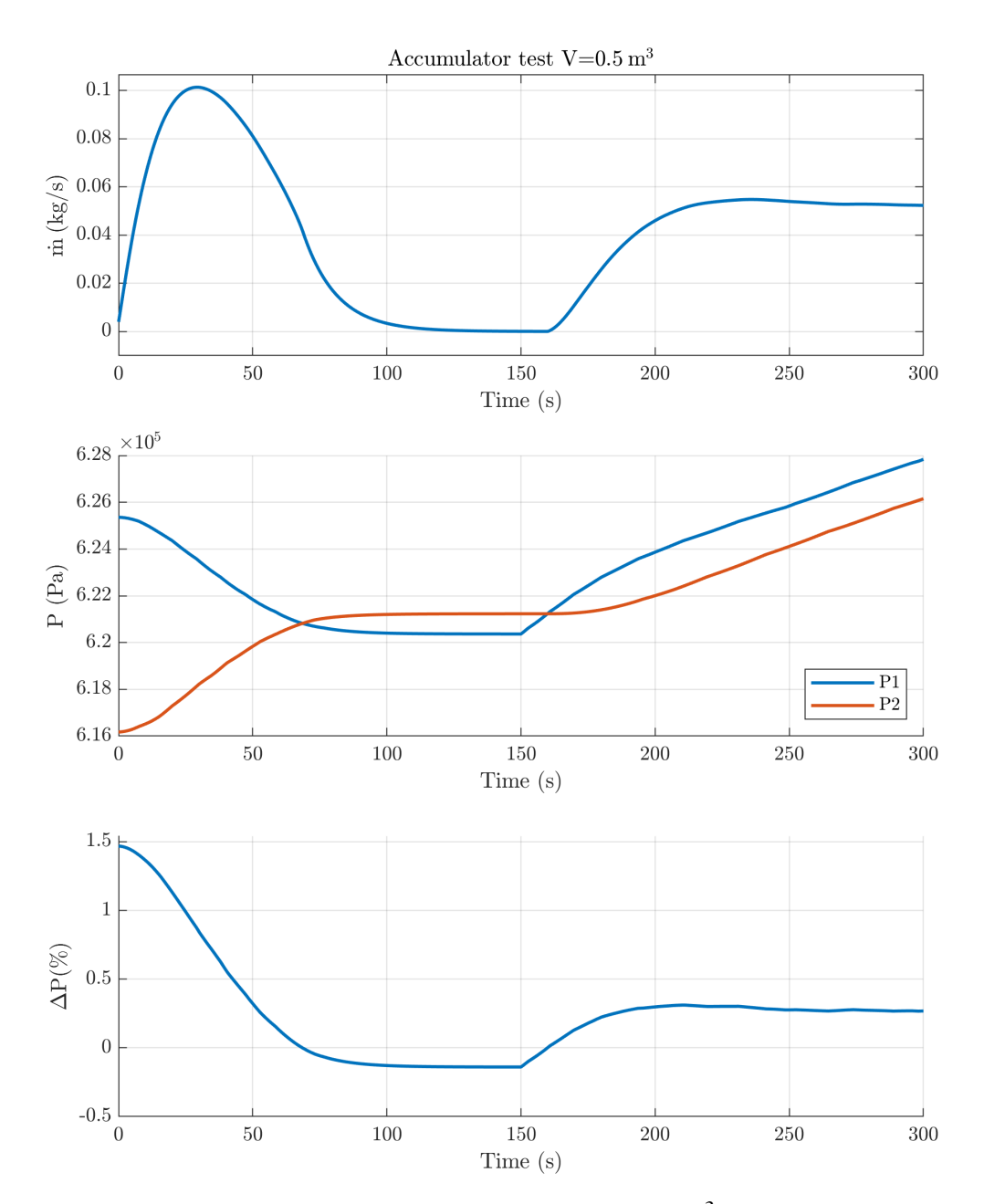


Figure 51: Numerical test of the accumulators (V=0.5 m<sup>3</sup> for both) and pipe. Starting from the bottom, mass flow rate through the pipe, pressure in the two vessels and deviation between them normalised by the pressure in the upstream vessel. In this case, the time constant of the pipe is imposed 10 times those of the upstream vessel, with a time step of 0.1 s.

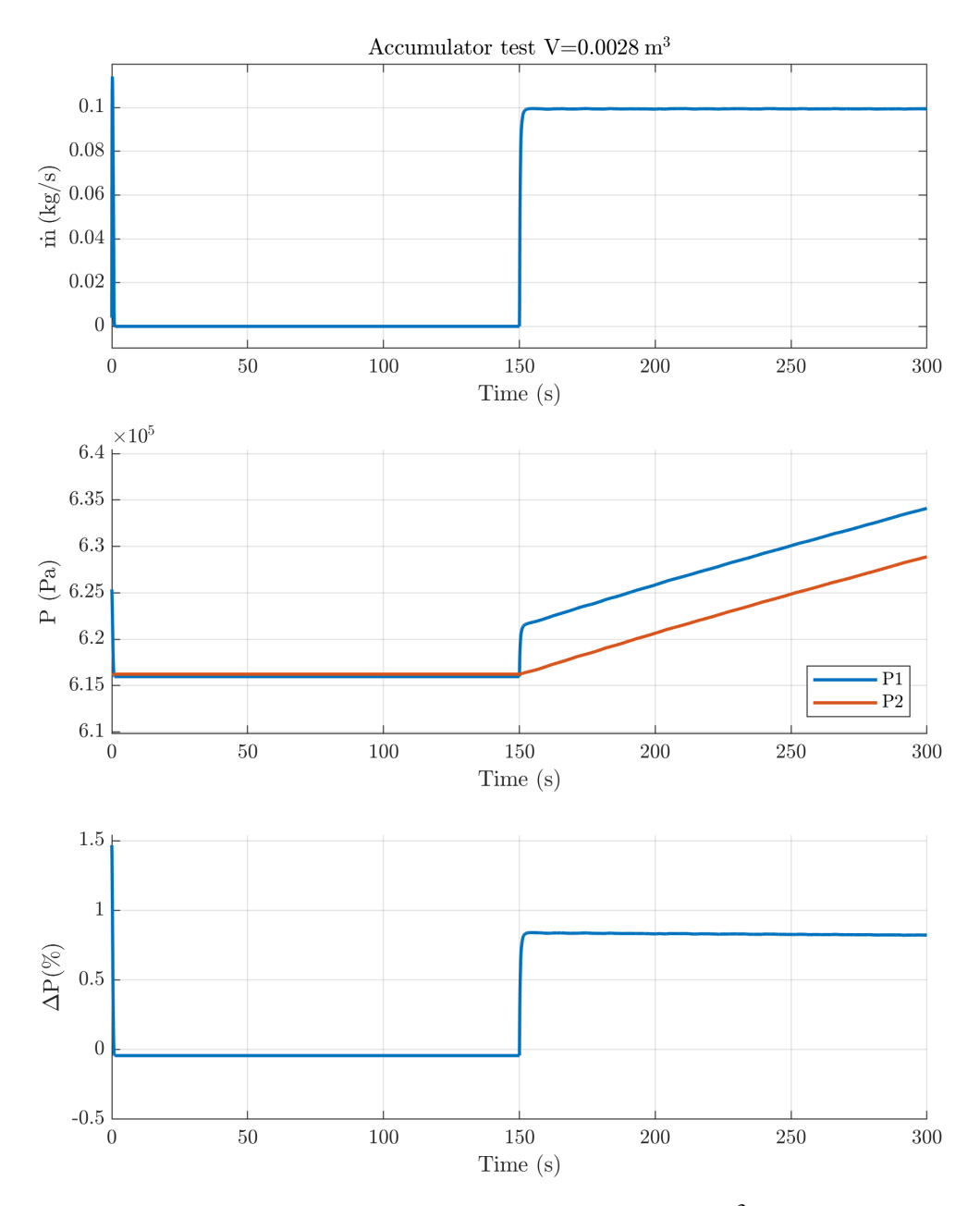


Figure 52: Numerical test of the accumulators ( $V_1$ =2.8 dm<sup>3</sup>  $V_2$ =0.5 m<sup>3</sup>) and pipe. Starting from the top, mass flow rate through the pipe, pressure in the two vessel and deviation between them normalised by the pressure in the upstream vessel. In this case the  $\tau_p$  of the pipe is imposed to 25 times the  $\tau_1$ of the upstream vessel and the solver time step in the same way.

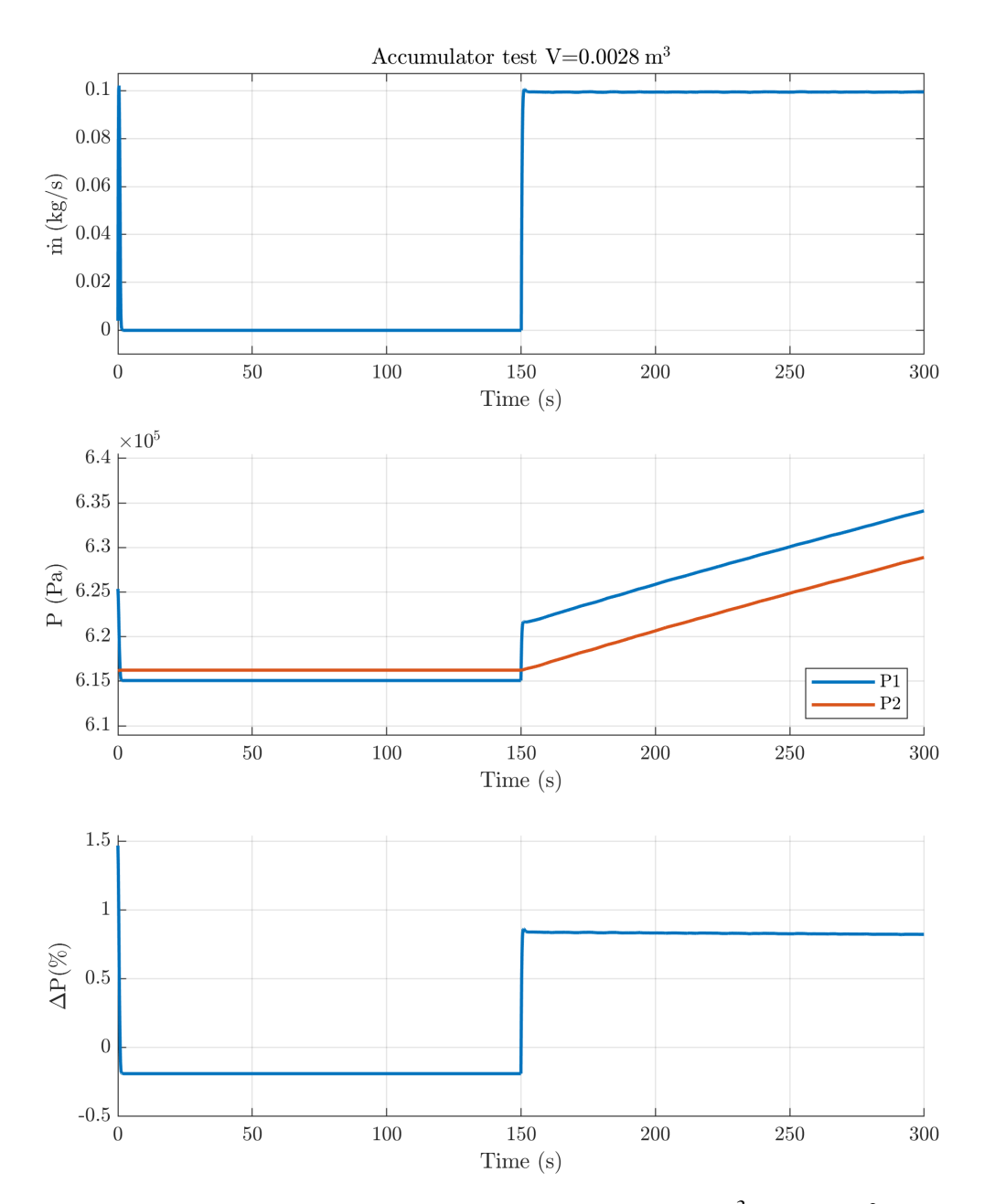


Figure 53: Numerical test of the accumulators ( $V_1$ =2.8 dm<sup>3</sup>  $V_2$ =0.5 m<sup>3</sup>) and pipe. Starting from the top, mass flow rate through the pipe, pressure in the two vessels and deviation between them normalised by the pressure in the upstream vessel. In this case, the  $\tau_p$  of the pipe is imposed to 50 times the  $\tau_1$ of the upstream vessel and the solver time step in the same way.

rate is around 0.85% while the steady-state deviation of the pressure is around 0.2% of the pressure in the upstream vessel; so they are of the same order of magnitude. To guarantee good accuracy, the error in the evaluation of the pressure should be at least one order of magnitude smaller, as is show in fig. 52.

Summarizing, in the Author's opinion a good time step relaxation should be less than 25 times like those employed in the third numerical test fig. 50, in which the relaxation factor was set to 20.

In conclusion, employing a suitable pipe time constant, it is possible to increase the fixed time step of the solver and the computational speed without a noticeable reduction in accuracy. Indeed, small vessels have a little time constant, which would lead to too small an integration time step. The pipe model downstream the vessel behaves as a filter for the faster upstream dynamics allowing the use of larger integration time step. Nevertheless, if the time step is too large and almost incompatible with the fastest system dynamics to capture, the results may become inaccurate and even unstable.

# 10 | HEAT EXCHANGERS NUMERICAL MODELLING

The heat exchangers play a key role in the behaviour of a VCS because the operating pressure levels are strictly connected with the heat transfer inside them. Moreover, the refrigerant undergoes a phase change during the process in both the evaporator and condenser for subcritical applications, while only in the evaporator for supercritical ones, leading to a considerable variation of its physical properties and, consequently, of the heat transfer conditions. Another key aspect from the point of view of numerical modelling is the time scales involved in the process; indeed, the thermal dynamics are usually slower by orders of magnitude than the mechanical ones, as pointed out by B. P. Rasmussen, 2012. This can lead to numerical instability and a reduction in the accuracy of the solution, typical of the socalled stiff problems. For these reasons, modelling such components is paramount for the whole VCS simulation. The process can be investigated by applying the general balance equations in a predefined control volume, so its definition is crucial. Based on this grounds, the different approaches available in the literature can be organized into three general categories: the lumped parameter, the finite volume technique, and the multi-region approach. The first assumes only one control volume coinciding with the HEX volume, and the physical properties of the fluids and the HTC are evaluated as an average over it. To the opposite end, the basis for the finite volume technique is the subdivision of the volume involved in the process into a certain amount of smaller control volumes to each of which the balance equations are applied; in this way, the physical properties and the HTCs are averaged over smaller volumes increasing the accuracy of the approximation. The control volumes can be of different sizes or equally sized; the last choice is easier to implement but may lead to overlooking some details. More precisely, the accuracy in the identification of the transition point relies on grid refinement. Finally, the multi-region approach is very interesting because considers the HEX composed of a number of control volumes depending on the refrigerant phase, so it is possible to have a maximum of three zones, corresponding to the superheated vapour, the subcooled liquid or the two-phase mixture. This approach is very attractive both for stationary or dynamical simulations; in the latter case, the volume of the zones becomes a state variable to describe the time evolution of each control volume, B. P. Rasmussen, 2012.

Since the lumped parameter approach relies on a rough approximation of the physical properties and HTCs, the other approaches

are better for two-phase flow in refrigeration applications. The finite volume technique was preferred in this work because it allows more framework flexibility and more accuracy in evaluating the HTCs. As a drawback, the finite volume can be more computationally intensive than the multi-region approach. Still, these limitations can be significantly reduced with proper precautions, as described by Pangborn et al., 2015. In the following, the finite volume model of a HEX for VCS applications is described, highlighting the main solutions adopted to reduce the computational loads and the numerical stiffness of the problem while guaranteeing a good accuracy of the solution.

#### FINITE VOLUME APPROACH 10.1

According to the finite volume technique, the volume of the heat exchangers is divided into a certain number of equally-sized control volumes, to which the governing equations (chapter 5) are applied. The numerical model is based on some assumptions presented in the next section.

### Basic assumptions 10.1.1

Despite the different arrangements employed in VCSs, in a HEX it is possible to make out a main direction in the flow of both working fluids. For the main flow path, it is reasonable to assume that the physical properties of both fluids and the heat transfer conditions are almost uniform in each section perpendicular to it. The HEX can therefore be modelled ad a series of one-dimensional finite volume. The main direction is that of the refrigerant. Different arrangements can be considered referencing the main refrigerant path; indeed, in the co-flow realization, the two fluids flow parallel in the same direction, and in the opposite direction for the counter-flow realization; finally, the two flows are perpendicular in cross-flow arrangements. Along the main direction in the control volume, the cross-sectional area is assumed constant for both fluids.

One-dimensional finite volume

In the HEX the contribution of gravitational forces are neglected. Indeed, for the case under consideration, the dimension of the HEX would lead to a non-significant contribution.

Gravitational forces

Moreover, thermal conduction is neglected, both along the fluid and through the wall elements, because the convective phenomena dominate the process.

Thermal conduction

Particular attention is devoted to the pressure losses due to friction. In general, this contribution may be more significant on the lowpressure side. Indeed, the pressure in the evaporator is about one

Friction pressure

order of magnitude lower than the condenser ones; since in the actual application the evaporation pressure is in the order of some bars, a pressure drop of some kilopascals is comparable with the measurement accuracy. Different approaches have been investigated to evaluate the pressure losses due to friction inside a finite volume model: the momentum equation can be included in the differential equations system, or the static pressure drop can be evaluated for each element leading to a Differential Algebraic system of Equation (DAE). In this context, Zhang et al., 2009 demonstrated that including the effects of momentum is not critical for large transient simulation but influences the instantaneous step change in mass flow regime, which is not of particular interest in this kind of application. Moreover, as pointed out by Desideri et al., 2016, a time scale observation can be made, given the low time constant characterizing the propagation of pressure throughout the heat exchanger compared to those related to mass and thermal energy transfer; for this reason, a static momentum balance can be assumed. To summary, to avoid increasing the complexity of the model and considering their effective contribution to the process, the pressure losses due to friction are neglected in this realization, and the pressure inside the HEX is assumed to be constant. Future works may integrate this effect.

#### Block interface 10.1.2

The HEX block function must interact with the other component of the VCS by means of inputs and outputs. As mentioned, the heat transfer conditions and the pressure levels are coupled, so the HEX model must evaluate them and provide them as outputs.

The inputs of the function block are:

Inputs

- refrigerant
  - refrigerant inlet mass flow rate
  - refrigerant outlet mass flow rate
  - refrigerant inlet temperature
- secondary fluid
  - mass flow rate
  - inlet temperature

The main outputs are the operating pressure and the outlet conditions of the working fluid; from these values, it is possible to evaluate the heat transfer rate.

# Development of the model equations

The governing equations presented in chapter 5 can be reformulated to be applied to each control volume for both working fluids.

A key aspect in setting up the finite volume scheme is the selection of the state variables. Indeed, the thermodynamic state of a fluid is fully defined by the knowledge of two intensive variables and an extensive one. In this case, the fluid volume in each element is known and time-invariant, so it is necessary to know the time evolution of two intensive variables. As suggested by B. P. Rasmussen and Shenoy, 2012 and Pangborn et al., 2015, pressure and specific enthalpy are chosen as state variables in this work.

State variables selection

A possible source of misconception is the difference between the boundary and the node values of a certain physical quantity; indeed in the governing equations both are needed. Regarding the state variables, pressure and enthalpy are the values averaged over the element corresponding to the node. More precisely, the pressure values are common to all the element nodes. Consequently, all the other physical quantities are an average element estimation. However, the balance equation also needs the boundary values of the quantities of interest. Since all elements are contiguous, the outlet conditions from the previous become the input for the next. So, where not directly specified by subscripts i for inlet and o for outlet, this discussion gives the boundary conditions for the outlet values expressed employing a superscript <sup>®</sup>.

Nodes and boundaries quantities

## Refrigerant side

Since all the elements are equivalent, the MASS BALANCE EQUATION mass conservation equation for the j-th element can be written as follows:

$$\frac{dm_{r,j}}{dt} = V_j \frac{d\rho_{r,j}}{dt} = \dot{m}_{r,i,j} - \dot{m}_{r,o,j} \tag{10.1} \label{eq:10.1}$$

According to the state variable chosen, the first term of eq. (10.1) is expanded as follows:

$$\frac{dm_{j}}{dt} = V_{j} \frac{d\rho_{j}}{dt} = V_{j} \left( \frac{\partial \rho_{j}}{\partial p} \Big|_{h} \frac{dp}{dt} + \left. \frac{\partial \rho_{j}}{\partial h_{j}} \right|_{p} \frac{dh_{j}}{dt} \right)$$
(10.2)

In the second term of the eq. (10.1) the comparison between the mass flow rate at the boundaries of each element can be expressed in terms of the value of the mass flow rate at the outlet boundary of each element  $\dot{\mathfrak{m}}_{r,j}^{\mathfrak{G}}$ . The final form of the refrigerant mass balance equation for each element is:

$$V_{j}\left(\frac{\partial \rho_{j}}{\partial p}\bigg|_{h}\frac{dp}{dt} + \frac{\partial \rho_{j}}{\partial h_{j}}\bigg|_{p}\frac{dh_{j}}{dt}\right) = \dot{m}_{r,j-1}^{\textcircled{\$}} - \dot{m}_{r,j}^{\textcircled{\$}}$$
(10.3)

ENERGY BALANCE EQUATION The energy balance for the refrigerant flowing throughout the j-th element can be written as follows (cfr eq. (5.3)):

$$\frac{dU_{r,j}}{dt} = \frac{d(m_j u_j)}{dt} = \dot{m}_{r,j-1}^{\text{\tiny \$}} h_{r,j-1}^{\text{\tiny \$}} - \dot{m}_{r,j}^{\text{\tiny \$}} h_{r,j}^{\text{\tiny \$}} + \dot{Q}_{r,j}$$
(10.4)

In the same way, the first term of the eq. (10.4) can be expanded according to the state variable chosen and employing the enthalpy definition:  $h \equiv u + \frac{p}{\varrho}$ .

$$\begin{split} \frac{d}{dt}(m_j u_j) &= m_j \frac{du_j}{dt} + u_j \frac{dm_j}{dt} \\ &= V_j \left( \rho_j \frac{du_j}{dt} + u_j \frac{d\rho_j}{dt} \right) \\ &= V_j \left[ \left( h_j - \frac{p}{\rho_j} \right) \frac{d\rho_j}{dt} + \rho_j \left( \frac{dh_j}{dt} - \frac{d(p/\rho_j)}{dt} \right) \right] \end{split}$$

Employing the quotient rule, eq. (10.4) after some algebraic manipulations leads to:

$$\frac{d}{dt}(m_{r,j}u_{r,j}) = V_j \left[ \frac{dp}{dt} \left( h_j \left. \frac{\partial \rho_j}{\partial p} \right|_h - 1 \right) + \frac{dh_j}{dt} \left( h_j \left. \frac{\partial \rho_j}{\partial h_j} \right|_p + \rho_j \right) \right]$$
 (10.5)

The energy balance equation for each element on the refrigerant side takes the final form:

$$V_{j} \left[ \frac{dp}{dt} \left( h_{j} \left. \frac{\partial \rho_{j}}{\partial p} \right|_{h} - 1 \right) + \frac{dh_{j}}{dt} \left( h_{j} \left. \frac{\partial \rho_{j}}{\partial h_{j}} \right|_{p} + \rho_{j} \right) \right] =$$

$$= \dot{m}_{r,j-1}^{\mathfrak{B}} h_{r,j-1}^{\mathfrak{B}} - \dot{m}_{r,j}^{\mathfrak{B}} h_{r,j}^{\mathfrak{B}} + \dot{Q}_{r,j}$$

$$(10.6)$$

# Secondary fluid

MASS BALANCE EQUATION According to the incompressible flow assumption, the mass balance reduces to the equality of the inlet and outlet flow rates. Indeed, there is no variation in the secondary fluid mass contained in each element.

$$\dot{\mathfrak{m}}_{s,j}^{\mathfrak{G}} = \dot{\mathfrak{m}}_{s} \qquad \forall j \tag{10.7}$$

**ENERGY BALANCE EQUATION** Considering that the secondary fluid pressure and temperature undergo small variations, it is possible to assume constant density and specific heat. So, the energy balance equation can be reformulated as follows.

$$\begin{split} \rho_s V_j \frac{d \mathfrak{u}_{s,j}}{dt} &= \rho_s c_{\mathfrak{p},s} V_j \frac{d T_{s,j}}{dt} = \dot{\mathfrak{m}}_s (h_{s,j-1}^{\scriptscriptstyle \textcircled{\tiny B}} - h_{s,j}^{\scriptscriptstyle \textcircled{\tiny B}}) + \dot{Q}_{s,j} \\ &= \dot{\mathfrak{m}}_s c_{\mathfrak{p},s} (T_{s,j-1}^{\scriptscriptstyle \textcircled{\tiny B}} - T_{s,j}^{\scriptscriptstyle \textcircled{\tiny B}}) + \dot{Q}_{s,j} \end{split} \tag{10.8}$$

This equation could be used in the scheme, but it would introduce an unnecessarily large number of state variables, while the heat transfer equation straightforwardly evaluates the temperature profile of the secondary fluid.

## HEX wall

**ENERGY BALANCE EQUATION** The mass of the HEX wall does not vary during normal operation, so only the evaluation of the wall's internal energy variation is needed. The HEX wall energy conservation for jth element is expressed by:

$$m_{w,j} \frac{du_{w,j}}{dt} = m_{w,j} c_{w,j} \frac{dT_{w,j}}{dt} = \dot{Q}_{\text{in},j} - \dot{Q}_{\text{out},j} = \dot{Q}_{s,j} - \dot{Q}_{r,j} \qquad \text{(10.9)}$$

#### SOLUTION SCHEMES 10.2

Starting from the above equations, the solution scheme of the HEX dynamical model is set up. The procedure described in the following is oriented to obtain an explicit formulation of the initial value problem represented in eq. (10.10), for the state variables p and  $h_{r,j}$ . In this way, the calculated time derivatives can be integrated with and explicit Ordinary Differential Equation (ODE) solver. For this purpose, the system of differential equations will be presented in matrix form. This formulation assumes that the system is linear, however the problem represented in eq. (10.10) is strongly non-linear, for two reasons: firstly the thermodynamic properties of the working fluid, density, enthalpy and pressure are related to one another by means of the state equation, which is a non-linear function; secondly, the right-hand side of eq. (10.10) entails the evaluation of heat transfer rate, which is a function of the thermodynamic conditions of the two working fluids in each element. The first source of non-linearities will be handled through the Lookup Table, which make a linear approximation of the state equation available. The other non-linearities will be treated by employing the value of the fluid properties from the previous time step for the calculation of the heat transfer rate in the right-hand side and for the evaluation of the boundary value of the refrigerant enthalpy  $h_{r,i}^{\text{(B)}}$ . In this way, the final form will be a linear system of ODEs, which can be brought to explicit form through matrix inversion.

Then, this first straightforward algorithm is integrated with some features to enhance the numerical stability, like a low pass filter applied to the mass flow rate. In both schemes the temperature profile of the secondary fluid at each time step is evaluated with the heat transfer equation discussed in section 10.4.

Finally, a version of the model in which the state variables are also associated to the secondary fluid temperature is presented.

#### First scheme 10.2.1

Equations (10.3), (10.6) and (10.9) are applied to each control volume; they are then rearranged with the known quantities on the right-hand side. Two independent systems can be written considering that the first refrigerant side differential equations are decoupled from the HEX wall energy balance equation.

$$\begin{cases} V_{j}\left(\frac{\partial\rho_{j}}{\partial p}\Big|_{h}\frac{dp}{dt}+\frac{\partial\rho_{j}}{\partial h_{j}}\Big|_{p}\frac{dh_{j}}{dt}\right)-\dot{m}_{r,j-1}^{\circledast}+\dot{m}_{r,j}^{\circledast}=0\\ V_{j}\left[\frac{dp}{dt}\left(h_{j}\frac{\partial\rho_{j}}{\partial p}\Big|_{h}-1\right)+\frac{dh_{j}}{dt}\left(h_{j}\frac{\partial\rho_{j}}{\partial h_{j}}\Big|_{p}+\rho_{j}\right)\right]\\ -\dot{m}_{r,j-1}^{\circledast}h_{r,j-1}^{\circledast}+\dot{m}_{r,j}^{\circledast}h_{r,j}^{\circledast}=\dot{Q}_{r,j}\\ m_{w,j}c_{w,j}\frac{dT_{w,j}}{dt}=C_{w,j}\frac{dT_{w,j}}{dt}=\dot{Q}_{s,j}-\dot{Q}_{r,j} \end{cases} \tag{10.10} \label{eq:10.10}$$

Where  $C_w$  is the thermal capacity of the HEX wall.

The differential equation systems are presented in matrix form, eq. (10.11), because it is useful for implementing them into Simulink<sup>®</sup>. Matrix form

$$Z_A X_A = F_A$$

$$Z_B X_B = F_B$$
(10.11)

Two column vectors gather the unknown for the refrigerant side  $X_A$ and the HEX wall  $X_B$ :

$$\mathbf{X}_{A} = \begin{bmatrix} \frac{dp}{dt} \\ \frac{dh_{r,j}}{dt} \\ \dot{m}_{r,j}^{\textcircled{b}} & (\forall j \in \{1,2,...,n\}) \\ \dot{m}_{r,j}^{\textcircled{b}} & (\forall j \in \{1,2,...,n-1\}) \end{bmatrix}$$
(10.12)

$$\mathbf{X}_{\mathrm{B}} = \begin{bmatrix} \frac{\mathrm{d}\mathsf{T}_{w,j}}{\mathrm{d}\mathsf{t}} & (\forall \mathsf{j} \in \{1,2,...,n\}) \end{bmatrix}$$
 (10.13)

Given a discretization in n elements, the system has 3n unknowns but only 2n + 1 state variables, which are the average pressure inside the HEX, the refrigerant enthalpy and the wall temperature for each element. The coefficient matrices can be expressed as a block matrix  $\mathbf{Z}_A$  2n × 2n and matrix  $\mathbf{Z}_B$  n × n. System A gathers the refrigerant's mass and energy balance equation, while system B accounts for the energy balance in the HEX wall.

The composition of matrix  $\mathbf{Z}_A$  is described in the following.

$$\mathbf{Z}_{A} = \begin{bmatrix} \mathbf{Z}(1,1) & \mathbf{Z}(1,2) & \mathbf{Z}(1,3) \\ \mathbf{Z}(2,1) & \mathbf{Z}(2,2) & \mathbf{Z}(2,3) \end{bmatrix}$$
(10.14)

where

$$\begin{split} & \boldsymbol{Z}_A \in \mathbb{R}^{2n \times 2n} \\ & \boldsymbol{Z}_A(1,1), \boldsymbol{Z}_A(2,1) \in \mathbb{R}^{n \times 1} \\ & \boldsymbol{Z}_A(1,2), \boldsymbol{Z}_A(2,2) \in \mathbb{R}^{n \times N} \\ & \boldsymbol{Z}_A(1,3), \boldsymbol{Z}_A(2,3) \in \mathbb{R}^{n \times (n-1)} \end{split}$$

The first row of the matrix **Z** corresponds to the refrigerant mass balance equations for all the elements. The block  $\mathbf{Z}_{A}(1,1)$  is column vector  $n \times 1$ .

$$\mathbf{Z}_{A}(1,1)_{j,1} = V_{j} \frac{\partial \rho_{r,j}}{\partial p} \Big|_{h} \quad \forall j \in \{1,2,...,n\}$$
 (10.15)

The block  $\mathbf{Z}_A(1,2)$  is a diagonal matrix  $n \times n$ .

$$\begin{split} & \boldsymbol{Z}_{A}(1,2)_{i,j} = 0 \quad \forall i \neq j \\ & \boldsymbol{Z}_{A}(1,2)_{i,j} = V_{j} \left. \frac{\partial \rho_{r,j}}{\partial h_{r,j}} \right|_{p} \quad \forall i,j \in \{1,2,...,n\} \end{split} \tag{10.16}$$

The block  $\mathbf{Z}_{A}(1,3)$  is a band rectangular matrix  $n \times n - 1$ 

$$\begin{split} & \textbf{Z}_{A}(1,3)_{i,j} = 0 \to j < i-1 \lor j > i \\ & \textbf{Z}_{A}(1,3)_{i,j} = 1 \to j = i \land j \in \{1,2,...,n-1\} \\ & \textbf{Z}_{A}(1,3)_{i,j} = -1 \to j = i-1 \land j \in \{1,2,...,n\} \end{split} \tag{10.17}$$

The second row of the matrix **Z** corresponds to the refrigerant energy balance equations for all the elements. The block  $\mathbf{Z}_{A}(2,1)$  is column vector  $n \times 1$ .

$$\mathbf{Z}_{A}(2,1)_{j,1} = V_{j} \left( h_{r,j} \left. \frac{\partial \rho_{r,j}}{\partial p} \right|_{h} - 1 \right) \quad \forall j \in \{1, 2, ..., n\}$$
 (10.18)

The block  $\mathbf{Z}_A(2,2)$  is a diagonal matrix  $n \times n$ .

$$\begin{split} & \boldsymbol{Z}_{A}(2,2)_{i,j} = \boldsymbol{0} \quad \forall i \neq j \\ & \boldsymbol{Z}_{A}(2,2)_{i,j} = V_{j} \left( h_{r,j} \left. \frac{\partial \rho_{r,j}}{\partial h_{r,j}} \right|_{p} + \rho_{r,j} \right) \quad \forall i,j \in \{1,2,...,n\} \end{split} \tag{10.19}$$

The block  $\mathbf{Z}_A(2,3)$  is a band rectangular matrix  $n \times n - 1$ 

$$\begin{split} & \textbf{Z}_{A}(2,3)_{i,j} = 0 \to j < i-1 \lor j > i \\ & \textbf{Z}_{A}(2,3)_{i,j} = h^{\text{\tiny \$}}_{r,j} \to j = i \land j \in \{1,2,...,n-1\} \\ & \textbf{Z}_{A}(2,3)_{i,j} = -h^{\text{\tiny \$}}_{r,j} \to j = i-1 \land j \in \{1,2,...,n\} \end{split} \tag{10.20}$$

The unknown vector is the concatenation of the derivatives of the state vector and the vector of the outlet mass flow rates.

$$\boldsymbol{X}_{A} = \begin{bmatrix} \frac{dp}{dt} & \frac{dh_{r,j}}{dt} & \dot{m}_{r,j}^{\textcircled{B}} \end{bmatrix}^{T}$$

Finally, the matrix  $\mathbf{Z}_{B}$  is a diagonal matrix  $n \times n$ .

$$\begin{split} & \mathbf{Z}_{B,i,j} = 0 \quad \forall i \neq j \\ & \mathbf{Z}_{B,i,j} = C_{w,j} \quad \forall i,j \in \{1,2,...,n\} \end{split} \tag{10.21}$$

The right-hand side of the system A is expressed in the following way, where the boundary conditions have already been implemented.

$$\begin{aligned} & \textbf{F}_{A,j,1} = \dot{m}_{r,in} & j = 1 \\ & \textbf{F}_{A,j,1} = 0 & \forall j \in \{2,...,n-1\} \\ & \textbf{F}_{A,j,1} = \dot{m}_{r,out} & j = n \\ & \textbf{F}_{A,j,1} = \dot{Q}_{r,j} + \dot{m}_{r,in} h_{r,in} & j = n+1 \\ & \textbf{F}_{A,j,1} = \dot{Q}_{r,j} & \forall j \in \{n+2,...,2n-1\} \\ & \textbf{F}_{A,j,1} = \dot{Q}_{r,j} - \dot{m}_{r,out} h_{r,out} & j = 2n \end{aligned}$$

The right-hand side of the system B is:

$$\mathbf{F}_{B,j,1} = \dot{Q}_{s,j} - \dot{Q}_{r,j} \quad \forall j \in \{1,2,...,n\}$$
 (10.23)

The two systems are reciprocally independent, so they are solved individually. The derivative of the state variables  $(P, h_{r,j}, T_{w,j})$  and the outlet mass flow rate  $\dot{\mathfrak{m}}_{r,j}^{\text{\tiny{\textcircled{B}}}}$  are evaluated at each time step by performing the matrix inversion.

$$\mathbf{X}_{\mathrm{A}} = \mathbf{Z}_{\mathrm{A}}^{-1} \mathbf{F}_{\mathrm{A}}$$

$$\mathbf{X}_{\mathrm{B}} = \mathbf{Z}_{\mathrm{B}}^{-1} \mathbf{F}_{\mathrm{B}}$$
(10.24)

The procedure described above leads to an explicit formulation of the initial value problem eq. (10.10), for the state variables p and  $h_{r,i}$ . In this way, the calculated time derivatives can be fed to an explicit ODE solver. However, the refrigerant enthalpy at the element boundary h<sub>ri</sub> is needed for the evaluation of the advection term in the second equation in eq. (10.10); this implies the knowledge of the value of h in the previous element according to the *upwind scheme* (eq. (10.20)), as will be discussed in the following section 10.5.1, eq. (10.20). To maintain the explicit form of the solution algorithm, the state vector of the refrigerant enthalpy in the previous time step is used to fill the matrix block  $\mathbf{Z}_{A}(2,3)$  (eq. (10.20)).

# Second scheme with mass flow rate filtering

A second scheme is developed to enhance the accuracy of the solution and reduce the calculation time. Indeed, according to Pangborn

et al., 2015, the introduction of a filter on the mass flow rate evaluation increases the robustness of the system A, because it reduces the conditioning number or the stiffness ratio of the matrix.

The low pass filter can be written in the Laplace domain in the following form:

$$\dot{\mathfrak{m}}_{f,r,j}^{\mathfrak{G}}(s) = \frac{1}{\mathsf{K}s+1}\dot{\mathfrak{m}}_{r,j}^{\mathfrak{G}}(s)$$
 (10.25)

Rearranging.

$$\dot{m}_{f,r,j}^{\text{\tiny (B)}}(s)Ks + \dot{m}_{f,r,j}^{\text{\tiny (B)}}(s) = \dot{m}_{r,j}^{\text{\tiny (B)}}(s)$$
 (10.26)

And coming back to the time domain.

$$K \frac{\dot{m}_{f,r,j}^{\oplus}}{dt} + \dot{m}_{f,r,j}^{\oplus} = \dot{m}_{r,j}^{\oplus}$$
 (10.27)

The matrix  $\mathbf{Z}_A$  can be rewritten in the following way by grouping the terms to highlight the state vector and the boundary mass flow vector.

$$\begin{cases} \mathbf{Z}_{A}(1,1)\frac{dp}{dt} + \mathbf{Z}_{A}(1,2)\frac{dh_{r,j}}{dt} + \mathbf{Z}_{A}(1,3)\dot{m}_{r,j}^{\textcircled{\$}} = \mathbf{F}_{A} \\ \mathbf{Z}_{A}(2,1)\frac{dp}{dt} + \mathbf{Z}_{A}(2,2)\frac{dh_{r,j}}{dt} + \mathbf{Z}_{A}(2,3)\dot{m}_{r,j}^{\textcircled{\$}} = \mathbf{F}_{B} \end{cases}$$
(10.28)

Equation (10.27) can be substituted into eq. (10.28), leading to a new problem formulation.

$$\begin{cases} \textbf{Z}_{A(1,1)} \frac{dp}{dt} + \textbf{Z}_{A(1,2)} \frac{dh_{r,j}}{dt} + \textbf{Z}_{A(1,3)} \frac{\dot{m}_{f,r,j}^{\textcircled{\textcircled{\$}}}}{dt} = \textbf{F}_{A} - \textbf{Z}_{A(1,3)} \dot{m}_{f,r,j}^{\textcircled{\textcircled{\$}}} \\ \textbf{Z}_{A(2,1)} \frac{dp}{dt} + \textbf{Z}_{A(2,2)} \frac{dh_{r,j}}{dt} + \textbf{Z}_{A(2,3)} \frac{\dot{m}_{f,r,j}^{\textcircled{\textcircled{\$}}}}{dt} = \textbf{F}_{B} - \textbf{Z}_{A(2,3)} \dot{m}_{f,r,j}^{\textcircled{\textcircled{\$}}} \end{cases}$$
 (10.29)

In a form ateq. (10.29) the number of state variables of the problem increases to 3N but with a suitable selection of the tuning parameter  $\tau_{\rm m}$  is possible to reduce the stiffness ratio of the matrix  ${\bf Z}_{\rm A}$ , leading to a more robust solution. Indeed, as described in the next, section 10.3, the matrix  $\mathbf{Z}_{A}$  is characterized by eigenvalues which differ by many orders of magnitude; this leads to numerical problems. The filter reduces the time constant of the mass flow rate eigenvalues, reducing the final matrix stiffness ratio and enhancing the accuracy and stability of the solution. A suitable value for the time constant relaxation is found for this application  $\tau_m$ =0.01 s. The filtered mass flow rate  $\dot{\mathfrak{m}}_{f,r,j}^{\mathfrak{B}}$  is employed in the remaining part of the model instead of the unfiltered one.

# Third scheme with secondary fluid states

A third scheme is proposed, in which the secondary fluid temperatures for each element are treated as state variable. The energy balance equation for secondary fluid eq. (10.8) can be added to the first resolution scheme eq. (10.10), leading to a new system eq. (10.30).

$$\begin{cases} V_{j}\left(\frac{\partial\rho_{j}}{\partial p}\Big|_{h}\frac{dp}{dt}+\frac{\partial\rho_{j}}{\partial h_{j}}\Big|_{p}\frac{dh_{j}}{dt}\right)-\dot{m}_{r,j-1}^{\textcircled{\$}}+\dot{m}_{r,j}^{\textcircled{\$}}=0\\ V_{j}\left[\frac{dp}{dt}\left(h_{j}\frac{\partial\rho_{j}}{\partial p}\Big|_{h}-1\right)+\frac{dh_{j}}{dt}\left(h_{j}\frac{\partial\rho_{j}}{\partial h_{j}}\Big|_{p}+\rho_{j}\right)\right]\\ -\dot{m}_{r,j-1}^{\textcircled{\$}}h_{r,j-1}^{\textcircled{\$}}+\dot{m}_{r,j}^{\textcircled{\$}}h_{r,j}^{\textcircled{\$}}=\dot{Q}_{r,j}\\ m_{w,j}c_{w,j}\frac{dT_{w,j}}{dt}=C_{w,j}\frac{dT_{w,j}}{dt}=\dot{Q}_{s,j}-\dot{Q}_{r,j}\\ \rho_{s}c_{p,s}V_{j}\frac{dT_{s,j}}{dt}=\dot{m}_{s}c_{p,s}(T_{s,j-1}^{\textcircled{\$}}-T_{s,j}^{\textcircled{\$}})+\dot{Q}_{s,j} \end{cases} \tag{10.30}$$

Equation (10.30) can be expressed in a matrix form.

$$\mathbf{Z}_{A}\mathbf{X}_{A} = \mathbf{F}_{A}$$
 $\mathbf{Z}_{B}\mathbf{X}_{B} = \mathbf{F}_{B}$ 
 $\mathbf{Z}_{C}\mathbf{X}_{C} = \mathbf{F}_{C}$ 
(10.31)

Matrix  $\mathbf{Z}_{C}$  is a diagonal matrix  $n \times n$ .

$$\begin{split} & \boldsymbol{Z}_{C,i,j} = \boldsymbol{0} \quad \forall i \neq j \\ & \boldsymbol{Z}_{C,i,j} = \rho_s c_{p,s} V_j \quad \forall i,j \in \{1,2,...,n\} \end{split} \tag{10.32}$$

The right hand side  $\mathbf{F}_C$  for the system C is

$$F_{C,j,1} = \dot{m}_s c_{p,s} (T_{s,j-1}^{\text{(1)}} - T_{s,j}^{\text{(1)}}) + \dot{Q}_{s,j} \quad \forall j \in \{1,2,...,n\} \tag{10.33}$$

As for the first and second scheme, the systems A, B and C, are independent.

The energy balance equation for the secondary fluid, eq. (10.8), implies the evaluation of the temperature at the boundary of each element; this may result in numerical issues, see section 10.5.1.

## EIGENVALUES ANALYSIS 10.3

Analysing the eigenvalues of the inverse matrix  $\mathbf{Z}_{A}^{-1}$  could contribute more information about the system dynamic. If the system matrix is diagonal, the state vector and the eigenvalue vector are directly matched, so it is straightforward to evaluate the contribution of each state to the whole system. However, the matrix  $\mathbf{Z}_A$  in the form presented above is quite different from the diagonal matrix, but with simple manipulations, the blocks can be rearranged to achieve a more diagonal distribution of the non-zero elements in the matrix. Indeed, eq. (10.29) can be rewritten as eq. (10.34), by changing the position of the pressure derivatives.

$$\begin{cases} Z_{A(1,2)} \frac{dh_{r,j}}{dt} + Z_{A(1,1)} \frac{dp}{dt} + Z_{A(1,3)} \frac{\dot{m}_{f,r,j}^{\textcircled{\$}}}{dt} = F_A - Z_{A(1,3)} \dot{m}_{f,r,j}^{\textcircled{\$}} \\ Z_{A(2,2)} \frac{dh_{r,j}}{dt} + Z_{A(2,1)} \frac{dp}{dt} + Z_{A(2,3)} \frac{\dot{m}_{f,r,j}^{\textcircled{\$}}}{dt} = F_B - Z_{A(2,3)} \dot{m}_{f,r,j}^{\textcircled{\$}} \end{cases}$$
(10.34)

A new matrix  $\mathbf{Z}'_A$  is introduced having the following structure.

$$\mathbf{Z}_{A}' = \begin{bmatrix} \mathbf{Z}_{A}(1,2) & \mathbf{Z}_{A}(1,1) & \mathbf{Z}_{A}(1,3) \\ \mathbf{Z}_{A}(2,2) & \mathbf{Z}_{A}(2,1) & \mathbf{Z}_{A}(2,3) \end{bmatrix}$$
(10.35)

and the new unknown vector

$$\mathbf{X}_{A}' = \begin{bmatrix} \frac{d\mathbf{h}_{r,j}}{dt} & \frac{d\mathbf{p}}{dt} & \dot{\mathbf{m}}_{r,j}^{\oplus} \end{bmatrix}^{\mathsf{I}}$$
 (10.36)

In this way, the eigenvalues of the inverse matrix of  $\mathbf{Z}'_{A}$  correspond more directly to the state variable vector.

The analysis of the eigenvalues applies only to linear or linearized systems of differential equations. In the present case, the system A is linear, even if the model is fully non-linear. It is the relation between the state variables and the transport phenomena that is responsible for the non-linearity of the model. As discussed above, these non-linearities are hidden in the matrix formulation implemented in Simulink<sup>®</sup>, eq. (10.11), by linearizing the state equation through the Lookup Table and employing the heat transfer calculation from the previous time step.

The numerical considerations on matrices  $\mathbf{Z}_A$  and  $\mathbf{Z}_B$  are carried out employing the first 200s of the measurement date related to Test 1 with R<sub>450</sub>A. As to matrix  $\mathbf{Z}_A$ , it is possible to appreciate that all the eigenvalues are negative except for the (n+1)-th which corresponds to the pressure dynamics. The first n eigenvalues correspond to the refrigerant enthalpy dynamics and have an order of magnitude of 10<sup>6</sup>, while the last (n-1), which correspond to the mass flow rate, are of the order of  $10^{-6}$ ; finally, the pressure eigenvalue, the (n+1)-th has an order of magnitude of 10<sup>1</sup>. This observation supports the statement that the system is driven by dynamics with very different time scales, leading to a ill conditioned system matrix. The dynamics related to the mass flow rate are slower than the thermal dynamics by several orders of magnitude. This has no a direct physical interpretation; indeed, the dynamic behaviour of the heat transfer rate is coupled with that of the refrigerant flow rate due to non-linearities. Still, this fact can be used for numerical purposes. In this context, the lowpass filter on the mass flow rate introduces a new dynamic that can be increased to approach the thermal dynamic. However, there is a suitable range of the time constant  $\tau_m$  to avoid numerical failure of the solution. In this work it was found that it can range between 100 and

Non-linearity disclaimer

Evaluation of the order of magnitude of the eigenvalues

0.01 second. The minimum stiffness is achieved with the lowest value of  $\tau_m$ , while employing higher values the mass flow rate dynamics is slowed allowing the application of larger integration time steps to achieve the prescribed accuracy. The matrix  $\mathbf{Z}_{\mathrm{R}}^{-1}$  is a square diagonal matrix, so the eigenvalues correspond to the values on the diagonal; they are positive and in the order of magnitude of  $10^{-3}$ .

From the point of view of the solver, the fastest dynamics influence the integration time step, needed to reach the prescribed accuracy. In this case, the smallest time constant is related to the specific enthalpy of the element. With a suitable filter, the corresponding time constant can be increased and, subsequently, the time step required, but introducing the filter would break the linear form of  $\mathbf{Z}_A$ .

## 10.4 HEAT TRANSFER RATE

The heat transfer rate between the HEX wall and the fluids can be estimated in two ways: assuming a linear or an exponential profile of the temperature of the working fluid. In both cases, the portion of HEX wall contained in the heat exchangers is considered to be at constant temperature corresponding to that of the node. The first method employs the mean temperature of the fluid in the element.

$$\dot{\mathbf{Q}}_{\mathbf{j}} = \alpha_{\mathbf{j}} \mathbf{A}_{\mathbf{j}} (\mathsf{T}_{w,\mathbf{j}} - \mathsf{T}_{\mathbf{j}}) \tag{10.37}$$

The second approach takes into account the temperature profile along the element, according to the procedure presented in appendix A

$$\mathsf{T}_{j}^{\text{\tiny{(b)}}} = \mathsf{T}_{w,j} - (\mathsf{T}_{j-1}^{\text{\tiny{(b)}}} - \mathsf{T}_{w,j})e^{-\mathsf{NTU}_{j}} \tag{10.38}$$

$$\dot{Q}_{j} = \dot{m}_{j} c_{p,j} [(T_{w,j} - T_{j-1}^{\text{\tiny (B)}})(1 - e^{-NTU_{j}})]$$
 (10.39)

The first approach is mandatory for the refrigerant in the two-phase zone because the fluid's thermal capacity is undefined during phase change. However, it can be also employed in the case of single-phase flow; indeed, if the temperature difference undergone by the working fluid is less than 50% of the available temperature difference between the incoming fluid and the wall, the error in the evaluation of the heat transfer rate employing the mean temperature is less than 5%, see appendix A. Moreover, the smaller the grid element, the more accurate the linear profile approximation will be. Equation (10.37) can be used to calculate the heat transfer rate, but some inaccuracies may be experienced when the fluid temperature approaches the wall temperature. This occurs near the outlet section of the HEX, in particular in counterflow arrangement; this corresponds to the subcooled zone of the condenser and to the superheated zone of the evaporator. The linear approximation is employed for the whole refrigerant flow without

distinguishing between two-phase and single-phase. The introduction of a distinct approach for the different refrigerant phases has been considered. Indeed, the block function for calculating the refrigerant side heat transfer rate realized by combining the linear profile in two-phase conditions and the exponential in single phase is cursorily tested. It did not increase the accuracy of the outlet temperature significantly in the test performed, it added a bit of numerical oscillation instead, which was due to the exponential form.

Combined mode for refrigerant heat transfer rate estimation

Conversely, the exponential profile is employed to evaluate the secondary fluid heat transfer rate in the first and second-resolution schemes. This ensures more accuracy even when the temperature of the fluid approaches that of the wall. A possible drawback is that the exponential profile needs a smaller integration time step due to the exponential relations.

Exponential profile for the secondary

Since the third scheme makes the node value of the temperature of the secondary fluid at each time step available, eq. (10.37) can be employed straightforwardly. In this scheme the evaluation of the outlet temperature of the secondary fluid can be realised assuming a linear profile. However, when the fluid approaches the wall temperature, the linear approximation could lead to an inaccurate estimation. Moreover, by employing the linear profile in a dynamic simulation, the temperature in each element can fluctuate around the real value leading to undesirables oscillations of the solution. On the other hand, the temperature should be evaluated assuming an exponential profile, but this implies an increased complexity of the code. In conclusion, the numerical instability due to the gradient reconstruction at the outlet section could be a source of inaccuracies to take into consideration. In this work, these sources of inaccuracies related to the linear profile assumption at the outlet section have been contained through appropriate definition of the integration time step and the spatial discretisation, as described in chapter 11.

To evaluate the heat transfer rate, it is necessary to estimate the HTC ( $\alpha$ ) by employing suitable correlations, as discussed next.

#### Correlations for the heat transfer coefficients 10.4.1

Estimating the convective HTC plays a key role in the model. The evaluation of the HTC is performed employing correlations developed from experimental data regression for that particular arrangement. The first criterion for selecting the correlation is thus the HEX configuration under investigation. The HTC correlation must consider the working fluid and the particular flow condition (single phase: gas/vapour or liquid; two-phase: boiling or condensing). Finally, the correlations are developed for a particular flow regime range defined by the Prandtl

and Reynolds numbers. Indeed, the general form of the correlation for forced convection is: Nu = f(Re, Pr).

A general assessment of the correlation available for fluid flow in Brazed Plate Heat Exchanger (BPHEX) can be found in García-Cascales et al., 2007 and Roberti, 2020. For single-phase flow, two correlations are tested in this work, those by Martin, 1996 and Y. Kim, 1999. The latter is preferred because it is less prone to numerical issues due to its simpler form; indeed, the presence of the evaluation of the viscosity at the wall temperature, in the Martin correlation, could become a source of instabilities and lead to unreliable results. For this reason, the suggestion of Y. Kim is employed for both refrigerant and water (mixture of water and glycol ethylene in the evaporator).

HTC correlations

Two-phase flow is dominant in this kind of application; for both the evaporator and condenser, the correlations developed by the Longo, Righetti, and Zilio group, who devoted many efforts to the investigation of refrigerant flow in BPHEX, are employed.

The correlations used are listed in more detail in appendix A.

## IMPLEMENTATION 10.5

This section provides some technical details about model implementation; the solutions adopted are discussed and motivated.

#### Boundary values 10.5.1

Knowing the value of a quantity in the grid node at each time step from the solution of the system differential equations, the boundary value can be estimated through *gradient reconstruction*. The simplest way to achieve this goal is to assume a linear profile of the physical quantity inside the element.

The boundary values needed in this model are:

- refrigerant mass flow rate at the outlet section of each element  $\mathfrak{m}_{\mathrm{r,i}}^{\mathbb{B}};$
- enthalpy of the refrigerant at outlet section of each element h<sup>®</sup><sub>r,i</sub>;
- temperature of the secondary fluid at the outlet section of each element  $T_{s,i}^{\oplus}$  (third scheme).

The mass flow rate at the element outlet is calculated directly with the inversion of matrix  $\mathbf{Z}_A$ . Then, the node value of the refrigerant mass flow rate can be evaluated assuming a linear profile:

$$\dot{\mathbf{m}}_{r,j} = \frac{\dot{\mathbf{m}}_{r,j-1}^{\oplus} + \dot{\mathbf{m}}_{r,j}^{\oplus}}{2}$$
 (10.40)

The element mass flow rate  $\dot{\mathfrak{m}}_{r,j}$  is employed for the local HTC evaluation on the refrigerant side.

The specific enthalpy of the refrigerant at the boundary is needed to for the energy balance (eq. (10.10)), but only the node enthalpy averaged over the element is known from the integration of the state variables. It is possible to compute the boundary enthalpy assuming a linear profile along the flow path. For the refrigerant enthalpy at the boundary:

$$h_{r,j}^{\oplus} = \frac{h_{r,j} + h_{r,j+1}}{2} \tag{10.41}$$

However, as highlighted by Pangborn et al., 2015, this leads to instability in the coefficient matrix and slows the simulation. Indeed, this approach for the calculation of the enthalpy at the boundary is nothing but a centred scheme; however, it has been proved that numerical issues involving advection terms requires discretisation with an upwind scheme to ensure convergence. For this reason, in this work an upwind scheme of the first order is employed, so the boundary value of the refrigerant enthalpy is assumed equal to the node value of the upstream element.

The same remarks can be made for the temperature of the secondary fluid in the third scheme proposed, eq. (10.30); in this case, the node temperature derives from the integration of the ODE, while its boundary value is calculated through an upwind scheme. In the other schemes the temperature profile of the secondary fluid is fully determined by the solution of the heat transfer equation; in this way, the values at the boundary are determined, and the corresponding node values are obtained assuming a linear profile.

$$T_{s,j} = \frac{T_{s,j}^{\oplus} + T_{s,j+1}^{\oplus}}{2}$$
 (10.42)

## Initial conditions

To solve the system of differential equations presented above, the initial condition for the state variables must be provided, i.e. average pressure, refrigerant enthalpy, and wall temperature for each element; in the third resolution scheme, also the secondary fluid temperature profile must be provided as an initial condition. Two possible ways can be undertaken to provide all the initial conditions.

The first assumes that the initial condition for the model corresponds to a condition of the machine off in stationary equilibrium. In this case, the temperature of the refrigerant in the HEX is equal to that of the secondary fluid. The mass flow rate of both fluids is null. Is necessary to assume the amount of refrigerant in the circuit.

In the second approach, the initial condition of the numerical simulation corresponds to an actual operating point for which mea-

surements are available. In this initial point, the inputs and the outputs are known. Starting from the inlet section, each element's stationary refrigerant energy balance is evaluated in sequence. Once evaluated, the profile of the characteristic physical variable (enthalpy and temperature of the refrigerant and temperature of the secondary fluid and of the HEX wall) can initialise the dynamical system. This algorithm is gathered in a script, which must be executed before the simulation starts.

In order to reduce the tuning time, a possible shortcut is tested. If the initial conditions or the tuning parameter related to the HTC or the flow rate through the compressor or the valve are not perfectly determined, is possible to ensure the initial pressure condition introduced during the first seconds of the simulation through a pipe block that simulates fictitious back pressure at the HEX outlet section. This guarantees an accurate matching of the initial conditions. Nevertheless, this operating point does not correspond to the stable point because the model configuration does not support it; so, at the first disturbance, the model returns to a more stable operating point. For these reasons, this initializing method has proven inaccurate and will no longer be used in the following.

# 10.5.3 Zones extension

The evaluation of the refrigerant phase in each element is useful for applying the suitable HTC correlation. The classification is made by comparing the average element enthalpy to the value of the enthalpy on the saturation curve corresponding to the actual pressure.

Zone extension estimation

$$\begin{array}{ll} h_{r,j} > h_{r,\nu} & \text{superheated} \\ h_{r,j} < h_{r,l} & \text{subcooled} \\ h_{r,l} \leqslant hr, j \leqslant h_{r,\nu} & \text{two-phase} \end{array}$$

#### HTC calculation tricks 10.5.4

On the secondary fluid side,, the flow conditions do not vary abruptly along the flow path, so the HTC does not undergo significant changes from one element to the next. It is possible to employ an averaged value of the HTC, for all the elements, allowing a unique calculation at each time step and reducing the computational cost of the model.

Average HTC on the secondary fluid side

On the other hand, the refrigerant undergoes a phase change during the process, so the physical properties and the heat transfer condition vary considerably along the flow path. The HTC increases by one order of magnitude, moving from the single-phase to the two-phase zone. This implies a sudden variation of the coefficients in the vectors  $\mathbf{F}_{A}$  and  $\mathbf{F}_{B}$ , leading to numerical instabilities. To overcome this issue,

HTC calculation: Lookup table vs direct function call

Pangborn et al., 2015 proposed to smooth the sharpness of the profile of the HTCs along the flow path by employing a filtered data table that collects pre-calculated values evaluated in a feasible operating range. A first attempt was made following this approach, but some drawbacks were observable. First, a multi-dimensional array that gathers the feasible values of HTC must be pre-calculated, likewise for the physical properties, chapter 4. Conversely, the form of the available correlations implies many parameters that vary in the operating range. For this reason, the process for creating the HTC table is prone to errors, hardly detectable. The pre-calculated table is not apt at testing different correlations, because it is necessary to recalculate the table with each change and often modify the corresponding script. Finally, the stability enhancement obtainable with the HTC filtering can be reached by employing the filtered mass flow rate or even the value averaged over all the elements, leading to good stability without losing accuracy. In this realization, the correlation is therefore directly calculated in the model by means of Matlab function available in the Simulink® environment. Following the suggestion of Pangborn et al., 2015, the vector with the HTC values for the refrigerant side is smoothed in order to enhance the stability of the model and avoid oscillations of the enthalpy profile along the flow path in the HEX. This spatial filter has proved more useful when the single and two-phase HTC differs significantly. More in detail, some lines of code added at the end of the Matlab function that calculates the HTC correlations, implement a moving window filter, seen in listing 1. The moving window has a size of 5 elements in the tests performed.

```
function filtered = movingMeanFilter(inputVector, windowSize)
    % inputVector: the original data vector to be filtered
    % windowSize: size of the moving window (odd or even)
    \% Initialize the output vector
    filtered = zeros(size(inputVector));
    % Define half window size
8
    halfWindow = floor (windowSize / 2);
9
   % Iterate over the input vector and apply the moving mean filter
11
    for i = 1:length(inputVector)
12
   % Define the window range
13
    startIdx = max(1, i - halfWindow); % Ensure we stay within bounds
   endIdx = min(length(inputVector), i + halfWindow); % Ensure we stay
15
      within bounds
16
   % Apply the mean to the values in the window
17
    filtered(i) = mean(inputVector(startIdx:endIdx));
18
    end
19
```

**Listing 1:** Spatial moving average filter implemented for HTC calcualtion in the Simulink® HEX model

The boiling correlation proposed by Longo, Mancin, et al., 2015 relies on that developed by Gorenflo, 1993 for pool boiling: this implies that the HTC is evaluated comparing with its reference values

Longo, Mancin, et al. reference values

 $\alpha_0$  which is obtained in specific operating conditions in terms of specific heat transfer rate q and wall roughness. Since this value is not available for all the newest refrigerants, the value available R134A  $\alpha_0 = 4200 \text{ kW m}^{-2} \text{ K}^{-1}$  is assumed as a guess value.

#### 10.5.5 Outlet conditions

The model allows the evaluation of the physical quantities at the node of each grid element. To evaluate the refrigerant condition at the outlet section of the HEX, a linear profile is assumed, as discussed in section 10.4. A linear extrapolation allows the determination of the refrigerant outlet conditions, temperature  $T_{r,out}$ , enthalpy  $h_{r,out}$ , vapour quality  $x_{out}$  and density  $\rho_{r,out}$ .

In the case of a counterflow arrangement, a possible source of instabilities must be avoided. Indeed, since the outlet refrigerant temperature approaches that of the secondary fluid at the inlet, the temperature difference between the working fluids in the subcooled zone allows a considerable heat transfer for each element. This situation is prone to numerical instabilities due to the variation in the number of elements attributed to each zone. Indeed, the variation in the length of the subcooled zone of only one element leads to a noticeable modification of the refrigerant outlet temperature. This value will be given as input at the next time step, and the operating conditions may vary just enough to produce an opposite modification of the outlet temperature from the previous step. This mechanism degenerates into an oscillating behaviour around the actual values. This oscillation can even propagate to quantities like the HEX pressure. To avoid this undesirable behaviour the straightforward way is to increase the grid refinement with a greater number of elements. On the other hand, this measure increases the stiffness of the numerical problem and requires smaller integration time steps, leading to longer run time. To overcome this issue, a running mean could be applied to the output temperature, if the time and spatial steps should be increased to speed up the simulation (according to the other constraints due to the numerical problem). The running mean can be calculated employing the values from a fixed number of previous time steps. The test shows the possibility of avoiding the implementation of a running mean function block on the outlet temperature with a  $\Delta t = 0.01$  s, accepting some minor oscillations of the calculated values.

A similar problem arises at the outlet section of the secondary fluid. In this case, the temperature is not evaluated by a linear profile, but employing the exponential one, as discussed in section 10.4, so the boundary values are directly calculated for each element and, subsequently, the outlet temperature. However, in this case, oscillations may set in due to the exponential form and the grid refinement. LikeOutlet temperature oscillations

Running mean correction

wise for the outlet refrigerant temperature, the moving average, could reduce the oscillations without increasing the number of elements. However, also in this case is possible to avoid this measure with a  $\Delta t$  = 0.01 s, accepting some limited oscillations.

# 10.5.6 Integration time step

The integration time step influences considerably the stability of the solution; it is correlated with the spatial discretisation employed. As briefly discussed above, the upwind scheme is required to ensure stability of advection problems. Without going into details, the von Neumann analysis demonstrates that the time step needed for the stability of the solution of Partial Differential Equations (PDEs) must satisfy a condition connected to the spatial step size and the transport velocity. In this work, the time step is chosen to ensure the compatibility of the model with the real-time control applications, and in this condition the effect of the spatial discretisation is investigated, as discussed in chapter 11.

## 10.6 REALIZATION

In fig. 54, the Simulink® code for the condenser is represented. The core of the model is the Matlab Function that calculates the derivatives of the state variables at each time step by inverting the system matrix. Starting from pressure and specific enthalpy values for each element, some blocks evaluate the refrigerant physical properties throughout Lookup Table and the extension of the zone occupied by superheated vapour, two-phase mixture or subcooled liquid. This information is employed to evaluate the heat transfer coefficient and the heat transfer rate for the refrigerant. For the secondary fluid, the average HTC is adopted for calculating the temperature profile and heat transfer rate. Finally, the outlet conditions of the refrigerant and the integral value of the heat transfer rate for both sides of the HEX are computed.

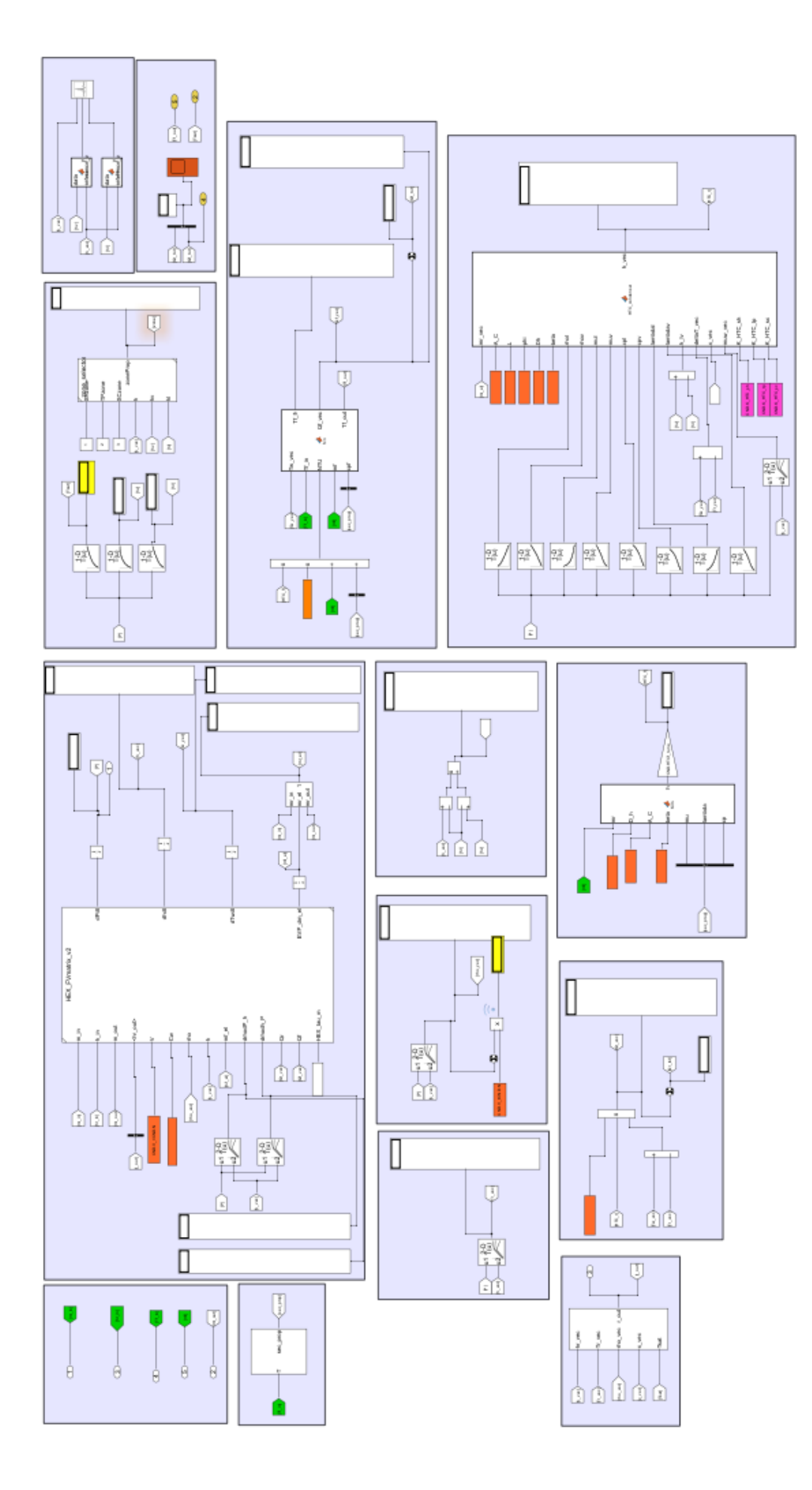


Figure 54: Scheme of the  $Simulink^{\otimes}$  code of the condenser.

# 11 | FULL MACHINE SIMULATION

## 11.1 NUMERICAL SETUP

In Simulink<sup>®</sup> it is possible to realize a numerical model of the actual VCS in the experimental facility setup. Two different realizations are developed; the first considers the four main components (compressor, expansion valve, evaporator and condenser); the latter also includes the two accumulation devices (LR and SA) and the connecting pipes.

Figure 55 shows the first numerical model realized in Simulink<sup>®</sup>, called Simplified Model. Each block corresponds to one of the four main components, which are connected by means of the inputs and outputs. The physical model of the compressor is employed. The dynamical correction is applied to the refrigerant outlet temperature in order to better capture the transient behaviour, see section 6.4.4. The expansion valve block is coupled with the corresponding controller, which can define the valve opening to follow the desired value of the superheating at the evaporator outlet. Currently, this controller has a proportional response to the deviation from the target. More advanced controllers can be implemented in this block to simulate the PID controller employed in the electronic expansion valve drivers or the thermostatic head of mechanically actuated valves. The two heat exchanger blocks have a very similar layout; the only differences are related to the evaluation of the heat transfer coefficients. In fact, the different correlations employed for the two-phase zone entails the calculation of different auxiliary quantities (for example, the heat flux for each element in the evaporator).

The second numerical model, called Full Model, includes also the accumulators, as presented in fig. 56. As discussed in chapter 7, the vessel are connected to the corresponding HEX by means of a pipe, which accounts for the evaluation of the mass flow rate between them. The condenser is connected to the LR through a pipe, likewise the evaporator and the SA. The pipes for the liquid line have a smaller diameter than that of the vapour line, as described in section 3.1. The valve is placed downstream of the LR, while the compressor is directly after the SA. Although its contribution is very small, particularly for the vapour line, the height difference between the vessel and the upstream HEX is accounted for.

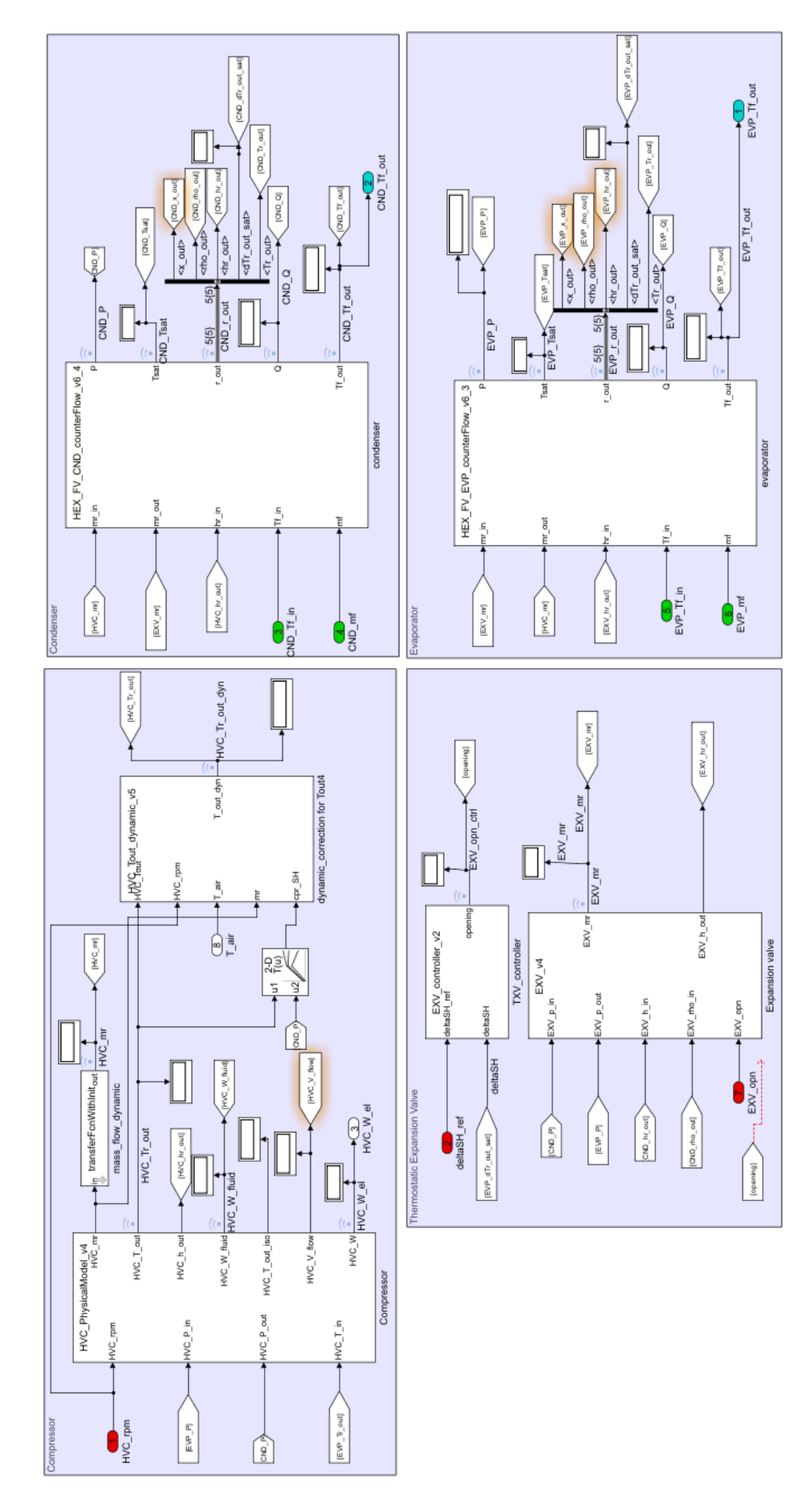


Figure 55: Scheme of the Simulink® code of the full VCS model composed by compressor, expansion valve, condenser and evaporator.

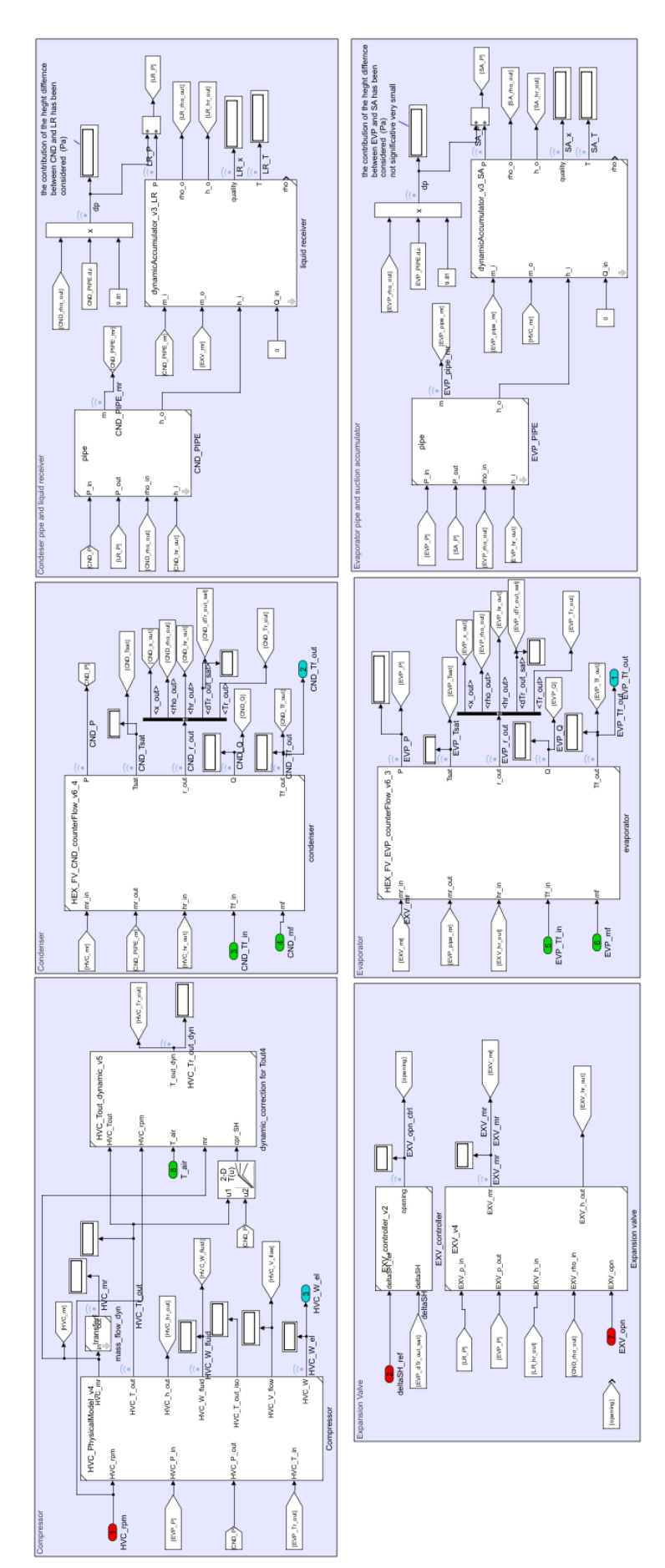


Figure 56: Scheme of the Simulink® code of the full VCS model composed by compressor, expansion valve, condenser, evaporator, LR and SA with the corresponding pipes.

## Basic configuration 11.1.1

The basic configuration of the simulation carried out is defined according to the goal of numerical robustness of the model to be easily employed in large systems for control purposes.

Unless stated otherwise, the fixed step solver in the Simulink® environment ode3 is used during the simulation execution. The integration step size is fixed to  $\Delta t = 0.01 \text{ s}$ .

### EFFECT OF THE NUMBER OF ELEMENTS 11.2

The effect of grid refinement is investigated using the first numerical set up, i.e. the Simplified Model. These tests are performed without applying any correction to the HTCs for both fluids and using as benchmark the experimental data from Test 2 with R450A.

The effect of grid refinement on the condenser pressure is shown in figs. 57 to 59; the test were realized with a grid of 20, 30 and 40 elements respectively. In all cases, the trend is well captured, with a maximum deviation 1 of the order of the 40 kPa, with the 20 elements grid. This is still acceptable, considering that the accuracy of the pressure measurements in the hot branch is  $\pm$  10 kPa. Moreover, considering the phenomenon from the temperature point of view, a deviation of about 20 kPa in pressure results in a difference of less than 1 °C in the saturation temperature estimation, as can be appreciated in fig. 60, where 30 elements are employed.

Steady state deviation

Condenser

pressure

Another aspect to evaluate is that the deviation of the pressure before and after the compressor speed variation is not the same in all cases; indeed, only with 30 and 40 elements the pressure difference stands at the same level before and after the transient. This effect testifies that the numerical accuracy of the model is related to the grid refinement. Indeed, with too few elements, the condenser model is imprecise in estimating the steady state point. From the evaluation of the zone length, the HTCs, the heat transfer rate and the contained refrigerant mass are derived. Given the high density and thermal capacity in the liquid phase, a variation of only one element attributed to this zone can considerably change the operating point of the condenser. For this reason, this model is sensitive to the grid refinement, which allows more accuracy in estimating the HEX portion occupied by each refrigerant phase. The work of Bendapudi et al., 2005 corroborates this consideration: the Authors states that with less than 15 elements the finite volume model of the HEX is inaccurate in capturing the steady

<sup>&</sup>lt;sup>1</sup> For what concerns the pressure estimation, the deviation of the calculated values from the experimental data is computed with reference to the experimental mean value between the inlet and the outlet

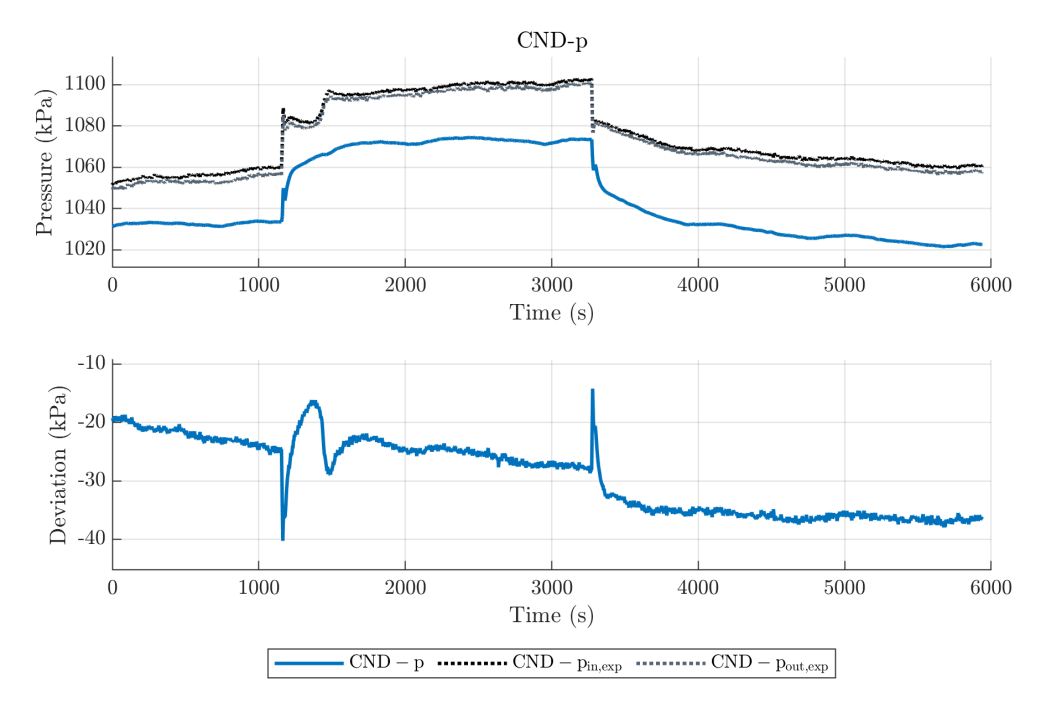


Figure 57: Condenser pressure: Simplified Model, Test 2 with R450A, HEX model with 20 elements.

state behaviour. Comparing figs. 58 and 59, it can be appreciated that increasing the number of elements leads to a reduction of the pressure deviation in steady state operation of about 10 kPa. This can guide the selection of a more refined grid. However, other aspects should be considered.

Estimating the secondary fluid outlet temperature is even more sensitive to grid refinement but in the opposite way than pressure. Indeed, from the figs. 61 and 62, obtained with the same test conditions Test 2 with R450A, but with 30 and 40 elements respectively, it can be concluded that the more refined grid leads to instability in the calculations. The behaviour is caused by a wrong selection of the integration time step which is not compatible with the spatial step of the grid. To avoid the occurrence of the behaviour shown in fig. 62, an integration time step below  $\Delta t = 0.01$  s would be necessary, but this would be inconsistent with a real-time simulation.

Similar conclusions can be drawn from the analysis of the refrigerant temperature at the condenser outlet, figs. 63 and 64. In this case oscillations are not present, but a deviation of the steady state behaviour with an increased number of elements is evident.

The analysis above leads to conclude that a suitable trade-off between accuracy and stability of the quantities predicted by the condenser model can be achieved with 30 equally sized elements.

The evaporator model shows a different trend relative to the grid refinement. The investigation of the grid dependence of the evaporator pressure with the different discretization of the HEX model equations Condenser water outlet temperature instability

Refrigerant temperature at the condenser outlet

**Evaporator** pressure

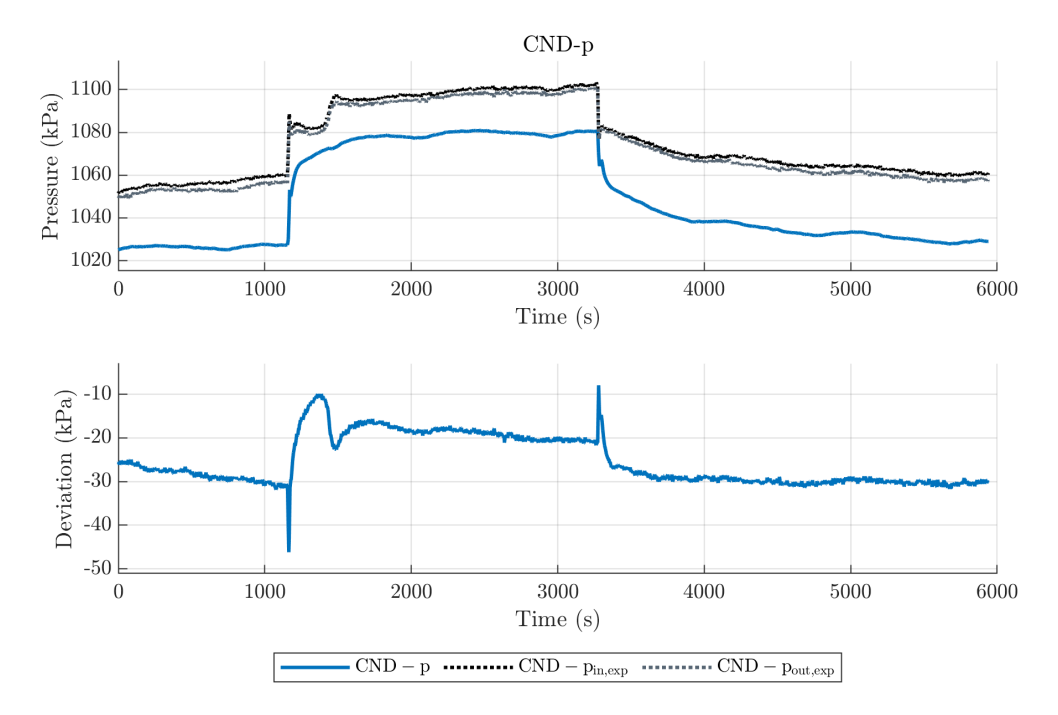


Figure 58: Condenser pressure: Simplified Model, Test 2 with R450A, HEX model with 30 elements.

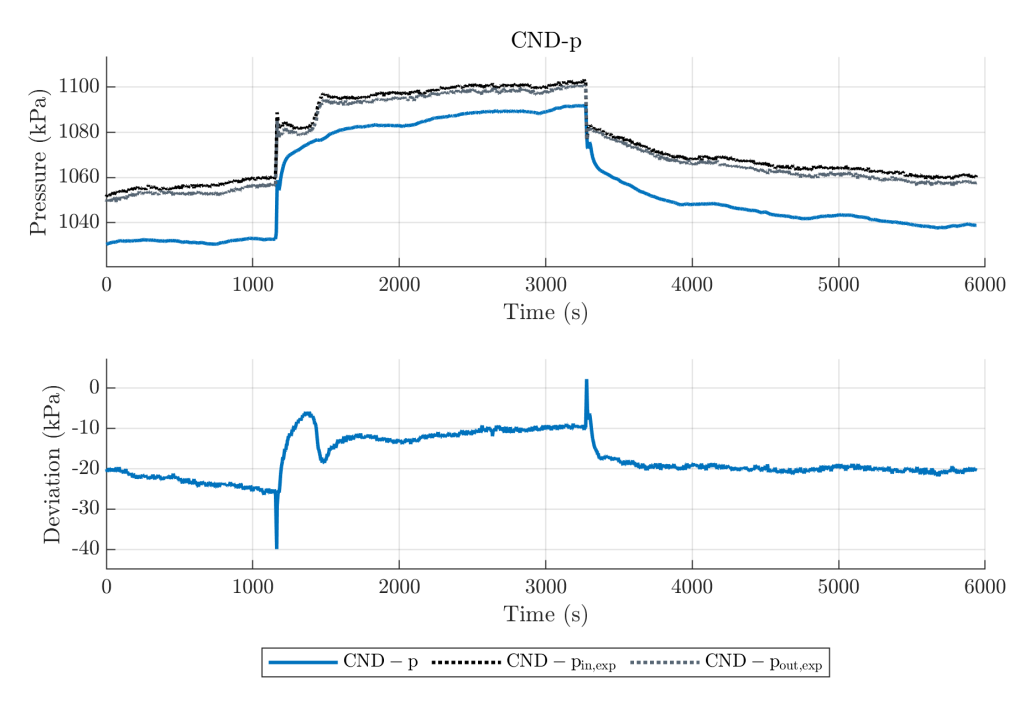


Figure 59: Condenser pressure: Simplified Model, Test 2 with R450A, HEX model with 40 elements.

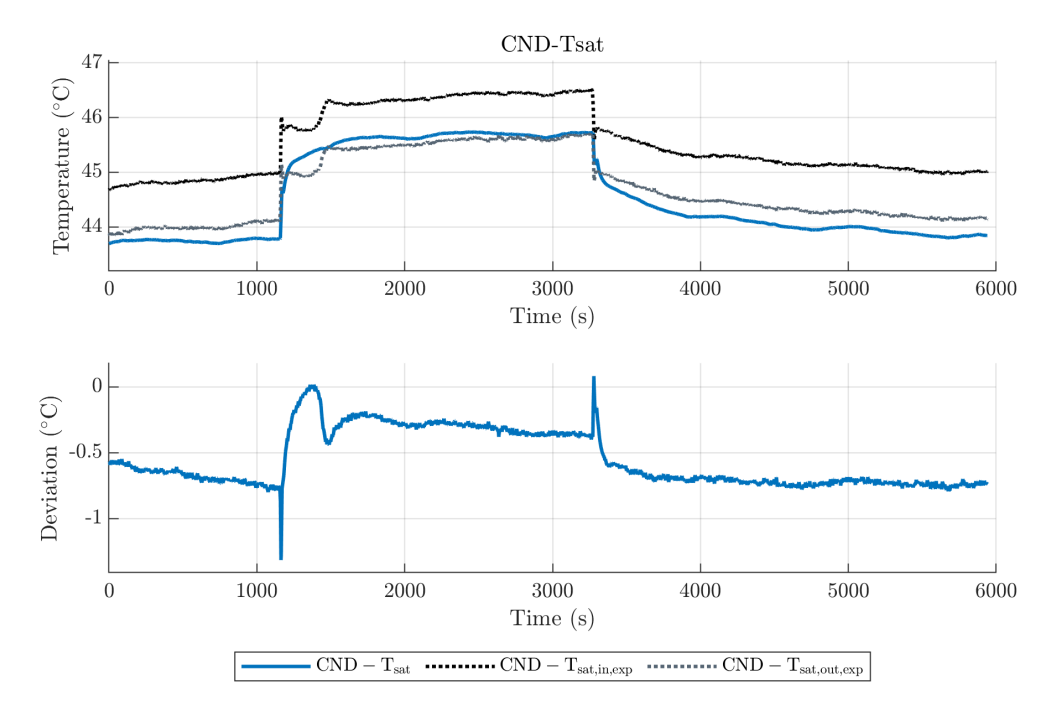


Figure 60: Condenser saturation temperature: Simplified Model, Test 2 with R450A, HEX model with 30 elements.

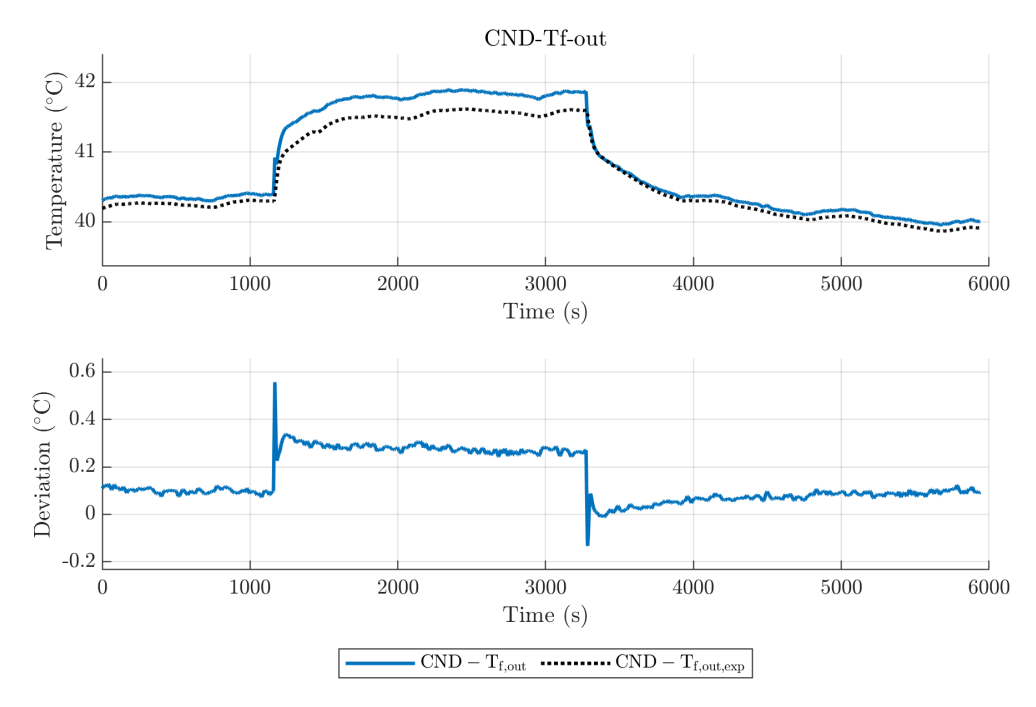


Figure 61: Condenser water outlet temperature: Simplified Model, Test 2 with R450A, HEX model with 30 elements.

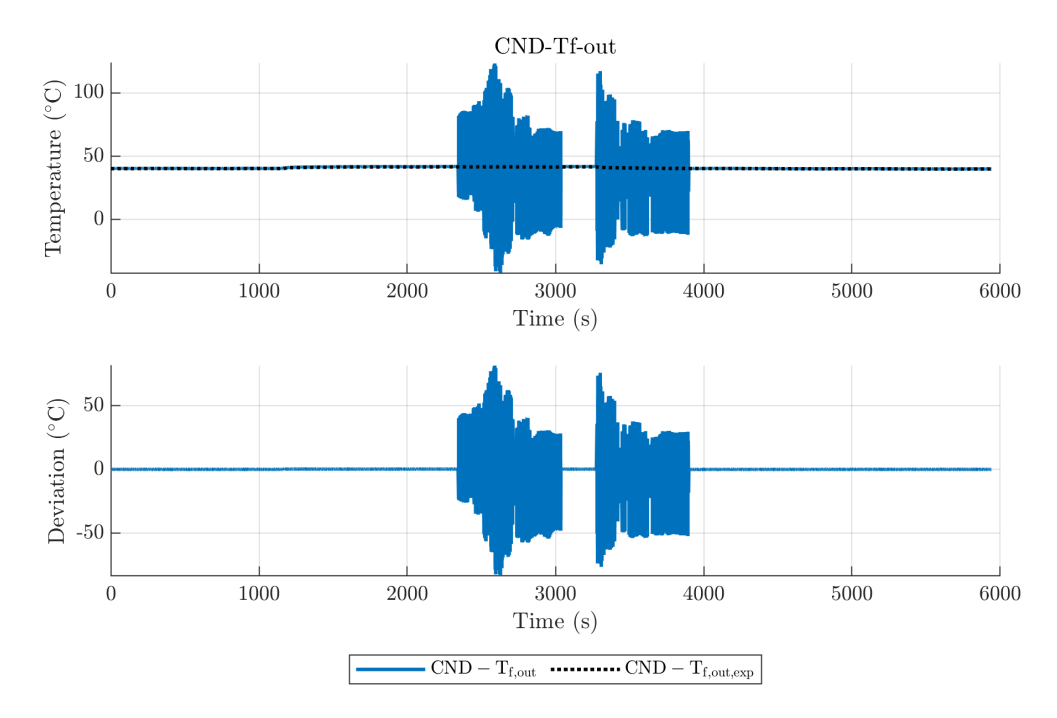


Figure 62: Condenser water outlet temperature: Simplified Model, Test 2 with R450A, HEX model with 40 elements.

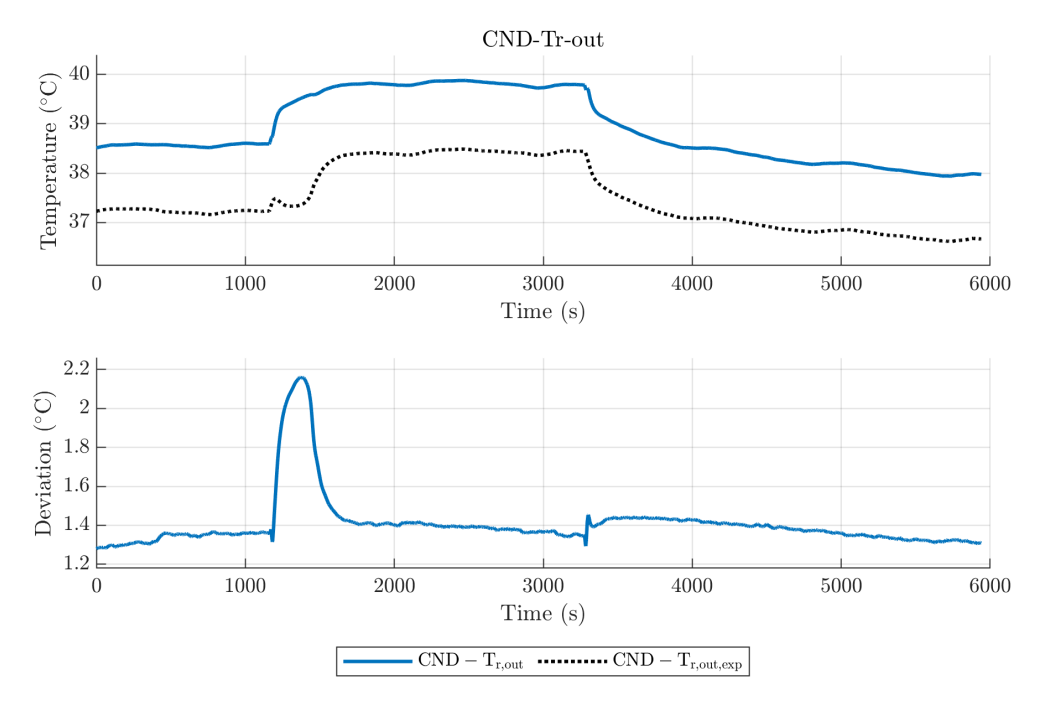


Figure 63: Condenser refrigerant outlet temperature: Simplified Model, Test 2 with R450A, HEX model with 30 elements.

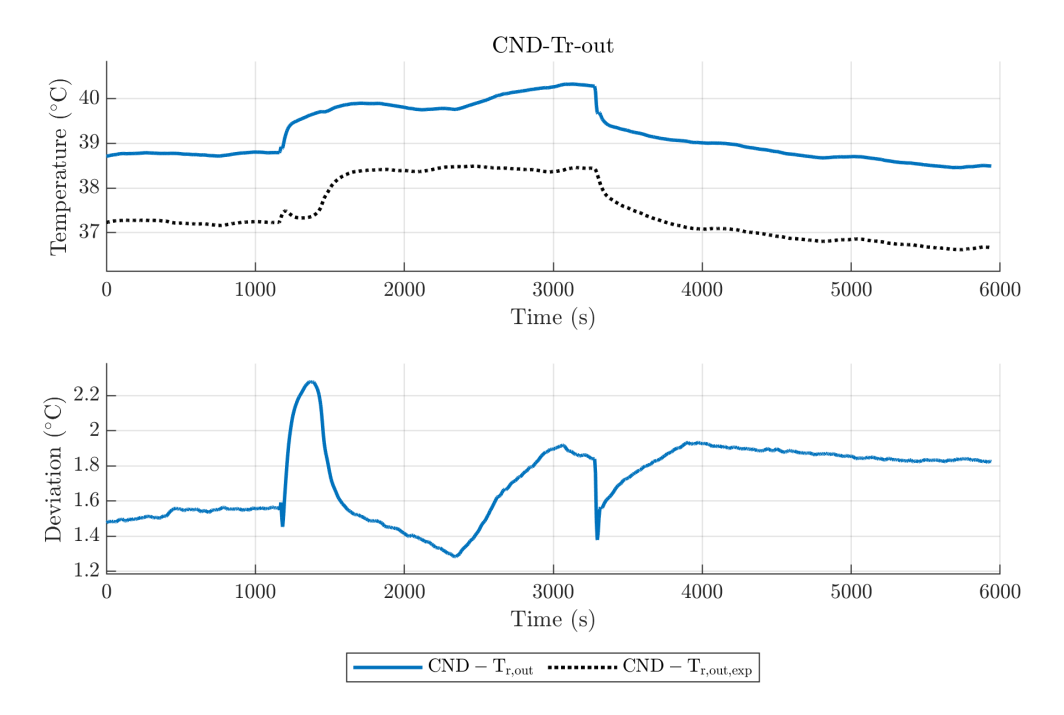


Figure 64: Condenser refrigerant outlet temperature: Simplified Model, Test 2 with R450A, HEX model with 40 elements.

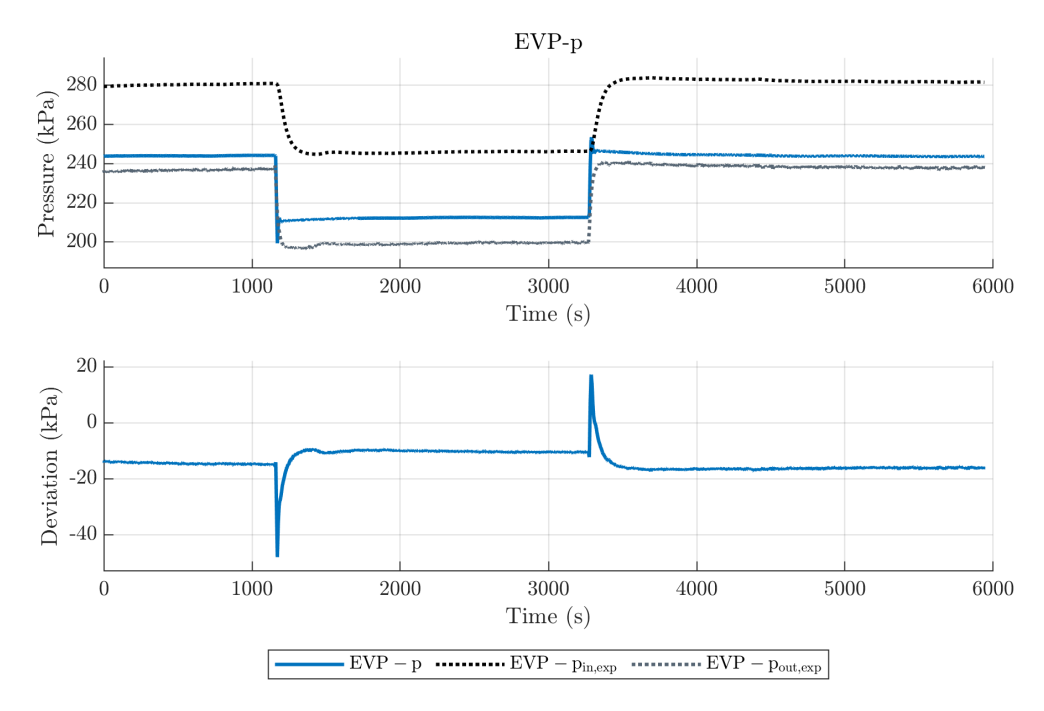


Figure 65: Evaporator pressure: Simplified Model, Test 2 with R450A, HEX model with 20 elements.

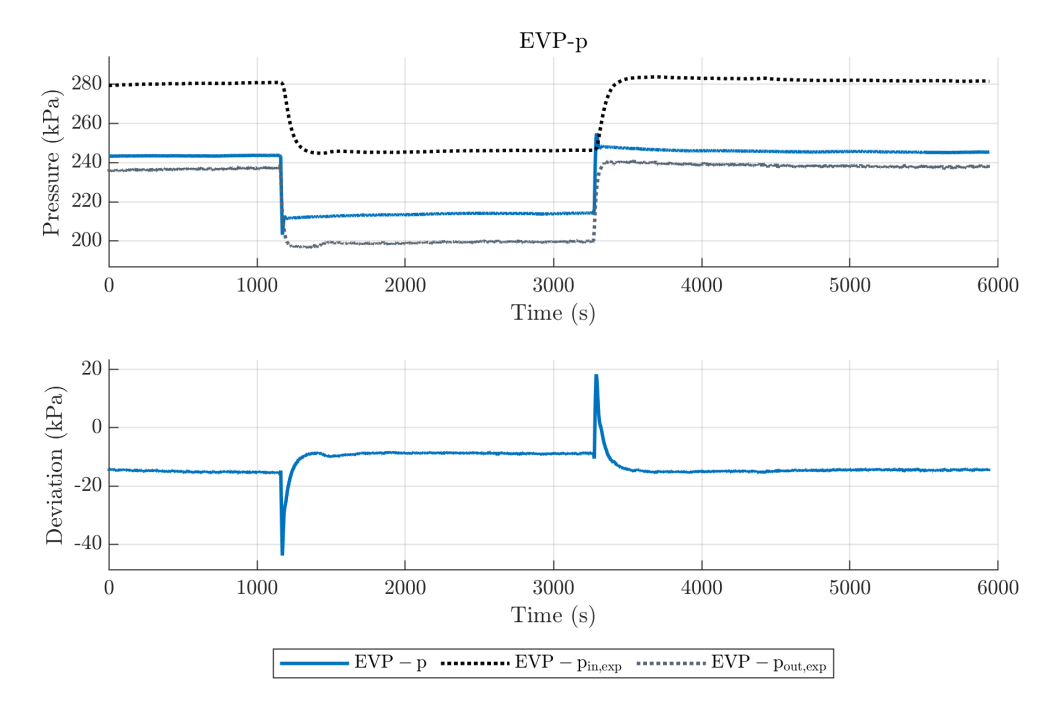


Figure 66: Evaporator pressure: Simplified Model, Test 2 with R450A, HEX model with 40 elements.

is presented in figs. 65 and 66 where 20 and 40 elements are employed respectively. It is clear that doubling the number of elements does not considerably affect the accuracy of the pressure estimation, so it is almost independent of the grid refinement; in both cases, the deviation settles around 20 kPa, corresponding to a difference in the saturation temperature of about 1 °C from the measured data, fig. 67. The evaporator model show a strong grid independence contrary to the condenser, due to a smaller variation of the physical properties of the refrigerant, in particular density and HTCs, along the flow path.

Concerning the outlet temperature of the secondary fluid, the behaviour is very similar to that of the condenser. Indeed, increasing the number of elements, the calculated values show large oscillations that reduce the stability of the model and the accuracy of its predictions; in fig. 69, the instability is not so severe as for the condenser nonetheless it is even significant. With only 20 elements, the oscillations disappear. As for the condenser model, this is related to an unsuitable selection of the time step with reference to spatial discretization.

Finally, the refrigerant temperature at the evaporator outlet exhibits good stability and independence with grid refinement. Some small oscillations are present with all the grids investigated, as shown in the cases of 20 and 40 elements in figs. 70 and 71 respectively. From this point of view, any grid just as good as the other.

It is concluded that suitable trade-off between accuracy and stability of the quantities predicted by the evaporator model can be achieved with 20 equally sized elements.

Secondary fluid temperature at the evaporator outlet

Refrigerant temperature at the evaporator outlet

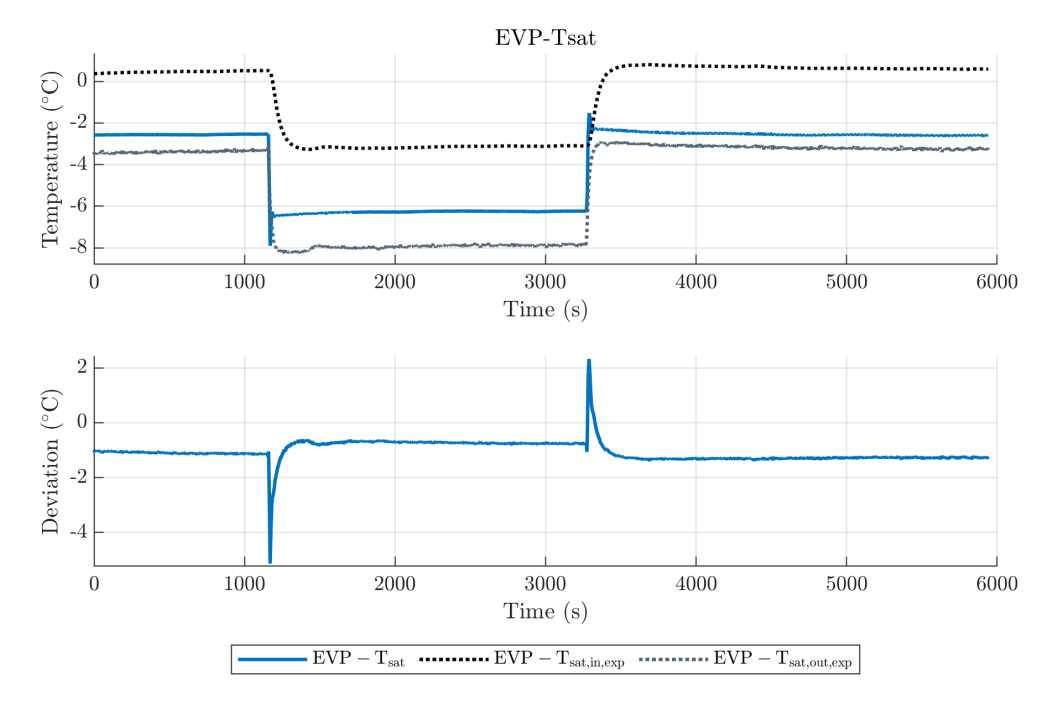


Figure 67: Evaporator saturation temperature: Simplified Model, Test 2 with R450A, HEX model with 20 elements.

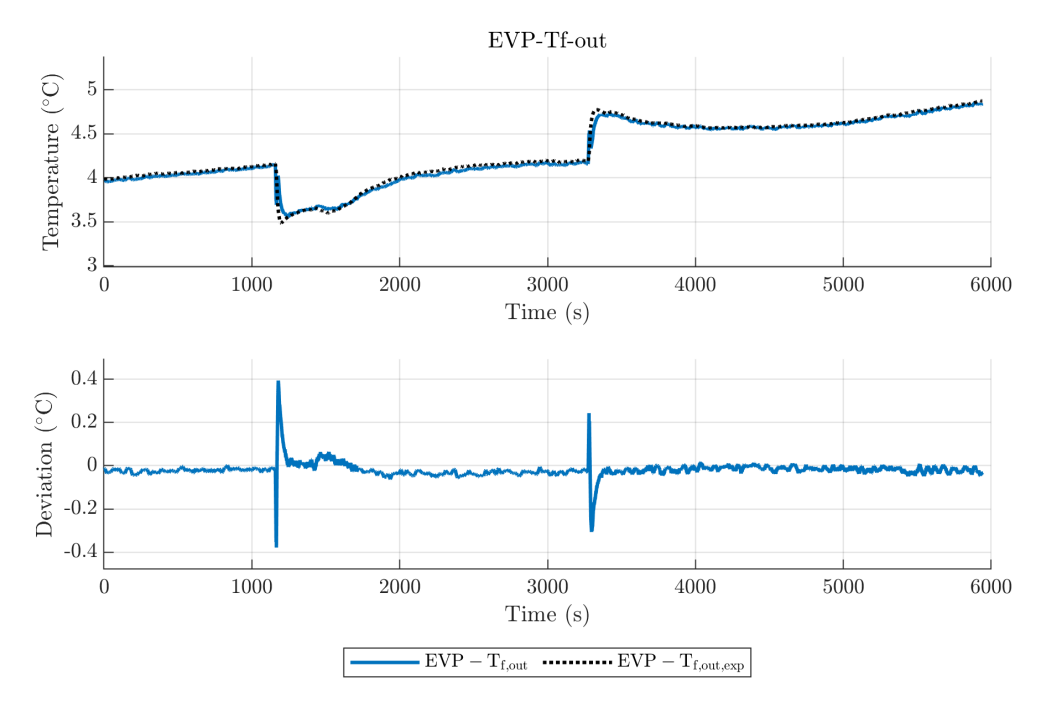


Figure 68: Evaporator water glycol ethylene mixture outlet temperature: Simplified Model, Test 2 with R450A, HEX model with 20 elements.

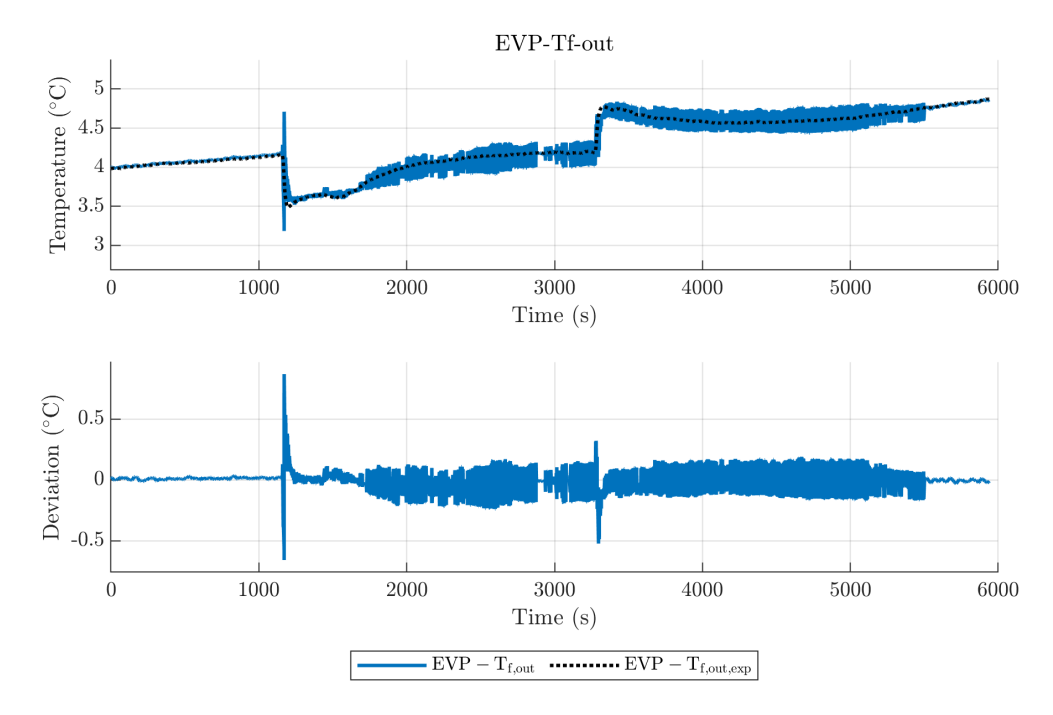


Figure 69: Evaporator water glycol ethylene mixture outlet temperature: Simplified Model, Test 2 with R450A, HEX model with 40 elements.

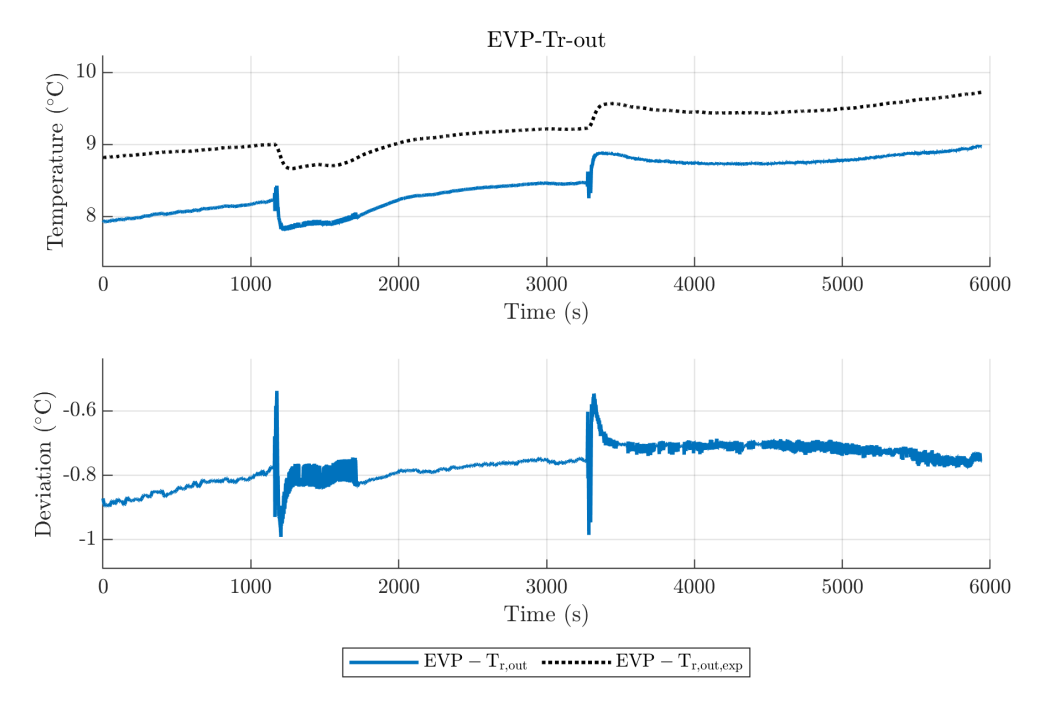


Figure 70: Evaporator refrigerant outlet temperature: Simplified Model, Test 2 with R450A, HEX model with 20 elements.

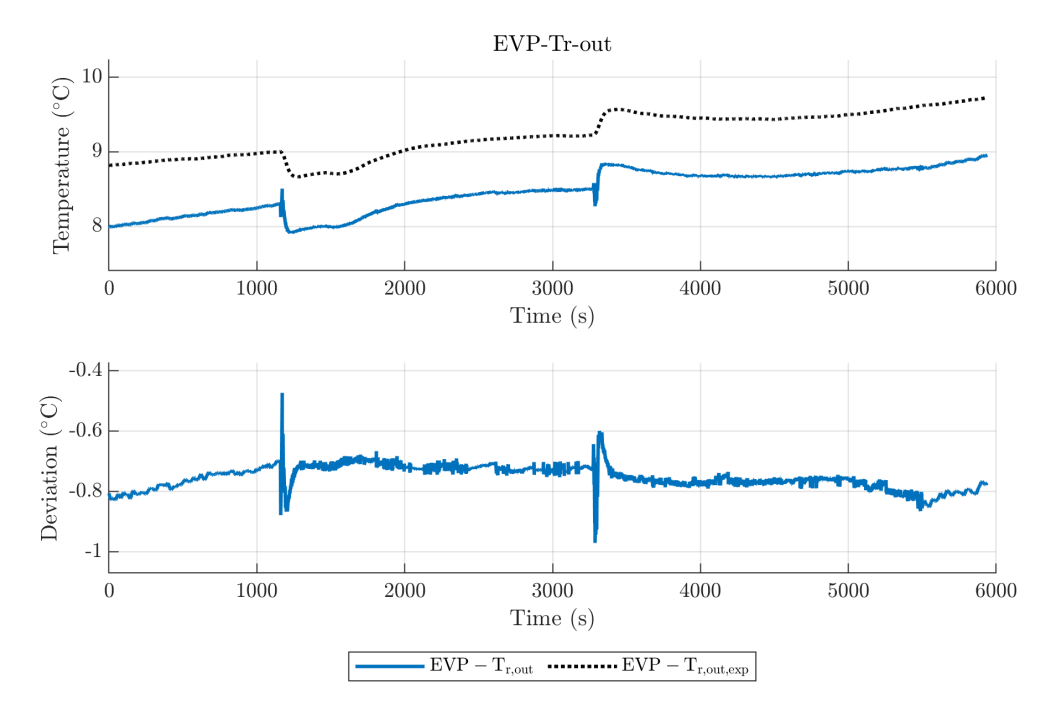


Figure 71: Evaporator refrigerant outlet temperature: Simplified Model, Test 2 with R450A, HEX model with 40 elements.

# Final remarks about the grid refinement

Grid refinement enhances the accuracy of the finite volume model, in particular when large variation of the refrigerant physical properties and of the heat transfer conditions occur; this effect is present in both the HEXs, but is more pronounced in the condenser.

A more refined grid requires nonetheless a smaller integration step size. This is related to the numerical solution of the differential system of equations which rest at the core of the finite volume HEX model. Indeed, the fastest time modes connected to refrigerant enthalpy need a smaller integration step size. Moreover, the stiffness of the problem is negatively influenced by an increased number of elements. The time step must therefore be adjusted if more refined grids are employed, lest the simulation fails out of numerical issues.

Integration time step and spatial discretisation

There is also another part of the model can show unexpected behaviour even without leading to simulation collapse, as in the case of the outlet temperature of the secondary fluid. The oscillations exhibited by both HEX models are caused by an inappropriate selection of the integration time step with respect to the spatial step size employed for the discretization of the system of differential equations.

Numerical oscillations

In conclusion, a trade-off should be pursued between model accuracy and simulation run time. The minimum number of elements should ensure a good prediction of the quantities of interest and avoid numerical oscillations due to an inappropriate selection of the time step relative to the spatial discretization.

#### 11.3 TUNING TO ENHANCE ACCURACY

In general, the HTC correlations can be applied within a certain confidence range because of the unavoidable differences between the operating conditions in the case under investigation and those of the experiments through which the correlations were developed. This consideration allows the possibility to apply a correction factor to the values of the HTC calculated employing the selected correlations in order to enhance the accuracy of the model. This tuning would be particularly beneficial for the condenser.

Tuning of HTCs

The evaporator proves to evaluate accurately both pressure and temperatures. The former is within less than 20 kPa from the experimental data, fig. 65, which corresponds to a difference of less than 1 °C in condensation temperature, fig. 67. The outlet refrigerant temperature is within 1 °C, fig. 70, while the secondary fluid temperature exhibits an almost negligible deviation, fig. 68. Thus no tuning of the HTCs is applied to the evaporator.

The condenser model is less accurate. The condensation pressure is estimated with about 20 kPa of deviation where 30 elements are employed, fig. 58 which corresponds to about 1 °C for the saturation temperature. A worst performance is recognizable when estimating the refrigerant temperature at the outlet. Indeed, a deviation of about 1.5 °C is appreciable, fig. 63. With a suitable choice for the grid, the secondary fluid temperature stays within 0.5 °C, fig. 61. In this context, tuning the HTCs can enhance the accuracy.

Lucchi, 2020 employed a correction factor for each refrigerant zone, namely for the superheated vapour, two-phase mixture and subcooled liquid zone, and another for the secondary fluid. In this work, the effect of tuning the HTCs is investigated in the following way. For the secondary fluid side, a gain is applied to the calculated value employing the selected single-phase correlation. For the refrigerant, two approaches are tested: a single gain for all the HTCs in each element or a different correction for the two-phase zone and the singlephase zone, whether superheated vapour or subcooled liquid.

Correction coefficients employed

In the following, more details are provided about the tuning of the condenser model employing the Simplified Model with the data of Test 2 with R450A. The tuned model is verified against the experimental data obtained with Test 1 with R450A.

#### Tuning according to data from Test 2 with R450A

#### Secondary fluid

The model appears insensitive to tuning on the water side. This behaviour is explained considering that the secondary fluid HTC in

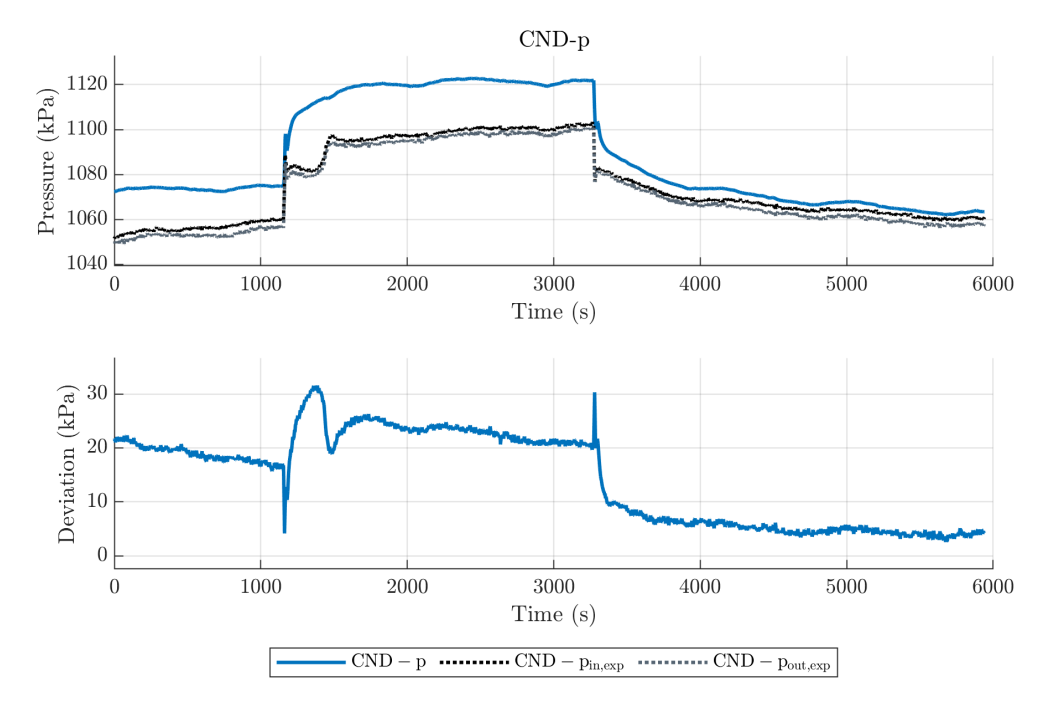


Figure 72: Condenser pressure: Simplified Model, Test 2 with R450A, condenser model with 30 elements and Tune o.

the operating conditions under exam (Test 2 with R450A) is almost 2.5 times thus of the refrigerant in the two-phase zone and 10 times thus in the single-phase zone. The heat transfer rate in the condenser is driven mainly by the conditions on the refrigerant side. For these reasons, the HTC for the secondary fluid is left unchanged.

## Refrigerant

The model underestimates the condenser pressure, so the correlations must overestimate the heat transfer rate. First, a single gain is applied to the HTC for all the elements. This causes a reduction in the overall heat transfer rate and a shift of the pressure to higher values. After some tests, the best compromise is obtained with a constant gain C = 0.865, named Tune o in table 20. The model is very sensitive to this value, as small variations lead to significant changes in the pressure levels; indeed, if the overall heat transfer rate is reduced on the refrigerant side, the average temperature difference between the working fluid increases, and the pressure level may undergo a sharp variation.

From fig. 72 the accuracy in the estimation of the condenser pressure is considerably enhanced in comparison to the untuned case, fig. 58. Conversely, the refrigerant temperature at the condenser outlet moves away from the experimental measurements, showing a deviation around 2.6 °C, fig. 73.

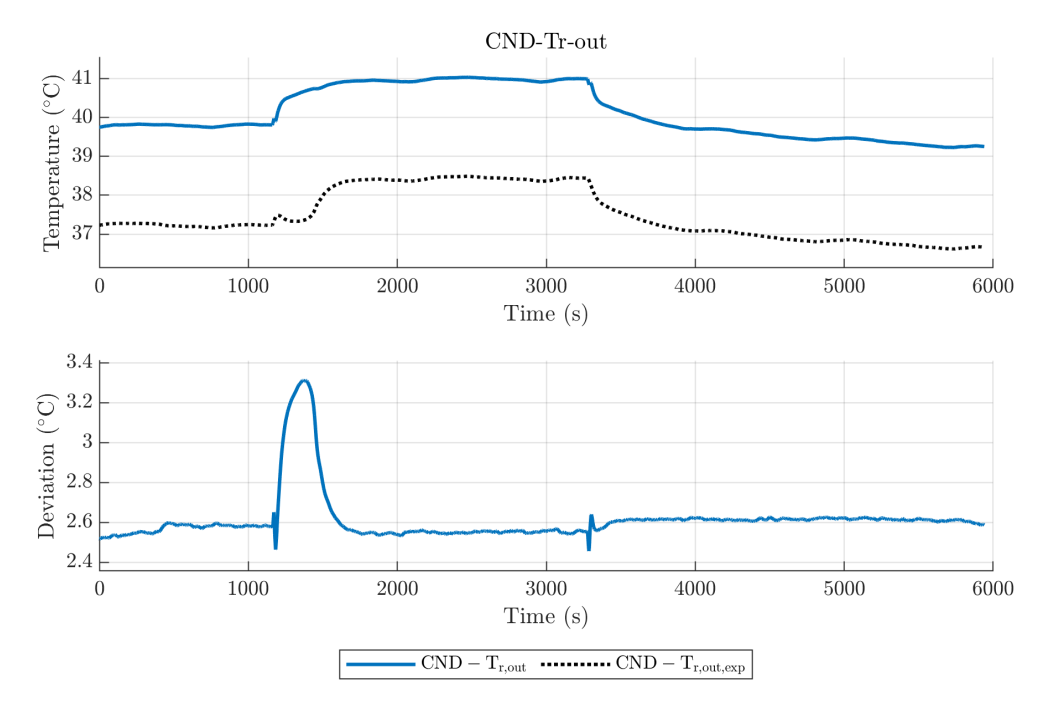


Figure 73: Condenser refrigerant outlet temperature: Simplified Model, Test 2 with R450A, condenser model with 30 elements and Tune o.

	Tune o	Tune 1	Tune 2
$C_{SP}$	0.865	2	1.5
$C_{TP}$	0.865	0.8	0.9

Table 20: Correction gains for the HTC tuning of the refrigerant side in the condenser model.

The above analysis testifies that using a single coefficient for tuning does not enhance the overall accuracy of the model. A two-factor correction is therefore investigated.

A different gain is applied to the HTC of each element depending on the local phase of the refrigerant; one for the two-phase zone and another for the single-phase zone. Reducing the HTC in the two-phase zone, where most of the heat is exchanged, the pressure level of the condenser rapidly increases. Yet, increasing the single phase HTC can reduce the mean temperature difference between the working fluid in these zones, reducing the refrigerant temperature in the outlet section.

After some tests, two different sets of gains have been proven suitable to enhance the accuracy of the condenser model, reported in table 20.

The more robust tuning named Tune 1 in table 20 is applied in fig. 74 which shows that pressure estimation does not change from that obtained with the same elements of the grid fig. 72. On the other hand, the deviation of the refrigerant temperature at the outlet is reduced to less than 0.8 °C, excluding the peaks, fig. 75.

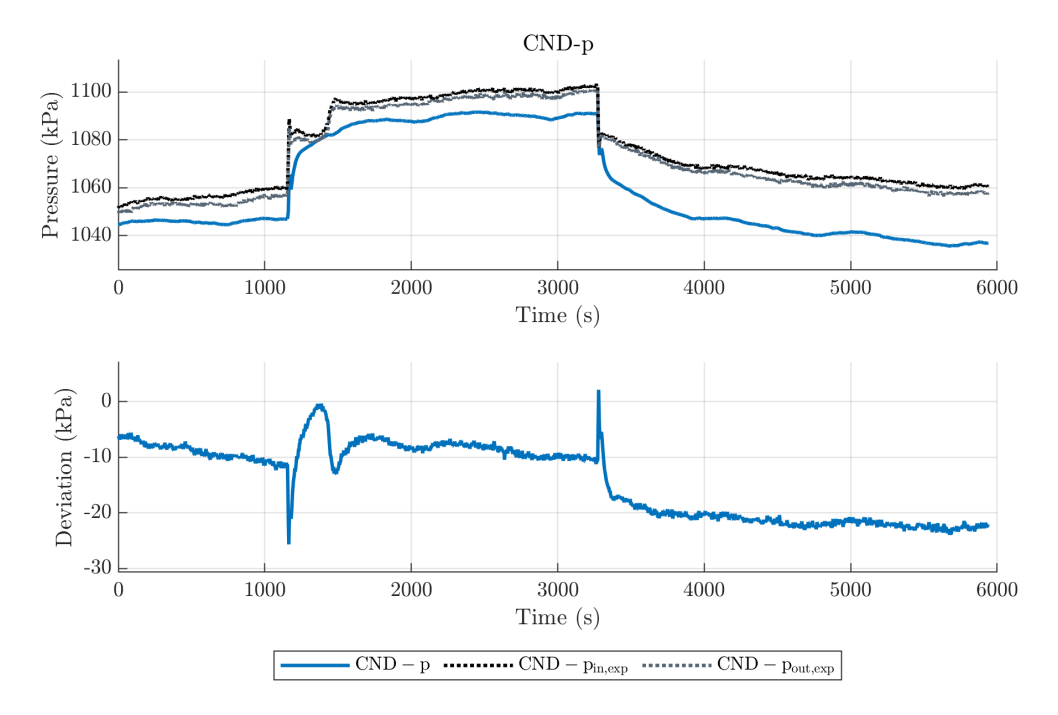


Figure 74: Condenser pressure: Simplified Model, Test 2 with R450A, condenser model with 30 elements and Tune 1.

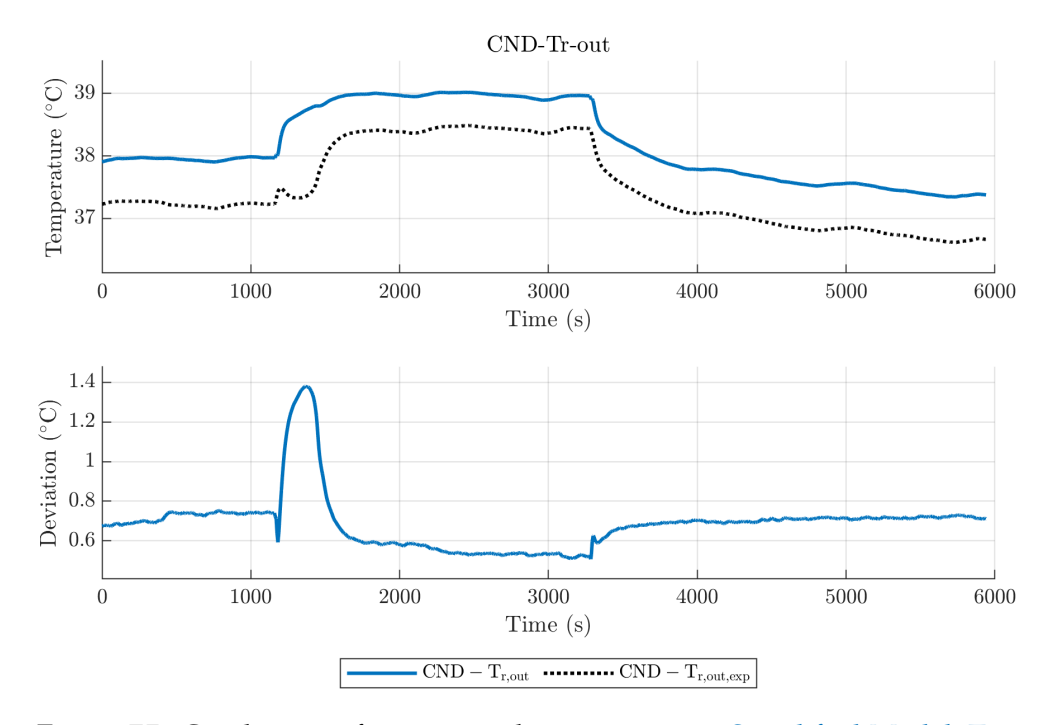


Figure 75: Condenser refrigerant outlet temperature: Simplified Model, Test 2 with R450A, condenser model with 30 elements and Tune 1.

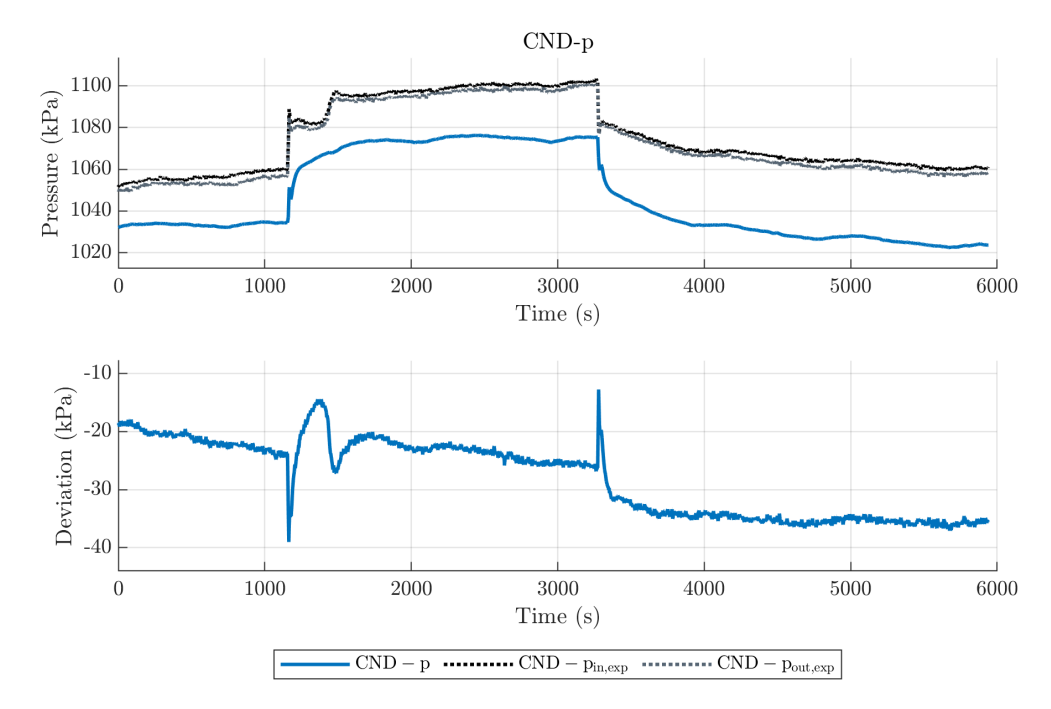


Figure 76: Condenser pressure: Simplified Model, Test 2 with R450A, condenser model with 30 elements and Tune 2.

Similarly, the second set of gains, Tune 2 in table 20, leads to improving the accuracy in the prediction of the refrigerant temperature, but the deviation settles around 1 °C, not including the peaks fig. 77.

It is necessary to mention that both corrections do not affect the evaluation of the secondary fluid outlet temperature, which keeps a deviation around 0.2 °C as in the untuned case, fig. 63.

# Tuning verification under Test 1 with R450A conditions

Since no improvements was obtained with a single value, the verification phase focused on the other two strategies proposed, Tune 1 and Tune 2.

From the exam of fig. 78 emerges that the condenser pressure during Test 1 with R450A is estimated with a deviation of around 20 kPa in steady state conditions corresponding to the initial value of the valve opening; this trend is very similar to that verified for the Test 2 with R450A. However, during the phase with the reduced opening, the pressure deviation settles around 40 kPa. The corresponding error in the evaluation of the condensation temperature is around 0.4 °C in the initial and final phase, and 1.2 °C in the central part, fig. 79. The refrigerant temperature in the outlet section of the condenser is calculated with a maximum deviation less than o.8 °C; the worst performance is recognisable during the phase of valve closing, as for the pressure. The temperature in the initial and final phases shows a deviation around 0.2 °C.

Effect of Tune 1

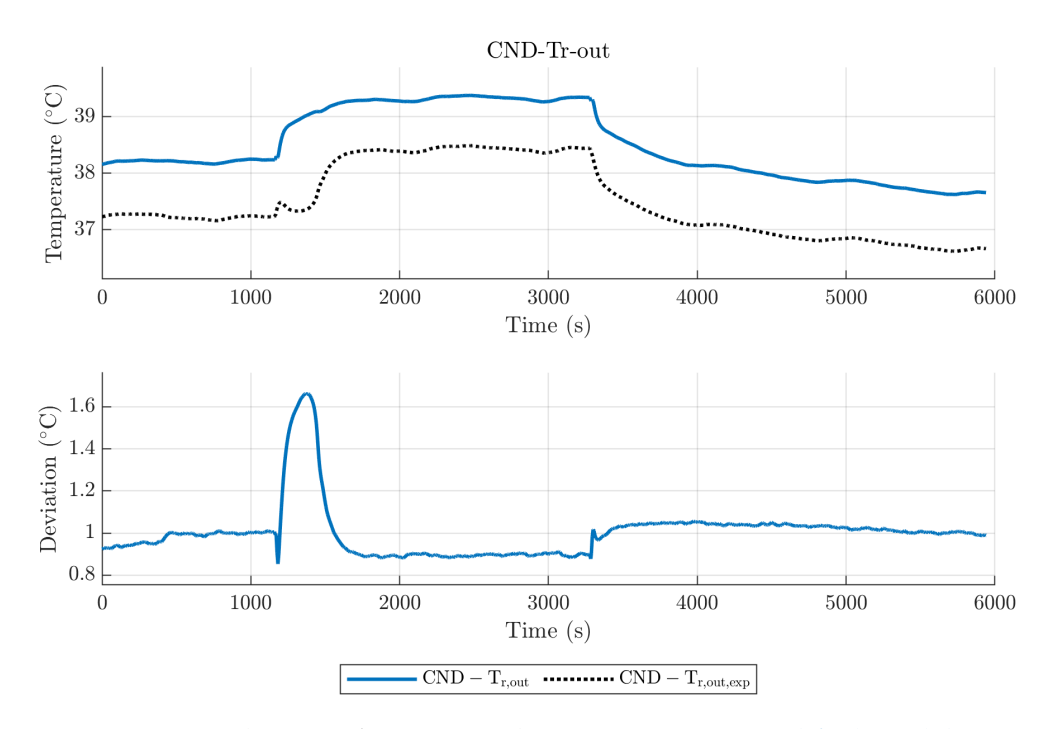


Figure 77: Condenser refrigerant outlet temperature: Simplified Model, Test 2 with R450A, condenser model with 30 elements and Tune 2.

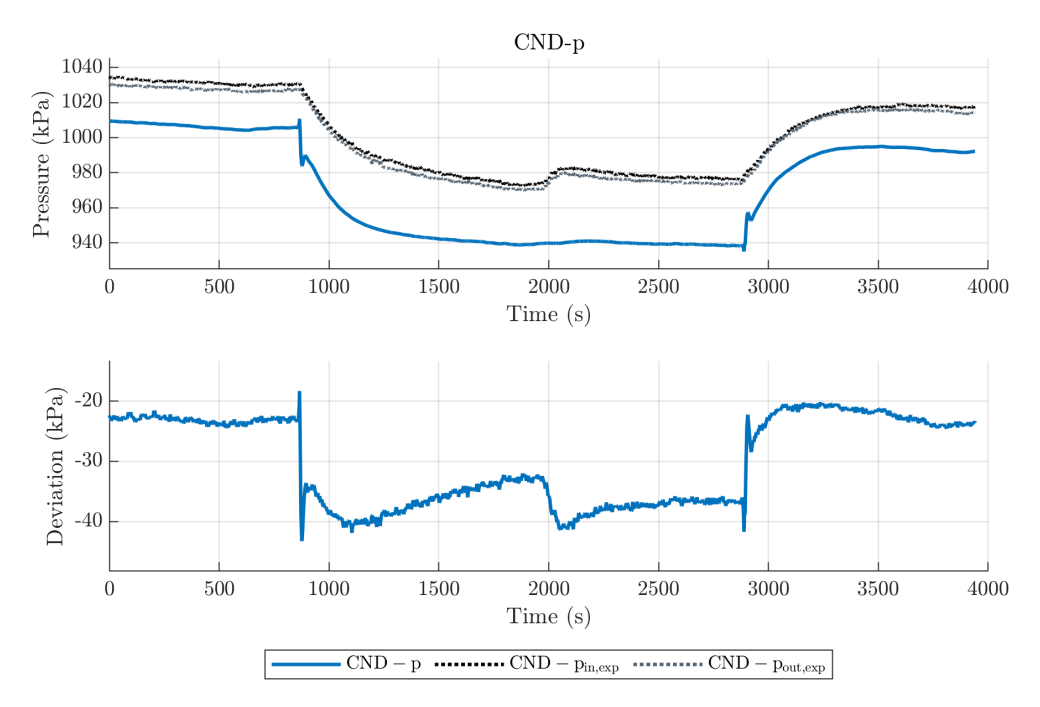


Figure 78: Condenser pressure: Simplified Model, Test 1 with R450A, condenser model with 30 elements and Tune 1.

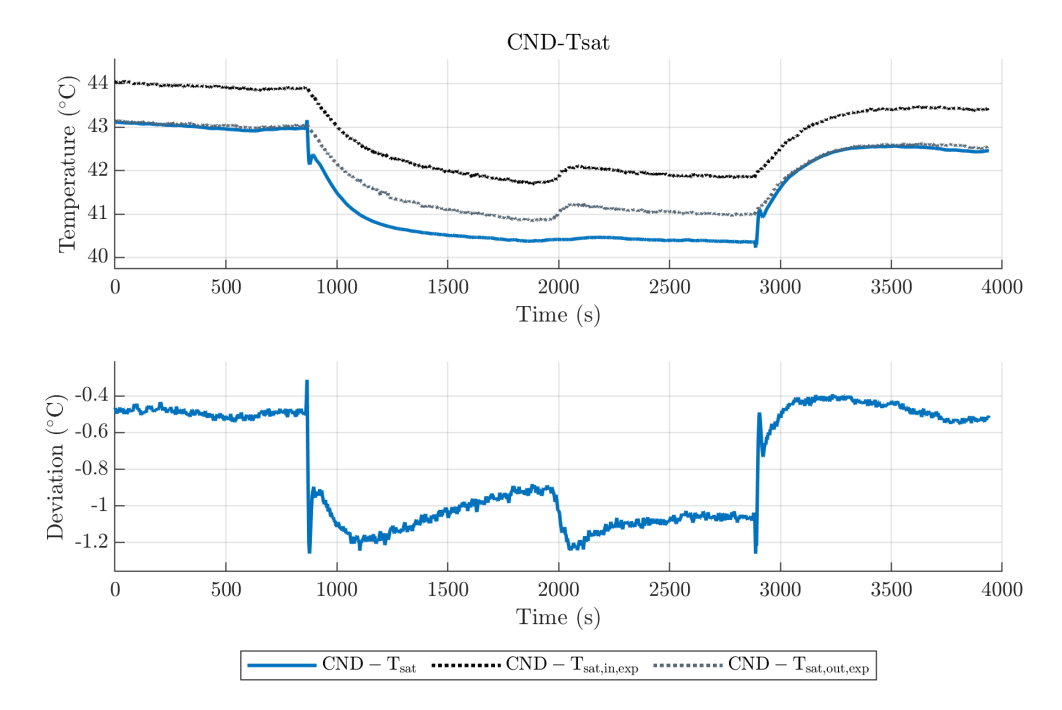


Figure 79: Condenser saturation temperature: Simplified Model, Test 1 with R450A, condenser model with 30 elements and Tune 1.

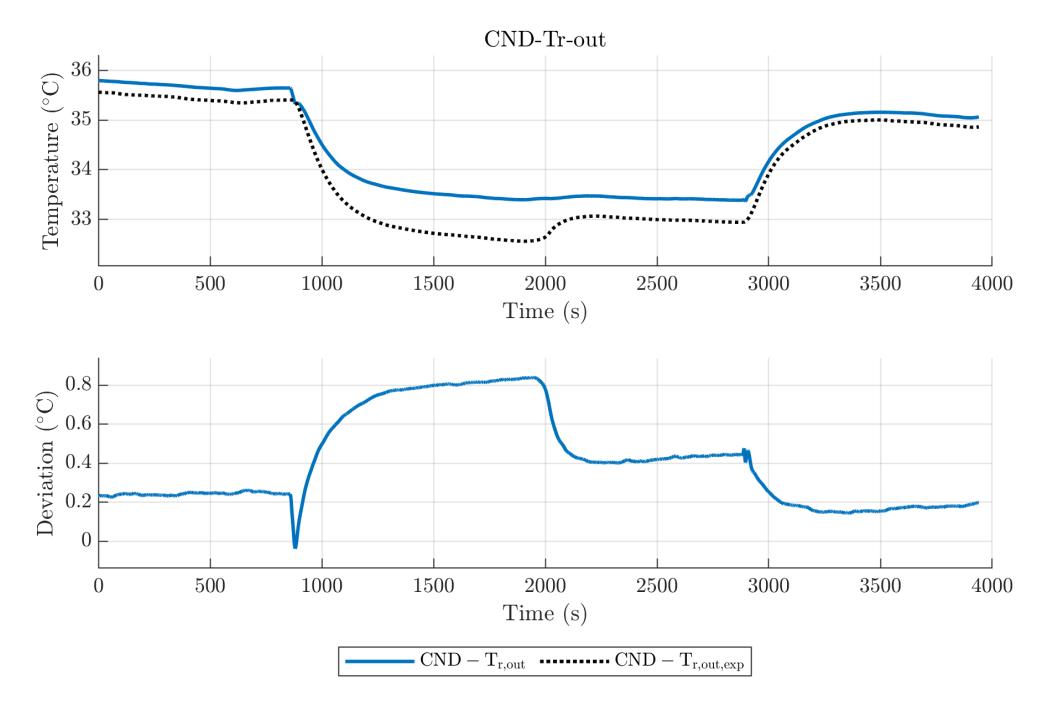


Figure 80: Condenser refrigerant outlet temperature: Simplified Model, Test 1 with R450A, condenser model with 30 elements and Tune 1.

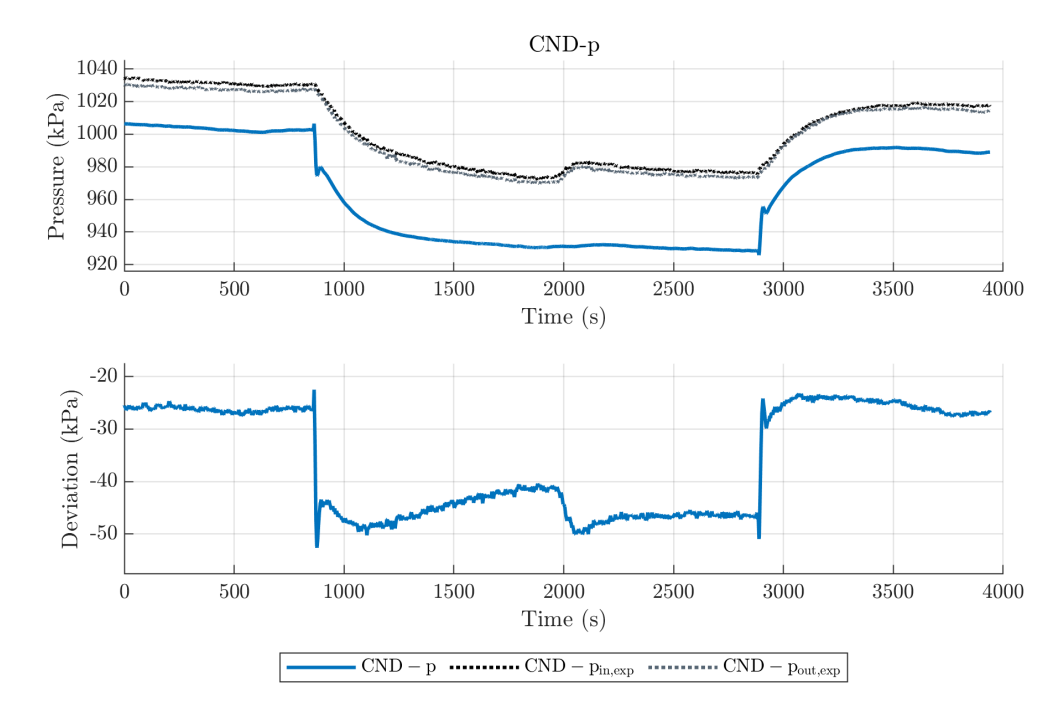


Figure 81: Condenser pressure: Simplified Model, Test 1 with R450A, condenser model with 30 elements and Tune 2.

The second set of coefficients Tune 2 leads to a lesser improvement in the accuracy of the condenser model accuracy, as for the Test 2 with R450A. Indeed, from fig. 81 is possible to appreciate that the error during the valve opening reduction phase is around 50 kPa, and while the valve is maintained at the reference position, it settles around 30 kPa. In this case, the condensation temperature is evaluated with an error between 0.5 and 1.5  $^{\circ}$ C, fig. 82. Also, the refrigerant outlet temperature is less ascertain than for the Tune 1 case, as can be appreciated in fig. 83.

In both cases, as discussed for the Test 2 with R450A, the secondary fluid temperature remains almost unaffected by the tuning of the refrigerant side HTCs. Figure 84, referring to Tune 1 under Test 1 with R<sub>450</sub>A conditions, shows that the water temperature at the condenser outlet is estimated by the model with a maximum deviation around 0.2 °C, excluding the peaks, as for the Test 2 with R450A, which was examined before. In this case, inceptive oscillations can also be found in the central part of the test.

The evaporator model was not tuned, because it exhibited a good accuracy when tried with the data from Test 2 with R450A. The verification under Test 1 with R450A conditions confirms this behaviour. The evaporation pressure is evaluated with a deviation below 20 kPa, fig. 85, that correspond to an error in the saturation temperature of the order of 1 °C, fig. 86. Also the refrigerant temperature at the evaporator outlet is well estimated by the model with a deviation around

Effect of Tune 2

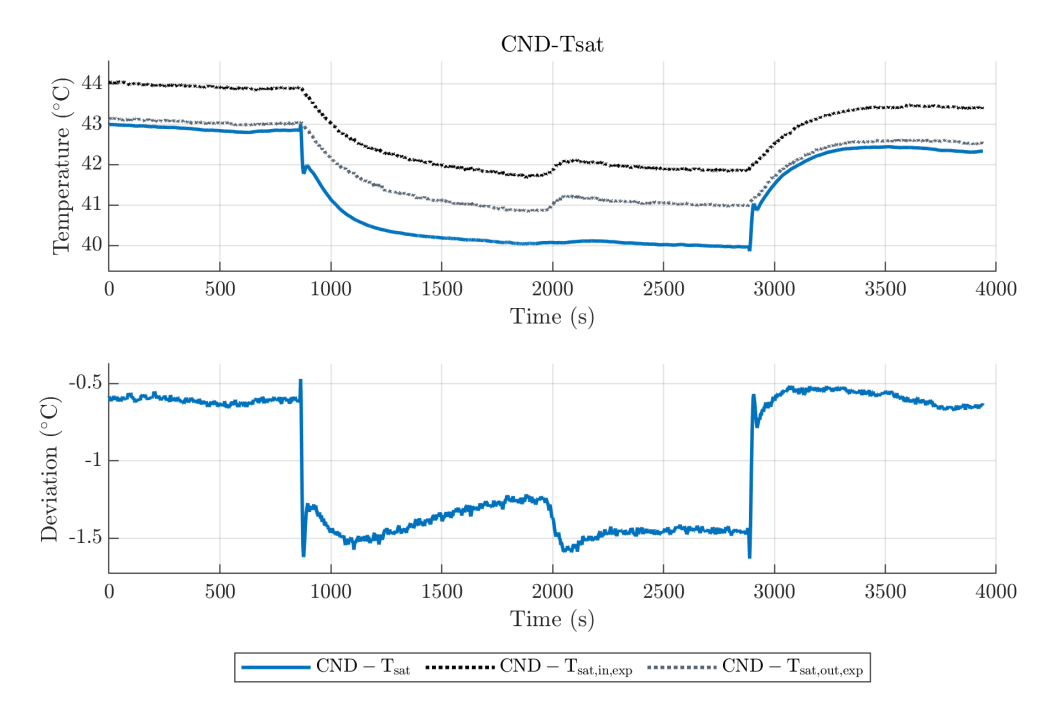


Figure 82: Condenser saturation temperature: Simplified Model, Test 1 with R450A, condenser model with 30 elements and Tune 2.

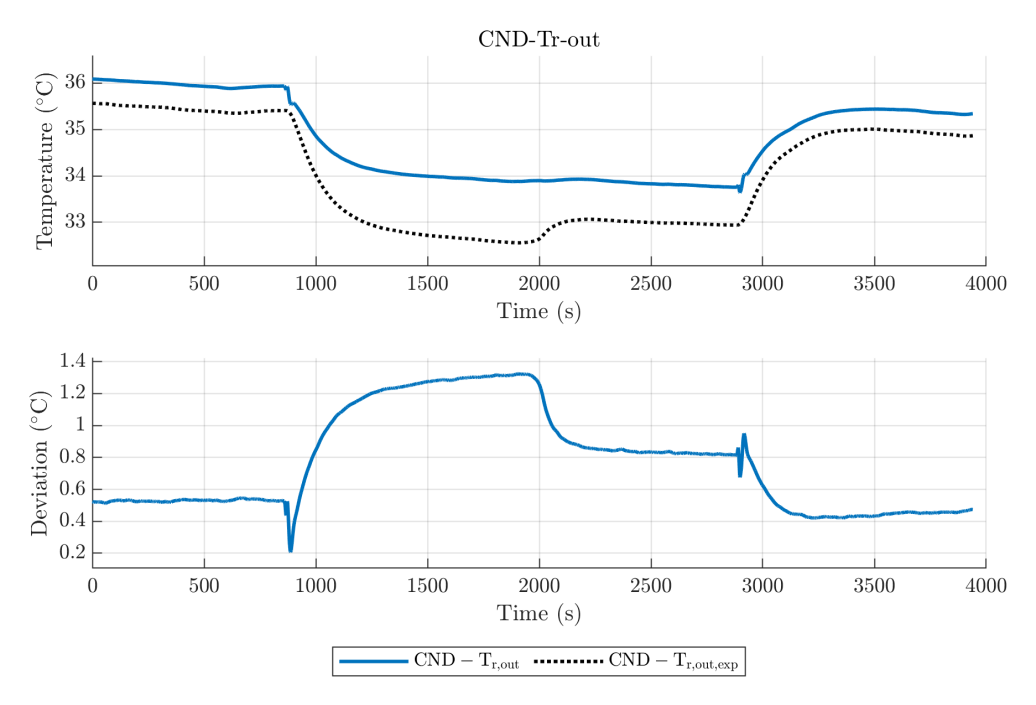


Figure 83: Condenser refrigerant outlet temperature: Simplified Model, Test 1 with R450A, condenser model with 30 elements and Tune 2.

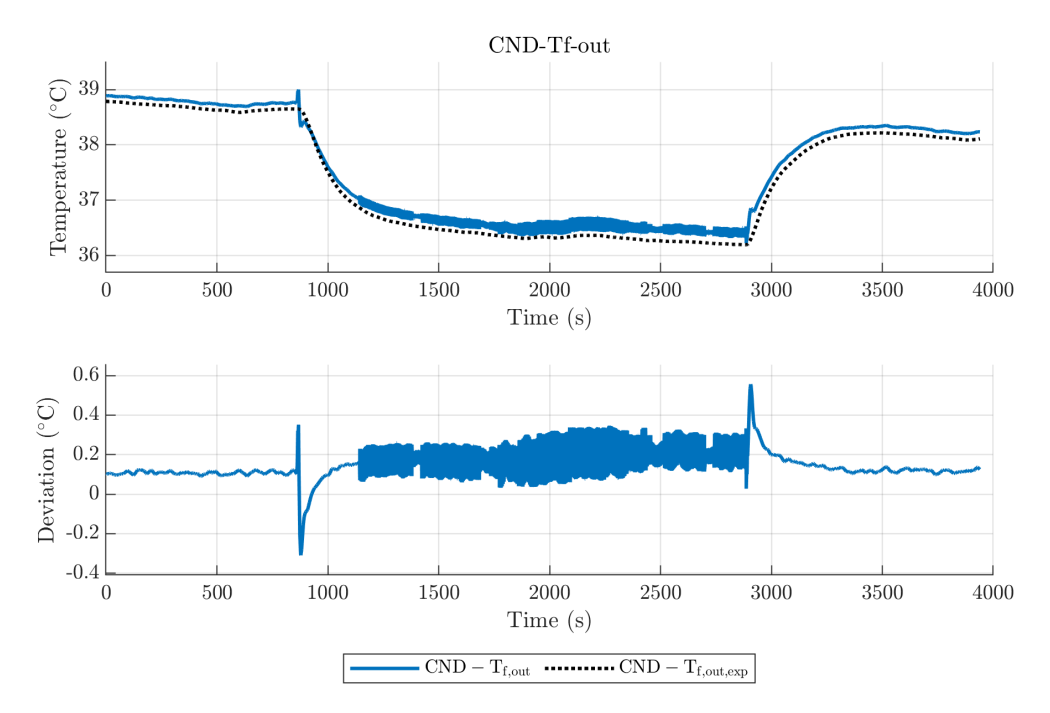


Figure 84: Condenser water outlet temperature: Simplified Model, Test 1 with R450A, condenser model with 30 elements and Tune 1.

0.5 °C, fig. 87. Finally, the temperature of the secondary fluid shows an almost negligible error, fig. 88.

#### 11.4 FULL MODEL ANALYSIS

In this section the performance of the Full Model is investigated. The configuration adopted in the following tests is drawn from the previous analysis of the behaviour of the Simplified Model. For the condenser model a discretization with 30 elements is adopted, while for the evaporator 20 elements are considered enough. The tests are performed by applying the tuning of the condenser HTC with the Tune 1 set of coefficients. Also, in this case, the ode 3 solver is employed with a fixed time step  $\Delta t$ =0.01 s. During the verification of the Full Model employing the experimental data from Test 2 with R450A some initialisation issue had to be solved before the analysis could be carried out.

Simulation configuration

#### Validation of Full Model in Test 2 with R450A

The accumulator models must be initialised in the Full Model. From the experimental data available, it is impossible to infer the amount of refrigerant contained in each vessel, be it the LR or the SA. AsAccumulator models initialisation

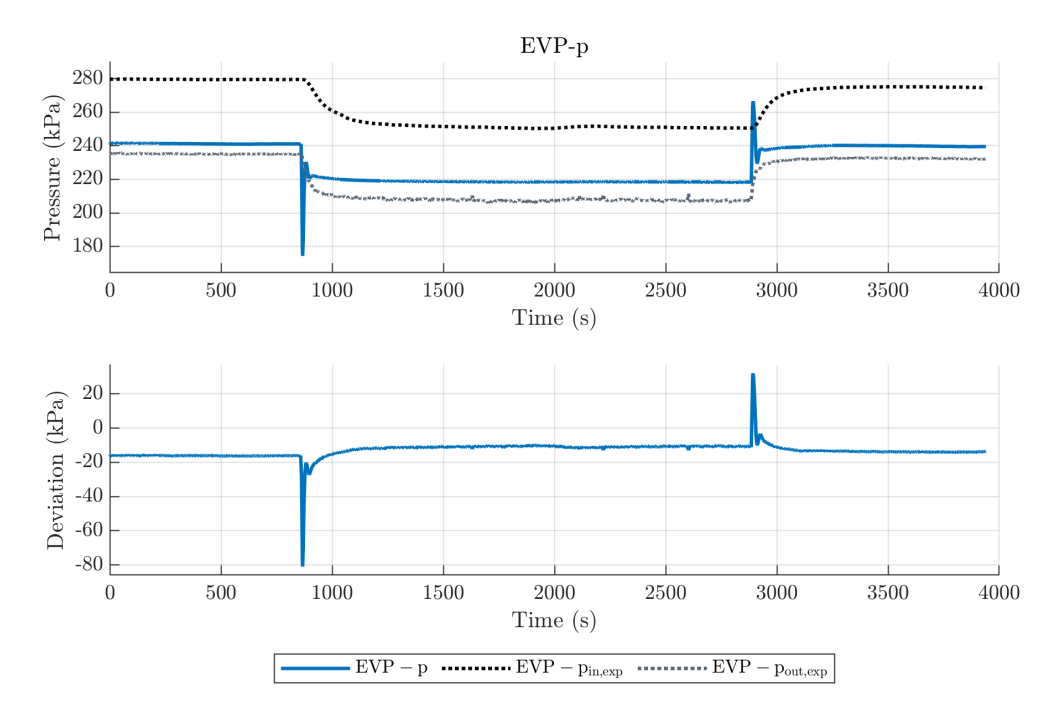


Figure 85: Evaporator pressure: Simplified Model, Test 1 with R450A, evaporator model with 20 elements and Tune 1.

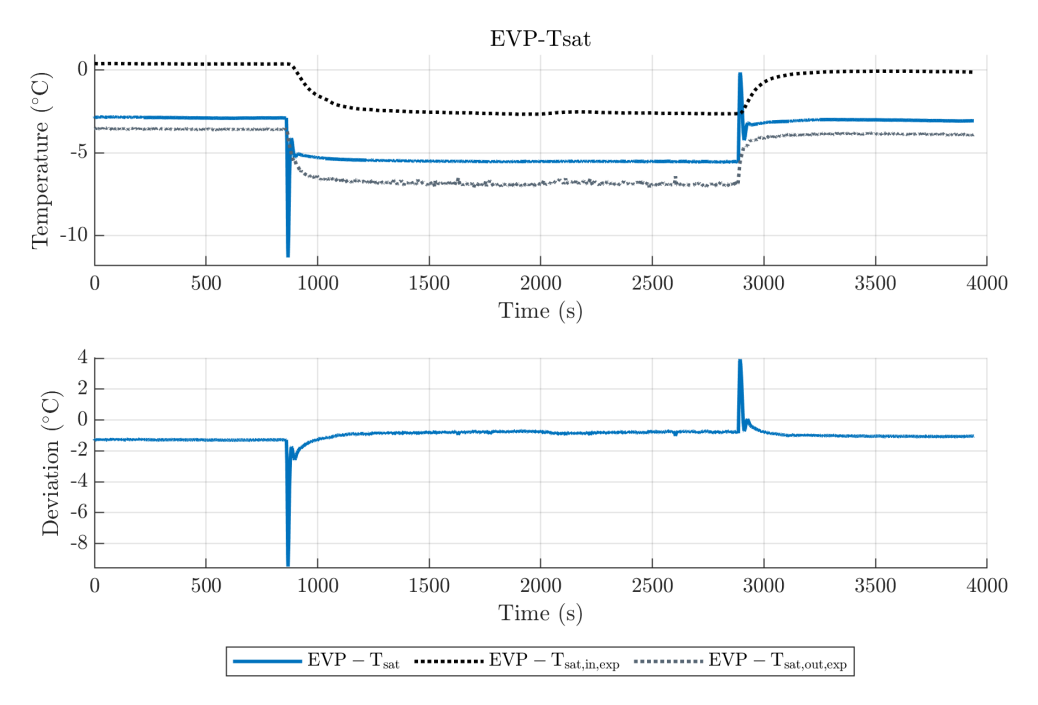


Figure 86: Evaporator saturation temperature: Simplified Model, Test 1 with R450A, evaporator model with 20 elements and Tune 1.

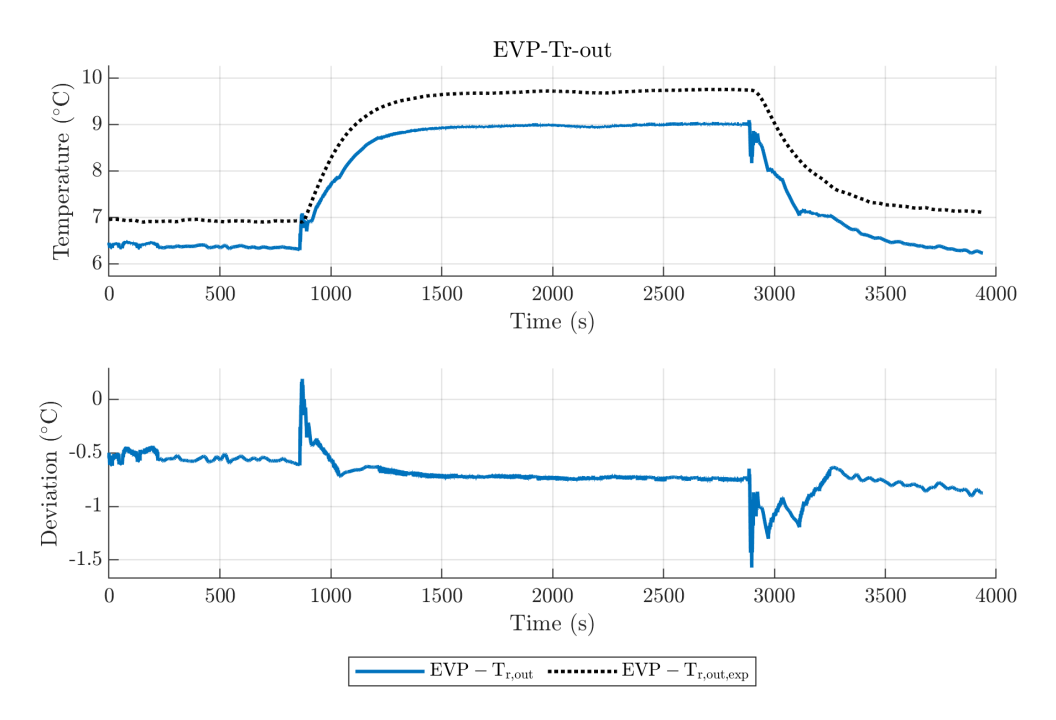


Figure 87: Evaporator refrigerant outlet temperature: Simplified Model, Test 1 with R450A, evaporator model with 20 elements and Tune 1.

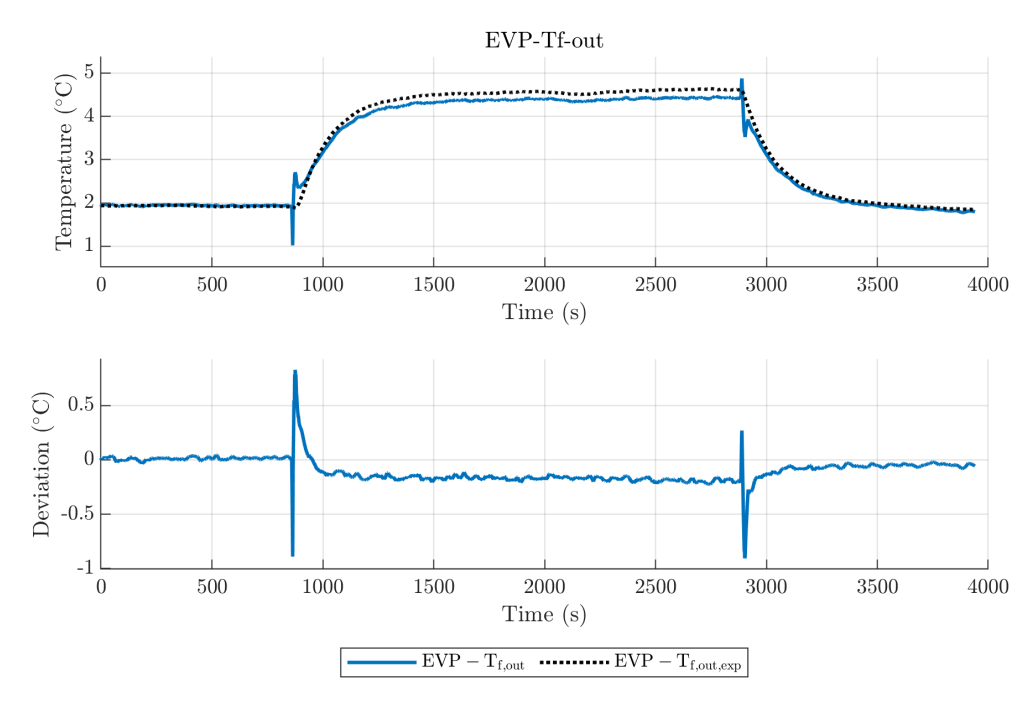


Figure 88: Evaporator secondary fluid outlet temperature: Simplified Model, Test 1 with R450A, evaporator model with 20 elements and Tune 1.

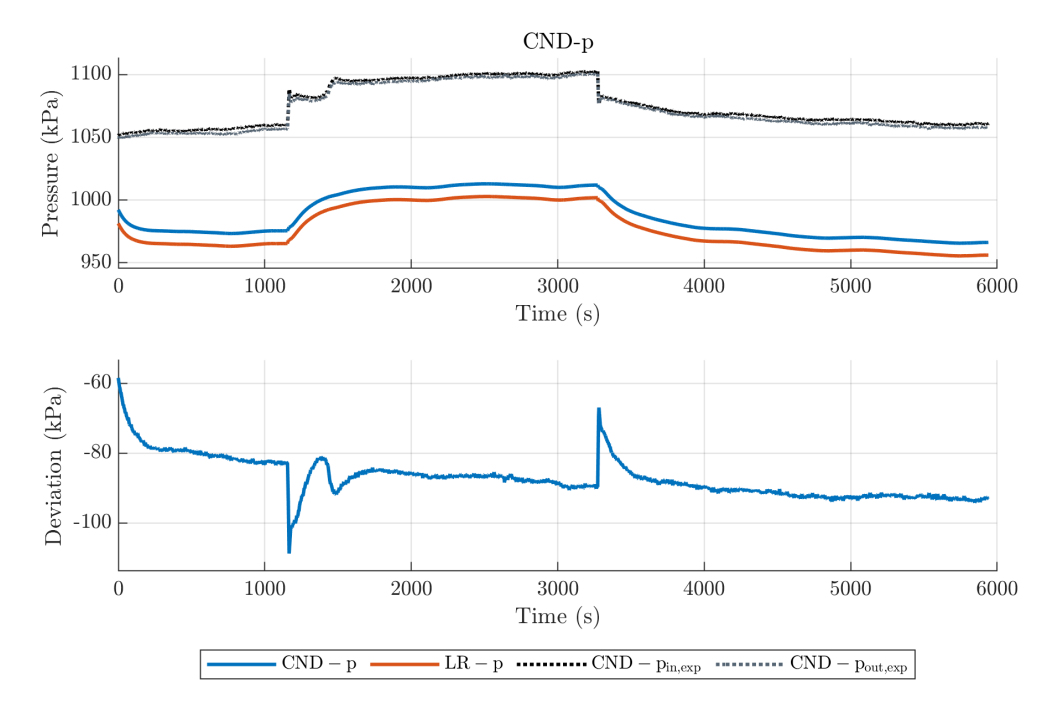


Figure 89: Condenser pressure: Full Model, Test 2 with R450A, condenser model with 30 elements and Tune 1,  $x_{0,LR} = 0.2$ .

sumptions must therefore be made concerning the initial state of the tanks.

The SA should be almost full of vapour during regular operation. Different initial conditions in terms of vapour quality were tested from x=0.2 to x=0.8; in all cases, after a short transient, the SA stabilises as completely full of superheated vapour, and the operating point of the systems seems to be unaffected by the initial choice. For these reasons, a vapour quality x=0.8 is assumed at t=0 s.

The initial condition of the LR has a considerable effect on the operating point of the assembly. This vessel should be almost full of liquid refrigerant during normal operation, so an initial vapour quality of x=0.2 appeared realistic. A preliminary test was carried out using the conditions of Test 2 with R450A. In figs. 89 and 90 the pressure levels in the two HEXs and in the corresponding accumulators are plotted. The condenser stabilises at a pressure of almost 80 kPa below the measured data and about 70 kPa below the computations of the Simplified Model in the same configuration, fig. 74. The evaporator pressure predicted by the Full Model is about 50 kPa less than the mean value of the experimental data and about 40 kPa less than the calculated values by the Simplified Model in the same configuration, fig. 91. After the initial transient the vapour quality in the LR settles around 0.1.

If the LR is assumed to be completely full of liquid at the beginning of the simulation, the operating point of the plant is more similar to that of the experiment. Indeed, from fig. 92 the condenser pressure is

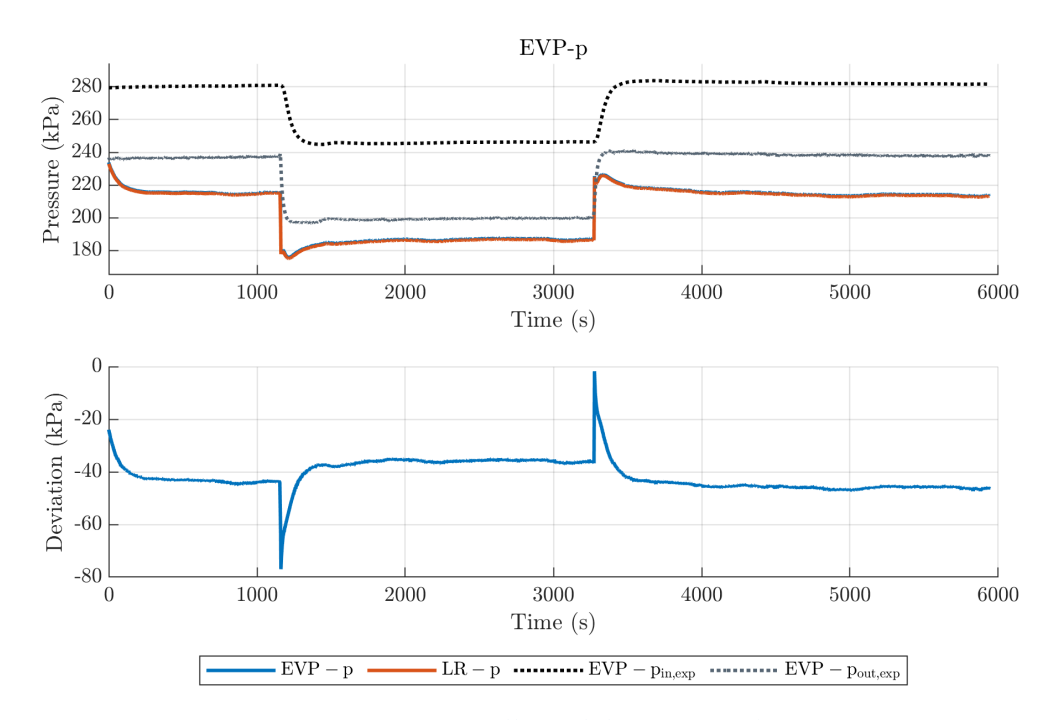


Figure 90: Evaporator pressure: Full Model, Test 2 with R450A, evaporator model with 20 elements and Tune 1,  $x_{0,LR} = 0.2$ .

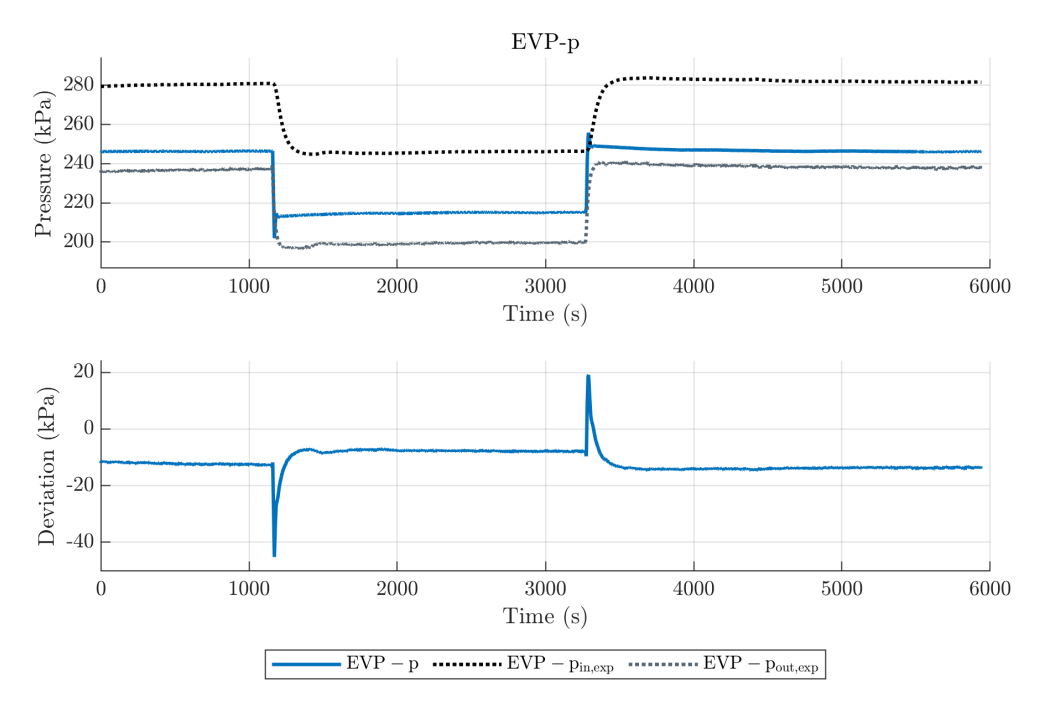


Figure 91: Evaporator pressure: Simplified Model, Test 2 with R450A, evaporator model with 20 elements and Tune 1.

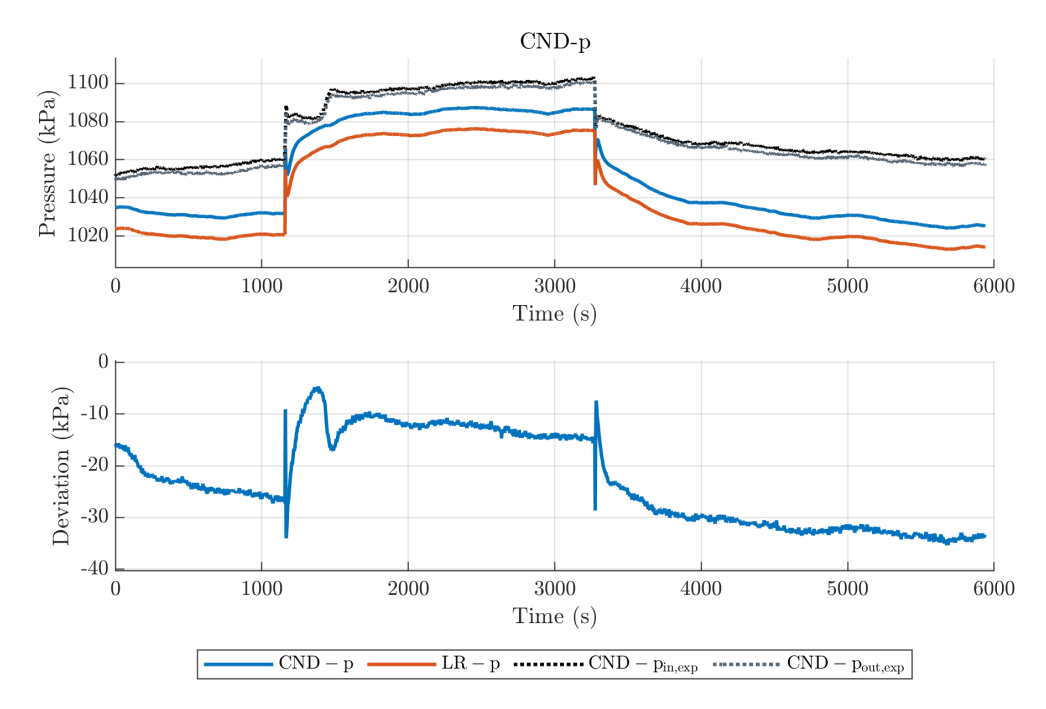


Figure 92: Condenser pressure: Full Model, Test 2 with R450A, condenser model with 30 elements and Tune 1, $x_{0,LR} = 0$ .

evaluated with a steady state deviation in the reference states below 20-30 kPa, which is in agreement with the Simplified Model which stabilises around a deviation of 20 kPa, fig. 74. In the central part of the test, where the compressor frequency is reduced, the pressure deviation is around 20 kPa, which is slightly worse than the Simplified Model, fig. 74. For what concerns the evaporator, the calculated pressure with the receiver completely full of liquid is in line with the results obtained by Simplified Model, as can be appreciated comparing the fig. 93 and fig. 91.

From the above analysis it can be concluded that the receiver downstream the condenser is completely full of subcooled liquid refrigerant during normal operation, and the SA is completely full of superheated vapour. Personal communication with prof L. Molinaroli who set up the experimental rig supports this statements. From fig. 94, the temperature of the liquid refrigerant in the receiver is about 5 °C less than the condensation temperature calculated by the model. This value agrees with the calculated temperature at the condenser outlet, as illustrated in fig. 95. With respect to the Simplified Model, the refrigerant temperature is predicted with a deviation around 1 °C.

In the low pressure branch, the temperature follows the same behaviour. In the suction accumulator the superheated vapour has a temperature of about 8 °C, fig. 96, in accordance with the refrigerant temperature at the evaporator outlet, fig. 97. In this case, the accuracy of this calculation is approximately the same as for the Simplified Model, fig. 70.

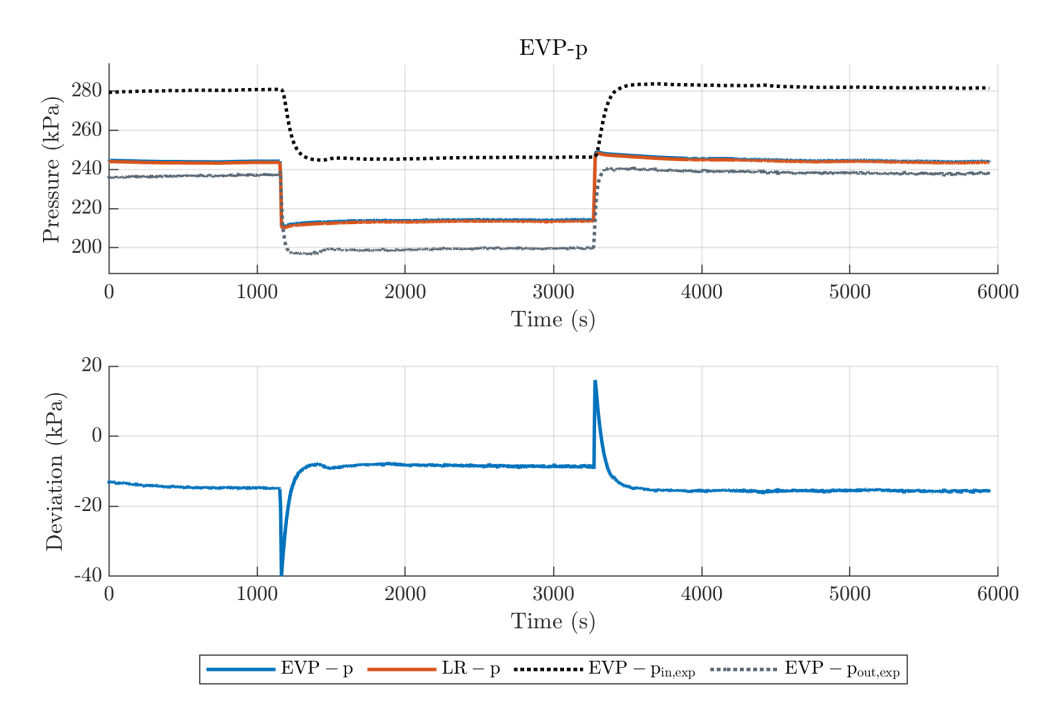


Figure 93: Evaporator pressure: Full Model, Test 2 with R450A, evaporator model with 20 elements and Tune 1,  $x_{0,LR} = 0$ .

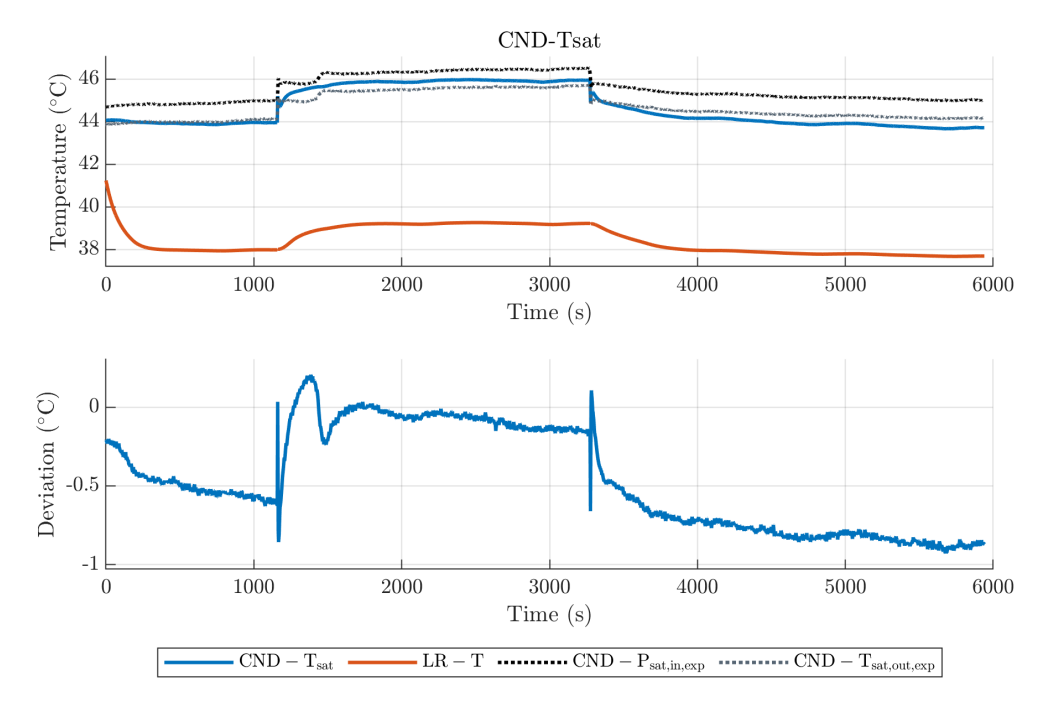


Figure 94: Condenser saturation and LR temperatures: Full Model, Test 2 with R450A, condenser model with 30 elements and Tune 1.

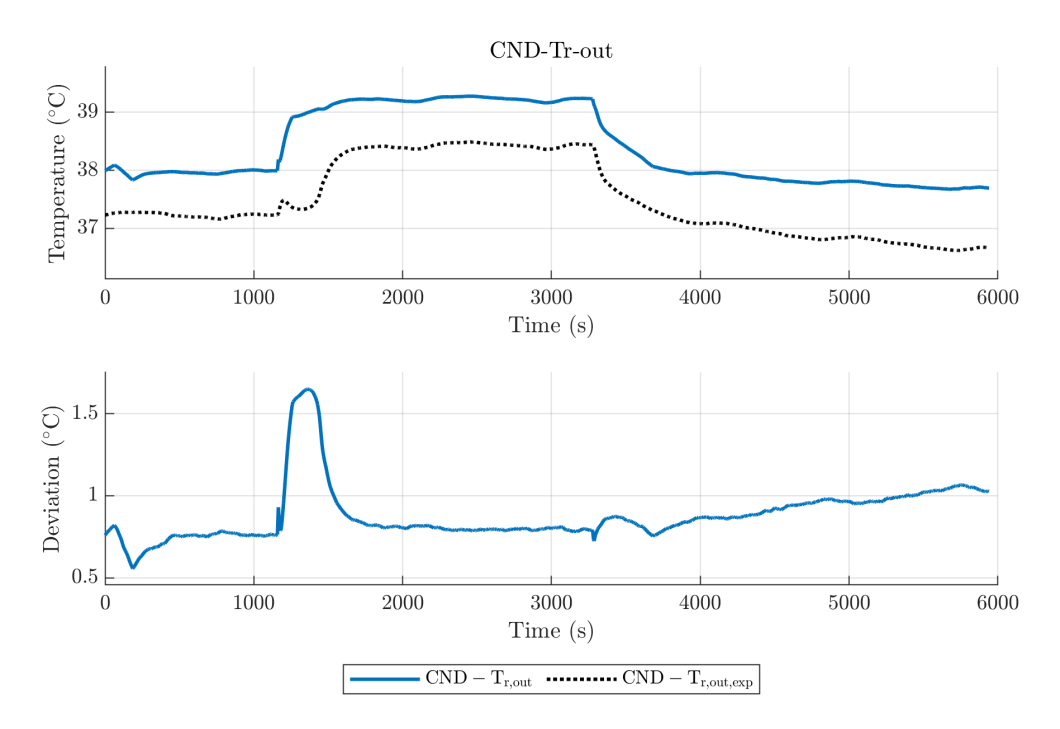


Figure 95: Condenser refrigerant outlet temperatures : Full Model, Test 2 with R450A, condenser model with 30 elements and Tune 1.

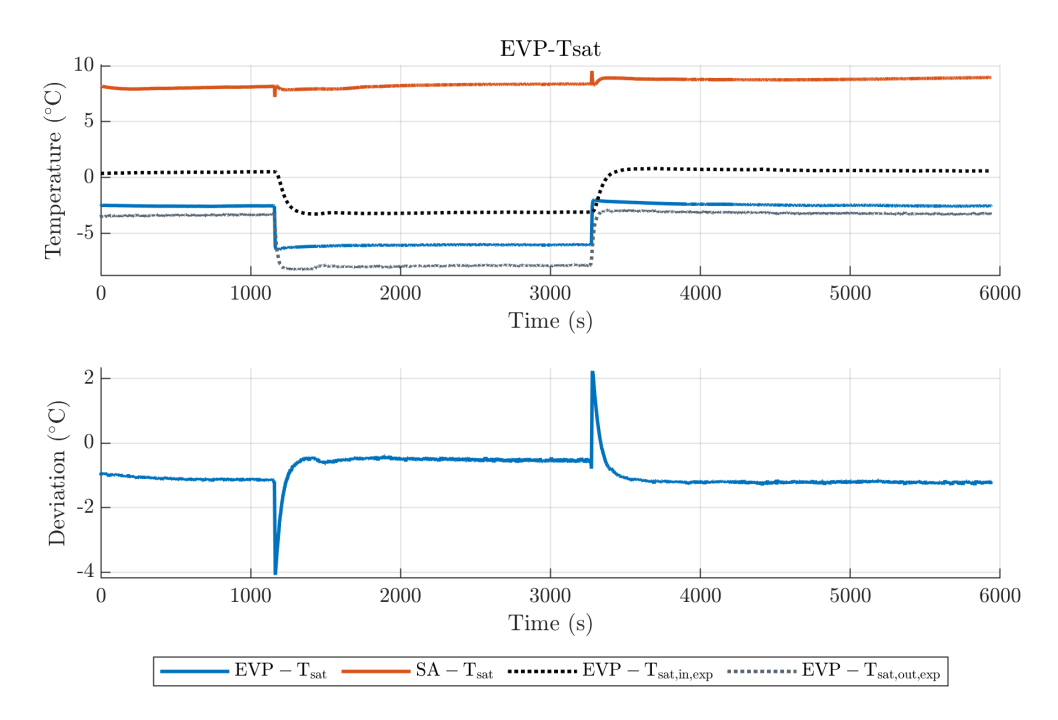


Figure 96: Evaporator saturation and SA temperatures: Full Model, Test 2 with R450A, evaporator model with 20 elements and Tune 1.

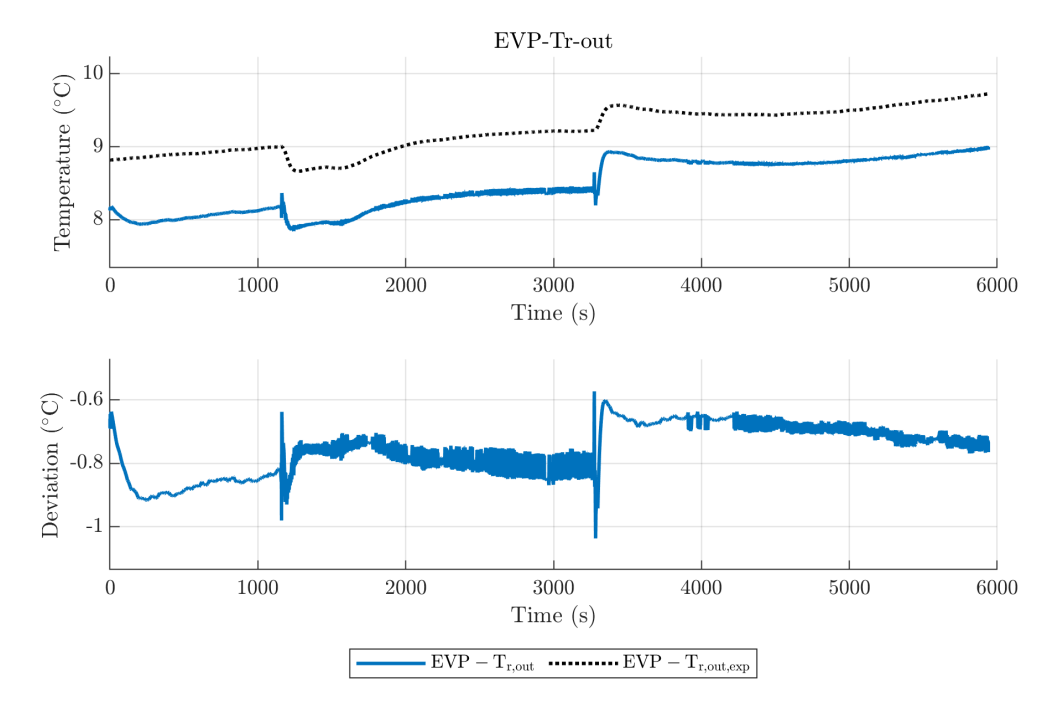


Figure 97: Evaporator refrigerant outlet temperatures : Full Model, Test 2 with R450A, evaporator model with 20 elements and Tune 1.

#### Validation of the Full Model in Test 1 with R450A

In this section, the performance of the Full Model is verified employing the experimental data of Test 1 with R450A. The set of correction factors of Tune 1 are applied to the condenser model HTCs, and it is assumed that the LR is completely filled with liquid.

Figure 98 shows the trends of the pressure levels in the condenser and in the LR calculated with the Full Model under Test 1 with R450A conditions. The average condenser pressure is underestimated by about 40-60 kPa. Despite a worse performance than that of Test 2 with R450A, fig. 92, it should be noticed that the saturation pressure is still within a maximum deviation of 2 °C, fig. 99. The temperature of the liquid refrigerant in the LR settles between 4-6 °C of subcooling, corresponding to the calculated temperature at the condenser outlet, fig. 100; the refrigerant temperature is estimated with deviation respect to the experimental data between 0.8-1.4 °C. The best accuracy is achieved by the water temperature at the condenser outlet, which shows a deviation around 0.1 °C, excluding the peaks. Finally, it should be noticed the presence of some bounded oscillations in both temperature profiles that correspond to the oscillations of the pressure in the LR. This numerical issue is inherent to the models of the accumulator and pipe. The straightforward solution is to reduce the integration time step, but it is undesirable due to the increasing of the run time. A different selection of the pipe time constant (see chapter 7) may lead to better performance.

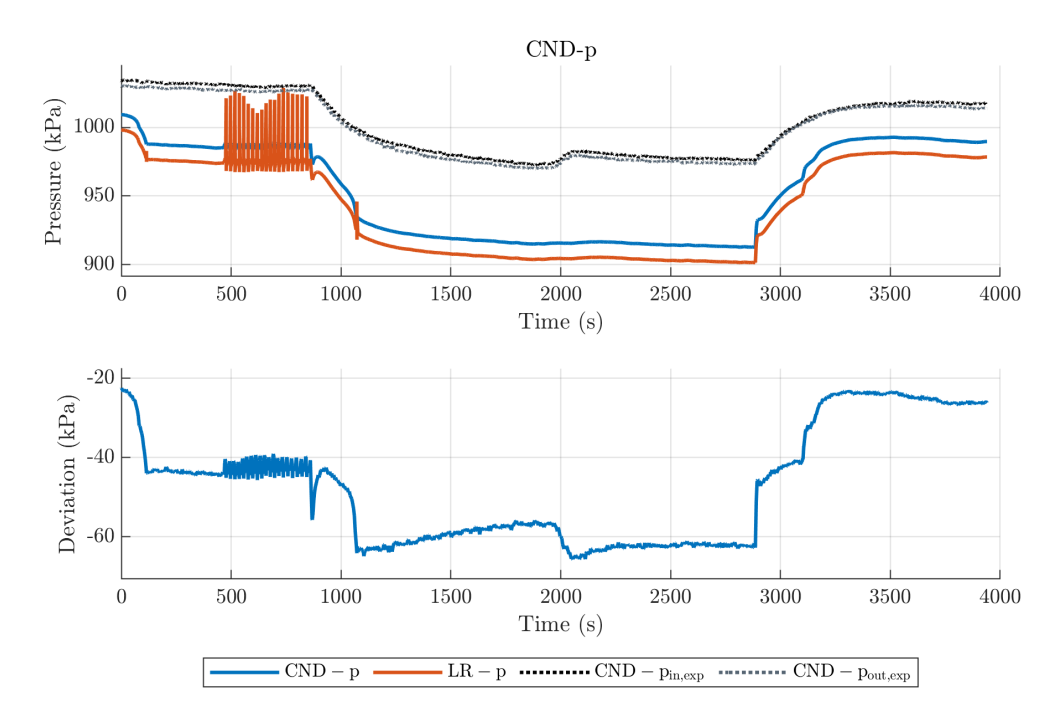


Figure 98: Condenser pressure:Full Model, Test 1 with R450A, condenser model with 30 elements and Tune 1,  $x_{0,LR} = 0$ .

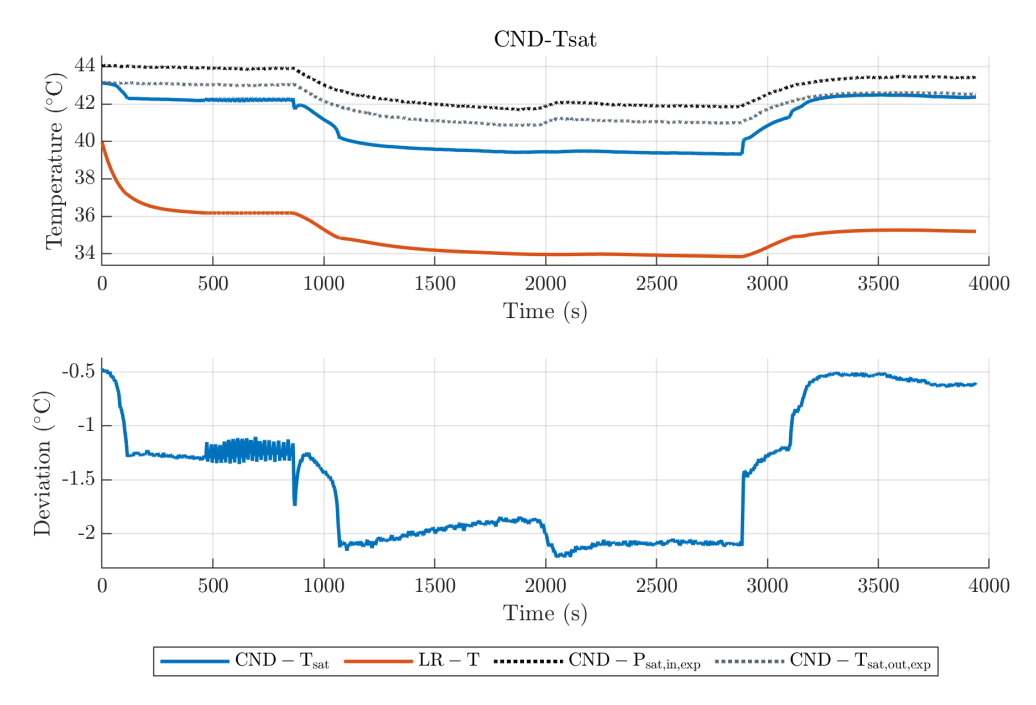


Figure 99: Condenser saturation and LR temperatures: Full Model, Test 1 with R450A, condenser model with 30 elements and Tune 1,  $x_{0,LR} = 0$ .

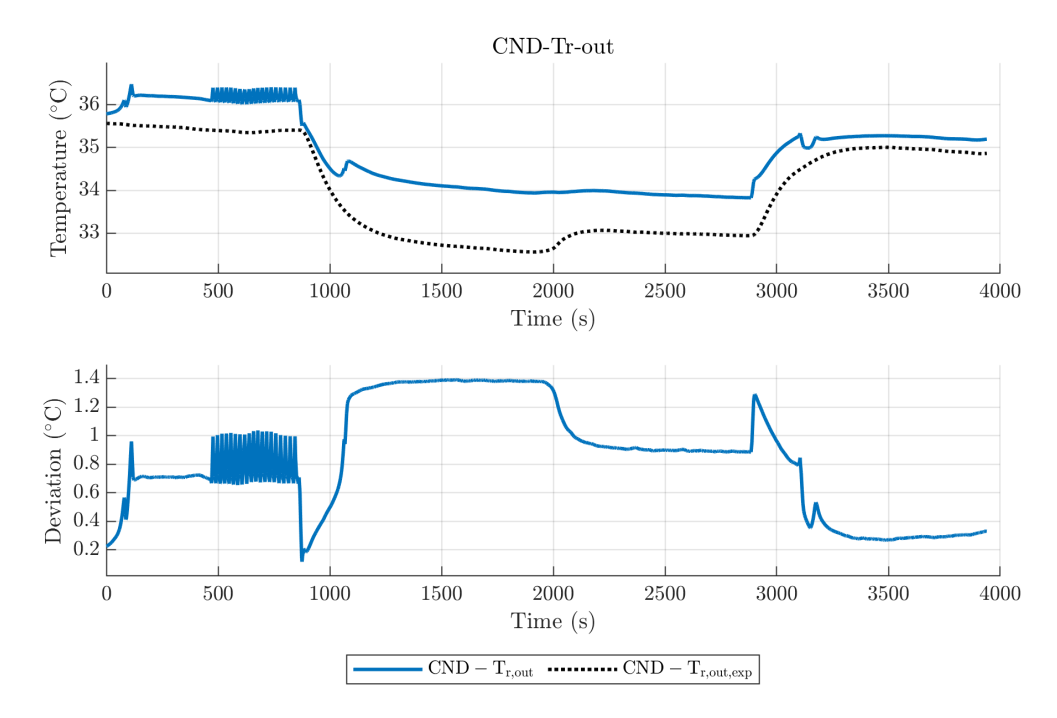


Figure 100: Condenser refrigerant outlet temperature: Full Model, Test 1 with R450A, condenser model with 30 elements and Tune 1,  $x_{0,LR} = 0$ .

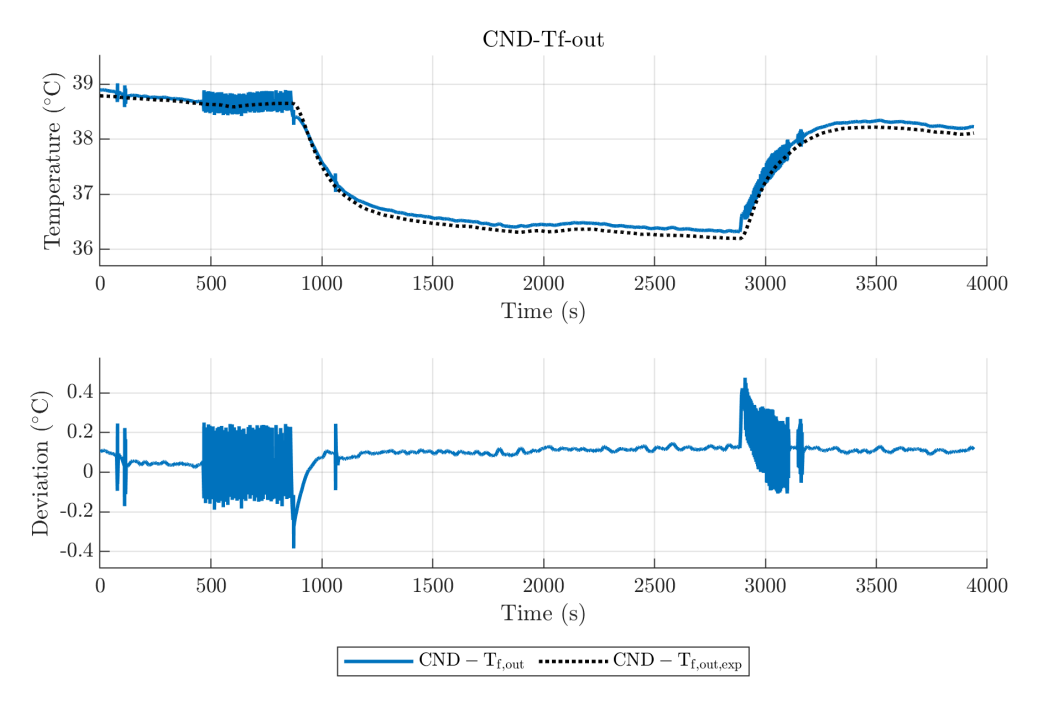


Figure 101: Condenser secondary fluid outlet temperature: Full Model, Test 1 with R450A, condenser model with 30 elements and Tune 1,  $x_{0,LR} = 0$ .

On the evaporator side, the saturation pressure is captured better; the calculated values stabilise around 20 kPa of deviation with respect to the mean measured pressure on the cold branch. Moreover, in this case, the calculated pressure is almost superimposed to the values of the inlet pressure from the experimental measurements, as can be appreciated in fig. 104. Also, the saturation temperature shows a very good accuracy, fig. 105. The outlet refrigerant temperature is slightly underestimated; the worst results are obtained during the opening reduction phase, with a deviation of about 1 °C. The steady state is slightly different before and after the transient. For the condenser, the best accuracy is similarly reached by the estimation of the temperature of the secondary fluid; in this case, the deviation is negligible, excluding the peaks.

# Evaluation of the pressure losses in the HEXs

From the pressure measurements available it is possible to estimate the contribution of the friction losses in the condenser at 3-5 kPa; this is true for both tests: see fig. 84 for Test 1 with R450A and fig. 58 for Test 2 with R450A. Conversely, a difference of the order of 40 kPa can be appreciated between the inlet and outlet section of the evaporator, see fig. 85 for Test 1 with R450A and fig. 65 for Test 2 with R450A. The first reason is imputable to the positioning of the pressure transducer, as discussed in section 3.1; indeed, the pressure measurement is available only at the compressor inlet. Secondly, the pressure at the evaporator inlet is calculated from the temperature and assuming an isoenthalpic process through the valve. The difference between the two values can be attributed to the pressure losses in the three components of the cold branch, the evaporator, the pipe and the suction accumulator. Also, the pipe contribution to the friction losses is evaluated in the order of 1-2 kPa m<sup>-1</sup>, see fig. 37. The last contribute is that due to the SA, which can be treated as a localised pressure losses. This evaluation is confirmed by the pressure measurements available in the hot branch, where the transducers are positioned at the ends of the condenser and at the compressor outlet. Between them, the oil separator is installed. Figure 102 and fig. 103 show the comparison between the pressure measurements in the hot branch of the cycle under Test 1 with R450A and Test 2 with R450A respectively. The pressure drop in the line between the compressor and the condenser can be estimated to be around 10 kPa in both cases.

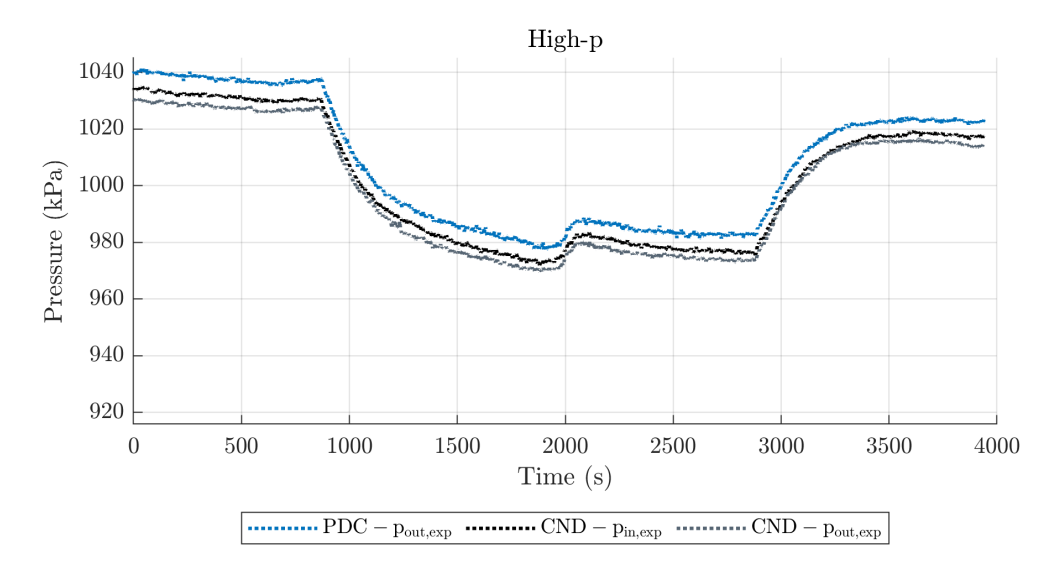


Figure 102: Pressures in the hot branch, condenser inlet and outlet and compressor outlet, during Test 1 with R450A.

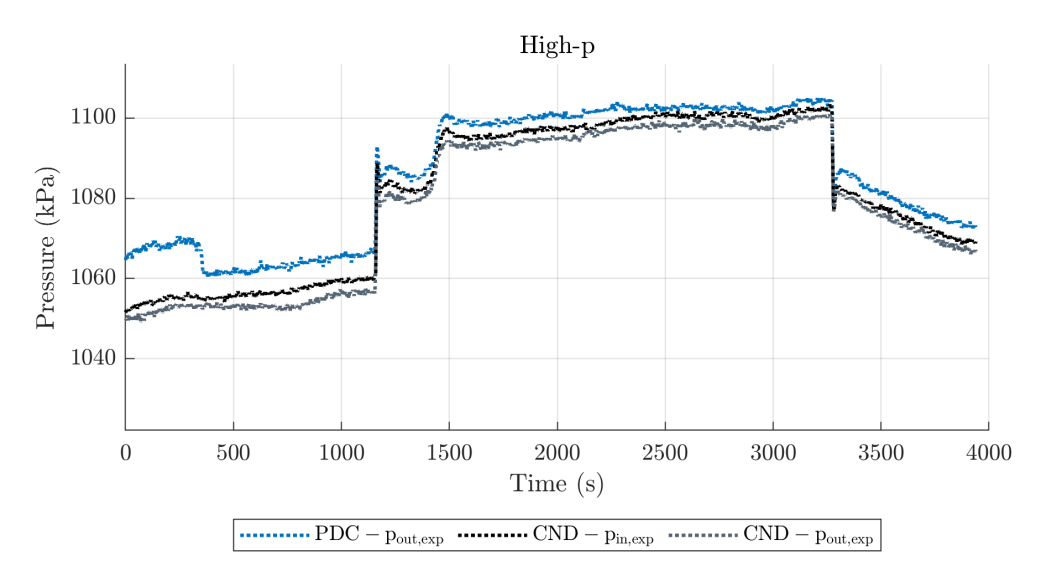


Figure 103: Pressures in the hot branch, condenser inlet and outlet and compressor outlet, during Test 2 with R450A.

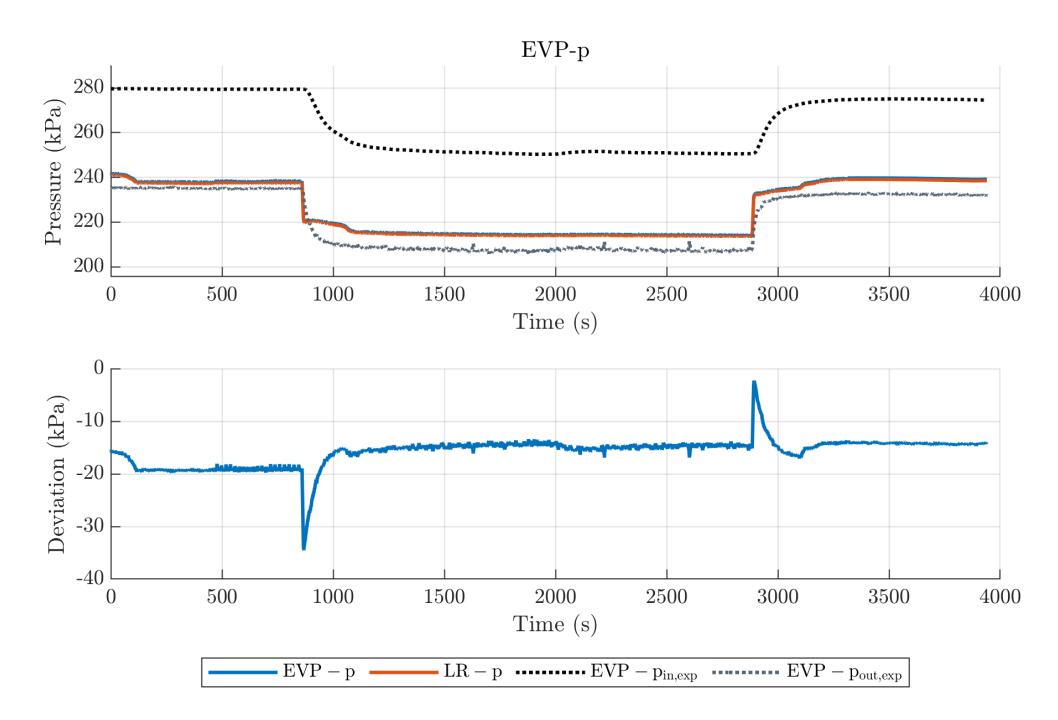


Figure 104: Evaporator pressure:Full Model, Test 1 with R450A, evaporator model with 20 elements and Tune 1,  $x_{0,LR} = 0$ .

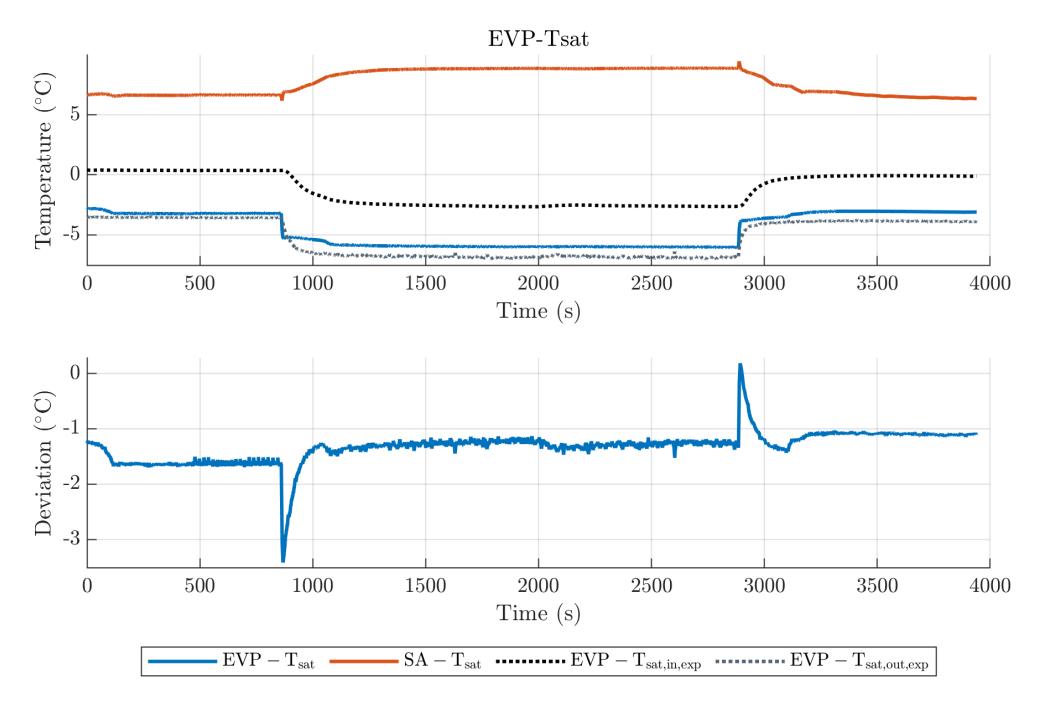


Figure 105: Evaporator pressure and SA temperatures: Full Model, Test 1 with R450A, evaporator model with 20 elements and Tune 1,  $x_{0,LR} = 0$ .

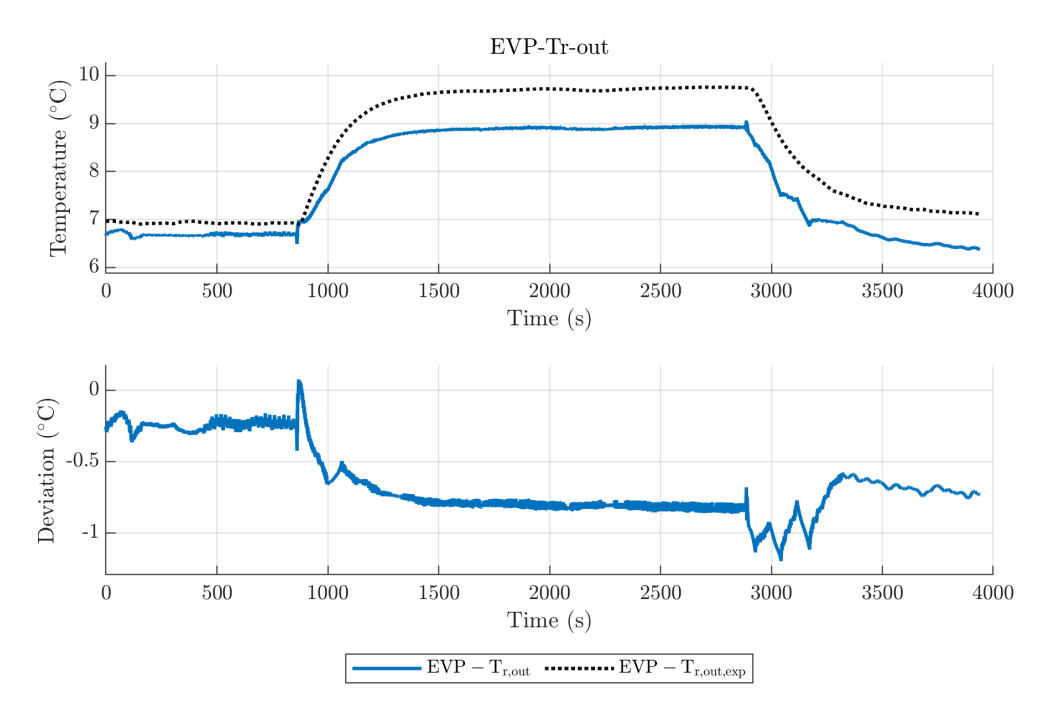


Figure 106: Evaporator refrigerant outlet temperatures: Full Model, Test 1 with R450A, evaporator model with 20 elements and Tune 1,  $x_{0,LR} = 0$ .

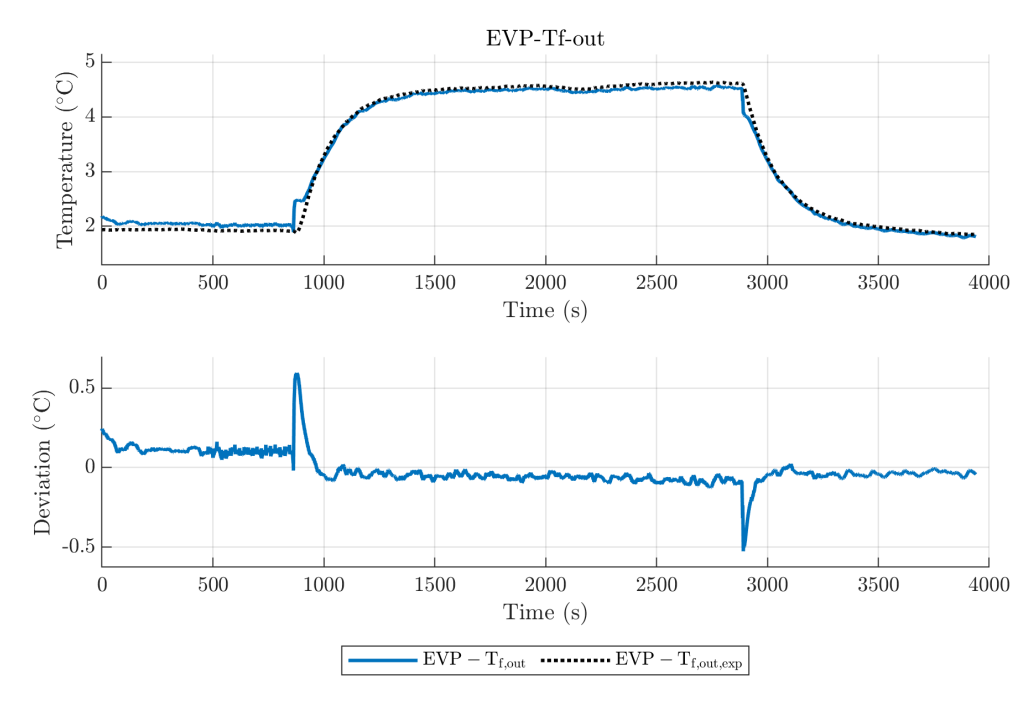


Figure 107: Evaporator secondary fluid outlet temperatures: Full Model, Test 1 with R450A, evaporator model with 20 elements and Tune 1,  $x_{0,LR} = 0$ .

#### 11.5 COMPRESSOR AND EXPANSION VALVE

In this section, the behaviour of the compressor and expansion valve model are investigated. Three quantities are examined: refrigerant mass flow rate, refrigerant outlet temperature and electric power consumption. Both the Simplified Model and Full Model are employed using the Test 1 with R450A and Test 2 with R450A experimental data.

#### Simplified Model Test 1 with R450A 11.5.1

### Refrigerant mass flow rate

The refrigerant mass flow rate is overestimated by the physical model of the compressor with a deviation of about 2.5% excluding the peaks in the proximity of the transients, as can be appreciated in fig. 108. This result is slightly different from that obtained during validation of the compressor model, fig. 25, in which the deviation was negligible. However, during the validation of the single component, the inputs provided to the model are direct measurements of the pressure and temperature at the inlet section and the pressure at the outlet. When used to simulate a whole VCS, the inputs provided are the values calculated by the other components, specifically the condenser pressure, the evaporator pressure and the refrigerant temperature at the evaporator outlet. Applying the Tune 1 correction to the condenser HTC, the averaged pressure level are underestimated with a deviation of the order of -20 kPa in the reference states and -40 kPa during the valve opening reduction, fig. 78. On the evaporator side, the average pressure is evaluated with a deviation below 20 kPa; however relative to the pressure measured at the compressor inlet, which is assumed equal to that at evaporator outlet, as discussed in section 3.1, the difference settles around -40 kPa, fig. 85. Overall, these variations shift the operating point of the compressor towards a slightly higher pressure ratio, which tends to reduce the mass flow rate; the decrease of the suction pressure results in the intake of superheated vapour with higher density. The combined effect is that the compressor model overestimates the mass flow rate by about 2.5%.

#### Refrigerant temperature at the compressor outlet

The temperature of the refrigerant at the compressor outlet is underestimated of a maximum of 2 °C, as can be appreciated in fig. 109. The significant peaks produced by the physical model in correspondence of the transients are an unpleasant behaviour. However, the dynamic correction applied allows for smoothing, improving the reliability of the predicted value and the stability of the condenser model, which receives it as input. The temperature deviation is greater than that

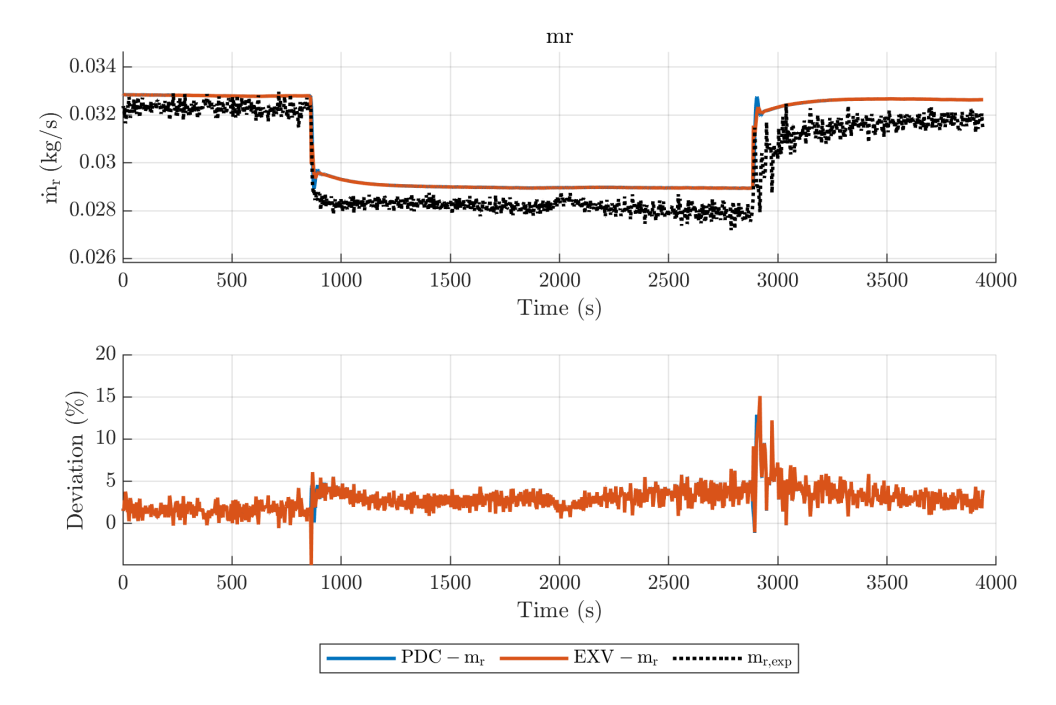


Figure 108: Refrigerant mass flow rate: Simplified Model, Test 1 with R450A,.

manifested during the validation procedure and the development of the dynamical correction. The reasons are the same as presented for the mass flow rate. Indeed, the model calculates the outlet temperature as a function of the pressure levels, which are slightly shifted towards smaller values, as said before. So, the calculated outlet temperature is lower than that of the experimental data. The dynamical correction allows better capturing of the transients but brings negligible improvements to the steady state estimation.

#### Electric power consumption

The electric power consumption is calculated with a deviation below 5%, as can be appreciated in fig. 110. This value is obtained by applying the efficiency factor of electric-mechanical energy conversion to the calculated value of the power delivered to the fluid by the compressor. Without better information, this efficiency is assumed to be  $\eta = 0.95$ ; the electric power consumption value provided by the physical model was proven in good agreement with that obtained employing the polynomial model, see section 6.4.2.

# Simplified Model Test 2 with R450A

#### Refrigerant mass flow rate

The Simplified Model under Test 2 with R450A conditions provides an estimation of the mass flow rate with a maximum deviation around

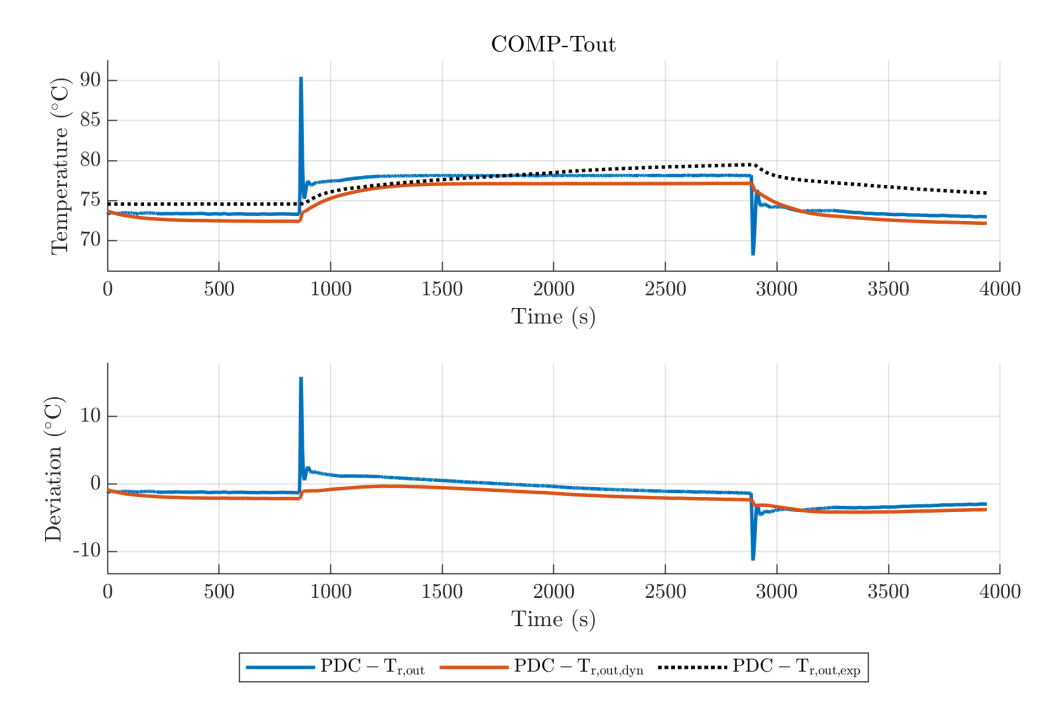


Figure 109: Refrigerant temperature at the compressor outlet: Simplified Model, Test 1 with R450A.

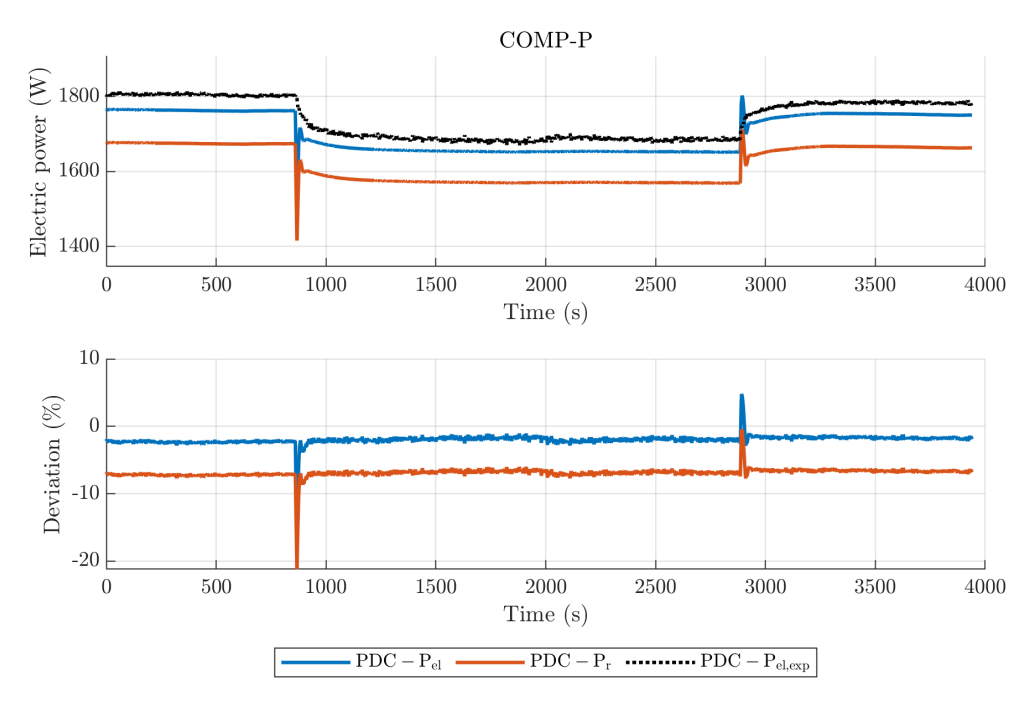


Figure 110: Electric power consumption and power delivered to the fluid by the compressor: Simplified Model, Test 1 with R450A.

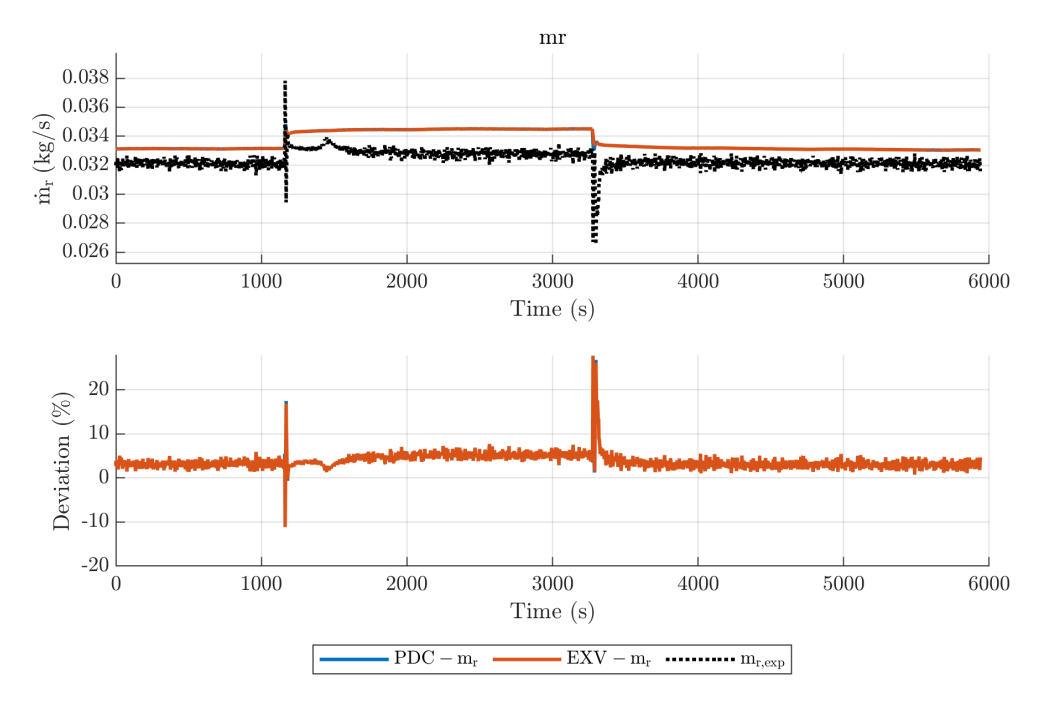


Figure 111: Refrigerant mass flow rate: Simplified Model, Test 2 with R450A.

5 % excluding the peaks, fig. 111. The accuracy is worse than in the previous case.

The condenser pressure is underestimated by about 10-20 kPa, fig. 74 The average pressure in the evaporator is calculated with a deviation below 20 kPa than the mean pressure. However, the pressure at the evaporator outlet, which is equal to those at the compressor inlet is larger than the calculated value of 30-40 kPa. The combined effect of these two factors leads to an overestimation of the mass flow rate by the physical model of the compressor.

### Refrigerant temperature at the condenser outlet

The temperature of the refrigerant at the compressor outlet is evaluated with a deviation below 5 °C, not considering the peaks, fig. 112. The dynamic correction enhances the accuracy of the predicted values during the transient but does not significantly affect the steady state evaluation. Indeed, the dynamic correction acts on the static temperature provided directly by the compressor model and depends on the operating pressure levels. Since the calculated pressure ratio during the initial and final phase is lower than that measured, the same occurs for the static refrigerant temperature. The opposite happens during the compressor frequency variation, when the static temperature exceeds the measured value.

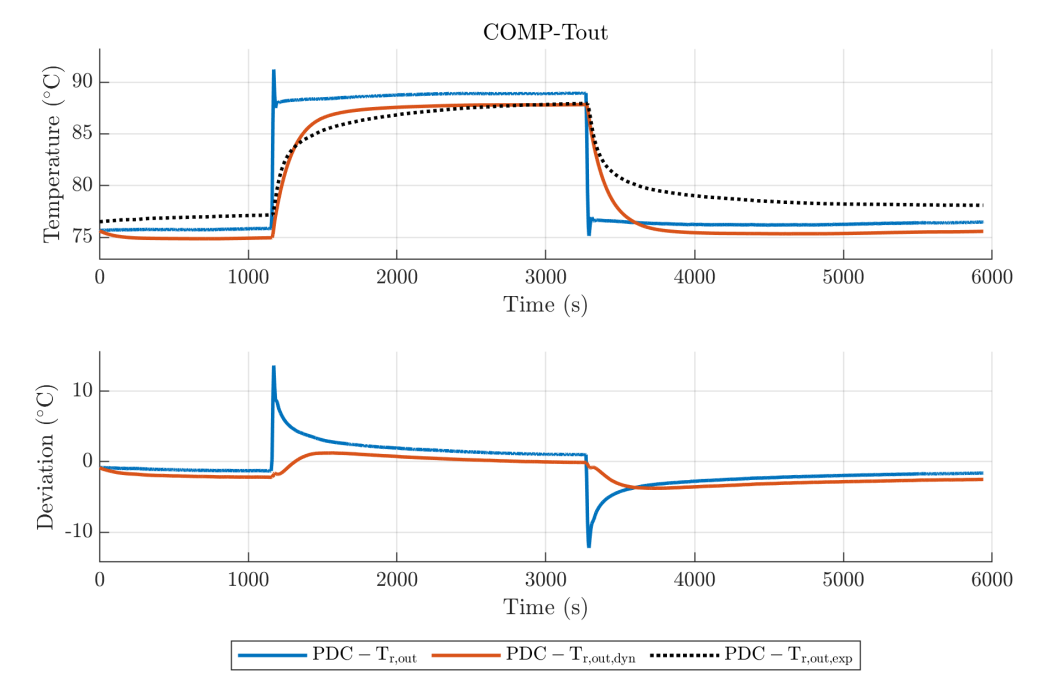


Figure 112: Refrigerant temperature at the compressor outlet: Simplified Model, Test 2 with R450A.

### Electric power consumption

The electric power consumption is accurately calculated in the initial and final phase when the compressor frequency is at 50 Hz. In the central portion of the test, when the compressor speed up, a deviation of about 5% is present, fig. 113.

#### Full Model Test 1 with R450A 11.5.3

## Refrigerant mass flow rate

Figure 114 shows the evaluation of the refrigerant mass flow rate obtained with the Full Model under Test 1 with R450A conditions, which is very accurate. Only the valve flow rate exhibits an oscillating behaviour in correspondence of the pressure oscillation in the LR seen in fig. 98. The maximum deviation is reached in the last part of the test, and is about 2.5%.

## Refrigerant temperature at the condenser outlet

The refrigerant temperature at the condenser outlet is affected by some inaccuracies. Indeed, in the first part of the test, the steady state value is captured with the static model with a deviation in the order of  $\ensuremath{^{\circ}\text{C}}.$  In the following, the model produces a different trend from that of the experimental data, and the maximum deviation reaches 4 °C. The dynamic correction, as for the Simplified Model allows to better

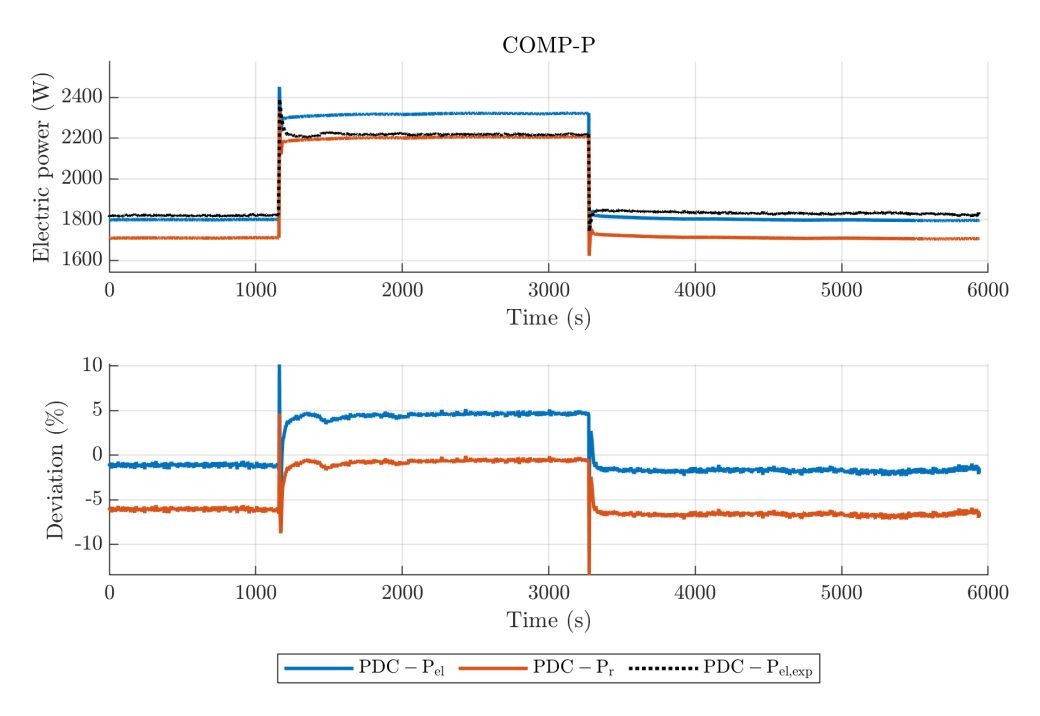


Figure 113: Electric power consumption and power delivered to the fluid by the compressor: Simplified Model, Test 2 with R450A.

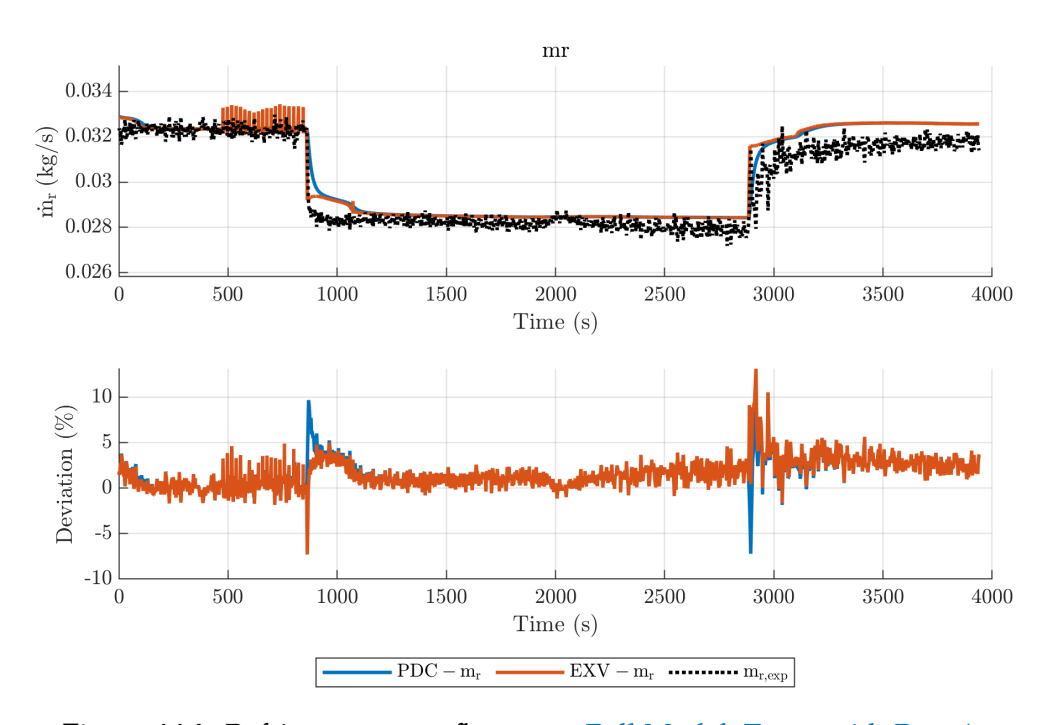


Figure 114: Refrigerant mass flow rate: Full Model, Test 1 with R450A.

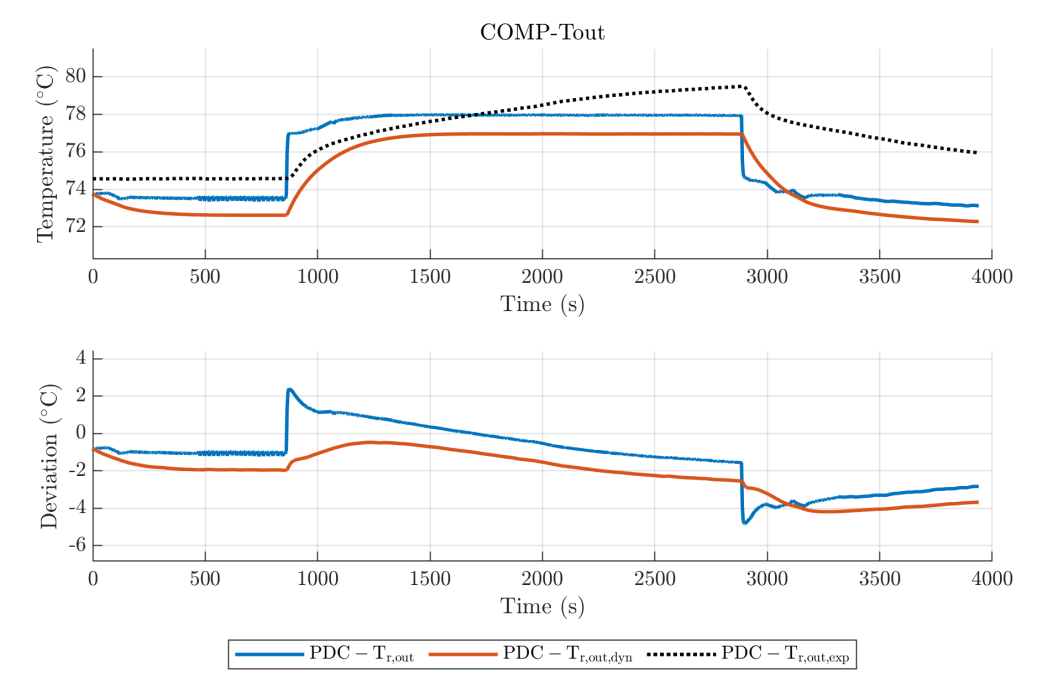


Figure 115: Refrigerant temperature at the compressor outlet: Full Model, Test 1 with R450A.

capture the transient behaviour, but the steady state value must be captured by the static model, otherwise the correction is useless. The static temperature is influenced by the pressure levels calculated by the models of the condenser and evaporator; the reduction of the pressure ratio in the experimental data leads to an underestimation of the outlet temperature. An improvement in the tuning of the dynamic correction block may probably lead to a further increase in the accuracy of the refrigerant temperature.

#### Electric power consumption

From fig. 116 the compressor power consumption is well estimated with a maximum deviation of 5%.

#### Full Model Test 2 with R450A

#### Refrigerant mass flow rate

As with the Simplified Model, the refrigerant mass flow rate is estimated with a deviation below 5%, fig. 117.

#### Refrigerant temperature at the condenser outlet

The refrigerant temperature at the compressor outlet is better captured during the Test 2 with R450A conditions than for Test 1 with R450A, almost independently of the presence of the accumulators, fig. 118.

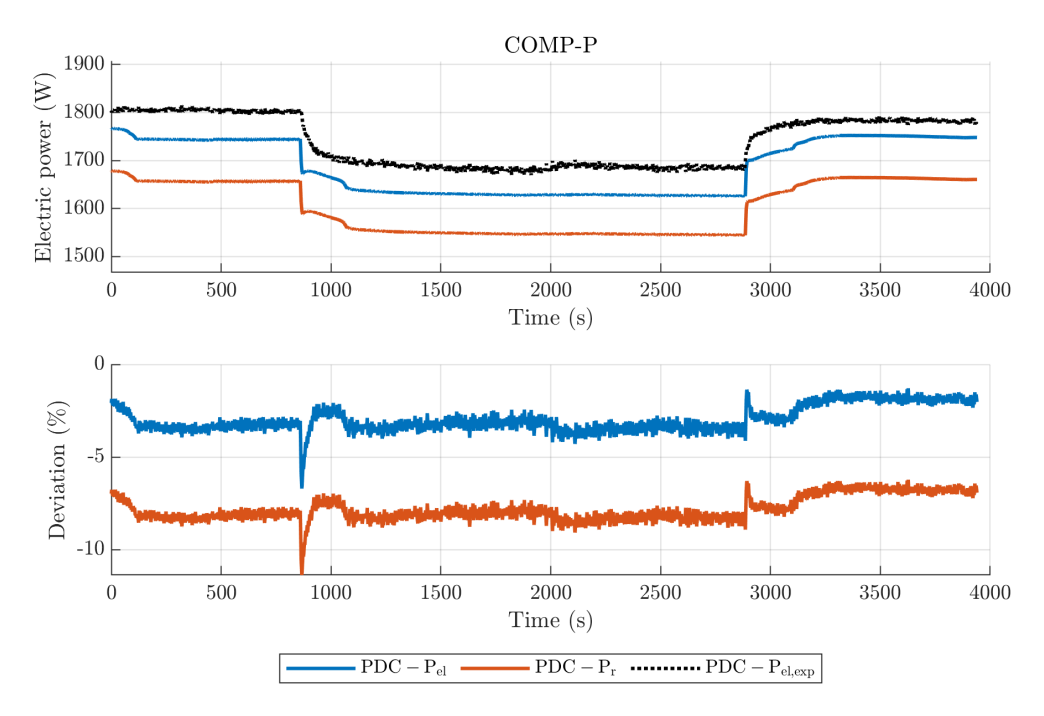


Figure 116: Electric power consumption and power delivered to the fluid by the compressor: Full Model, Test 1 with R450A.

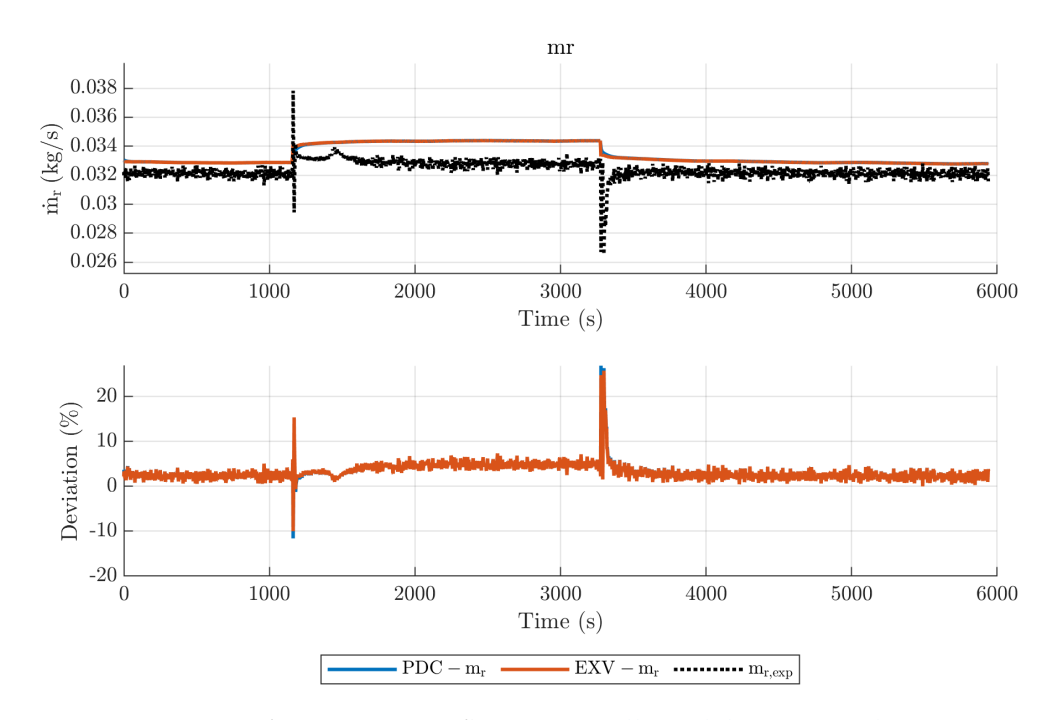


Figure 117: Refrigerant mass flow rate: Full Model, Test 2 with R450A.

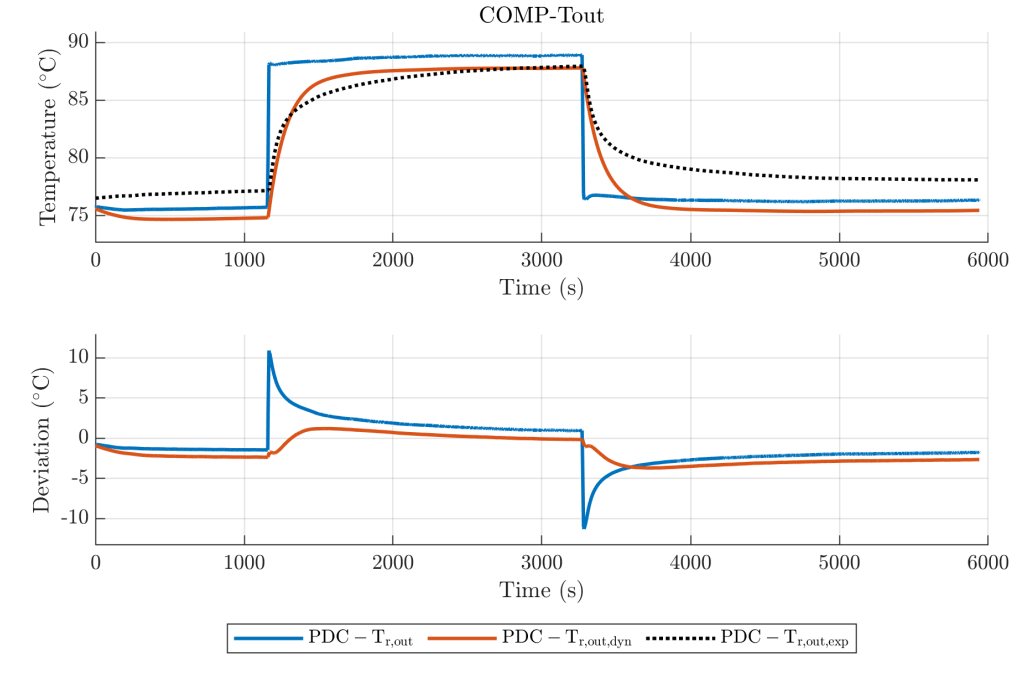


Figure 118: Refrigerant temperature at the compressor outlet: Full Model, Test 2 with R450A.

#### Electric power consumption

Figure 119 shows that the electric power consumption is accurately calculated in the initial and final phase with an absolute error of about 1%, as for with the Simplified Model, fig. 113; when the compressor speed up the deviation increase to about 5%.

#### 11.6 SUMMARY OF THE RESULTS

All in all, the VCS dynamical model realized in this work is able to predict the process variable with good accuracy. Two numerical models were tested, the Simplified Model and the Full Model, against the experimental data collected in two tests Test 1 with R450A and Test 2 with R450A.

The average pressure in the condenser settles around 20-40 kPa of deviation from the experimental data corresponding to about 1 °C in the estimation of the saturation temperature. The accuracy of both models is very similar; the worst case occurs employing the data from Test 1 with R450A, where the condensation pressure exhibits a maximum deviation around 50 kPa. The refrigerant temperature at the condenser outlet is affected by a lager deviation, around 1.5 °C without HTC tuning. On one side, the single coefficient tuning improves the pressure evaluation, but also increases the error on refrigerant

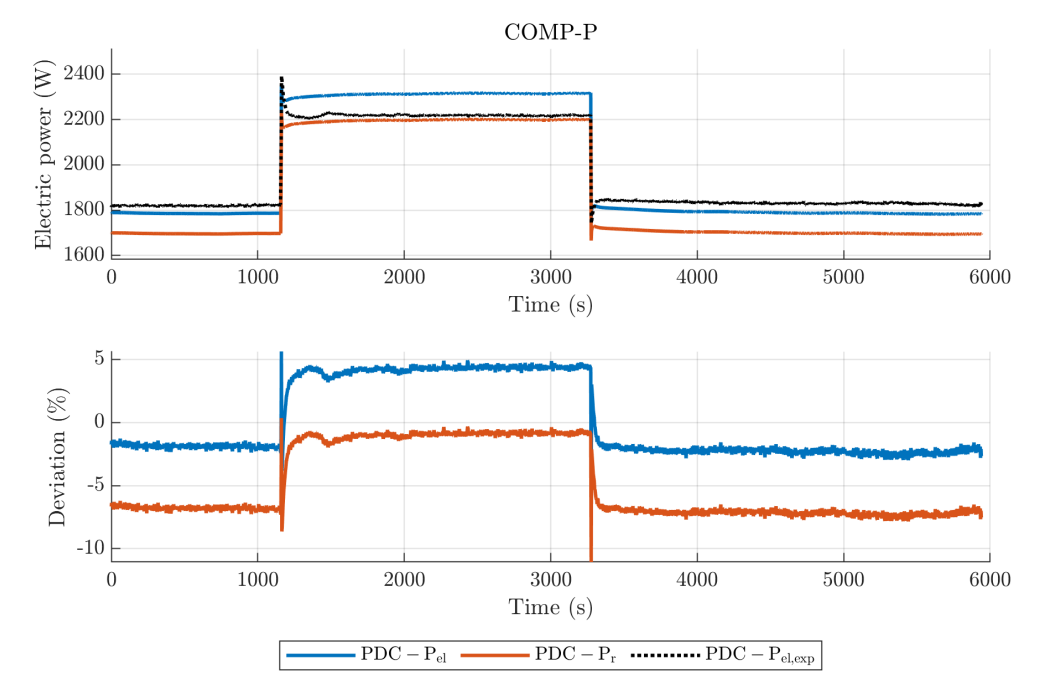


Figure 119: Electric power consumption and power delivered to the fluid by the compressor: Full Model, Test 2 with R450A.

temperature to almost 2.5 °C. Introducing two coefficients reduces this deviation to less than 1 °C.

At the evaporator, the evaluation of the interesting quantities shows better reliability; indeed, no tuning is deemed necessary. The saturation pressure shows a maximum deviation around 20 kPa corresponding to less than 1 °C in the saturation temperature. The estimation of the refrigerant temperature stays within 1 °C of the data. The best results was obtained in the secondary fluid temperature calculation in both HEXs. The temperature deviation is below 0.5 °C and is even better in some tests.

The accumulator's models do not seem to provide a decisive variation in the estimation of the steady-state operating point of the plant. Their contribution regards the damping of the variation of the mass flow rate induced by the compressor. Indeed, the static model of the compressor provides a step variation of the output quantities, which are not physically consistent and even lead to numerical failure of one of the HEX models (more often the condenser); to overcome this problem a first-order dynamic is introduced to damper the calculated mass flow rate with a time constant  $\tau$ =20 s. This is an unnecessary correction in the Full Model. If it used, the Full Model cannot reach a stable operating point due to different response times of the compressor and expansion valve; a variation of the mass flow rate calculated by the former is perceived with a certain delay by the latter.

The LR pressure is lower than that in the condenser due to friction losses in the pipe and liquid head, which is the dominating effect. In

Accumulator dynamic effects

Accumulator pressure levels contrast, the pressure in the SA is very similar to that in the evaporator because the pressure losses and the vapour head are negligible.

The LR initial conditions considerably influence the working point of the plant; the tests performed lead to the conclusion that the LR should be full of liquid refrigerant in both the experimental conditions examined. However, with the experimental apparatus available, verifying this information and validating the accumulator models in detail was impossible.

The refrigerant mass flow rate is calculated within 5% of the experimental data. The worst case occurs in the compressor frequency transients Test 2 with R450A. The compressor power consumption is evaluated with a maximum deviation of 5% employing the physical model. Finally, the refrigerant temperature at the compressor outlet exhibited a deviation of 1-2 °C. The imprecision in the evaluation of these quantities is related to the propagation of the error in the compressor model; indeed, although during component validation the compressor model exhibits a very good accuracy, the deviation of the input pressure values provided by the HEX models results in a variation of the working point of the compressor.

These deviations found in the evaluation of the process variables lead to a cumulative error when they are used for the estimation of the global performance of the VCS. Starting with the low pressure branch, from the experimental data (see figs. 16 and 17) the evaporator operates with a temperature difference of about 4.5 °C on the secondary fluid side. An error of 0.5 °C on its outlet temperature correspond to a 10% of relative deviation. Moreover, given a mass flow rate around  $0.27 \text{ kg s}^{-1}$ , this inaccuracy on the temperature leads to about 500 W of deviation on the thermal power exchanged with the environment over the total of about 5 kW. The same considerations can be made for the condenser. Indeed, the experimental data shows that it operates with a temperature difference of about 4 °C with a water mass flow rate of about 0.35 kg s<sup>-1</sup>. A deviation of 0.5 °C on the outlet temperature of the secondary fluid leads to a relative deviation of about 10% on the thermal power. The numerical simulations performed show that the deviation of the outlet temperature is almost independent on the thermal power exchanged; this can be appreciated in both Test 1 with R450A and Test 2 with R450A, and for both the HEXs. This behaviour implies larger inaccuracy in the heat transfer rate evaluation for small size systems.

### 12 | CONCLUSIONS

In this work, a fully dynamical simulation of a VCS is developed in the Simulink® environment. The model of each component was developed and validated individually: compressor, expansion valve, heat exchangers, liquid receiver suction, accumulator and pipes. Then, the single models were assembled to create a whole VCS, which was tested against experimental data collected from an experimental facility at the Polytechnic of Milan. Only the heat exchangers were treated with a distributed parameter approach; a lumped-parameter description was deemed to suffice for the remaining components.

Although the test rig was fully extant, extensive work on data processing was required to arrange them in the most suitable way for model validation, chapter 3. The experimental facility is described in detail and all the available measurements are analised in terms of accuracy and reliability for the simulation of transients. Similarly, thermodynamic data available from Coolprop and RefProp had to be arranged into Lookup Tables carefully defining both the bounds for the independent variables and the way in which the derivatives of the dependent quantities had to be obtained, chapter 4.

In chapter 6, the basic compressor model was defined as a static system; indeed, no state variables have been proven necessary. Two different realizations were proposed: a black-box model employing third-degree polynomial correlations according to the reference standards, and a grey-box model using the fundamental physical relation that describes the compression of a fluid. The volumetric and isoentropic efficiencies were estimated from the rated data of the manufacturer. The model was validated by comparison of the calculated mass flow rate, power consumption, and refrigerant outlet temperature with experimental data for R450A. A dynamic correction was developed to enhance the accuracy in the prediction of the outlet temperature, capturing the transient due to the thermal capacitance of the compressor case. Different realizations were investigated; the best performance was obtained with a dynamic correction which accounts for the thermal capacitance of the case and the heat transfer between the refrigerant and the ambient air.

A static model was also devised for the expansion valve in chapter 8, using an empirical correlation provided by the manufacturer. Nonetheless, tuning the flow coefficient was necessary to achieve a satisfactory accuracy in the estimation of the steady-state mass flow rate compared with the experimental data.

The model for piping was developed as described in chapter 7, to evaluate the flow rate between components that can store refrigerant mass and energy, such as heat exchangers or vessels; the static model can deal with both single and two-phase fluids by employing the homogeneous flow assumption for the evaluation of the friction factor. The localised pressure losses are also integrated in the model with the equivalent length approach. .

Dynamical modelling of pieces of equipment for refrigerant storage, such as liquid receivers and suction accumulators was described in chapter 9. Two numerical set-ups were developed to investigate the numerical stability and reliability of both accumulators and piping, before employing them in the simulation of the whole VCS.

The largest effort was devoted to developing the dynamical model of the heat exchangers. The finite volume approach was selected, pursuing accuracy and flexibility. However, some manipulations became necessary to ensure numerical stability, robustness and suitable run time. Beside the mass filtering that reduces the stiffness of the problem, the spatial smoothing of the HTCs was proven capable to enhance the robustness of the model. The HTCs were evaluated directly by employing the correlations ideal for the specific arrangement to enhance the accuracy. In this way, replacing the correlation used to suit the HEX configuration employed is relatively easy. This work presents a counter-flow configuration but also co-flow and cross-flow arrangements were developed and tested.

Finally, the simulation of the whole system was carried out assembling the component models previously developed. It was validated in two configurations: one employing only the four main components, compressor, expansion valve, condenser and evaporator, the other including also the liquid receiver and the suction accumulator with the connecting pipes.

A great effort was devoted to investigating the physical, mathematical, and numerical assumptions made while developing the models to highlight their positive and negative factors. Many of the auxiliary options related to the development and experimental validation of the models were investigated: the mathematical formulation of the dynamical system, the evaluation of the physical properties of the working fluids, the accuracy of the experimental data and their dynamic reliability, the effect of the integration time step and the grid dependence of the finite volume model.

Overall, the VCS dynamical model realized in this work can predict the process variables with reasonable accuracy. The refrigerant mass flow rate is calculated within 5% of the experimental data. The average pressure in the condenser settles around a deviation of 30-40 kPa corresponding to less than 1 °C in the estimation of the saturation temperature. The refrigerant temperature at the condenser outlet is

affected by a larger deviation from the experimental data, around 1.5 °C without HTC tuning. Introducing proper correction coefficients reduces this deviation to less than 1 °C. On the evaporator side, the evaluation of the quantities of interest shows better reliability; indeed, no tuning was deemed necessary. The saturation pressure shows a maximum deviation around 20 kPa corresponding to less than 1 °C in the saturation temperature. The refrigerant temperature at the outlet is estimated within 1 °C of the data. The best results were observed in the calculation of the temperature of the secondary fluid in both HEXs. The temperature deviation is less than 0.5 °C and is even better in some tests.

A future development for this work is the integration of the VCS model developed with the dynamical model of a controlled environment under real-life operating conditions. For example, the simulation of a refrigerated warehouse could be carried out, investigating the control strategies to minimise the overall energy consumption. The VCS model could also be interfaced with a heat-storage component, such as a phase change material, to investigate the advantages of this solution for demand shifting of the electric energy to more cost-effective time slots. Furthermore, this work deals with a water-to-water system with the HEXs in counterflow; different configurations can be investigated, like an air-to-air system with the HEX in crossflow or a VCS which integrates an evaporative condenser unit as those employed in large industrial applications. Finally, this model can also be employed for the simulation of the thermal management system of modern electric vehicles.

**Future** developments

# A | FUNDAMENTALS OF HEAT TRANSFER

### A.1 CONVECTIVE HEAT TRANSFER AT CONSTANT WALL TEMPERATURE

The global thermal power exchanged by a fluid flowing inside a tube can be evaluated as follows.

$$\dot{Q} = \dot{m}c_{p}(T_{f,o} - T_{f,i}) \tag{A.1}$$

This can be also evaluated employing the wall temperature. In this case the temperature profile in the portion of fluid involved in the process must be evaluated. Two approaches are compared: the exponential and the linear profile.

#### A.1.1 Exponential temperature profile

The local heat transfer rate is:

$$\begin{cases} d\dot{Q} = \dot{m}c_{p}dT_{f} \\ d\dot{Q} = \alpha A(T_{w} - T_{f}) \end{cases} \tag{A.2}$$

The above equations are manipulated to evaluate the fluid temperature distribution.

$$\begin{split} \dot{m}c_{p}dT_{f} &= \alpha(T_{w} - T_{f})dA \\ \frac{dT}{T_{w} - T_{f}} &= \frac{\alpha}{\dot{m}c_{p}}dA \\ -ln(T_{w} - T_{f}) &= \frac{\alpha A}{\dot{m}c_{p}} + C \\ T_{w} - T_{f} &= e^{-\frac{\alpha A}{\dot{m}c_{p}}}e^{-C^{*}} &= Ce^{-\frac{\alpha A}{\dot{m}c_{p}}} \\ T_{f} &= T_{w} - Ce^{-\frac{\alpha A}{\dot{m}c_{p}}} \end{split}$$

Employing the initial condition of the fluid the integration constant can be determined.

$$T_{f,0} = T_{f,in} = T_w - Ce^{\frac{\alpha \mathcal{X}}{\text{mcp}}}$$

$$C = T_w - T_{f,in}$$
(A.3)

Finally the outlet temperature can be evaluated as

$$T_{f,o} = T_w - (T_w - T_{f,in})e^{-\frac{\alpha A}{\text{incp}}}$$
 (A.4)

The exponent is similar to that is usually called Number of Transfer Units (NTU).

$$NTU \equiv \frac{\alpha_{\text{tot}}A}{\dot{m}c_{p}} \tag{A.5}$$

where  $\alpha_{tot}$  is the global HTC, which accounts for two interacting fluids in the HEX.

Employing eq. (A.4), the total heat transfer rate can be evaluated without knowing the outlet temperature of the fluid.

$$\dot{Q} = \dot{m}c_{p}[T_{w} - (T_{w} - T_{f,i})e^{-\frac{\alpha A}{\dot{m}c_{p}}} - T_{f,i}] 
= \dot{m}c_{p}[(T_{w} - T_{f,i})(1 - e^{-\frac{\alpha A}{\dot{m}c_{p}}})]$$
(A.6)

This approach employs the exponential temperature profile to evaluate the heat transfer rate between the wall and the fluid.

#### Linear temperature profile

Assuming a linear temperature profile in the portion of fluid involved in the process, the heat transfer rate is evaluated with:

$$\dot{Q} = \dot{\mathfrak{m}} c_{\mathfrak{p}} (\mathsf{T}_{w} - \mathsf{T}_{\mathsf{f.m}}) \tag{A.7}$$

where  $T_{f,m}$  is the mean temperature between the inlet and the outlet.

$$T_{f,m} = \frac{T_{f,i} + T_{f,o}}{2}$$
 (A.8)

#### Comparison of the accuracy of two methods

In this section the accuracy of the evaluation of the heat transfer rate between a wall maintained at constant temperature and the fluid realized employing the linear profile assumption is compared with the results obtained using the exponential profile.

Figure 120 shows on the ordinate the deviation between the linear and the exponential method normalised by the latter, and on the abscissa the relative temperature difference calculated as:

$$\Delta T = \frac{T_{f,o} - T_w}{T_{f,i} - T_w}; \tag{A.9}$$

From fig. 120 is possible to appreciate that the error made employing the linear profile assumption reduces below the 5% if the relative temperature difference is larger than 50%.

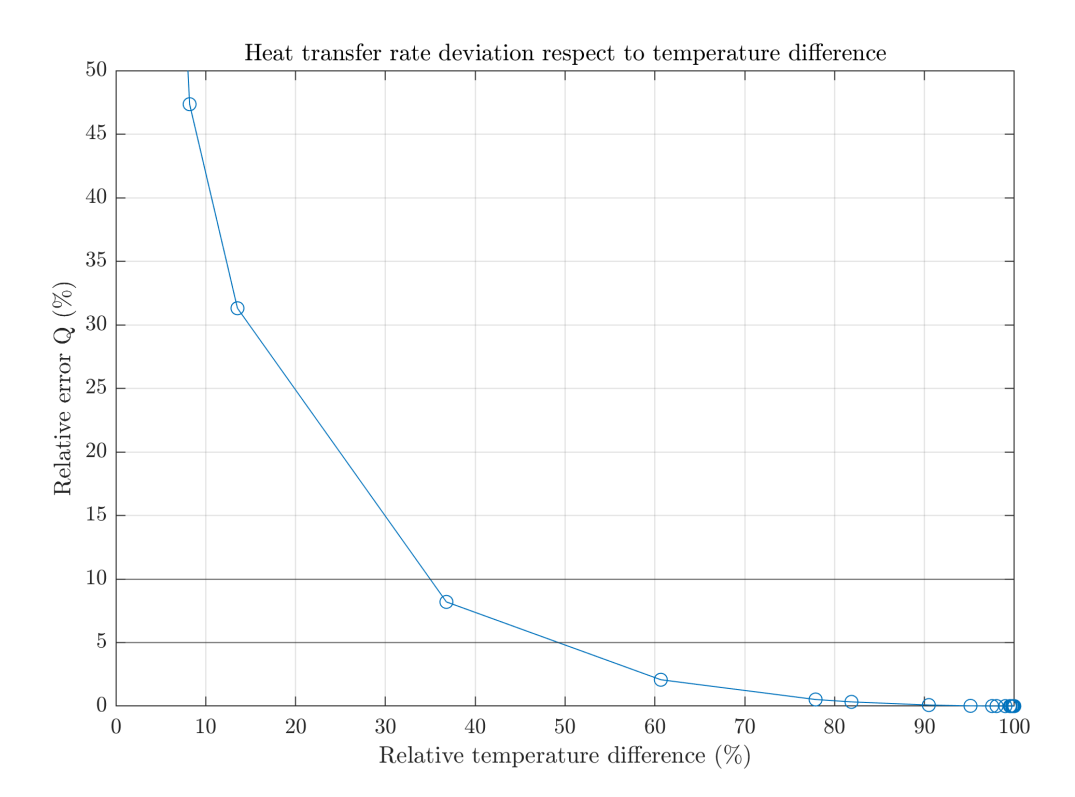


Figure 120: The graph shows the error made computing the heat transfer rate employing the mean temperature instead the exponential mean temperature profile.

## B | HEAT TRANSFER CORRELATIONS

## B.1 HEAT TRANSFER CORRELATIONS FOR BRAZED PLATE HEAT EXCHANGERS (BPHEX)

The heat transfer coefficient relies on the flow regime and on the physical properties of the working fluid, as well as on the configuration of the BPHEX in term of number of plates, channels and passages. During phase change, the heat transfer conditions strongly differ from those under single phase. So *ad hoc* correlations are developed to compute the heat transfer during boiling and condensation.

#### B.1.1 BPHEX geometrical parameters

The main parameters involved in the definition of the HTC correlation in BPHEXs are reported in table 21. These parameters are employed for the development of the correlations to estimate the HTC.

#### B.1.2 Single phase flow

Many correlations are available for single phase flow in plate HEXs, and a critical review of them is provided by García-Cascales et al., 2007. Roberti, 2020 realised a interesting analysis of the behaviour of some available correlations for single phase flow of water and refrigerant in BPHEX for different flow regimes compatible with small refrigeration applications. With the aim of combining accuracy and

Symbol	Description	UoM
В	Plate width	m
L	Plate length	m
b	Offset between two plates	m
ф	Plate area enlargement factor	-
β	Chevron angle	0
$n_{pl}$	Number of plates	-
$n_{ch,r}$	Number of refrigerant channel	-
$n_{ch,s}$	Number of secondary fluid channel	-

**Table 21:** Main geometrical employed in the HTC correlations for BPHEXs.

relative simplicity of the correlation, so as to reduce numerical issues and computation time, two correlations are selected to be employed in this work, those by Martin, 1996 and by Y. Kim, 1999.

An accurate correlation for single phase flow in plate HEXs was developed by Martin, 1996.

Martin

$$Nu = 0.122 \, Pr^{1/3} \, \left(\frac{\mu}{\mu_w}\right)^{1/6} \, \left(f \, Re^2 \sin 2\beta\right)^{0.374} \tag{B.1}$$

The f factor depends on the Chevron angle  $\beta$  and on the flow regime through the coefficients f<sub>0</sub> and f<sub>1</sub>

$$\frac{1}{\sqrt{f}} = \frac{\cos \beta}{(0.18 \tan \beta + 0.36 \sin \beta + f_0 \cos \beta)^{-1})^{1/2}} + \frac{1 - \cos \beta}{\sqrt{3.8 f_1}}$$
 (B.2)

$$\begin{cases} \text{Re} < 2000 \implies \begin{cases} f_0 = 64 \, \text{Re}^{-1} \\ f_1 = 597 \, \text{Re}^{-1} + 3.85 \end{cases} \\ \text{Re} \geqslant 2000 \implies \begin{cases} f_0 = (1.8 \, \log_{10} \, \text{Re} - 1.5)^{-2} \\ f_1 = 39 \, \text{Re}^{-0.289} \end{cases}$$
(B.3)

Another correlation for single phase flow employed in this work is provided by Y. Kim, 1999.

Y. Kim

Nu = 0.295 Re<sup>0.64</sup> Pr<sup>0.32</sup> 
$$\left(\frac{\pi}{2} - \beta \frac{\pi}{180}\right)^{0.09}$$
 (B.4)

#### Refrigerant two phase flow: boiling

Roberti, 2020 provides also a useful assessment of some HTC correlations for flow boiling in plate HEXs. The Longo, Mancin, et al., 2015 appears the more conservative especially for low Reynolds number, compatible with small VCSs. For this reason, this correlation is selected for the evaporator.

Longo, Mancin, et al., 2015 present a model for boiling developed from a set of experimental data. This model includes specific equations for the heat transfer coefficient in nucleate and convective boiling. For convective boiling, the HTC is a simple function of  $Re_{eq}$ 

Longo, Mancin, et al.

$$\alpha_{cb} = 0.122 \, \phi \, \frac{\kappa_l}{D_h} \, Re_{eq}^{0.8} \, Pr^{\frac{1}{3}}$$
 (B.5)

where  $Re_{eq}$  is

$$Re_{eq} = G \left[ (1 - x) + x \left( \frac{\rho_l}{\rho_v} \right)^{\frac{1}{2}} \right] \frac{D_h}{\mu_l}$$
 (B.6)

with the mass flux G calculated as

$$G = \frac{m}{n_{ch} W b}$$

The evaluation of the nucleate boiling contribution is obtained starting from the pool boiling correlation developed by Gorenflo, 1993.

$$\alpha_{nb} = 0.58 \, \phi \, \alpha_{nb,0} \, C_{Ra} \, F(\hat{p}) \, \left(\frac{q}{q_0}\right)^n \tag{B.7}$$

where the exponent n=0.467. Similarly to the Gorenflo correlation, the evaluation of the nucleate boiling coefficient is made starting from a HTC reference value  $\alpha_{nb,0}$  obtained experimentally or numerically under fixed operating conditions, in terms of heat flux  $q_0 = 20 \text{ kW m}^{-2}$ and roughness  $\epsilon_0$ =0.4 µm of the plate. This reference value  $\alpha_{nb,0}$  is dependent on the refrigerant and is available only for some substances, Gorenflo, 1993. In this work as guess value is assumed the  $\alpha_{nb,0}$  of the R134A refrigerant,  $\alpha_{nb,0} = 4200 \text{ W m}^{-2}$ . The coefficient  $C_{Ra}$  account for the dependence on roughness.

$$C_{R\alpha} = \left(\frac{R_{\alpha}}{0.4}\right)^{0.1333}$$

$$F(\hat{p}) = 1.2 \,\hat{p}^{0.27} + \left(2.5 + \frac{1}{1 - \hat{p}}\right) \,\hat{p}$$

$$\hat{p} = \frac{p}{p_{cr}}$$
(B.8)

While the function  $F(\hat{p})$  depends on the ratio operating and the critical pressure  $\hat{p} = p/p_{crit}$ .

$$F(\hat{p}) = 1.2 \,\hat{p}^{0,27} + \left(2.5 + \frac{1}{1 - \hat{p}}\right) \,\hat{p} \tag{B.9}$$

According to other boiling models Manservisi and Scardovelli, 2012, the final HTC is the maximum value of the nucleate and convective boiling heat transfer coefficient.

$$\alpha_b = \max(\alpha_{nb}, \alpha_{cb}) \tag{B.10}$$

#### Condensation

According to Roberti, 2020, after a comparison with other available correlations for the HTC of a condensing refrigerant, in this work that by Longo, Righetti, and Zilio, 2015 is selected. Based on the flow regime, they distinguish two heat transfer processes, the first is gravity driven and the second which is more influenced by the forced convection.

Longo, Righetti, and Zilio

For  $Re_{eq}$  < 1600 natural convection prevails, and the HTC is evaluated with a model derived from the work of Nusselt, 1916 on vertical plate.

$$\alpha_{\text{grav}} = 0.943 \, \phi \, \left( \frac{\lambda_l^3 \, \rho_l^2 \, g \, h_{l\nu}}{\mu_l \, \Delta T \, L} \right)^{\frac{1}{4}} \tag{B.11}$$

where  $h_{l\nu}$  is the latent heat of condensation and  $\Delta T$  is the temperature difference between the wall and the refrigerant.

For  $Re_{eq} > 1600$  forced convection prevails and the process is driven by the mass flux G.

$$\alpha_{fc} = 1.875 \, \phi \, \frac{\lambda_l}{D_h} \, Re_{eq}^{0.445} \, Pr^{\frac{1}{3}}$$
 (B.12)

### BIBLIOGRAPHY

- AHRI 540 (SI/I-P): Performance Rating of Positive Displacement Refrigerant Compressors and Compressor Units. (2020). Air-Conditioning, Heating, and Refrigeration Institute. Retrieved October 27, 2024, from https://www.ahrinet.org/search-standards/ahri-540si-i-p-performance-rating-positive-displacement-refrigerantcompressors-and-compressor
- American Society of Heating, R., & Engineers, A.-C. (2018). 2018

  ASHRAE Handbook: Refrigeration. Ashrae. https://books.google.
  it/books?id=-R7GwwEACAAJ
- Bell, I. H., Wronski, J., Quoilin, S., & Lemort, V. (2014). Pure and Pseudo-pure Fluid Thermophysical Property Evaluation and the Open-Source Thermophysical Property Library CoolProp. *Industrial & Engineering Chemistry Research*, 53(6), 2498–2508. https://doi.org/10.1021/ie4033999
- Bendapudi, S., Braun, J. E., & Groll, E. A. (2005). Dynamic Model of a Centrifugal Chiller System-Model Development, Numerical Study, and Validation. *ASHRAE Transactions*, 111, 132–148. Retrieved March 7, 2023, from https://www.proquest.com/docview/192517131/citation/F379EEF8747C456EPQ/1
- Bendapudi, S., Braun, J. E., & Groll, E. A. (2008). A comparison of moving-boundary and finite-volume formulations for transients in centrifugal chillers. *International journal of refrigeration*, 31(8), 1437–1452.
- Brkić, D. (2011). Review of explicit approximations to the Colebrook relation for flow friction. *Journal of Petroleum Science and Engineering*, 77(1), 34–48. https://doi.org/10.1016/j.petrol.2011.02.006
- Carel. (2010). E2V: Proportional electronic expansion valve.
- Carel. (2018). E2V-Z: Electronic valves for refrigeration Performance and simplicity without compromises.
- Carel. (2023). Passive Temperature Probes Carel.
- Çengel, Y. A., & Cimbala, J. M. (2014). *Fluid mechanics: Fundamentals and applications* (Third edition). McGraw Hill.
- Chi, J., & Didion, D. (1982). A simulation model of the transient performance of a heat pump. *International Journal of refrigeration*, 5(3), 176–184.
- Churchill, S. (1977). Friction Factor Equation Spans All Fluid Flow Regimes. *Chemical Engineering*, 91–92.
- Cicchitti, A., Lombardi, C., Silvestri, M., Soldaini, G., & Zavattarelli, R. (1959). *Two-phase cooling experiments: Pressure drop, heat transfer*

- and burnout measurements. Centro Informazioni Studi Esperienze, Milan.
- Colebrook, C. F. (1937). Experiments with fluid friction in roughened pipes. Proceedings of the Royal Society of London. Series A - Mathematical and Physical Sciences, 161(906), 367–381. https://doi.org/ 10.1098/rspa.1937.0150
- Control, H. (2020). Vortex flow sensor 210 Huba Control.
- Control, H. (2024). Pressure sensor 520 Huba Control.
- Copeland. (2023). OSH-407 OS.
- Desideri, A., Dechesne, B., Wronski, J., Van den Broek, M., Gusev, S., Lemort, V., & Quoilin, S. (2016). Comparison of Moving Boundary and Finite-Volume Heat Exchanger Models in the Modelica Language. Energies, 9(5), 339. https://doi.org/10. 3390/en9050339
- Dhar, M. (1978). Transient analysis of refrigeration system. https://docs. lib.purdue.edu/dissertations/AAI8113789
- Dukler, A. E., Wicks, M., & Cleveland, R. G. (1964). Frictional pressure drop in two-phase flow: B. An approach through similarity analysis. AIChE Journal, 10(1), 44-51. https://doi.org/10.1002/ aic.690100118
- Dupont, J.-L., Domanski, P., Lebrun, P., & Ziegler, F. (2019). 38th Note on Refrigeration Technologies: The Role of Refrigeration in the Global Economy. International Institute of Refrigeration (IIR). https: //doi.org/10.18462/IIF.NITEC38.06.2019
- Duprez, M.-E., Dumont, E., & Frère, M. (2007). Modelling of reciprocating and scroll compressors. International Journal of Refrigeration, 30(5), 873–886. https://doi.org/10.1016/j.ijrefrig.2006.11.014
- Eames, I. W., Milazzo, A., & Maidment, G. G. (2014). Modelling thermostatic expansion valves. International Journal of Refrigeration, 38, 189–197. https://doi.org/10.1016/j.ijrefrig.2013.06.010
- EN 12900:2013 Refrigerant compressors-rating conditions, tolerances and presentation of manufacturer's performance data. (2013).
- Fasl, J. (2013). Modeling and control of hybrid vapor compression cycles [Doctoral dissertation, University of Illinois at Urbana-Champaign].
- Field, B., & Hrnjak, P. (2007). Two-Phase Pressure Drop and Flow Regime of Refrigerants and Refrigerant-Oil Mixtures in Small Channels.
- Friedel, L., et al. (1980). Pressure drop during gas/vapor-liquid flow in pipes. Int. Chem. Eng, 20(3), 352-367.
- García-Cascales, J., Vera-García, F., Corberán-Salvador, J., & Gonzálvez-Maciá, J. (2007). Assessment of boiling and condensation heat transfer correlations in the modelling of plate heat exchangers. International Journal of Refrigeration, 30(6), 1029–1041. https:// doi.org/10.1016/j.ijrefrig.2007.01.004

- Giuffrida, A. (2016). A semi-empirical method for assessing the performance of an open-drive screw refrigeration compressor. Applied Thermal Engineering, 93, 813–823. https://doi.org/10.1016/j. applthermaleng.2015.10.023
- Gorenflo, D. (1993). Pool boiling. In VDI Heat Atlas, (Dusseldorf, Ha 1-25).
- Grald, E. W., & MacArthur, J. W. (1992). A moving-boundary formulation for modeling time-dependent two-phase flows. International Journal of Heat and Fluid Flow, 13(3), 266-272.
- Haaland, S. E. (1983). Simple and Explicit Formulas for the Friction Factor in Turbulent Pipe Flow. Journal of Fluids Engineering, 105(1), 89–90. https://doi.org/10.1115/1.3240948
- Hauser, E. (2022). Proline Promass E 300 Coriolis flowmeter Technical Information.
- Hauser, E. (2024). Proline Promass E 300 Coriolis flowmeter Operating Instruction.
- He, X.-D., Liu, S., Asada, H. H., & Itoh, H. (1998). Multivariable Control of Vapor Compression Systems. HVAC&R Research, 4(3), 205-230. https://doi.org/10.1080/10789669.1998.10391401
- Huber, M., Harvey, A., Lemmon, E., Hardin, G., Bell, I., & McLinden, M. (2018). NIST Reference Fluid Thermodynamic and Transport Properties Database (REFPROP) Version 10 - SRD 23. [object Object]. https://doi.org/10.18434/T4/1502528
- Kim, M., Yoon, S. H., Domanski, P. A., & Vance Payne, W. (2008). Design of a steady-state detector for fault detection and diagnosis of a residential air conditioner. International Journal of Refrigeration, 31(5), 790-799. https://doi.org/10.1016/j.ijrefrig.2007.11. 008
- Kim, Y. M., Kim, C. G., & Favrat, D. (2012). Transcritical or supercritical CO2 cycles using both low- and high-temperature heat sources. Energy, 43(1), 402–415. https://doi.org/10.1016/j.energy.2012. 03.076
- Kim, Y. (1999). An Experimental Study on Evaporation Heat Transfer Characteristics and Pressure Drop in Plate Heat Exchanger [M.S.Thesis]. Yonsei University.
- Li, B., & Alleyne, A. G. (2010). A dynamic model of a vapor compression cycle with shut-down and start-up operations. International Journal of refrigeration, 33(3), 538-552.
- Li, P., Qiao, H., Li, Y., Seem, J. E., Winkler, J., & Li, X. (2014). Recent advances in dynamic modeling of HVAC equipment. Part 1: Equipment modeling. HVAC&R Research, 20(1), 136–149.
- Li, W. (2012). Simplified steady-state modeling for hermetic compressors with focus on extrapolation. International Journal of Refrigeration, 35(6), 1722-1733. https://doi.org/10.1016/j.ijrefrig.2012. 03.008

- Li, W. (2013). Simplified steady-state modeling for variable speed compressor. *Applied Thermal Engineering*, 50(1), 318–326. https: //doi.org/10.1016/j.applthermaleng.2012.08.041
- Lockhart, W. R., & Martinelli, R. C. (1949). Proposed correlation of data for isothermal two-phase, two-component flow in pipes. Chemical engineering progress, 45(1), 39-48.
- Longo, G. A., & Gasparella, A. (2003). Unsteady state analysis of the compression cycle of a hermetic reciprocating compressor. International Journal of Refrigeration, 26(6), 681–689. https://doi. org/10.1016/S0140-7007(03)00024-0
- Longo, G. A., Mancin, S., Righetti, G., & Zilio, C. (2015). A new model for refrigerant boiling inside brazed plate heat exchangers (BPHEs). International Journal of Heat and Mass Transfer, 91, 144-149.
- Longo, G. A., Righetti, G., & Zilio, C. (2015). A new computational procedure for refrigerant condensation inside herringbone-type Brazed Plate Heat Exchangers. International Journal of Heat and Mass Transfer, 82, 530-536.
- Lucchi, M. (2020, March). Dynamic models for the analysis of vapourcompression refrigerating machines. http://amsdottorato.unibo.it/
- MacArthur, J. W. (1984). Transient heat pump behaviour: A theoretical investigation. *International Journal of refrigeration*, 7(2), 123–132.
- Manservisi, S., & Scardovelli, R. (2012). Termodinamica dei flussi bifase. Società Editrice Esculapio.
- Martin, H. (1996). A theoretical approach to predict the performance of chevron-type plate heat exchangers. Chemical Engineering and Processing: Process Intensification, 35(4), 301–310. https://doi. org/10.1016/0255-2701(95)04129-X
- MathWorks. (2024a). Lookup Tables Matlab & Simulink. Retrieved November 12, 2024, from https://it.mathworks.com/help/ simulink/lookup-tables.html?lang=en
- MathWorks. (2024b). Smooth response data Matlab MathWorks Italia. Retrieved November 6, 2024, from https://it.mathworks. com/help/curvefit/smooth.html#mw\_7695cbca-640d-4029a239-81c9dd8192do
- McAdams, W. H., Woods, W. K., & Heroman, L. C. (1942). Vaporization Inside Horizontal Tubes—II Benzene-Oil Mixtures. Journal of Fluids Engineering, 64(3), 193–199. https://doi.org/10.1115/1. 4019013
- McKinley, T. L., & Alleyne, A. G. (2008). An advanced nonlinear switched heat exchanger model for vapor compression cycles using the moving-boundary method. International Journal of refrigeration, 31(7), 1253-1264.

- Molinaroli, L., Joppolo, C. M., & De Antonellis, S. (2017). A semiempirical model for hermetic rolling piston compressors. International Journal of Refrigeration, 79, 226-237. https://doi.org/10. 1016/j.ijrefrig.2017.04.015
- Navarro, E., Granryd, E., Urchueguía, J. F., & Corberán, J. M. (2007). A phenomenological model for analyzing reciprocating compressors. International Journal of Refrigeration, 30(7), 1254–1265. https://doi.org/10.1016/j.ijrefrig.2007.02.006
- Negrão, C. O. R., Erthal, R. H., Andrade, D. E. V., & Silva, L. W. da. (2011). A semi-empirical model for the unsteady-state simulation of reciprocating compressors for household refrigeration applications. *Applied Thermal Engineering*, 31(6), 1114–1124. https: //doi.org/10.1016/j.applthermaleng.2010.12.006
- Nusselt, W. (1916). Die oberflachenkondensation des wasserdampfes. https://api.semanticscholar.org/CorpusID:222445957
- Pangborn, H., Alleyne, A. G., & Wu, N. (2015). A comparison between finite volume and switched moving boundary approaches for dynamic vapor compression system modeling. International Journal of Refrigeration, 53, 101-114. https://doi.org/10.1016/j. ijrefrig.2015.01.009
- Rasmussen, B. D., & Jakobsen, A. (2000). Review of Compressor Models and Performance Characterizing Variables.
- Rasmussen, B. P. (2012). Dynamic modeling for vapor compression systems—Part I: Literature review. HVAC&R Research, 18(5), 934-955.
- Rasmussen, B. P., & Alleyne, A. G. (2004). Control-Oriented Modeling of Transcritical Vapor Compression Systems. Journal of Dynamic Systems, Measurement, and Control, 126(1), 54-64. https://doi. org/10.1115/1.1648312
- Rasmussen, B. P., & Shenoy, B. (2012). Dynamic modeling for vapor compression systems—Part II: Simulation tutorial. HVAC&R Research, 18(5), 956-973.
- Reindl, D. I. J. D. T., & Klein, P. S. A. (2000). A semi-empirical method for representing domestic refrigerator/freezer compressor calorimeter test data. ASHRAE transactions.
- Rigola, J., Pérez-Segarra, C. D., Oliva, A., Serra, J. M., Escriba, M., & Pons, J. (2001). Parametric study of hermetic reciprocating compressors-detailed numerical analysis and experimental validation. Proceedings of the International Conference on Compressors and Their Systems, City University, London, UK, 337-348.
- Roberti, G. (2020, January 9). Steady-state Modelling of a Vapor Compression Refrigeration Cycle [Tesi di laurea]. Retrieved March 28, 2023, from https://amslaurea.unibo.it/19438/
- Salazar-Herran, E., Martin-Escudero, K., del Portillo-Valdes, L. A., Flores-Abascal, I., & Romero-Anton, N. (2020). Flexible dynamic

- model of PHEX for transient simulations in Matlab/Simulink using finite control volume method. International Journal of Refrigeration, 110, 83-94. https://doi.org/10.1016/j.ijrefrig.2019.11.003
- Sarr, J., Dupont, J.-L., & Guilpart, J. (2021). The carbon footprint of the cold chain, 7th Informatory Note on Refrigeration and Food. International Institute of Refrigeration (IIR). Retrieved December 28, 2023, from https://iifiir.org/datacite\_notices/143457
- Silmet. (2024). ICE: Copper tubes for air-conditioning and refrigeration systems. Silmet. Retrieved November 22, 2024, from https:// www.silmet.com/en/copper-tubes/products/ice/
- Willatzen, M., Pettit, N. B. O. L., & Ploug-Sørensen, L. (1998). A general dynamic simulation model for evaporators and condensers in refrigeration. part i: Moving-boundary formulation of two-phase flows with heat exchange: Modèle général dynamique pour évaporateurs et condenseurs frigorifiques. partic i: Formulation des conditions aux limites variables de flux biphasiques avec échange de chaleur. International Journal of refrigeration, 21(5), 398-403.
- Winandy, E., Saavedra O, C., & Lebrun, J. (2002). Simplified modelling of an open-type reciprocating compressor. International Journal of Thermal Sciences, 41(2), 183-192. https://doi.org/10.1016/S1290-0729(01)01296-0
- Yang, L., Zhao, L.-X., Zhang, C.-L., & Gu, B. (2009). Loss-efficiency model of single and variable-speed compressors using neural networks. International Journal of Refrigeration, 32(6), 1423-1432. https://doi.org/10.1016/j.ijrefrig.2009.03.006
- Zhang, W.-J., Zhang, C.-L., & Ding, G.-L. (2009). On three forms of momentum equation in transient modeling of residential refrigeration systems. International Journal of Refrigeration, 32(5), 938–944. https://doi.org/10.1016/j.ijrefrig.2008.11.002